Harminder Singh

Particle image velocimetry and computational fluid dynamics applied to study the effect of hydrodynamics forces on animal cells cultivated in Taylor vortex bioreactor

Universidade Federal do São Carlor – UFSCar

Programa de Pós-Graduação em Engenharia Química – PPGEQ

Laboratório de Technologia de Cultivo Celular – LATECC

Orientador: Prof. Dr. Claudio Alberto Torres Suazo

São Carlos - SP

Março 2016

UNIVERSIDADE FEDERAL DE SÃO CARLOS
LABORATÓRIO DE TECHNOLOGIA DE CULTIVO CELULAR
DEPARTAMENTO DE ENGENHARIA QUÍMICA

HARMINDER SINGH

PARTICLE IMAGE VELOCIMETRY AND COMPUTATIONAL FLUID DYNAMICS APPLIED TO STUDY THE EFFECT OF HYDRODYNAMICS FORCES ON ANIMAL CELLS CULTIVATED IN TAYLOR VORTEX BIOREACTOR

Tese apresentado ao Programa de Pós-Graduação em Engenharia Química para obtenção do titulo de doutor em Engenharia Química.

Orientação: Prof. Dr. Claudio Alberto Torres Suazo

SÃO CARLOS - SP
2016

Ficha catalográfica elaborada pelo DePT da Biblioteca Comunitária UFSCar
Processamento Técnico
com os dados fornecidos pelo(a) autor(a)

Singh, Harminder
S617p Particle image velocimetry and computational fluid dynamics applied to study the effect of hydrodynamics forces on animal cells cultivated in Taylor vortex bioreactor / Harminder Singh. -- São Carlos : UFSCar, 2016.
203 p.

Tese (Doutorado) -- Universidade Federal de São Carlos, 2016.

1. DNS. 2. LES-WALE. 3. RANS. 4. Viscous energy dissipation rate. 5. Turbulence. I. Título.

MEMBROS DA BANCA EXAMINADORA DA DEFESA DE TESE DE HARMINDER SINGH APRESENTADA AO PROGRAMA DE PÓS-GRADUAÇÃO EM ENGENHARIA QUÍMICA DA UNIVERSIDADE FEDERAL DE SÃO CARLOS, EM 28 DE MARÇO DE 2016.

BANCA EXAMINADORA:

Claudio Alberto Torres Suazo
Orientador, UFSCar

R Giordano

Roberto de Campos Giordano
UFSCar

José Antonio Silveira Gonçalves
UFSCar

Resende

Miriam Maria de Resende
UFU

Santiago

Patrícia Aparecida Santiago Monteiro
USP

Agradecimentos

First and foremost, I would like to sincerely thank the Almighty, the One True Lord, for blessing the knowledge, will power, patience and numerous other skills required to become a researcher. There are three direct contributors who have enabled me to reach this stage of completing this thesis: my supervisor Prof. Dr. Claudio A. T. Suazo, "doutorado sanduìche"supervisor Prof. Dr. Alain Liné and financial supporter CNPq, Brasil. Without the conjunction of these three stepping stones, this study would not have been feasible. For the financial support, i would like to offer my gratitude to the Conselho Nacional de Desenvolvimento Cientifico e Tecnologico (CNPq), Brasil for the postgraduate (processo nº 140756/2012-4) and "Doutorado Sanduíche"(processo nº - 241739/2012-8) Scholarship programs.

I am really grateful to Prof. Dr. Claudio A. T. Suazo for always having faith in my capabilities, giving me space and independence, and at the same time guiding me through whenever needed. His vast knowledge and experience in the field of bioreactors always opened various doors when things looked bleak. Apart from his able guidance, friendliness and carefulness, his support will always be appreciated.

On the third front, i am indebted to Prof Dr. Alain Liné for accepting me as his "doutorado sanduìche"student, his support, care and participation in this work even now, long after the program ended in April 2014. Sharing of his wonderful ideas, vast knowledge and experience in the field of hydrodynamics kept me alive and ticking, and gave direction every time i got a bit lost. Major part of this thesis work has been conducted under his able guidance, and his critique only enhanced the quality of this work.

I am thankful to Prof Dr. Roberto de Campos Giordano and Prof. Dr. José Antônio Silveira Gonçalves for their support, and sharing of their thoughts which helped in the improvement of this work. I am also grateful to all of the technicians, post-grads, and staff of the Chemical Engineering department in making this an enjoyable place to work.

Finally, I would like to give my heartfelt thanks to all the family members, especially my spouse Tatiana Villela de Andrade Monteiro, and friends for their support from the beginning to the end of this project. They are the indirect contributors which held my hand and kept me up and floating in this vast ocean so that i could benefit something from the direct contributors.

"Mamma Man seu kaj hai,man saddey sidd hoi//
A soul's primal aim of being born as a human is to tame the mind.
Only if the mind can be tamed,
that a soul's objective can be achieved.
Kabeer

Resumo

O biorreator de Vórtices de Taylor (TVB) está se tornando uma nova descoberta, devido ao seu cisalhamento mais suave e fluxo homogêoneo em comparações com os biorretores de tanque agitados. Na literatura acadêmica há pouca informação sobre este biorreator quanto a taxa de dissipação de energia viscosa (VEDR), que é o parêmetro ideal para caracterizar a morte celular, e seus aspectos geométricos, que afetam o cultivo das células animais, resultando em baixa eficiência. A presente pesquisa, portanto, objetivou focar na estimativa da VEDR de fluxo médio e de energia cinética turbulenta (TKE) no TVB usando os métodos: experimental de 2D de velocimetria das partículas por imagem (PIV) e númerico de dinâmica de fluídos computacional (CFD) com diferentes modelos de turbulência, principalmente a simulação numérica direta (DNS). E focar nos aspectos geométricos do impacto da área de apuramento entre o cilindo interno e externo e na forma da base do cilindro externo na estrutura de fluxo do TVB.

Os dois métodos experimental e númerico demonstraram que, em aproximadamente 80 % da área lateral entre os cilindros interno e externo onde as células vão passar a maior parte do tempo, a magnitude de velocidade é de cerca de 50 % da máxima e os valores de VEDR são 10 vezes menores do que nas paredes. Qualitativamente, o DNS mostrou boas comparações dos fluxos médios e dos parâmetros turbulentos em relação aos resultados apresentados pelo PIV para o TVB. No entanto, quantitativamente, apenas as previsões médias de velocidade estão em boa concordância com os dados do PIV, pois os parâmetros turbulentos foram sub-estimados. Entre os diferentes modelos de turbulência utilizados, o modelo simulação de grande escala (LES) - Wall Adapting Local Eddy-Viscosity apresentou a melhor comparação com os dados do DNS para todos os parâmetros do fluxo. O modelo de estresse Reynolds e LES - Smagorinsky, por sua vez, apresentaram as piores comparações. Os modelos de duas equações de RANS, entretanto, apesar de estimarem bem os componentes de velocidade média em comparação com os dados do modelo DNS, não captaram bem as estruturas de fluxo dos componentes de turbulência. Quanto aos aspectos geométricos, as alterações nas características da área de apuramento entre o cilindo interno e externo e a estrutura curva da base do cilindro externo, que são de importância prática em tanque agitados, neste estudo, afetaram negativamente o fluxo no TVB devido ao seu baixo componente de velocidade axial. Por fim, a comparação entre o TVB e o Spinner Flask, considerado também um biorretor com baixo cissalhamento, demostrou que para Re/Re_T semelhante, os valores máximo e médio do VEDR foram sempre inferiores, e devido à diferença muito menor entre o os valores máximo e médio, o TVB apresenta estruturas mais uniformes em comparação com o Spinner Flask.

Palavras-chave: DNS. LES-WALE. RANS. dissipação de energia viscosa. turbulência.

Abstract

Taylor-Vortex reactor (TVB) is fast becoming the next bioreactor to culture animal cells due to milder shear and homogeneous flow structures through-out the bioreactor in comparison to the traditional stirred vessels. However, there is little information in the literature for the TVB on the viscous energy dissipation rate (VEDR), which is considered the ideal parameter to characterize the cell death, and its geometrical aspects, which may affect the culture of animal cells resulting in poor efficiency. Consequently, this work focuses on: the estimation of the VEDR of mean flow and turbulent kinetic energy (TKE) using an experimental 2D particle image velocimetry (PIV) method and a computational fluid dynamics (CFD) method using different turbulence models, principally the direct numerical simulation (DNS) model; and, the impact of the off-bottom clearance area and the external cylinder's bottom shape on the flow structures of TVB.

Both numerical and experimental methods confirm that the bulk zone comprising of the 80 % of the gap-width, where the cell cultures will spend most of the time, has a near constant velocity magnitude of around 50 % of the tip velocity and VEDR values which are around 10 times lower than at the walls. Qualitatively, the DNS model predicted well the flow structure of both mean and turbulence parameters in comparison with the experimental PIV predictions. However, quantitatively only the mean velocity predictions are in good agreement with the PIV data with certain amount of under-estimation of the turbulence parameters. Among different turbulence models, the large eddy simulation (LES) - wall adapting local eddy-viscosity (WALE) model presented best comparison with the DNS model data for all the flow parameters; while, the Reynolds stress model and the LES-Smagorinsky models were the poorest. On the other hand, the Reynolds averaged Navier-Stokes (RANS) based two equation models estimated well the mean velocity components in comparison with the DNS model data, but could not capture well the flow structures of the turbulence components.

The geometrical features of curved surface of outer bottom and off-bottom clearance area which are of practical importance in stirred vessels, impact adversely the flow structures in the TVB due to poor axial velocity component. In comparison with the spinner vessel, a stirred tank type bioeactor but with lower shear, for similar Re/Re_T ratio, the maximum and mean VEDR were always found to be of lower magnitude values, and due to much less difference between the maximum and the mean values, the TVB presents more uniform structures in comparison to the spinner vessel.

Keywords: DNS. LES-WALE. RANS. viscous energy dissipation rate. turbulence.

Lista de ilustrações

Figura 1 – Annual sales of recombinant proteins and monoclonal antibodies in the 2008-2013 period. Source: Ecker, Jones e Levine (2015). 31

Figura 2 – PIV system consisting of the TVB, laser, camera, synchronization system and computer. 45

Figura 3 – Convergence statistics of moment of order one (a) and two (b) on a horizontal plane located at Z_L=0.725 and radially at R_b=0.082. 48

Figura 4 – Concentration of particles in a horizontal plane in the TVB at two different rotational rates: 114 (the one behind) and 30 (the one in front) rpm without grid (a) and with a 32 square grid (b). 50

Figura 5 – Impact of particle size on the estimations of mean tangential velocity (a) and squared fluctuating velocity (b) for the horizontal plane located at $Z_h = 0.725 \pm 0.005$. 52

Figura 6 – Impact of time-step on the estimations of mean tangential velocity (a) and squared fluctuating velocity (b) for the horizontal plane located at $Z_h = 0.725 \pm 0.005$ using particle size of 20 μm. 54

Figura 7 – Influence of the time-step and particle size on the VEDR of mean flow kinetic energy. 55

Figura 8 – Radial profile of mean tangential velocity at different overlap ratios and ICS values at $Z_L = 0.725 \pm 0.005$. 56

Figura 9 – Radial profile of squared fluctuating tangential velocity at different overlap ratios and ICS values at $Z_L = 0.725 \pm 0.005$. 58

Figura 10 – Radial profile of the viscous dissipation of mean flow kinetic energy at different overlap ratios and ICS values at $Z_L = 0.725 \pm 0.005$. 59

Figura 11 – Radial profile of the viscous dissipation of mean flow kinetic energy at different overlap ratios and ICS values at $Z_L = 0.725 \pm 0.005$. 60

Figura 12 – Radial profile of the viscous dissipation of turbulent kinetic energy at different overlap ratios and ICS values at $Z_L = 0.725 \pm 0.005$. 61

Figura 13 – Figure no 20 of Tokgoz et al. (2012) presenting dissipation rate estimations for changing interrogation window sizes (IW) for Re_s=14,000 with exact counter-rotation of cylinders. 75 % overalap ratio was used for all IWs. 62

Figura 14 – Influence of the dimensionless spatial resolution of the maximum viscous dissipation of turbulent kinetic energy estimated at $Z_L = 0.725 \pm 0.005$ for different rotational speeds at different ICS and overlap ratios. . . . 62

Figura 15 – The tangential (a) and radial (b) velocity flow profiles at 114 rpm. . . 64

Figura 16 – The tangential (a) and radial (b) velocity flow profiles at 90 rpm. . . . 65

Figura 17 – The tangential (a) and radial (b) velocity flow profiles at 70 rpm. . . . 66
Figura 18 – The tangential (a) and radial (b) velocity flow profiles at 50 rpm. . . . 67
Figura 19 – The tangential (a) and radial b) velocity flow profiles at 30rpm. 68
Figura 20 – The total viscosity at different rotational speeds in the center of vortex region. 71
Figura 21 – The evaluation of the constant C presented in the Equation 2.14. . . . 72
Figura 22 – The log-law profile of the velocity in the center of vortex region of the inner cylinder boundary layer. 73
Figura 23 – The tangential (a) and radial (b) normal stress profiles at 114 rpm. . . 74
Figura 24 – The tangential (a) and radial (b) normal stress profiles at 90 rpm. . . 75
Figura 25 – The tangential (a) and radial (b) normal stress profiles at 70 rpm. . . 76
Figura 26 – The tangential (a) and radial (b) normal stress profiles at 50 rpm. . . 77
Figura 27 – The tangential (a) and radial b) normal stress profiles at 30rpm. . . . 78
Figura 28 – The Reynolds shear stress, $\overline{u'_r u'_\theta}$, profiles at 114rpm. 80
Figura 29 – The Reynolds shear stress, $\overline{u'_r u'_\theta}$, profiles at 90 (a) and 70 (b) rpm. . . 81
Figura 30 – The Reynolds shear stress, $\overline{u'_r u'_\theta}$, profiles at 50 (a) and 30 (b) rpm. . . 82
Figura 31 – The estimation of VEDR of mean flow kinetic energy and its 5 gradients at Z_L= 0.725 ± 0.005. 83
Figura 32 – The estimation of VEDR of turbulent kinetic energy and its 5 gradients at Z_L= 0.725 ± 0.005. 84
Figura 33 – Comparison of isotropy assumptions on radial profiles at Z_L= 0.725 ± 0.005. 85
Figura 34 – Variation in the K_{ijkl} ratios influenced by the dimensionless spatial resolution for the radial profiles located at Z_L= 0.725 ± 0.005. 86
Figura 35 – The VEDR of the mean flow, ϵ_m, and turbulent, ϵ_t, kinetic energy at 114 rpm. 88
Figura 36 – The VEDR profiles of the mean flow, ϵ_m, and turbulent, ϵ_t, kinetic energy at 90 (a) and 70 (b) rpm. 89
Figura 37 – The VEDR profiles of the mean flow, ϵ_m, and turbulent, ϵ_t, kinetic energy at 50 (a) and 30 (b) rpm. 90
Figura 38 – The Kolmogorov scale for different rotational speeds at the center of vortex region. 93
Figura 39 – Geometry and mesh of the TVB used in the PIV experiments. 103
Figura 40 – Comparison of different grid sizes for the DNS and LES models of dimensionless mean axial velocity (a), radial velocity (b), tangential velocity (c) and mean square of fluctuating tangential velocity (d) axially at R_b=0.067. The legend is same in all figures. 104
Figura 41 – Validation of the numerical DNS model with the PIV results of dimensionless mean tangential (a) and radial (b) velocity components. 107

Figura 42 – Validation of the numerical DNS model with the PIV results of the log-law profiles for the tangential component at the inner (a) and outer (b) boundary layers. The $\kappa = 0.4$ and B = 5.2 is used in the log profile. 108
Figura 43 – Validation of the numerical DNS model with the PIV results of dimensionless mean squared fluctuating tangential velocity component. . . . 109
Figura 44 – Validation of the numerical DNS model with the PIV results of the VEDR of mean flow (a) and turbulence (b) kinetic energy. 110
Figura 45 – Identification of the Taylor's vortexes through λ_2 (a) and a pair of secondary Taylor's vortexes (b) for the DNS model. 116
Figura 46 – Identification of the Taylor's vortexes through λ_2 for the LES-WALE (a), and LES-Smagorinsky (b) models. 118
Figura 47 – Identification of the Taylor's vortexes through λ_2 for the k-ϵ (a) and RSM (b) models. 119
Figura 48 – Identification of the Taylor's vortexes through λ_2 for the SST (a), and SAS-SST (b) models. 120
Figura 49 – Radial profiles of the tangential velocity component near the outward region of a Taylor vortex. 121
Figura 50 – Radial profiles of the tangential velocity component near the inward region of a Taylor vortex. 121
Figura 51 – Radial profiles of the tangential velocity component near the center of vortex region of a Taylor vortex. 122
Figura 52 – Radial profiles of the radial velocity component near the outward region of a Taylor vortex. 124
Figura 53 – Radial profiles of the radial velocity component near the inward region of a Taylor vortex. 124
Figura 54 – Radial profiles of the radial velocity component near the center of vortex region of a Taylor vortex. 125
Figura 55 – Radial profiles of the axial velocity component near the outward region of a Taylor vortex. 126
Figura 56 – Radial profiles of the axial velocity component near the inward region of a Taylor vortex. 126
Figura 57 – Radial profiles of the axial velocity component near the center of vortex region of a Taylor vortex. 127
Figura 58 – Radial profiles of the log-law profiles of the axial mean of tangential velocity component for the inner (a) and outer (b) walls for the different turbulence models. 128
Figura 59 – Radial profiles of the log-law profiles for the inner (a) and outer (b) walls near the outward, center of vortex and inward regions of a Taylor vortex for the DNS model only. 130

Figura 60 – Radial profiles of the tangential velocity component near the outward region of a Taylor vortex. 131
Figura 61 – Radial profiles of the tangential velocity component near the inward region of a Taylor vortex. 131
Figura 62 – Radial profiles of the tangential velocity component near the center of vortex region of a Taylor vortex. 132
Figura 63 – Radial profiles of the radial velocity component near the outward region of a Taylor vortex. 132
Figura 64 – Radial profiles of the radial velocity component near the inward region of a Taylor vortex. 133
Figura 65 – Radial profiles of the radial velocity component near the center of vortex region of a Taylor vortex. 133
Figura 66 – Radial profiles of the axial velocity component near the outward region of a Taylor vortex. 134
Figura 67 – Radial profiles of the axial velocity component near the inward region of a Taylor vortex. 134
Figura 68 – Radial profiles of the axial velocity component near the center of vortex region of a Taylor vortex. 135
Figura 69 – Radial profiles of the tangential velocity component near the outward region of a Taylor vortex. 137
Figura 70 – Radial profiles of the tangential velocity component near the inward region of a Taylor vortex. 138
Figura 71 – Radial profiles of the tangential velocity component near the center of vortex region of a Taylor vortex. 138
Figura 72 – Radial profiles of the radial velocity component near the outward region of a Taylor vortex. 139
Figura 73 – Radial profiles of the radial velocity component near the inward region of a Taylor vortex. 139
Figura 74 – Radial profiles of the radial velocity component near the center of vortex region of a Taylor vortex. 140
Figura 75 – Radial profiles of the axial velocity component near the outward region of a Taylor vortex. 140
Figura 76 – Radial profiles of the axial velocity component near the inward region of a Taylor vortex. 141
Figura 77 – Radial profiles of the axial velocity component near the center of vortex region of a Taylor vortex. 141
Figura 78 – Radial profiles of the turbulent kinetic energy near the outward region of a Taylor vortex. 143

Figura 79 – Radial profiles of the turbulent kinetic energy near the inward region of a Taylor vortex. 144
Figura 80 – Radial profiles of the turbulent kinetic energy near the center of vortex region of a Taylor vortex. 144
Figura 81 – Comparison of the modeled turbulent kinetic energy with the one estimated from the velocity data in the center of vortex region of a Taylor vortex. 145
Figura 82 – Presentation of anisotropy through Lumley-Newmann and AG graphs axially near the walls, a) and b), and radially at the outward, center of vortex and inward regions of Taylor vortex, c) and d) respectively, for the DNS model. Note: in part a) and b) * represent the data near the inner and outer boundaries, while in c) and d) o, + and pentagram represent the outward, center of vortex and inward regions, respectively. 147
Figura 83 – The twelve gradients of the VEDR of mean flow (a) and turbulent (b) kinetic energy for the DNS model. 149
Figura 84 – The estimation of the VEDR of mean flow and turbulent kinetic energy of the DNS model in the outward, center of vortex and inward regions . 150
Figura 85 – The Kolmogorov estimations of the DNS model calculated through the VEDR of turbulent kinetic energy for the respective model and the mesh size. 152
Figura 86 – The estimation of the VEDR of TKE for the different turbulence model for axial mean of all the radial profiles. 153
Figura 87 – Three different shapes of the outer bottom cylinder at 15 mm off-bottom clearance and 1.968 × 10^6, 2.24 × 10^6 and 2.22 × 10^6 node meshes, respectively, for each geometry. Green and purple markers signify interface area and periodic boundaries respectively. Please note that not all interface areas and periodic boundaries are shown here. . . 160
Figura 88 – Radial flow profiles of the mean velocity for the mesh and time-step independence study in the TVB with 5 mm off-bottom clearance and flat bottom at Z_L=0.57. 163
Figura 89 – Mean velocity comparisons between the sliding mesh and MRF techniques in the TVB with 5 mm off-bottom clearance and flat bottom at Z_L=0.57. 164
Figura 90 – Comparison of numerical tangential velocity results with the PIV results of (COUFORT; BOUYER; LINE, 2005). 166
Figura 91 – Velocity and its three components in an axial profile located at R_b=0.009. 167
Figura 92 – Vector profile of the secondary vortex. 167
Figura 93 – Dimensionless mean velocity at various radial (a) and axial positions (b). 168
Figura 94 – Mean velocity vectors for different shapes and off-bottom clearance areas. 170

Figura 95 – Dimensionless mean velocity at different radial (a) and axial (b) positions for different geometry types. 171
Figura 96 – VEDR values for different hydrodynamic conditions in bioreactors and regions of lethal and sub-lethal impacts on cell lines. Adapted from Godoy-Silva et al. (2009). 172

Lista de tabelas

Tabela 1 – Various parameters used to correlate to cell death in a Stirred tank. . 34
Tabela 2 – Dimensions and geometrical characteristics of the TVB used in the PIV system. 44
Tabela 3 – Analytical estimations for the TVB used in the PIV system. 46
Tabela 4 – Different ICS and overlap windows tested at Z_L= 0.725 ± 0.005. . . . 47
Tabela 5 – Dimensionless Spatial resolution,$\delta/\langle\eta\rangle$, for different rotational velocities, ICS values and overlap ratios located at Z_L= 0.725 ± 0.005. 60
Tabela 6 – Mesh configurations used to model the TVB. 103
Tabela 7 – Torque and Power estimations in TVB through numerical and analytical methods. 154
Tabela 8 – Dimensions and geometrical characteristics of the TVB used for studying the different geometrical structures. 159
Tabela 9 – Grid independence study with the flat-bottom TVB at 5 mm off-bottom clearance. 162
Tabela 10 – Mean percentage difference of the mean velocity between different meshes. 163
Tabela 11 – Analytical and numerical estimations of the Taylor reactor at 200 rpm. 173
Tabela 12 – Summary of VEDR and Kolmogorov micro-scales for different geometrical conditions. 173

Lista de abreviaturas e siglas

CHO	**C**hinese **H**amster **O**vary
CFD	**C**omputational **F**luid **D**ynamics
DNS	**D**irect **N**umerical **S**imulation
ICS	**I**nterogation **C**ell **S**ize
LES	**L**arge **E**ddy **S**imulation
LDA	**L**aser **D**oppler **A**nemometry
MFKE	**M**ean **F**low **K**inetic **E**nergy
MRF	**M**ultiple **R**eference **F**rame
OBC	**O**ff **B**ottom **C**learance
PIV	**P**article **I**mage **V**elocimetry
RANS	**R**eynolds **A**veraged **N**avier **S**tokes
RMS	**R**oot **M**ean **S**quare
RSM	**R**eynolds **S**tress **M**odel
SAS	**S**cale **A**daptive **S**imulation

SGS	**S**ub **G**rid **S**cale
SST	**S**hear **S**tress **T**ransport
TKE	**T**urbulence **K**inetic **E**nergy
TVB	**T**aylor **V**ortex **B**ioreactor
VEDR	**V**iscous **E**nergy **D**issipation **R**ate
WALE	**W**all **A**dapting **L**ocal **E**ddy

Lista de símbolos

b	Gap width, r_o - r_i, m
b_{ij}	Reynolds stress anisotropy tensor, $m^2 s^{-2}$
d+	Radial coordinate at the inner wall, r$u_{\tau i}/\nu$, (-)
C	Constant of SAS-SST turbulence model, 2, (-)
$C_{1\epsilon}$	Constant of k-ϵ model, 1.44 (-)
$C_{2\epsilon}$	Constant of k-ϵ model, 1.92 (-)
$C_{1\epsilon RSM}$	Constant of LRR-IP RSM model, 1.45 (-)
$C_{2\epsilon RSM}$	Constant of LRR-IP RSM model, 1.9 (-)
C_{1RSM}	Constant of LRR-IP RSM model, 1.44 (-)
C_{2RSM}	Constant of LRR-IP RSM model, 1.92 (-)
C_{μ}	Constant of k-ϵ model, 0.09 (-)
C_S	LES-Smagorinsky constant, 0.2 (-)
C_{S-RANS}	Constant of LLR-RSM turbulence model, 0.22 (-)
C_W	LES-WALE constant, 0.325 (-)

$d+_e$	Radial coordinate at outer wall, $r_e(= r_{max} - r)u_{\tau e}/\nu$, (-)
F_1	Blending function for the SST turbulence model, (-)
F_2	Blending function for the SST turbulence model, (-)
G_k	Generation of TKE for k-ϵ model, $\nu_t S^2$, $m^2 s^{-3}$
k	Turbulence kinetic energy, $m^2 s^{-2}$
L	Lenght of the outer cylinder, m
L_{vk}	von Karmen length scale, (-)
obc	Off-bottom clearance, m
p	Pressure, Pa
p’	Modified pressure for RANS based two equation models, Pa
p”	Modified pressure for RANS based RSM models, Pa
P	Power, P = $\tau\omega = \iiint\limits_{v} \rho\epsilon$dv, Watts
r	radial direction, m
r_i	Inner cylinder radius, m
r_o	Outer cylinder radius, m
R_b	Dimensionless radial coordinate, $\frac{r-r_i}{b}$, (-)

Re	Reynolds number, $\frac{r_i \omega (r_o - r_i)}{\nu}$, (-)
S_{ij}	Strain rate, s^{-1}
Ta	Taylor number, $\frac{r_i^{1/2} \omega (r_o - r_i)^{3/2}}{\nu}$, (-)
$u_r^{'}$	Fluctuating radial velocity component, ms^{-1}
$u_\theta^{'}$	Fluctuating tangential velocity component, ms^{-1}
$u_z^{'}$	Fluctuating axial velocity component, ms^{-1}
$u_\tau i$	Friction velocity at inner cylinder, ms^{-1}
$u_\tau e$	Friction velocity at outer cylinder, ms^{-1}
U_θ	Tangential component of the velocity, ms^{-1}
U_r	Radial component of the velocity, ms^{-1}
U_{tip}	Tip velocity, rω, ms^{-1}
U_z	Axial component of the velocity, ms^{-1}
v	Volume of the reactor, m^3
z	Axial direction, m
Z_L	Dimensionless axial coordinate, $\frac{z}{L}$, (-)
ϵ	Viscous energy dissipation rate, $m^2 s^{-3}$

$\langle\epsilon\rangle$	Mean viscous energy dissipation rate, m^2s^{-3}
$\epsilon_{innerwall}$	Mean viscous energy dissipation rate at inner wall, u_τ^4/ν, m^2s^{-3}
η_{rr}	Radius ratio, $\frac{r_i}{r_o}$, (-)
η	Kolmogorov's micro-scale, μm
δ_{ij}	kronecker delta, (-)
Δ	local gird scale, m
κ	von Kárman constant, (-)
Λ	Taylors's micro-scale, mm
$\lambda_1, \lambda_2 and \lambda_3$	Three eigenvalues of the vector $S^2 + \Omega^2$, s^{-2}
ν	Kinematic viscosity, m^2s^{-1}
ν_{eff}	Modified kinematic viscosity of RANS based models, $\nu + \nu_t$, m^2s^{-1}
ν_{sgs}	Subgrid scale eddy viscosity, m^2s^{-1}
ν_t	Turbulent viscosity of RANS based models, m^2s^{-1}
η_2	Constant of SAS-SST turbulence model, 3.51 (-)
Γ	Aspect ratio, $\frac{L}{b}$, (-)
ρ	Density, kgm^{-3}

σ_k	Constant of k-ϵ model, 1.0 (-)
σ_{kSST}	Constant of SST turbulence model, $1/(F_1/\sigma_{k,1} + (1 - F_1)\sigma_{k,2})$, (-)
$\sigma_{k,1}$	Constant of SST turbulence model, 1.176 (-)
$\sigma_{k,2}$	Constant of SST turbulence model, 1.0 (-)
σ_ϵ	Constant of k-ϵ model, 1.3 (-)
$\sigma_\epsilon RSM$	Constant of LRR-IP RSM model, 1.1 (-)
$\sigma_{\omega SST}$	Constant of SST turbulence model, $1/(F_1/\sigma_{\omega,1} + (1 - F_1)\sigma_{\omega,2})$, (-)
$\sigma_{\omega,1}$	Constant of SST turbulence model, 2.0 (-)
$\sigma_{\omega,2})$	Constant of SST turbulence model, 1.168 (-)
σ_Φ	Constant of SAS-SST turbulence model, 2/3 (-)
$\beta_{i,1}$	Constant of SST turbulence model, 0.075 (-)
$\beta_{i,2}$	Constant of SST turbulence model, 0.828 (-)
β^*_∞	Constant of SST turbulence model, 0.09 (-)
τ	Torque, Nm
τ_w	Wall shear stress, Nm^{-2}
θ	Tangential direction, m

ω	Angular velocity, rads^{-1}
ω_{tef}	turbulence eddy frequency of k-ω models, s^{-1}
Ω_{ij}	Rotation rate, s^{-1}

Sumário

1 INTRODUCTION . . . 31
1.1 Bioreactors and Hydrodynamics . . . 31
1.2 Understanding Hydrodynamics . . . 36
1.2.1 Experimental method . . . 37
1.2.2 Numerical method-CFD . . . 38
1.3 Overall project . . . 41
1.3.1 Main aim of this thesis . . . 42

2 EXPERIMENTAL METHOD - PIV . . . 43
2.1 Description of case set-up . . . 43
2.2 PIV set-up . . . 44
2.3 Estimation of VEDR . . . 47
2.4 Basic Aspects of PIV . . . 49
2.4.1 Concentration of particles . . . 49
2.4.2 Size of particles . . . 51
2.4.3 Time-step between frames . . . 53
2.4.4 Choosing overlap & ICS . . . 55
2.5 Results and discussion . . . 63
2.5.1 Mean velocity flow field . . . 63
2.5.2 Logarithmic velocity profiles . . . 69
2.5.3 Reynolds stresses . . . 72
2.5.3.1 Normal stress . . . 72
2.5.3.2 Shear Stress . . . 79
2.5.4 Viscous energy dissipation rate . . . 80
2.5.4.1 Composition of the VEDR . . . 80
2.5.4.2 EDR structure . . . 87
2.5.5 Kolmogorov scale . . . 92
2.6 Conclusions . . . 93

3 NUMERICAL METHOD AND ITS VALIDATION . . . 97
3.1 Turbulence modelling . . . 97
3.2 Numerical methodology . . . 102
3.2.1 Geometry and Meshing aspects . . . 102
3.2.2 Pre-processing aspects . . . 105
3.2.3 Solver & Post-processing aspects . . . 105
3.2.4 Estimation of VEDR . . . 105

3.3 Validation of the computational model . . . 106
3.4 Conclusions . . . 113

4 TURBULENCE MODELS . . . 115
4.1 Vortex identification . . . 115
4.2 Mean velocity flow field . . . 117
4.2.1 Tangential velocity . . . 117
4.2.2 Radial velocity . . . 123
4.2.3 Axial velocity . . . 123
4.2.4 Log law profiles of tangential velocity . . . 125
4.3 Normal stresses . . . 129
4.4 Reynolds shear stresses . . . 137
4.5 Turbulent kinetic energy . . . 143
4.6 Anisotropy . . . 145
4.7 Viscous energy dissipation rate . . . 147
4.7.1 Composition of VEDR . . . 147
4.7.2 Structure of VEDR . . . 149
4.7.3 Power Estimation . . . 153
4.8 Conclusions . . . 154

5 AN APPLICATION OF CFD . . . 157
5.1 Problem description . . . 157
5.2 Computational model . . . 159
5.2.1 Description of case set-up . . . 159
5.2.2 Turbulence modeling . . . 161
5.2.3 Computational mesh and time-step . . . 161
5.2.4 Sliding mesh or MRF technique . . . 162
5.2.5 Computational aspects . . . 165
5.3 Validation of the computational model . . . 165
5.4 Results and discussion . . . 166
5.4.1 Mean velocity flow field . . . 166
5.4.2 Outer cylinder's bottom shapes . . . 169
5.4.3 Off-bottom clearance . . . 170
5.4.4 Viscous energy dissipation rate(VEDR) . . . 172
5.5 Conclusions . . . 176

6 CONCLUSIONS . . . 179

Referências . . . 183

APÊNDICE A – MATLAB FILE 193

Índice 203

1 Introduction

1.1 Bioreactors and Hydrodynamics

The cultivation of animal cells (including human), a sub-area of biotechnology, in *in vitro* is a process of over 100 years old, but the emerging need of vaccines in the 1950s imparted some momentum to this process leading to the development of various vaccines such as measles (1963), rabies (1964), mumps (1967) and rubella (1969) (KRETZMER, 2002). In the mid-1970s, a second set of products hit the market - monoclonal antibodies by forming hybridomas from the fusion of cells, and genetic engineering (KRETZMER, 2002).f Nowadays, the animal cell product list has increased to a huge number, namely, human and veterinary vaccines, diagnostics monoclonal antibodies and therapeutics, such as tPA, erythropoietin and interferons, with many animal cell products being highly costly in the order of US \$ 10^4 to \$ 10^9 per kilogram (KRETZMER, 2002; ECKER; JONES; LEVINE, 2015). The ever-increasing sales forecasts of the recombinant proteins and monoclonal antibodies till 2013 presented by Ecker, Jones e Levine (2015) can be seen in Figure 1, of which currently ≈ 54 % are being produced by animal cells (ECKER; JONES; LEVINE, 2015).

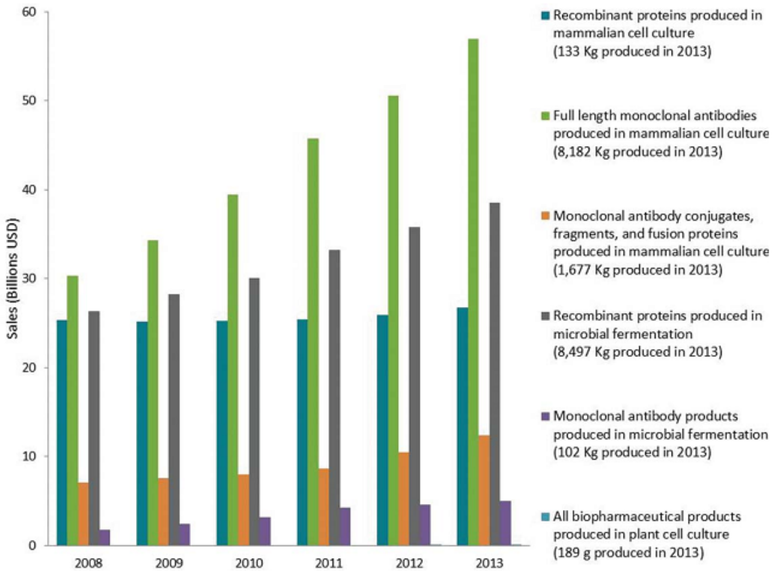

Figura 1 – Annual sales of recombinant proteins and monoclonal antibodies in the 2008-2013 period. Source: Ecker, Jones e Levine (2015).

To achieve maximum yields, it becomes important to provide the cells with an *in vitro* environment as similar as possible to the natural cell environment, leading to studies regarding the composition of culture media, process controls (pH, temperature, dissolved oxygen), and especially the bioreactors. Major improvements, mainly, in the culture media composition and process control, have resulted in over 100-fold yield increase in the cultivation of mammalian cells in the bioreactors for similar processes that were used in the mid-1980s (WURM, 2004). Nonetheless, there are still possibilities of further improvements in the yield through the optimization of various processes in the cultivation of animal cells (KRETZMER, 2002; WURM, 2004; JAIN; KUMAR, 2008; COSTA et al., 2010).

One of the most crucial factors that play a significant role in the design of a bioreactor using animal cells is that they do not possess a cell wall, unlike bacteria, fungi and plant cells. Lack of cell wall makes the animal cells extremely sensitive to external environment such as pH, temperature, nutrients or culture media, regulatory molecules, oxygenation through bubbling and hydrodynamic forces resulting from aeration through bubbling and agitation in a bioreactor. These unique characteristics of animal cells makes it imperative to develop bioreactors designed with agitation and oxygenation systems that generate hydrodynamic forces milder than those found in bioreactors cultivating microbes (NIENOW, 2006).

Presently, the two most commonly employed bioreactors in large scale are the stirred or agitated tank and airlift reactor (CHU; ROBINSON, 2001; KRETZMER, 2002; JAIN; KUMAR, 2008; NIENOW, 2006). From the 30 L in the 1960s to 8,000 L in 1980s to 20,000 L in the mid-2000s has been the increase in the capacity of a traditional agitated bioreactor to produce vaccines, monoclonal antibodies and therapeutics (NIENOW, 2006; KRETZMER, 2002). On the other hand, the airlift bioreactor has been scaled up-to 2,000 L to produce monoclonal antibodies with reports of a 10,000 L airlift bioreactor which successfully cultured hybridoma cells to produce monoclonal antibodies (JAIN; KUMAR, 2008). Although, both bioreactor types have the versatility of cultivating both suspension and anchorage-dependent cells, the stirred tank has been the preferred choice of the industrialists due to easy scale-up, homogeneous environment and vast industrial experience of working with this reactor type (CHU; ROBINSON, 2001; NIENOW, 2006).

However, certain cell lines demand a surface for adherent culture systems which lead to the development of high density cell culture systems, such as hollow fiber, packed bed and fluidized-bed bioreactors (JAIN; KUMAR, 2008). Although, these compact bioreactors have the advantage of high volumetric productivity, they suffer from concentration gradients due to non-homogeneity and difficulty in monitoring and scale-up (OZTURK, 1996). Disposable bioreactor is another genre that has entered the market in the start of the twenty-first century largely to reduce hydrodynamic stress and process cost, and have easier process control, for example, wave bioreactor (SINGH, 1999). Although, wave bioreactors have been scaled up-to 1,000 L capacity (JAIN; KUMAR, 2008), industrial-scale capacities are still under question. Another disposable bioreactor is being developed by the Jain e Kumar (2008) group, named cryogel bioreactor, with a capacity of up-to 1L and functioning similar to that of hollow fiber bioreactor.

In addition, in recent years, another reactor type, named Taylor-Vortex Bioreactor (TVB) has emerged as a choice for culturing cells (O'CONNOR et al., 2002; HAUT et al., 2003; CURRAN; BLACK, 2004; CURRAN; BLACK, 2005; GONG et al., 2006; TANZEGLOCK, 2008; SANTIAGO; GIORDANO; SUAZO, 2011; ZHU et al., 2010). These researchers successfully cultured various animal and insect cell lines, namely Chinese Hamster Ovaries (CHO), Human Embryonic Kidney, rat bone marrow stroma, and Sf-9 *Spodoptera frugiperda*, in suspension in a TVB. The oxygen is easily provided through gas-permeable membranes in these reactor types thus reducing the hydrodynamic stress due to aeration by bubbling (CURRAN; BLACK, 2005; SANTIAGO; GIORDANO; SUAZO, 2011). Another advantage of the TVB is the possibility of scale-up to an industrial level bioreactor, thus making it a serious contender for culturing animal cells (CHAUDHURI; AL-RUBEAI, 2005).

The design, scale-up and operation of bioreactors for animal cell culture require a comprehensive understanding of the mechanisms of cell damage and death caused by the fluid-mechanical forces associated with the equipment type (BRIONES; CHALMERS, 1994). Therefore, the parameters characterizing the effect of hydrodynamic forces causing cellular destruction are of crucial importance in the validation of bioprocess development studies conducted primarily in the mini-bioreactors and later transferred to the larger-scale bioreactors. Numerous parameters have been used to characterize cell death or damage in the various studies, as shown in Table 1, and a consensus has not been reached. Moreover, there is little information available on how to use flow parameters that correlate well with cell damage in one particular system to predict cell damage in a different system.

Briones e Chalmers (1994) stated that cell damage should ideally be predicted by knowing the actual stresses that the cell experiences, determined from intrinsic cell mechanical properties and the resulting cell deformation. Should the cell deformation exceed a critical value, the disruption of the cell structure would be expected. They suggested that the parameter chosen to correlate with cell damage should be 1) general in nature and not be dependent on the particular geometry and 2) be local, that is, not be averaged throughout the flow domain.

Briones e Chalmers (1994) rejected the Kolmogorov eddy scale as a basis for predicting cell damage, because essentially cell size becomes the only correlation parameter when this parameter is used, and therefore cell mechanical properties are neglected. Kunas e Papoutsakis (1990) suggested that, although Kolmogorov eddy length can be used as a predictor of cell damage, it does not provide any details of how cells are damaged by their interaction with these eddies or even prove that there is a direct cell-eddy interaction. Echoing this sentiment, Joshi, Elias e Patole (1996) stated that it is very difficult to predict the relationship between the eddy size and its role in cell damage.

Tabela 1 – Various parameters used to correlate to cell death in a Stirred tank.

Cells used	Range of hydrodynamic Parameters	Important Observations	Reference
Insect Cells, SF-21	210- 510 rpm $\tau = 3$ N/m^2Cell death rate proportional to volumetric gas flow rate	"Viability of cells decreased at shear stresses of 1 N/m^2"	Tramper et al. (1986)
Hybridoma, CRl-8018	60-900 rpm, Cell death correlates to Kolmogorov eddy size similar to or smaller than the cell	"In absence of gas sparging, cells are damaged only at speed above 700 rpm. No damage at speeds less than 600 rpm"	Kunas e Papoutsakis (1990)
Hybridoma, HDP-1	100-440 rpm, Impeller tip speed 19-73.3 cm/s	" Death rate constant, k_d, increased sharply at impeller tip speeds above 40 cm/s"	Abu-Reesh e Kargi (1989)
SF-9 and Hybridoma, serum containing, gas free	$<$ 0.7 impeller tip speed, $<$ 350 W/m^3 Power Inputs	"Damaging threshold values of impeller tip speed or specific Power inputs for some animal cells"	Chisti (2001)

In the last 15 years, the group of Prof. Jeffrey Chalmers from the Ohio state university in USA have presented various meticulous studies of probably the ideal parameter to characterize the potential of hydrodynamic stresses to damage cells (GREGORIADES et al., 2000; MA; KOELLING; CHALMERS, 2002; MOLLET et al., 2004; MOLLET et al., 2007; MOLLET et al., 2008; GODOY-SILVA et al., 2009; GODOY-SILVA; MOLLET; CHALMERS, 2009).

There have been various studies estimating the lethal effects of Viscous energy dissipation rate (VEDR) on cell cultures using various types of devices, such as microfluidic channel, contractional flow device and capillary flow device (THOMAS; AL-RUBEAI; ZHANG, 1994; ALOI; CHERRY, 1996; GREGORIADES et al., 2000; MA; KOELLING; CHALMERS, 2002; MOLLET et al., 2007). According to Ma, Koelling e Chalmers (2002), lethal VEDR are at least 1000 times greater than those used in stirred tank bioreactors operated successfully in sizes ranging from 10 L and 22,000 L capacity. The cell cultures of Ma, Koelling e Chalmers (2002) were tested in a transient flow contractional device with residence times similar to a stirred tank having a rotational speed of 500 rpm. However, these cells were exposed to high levels of VEDR only once, as in the research work of Thomas, Al-Rubeai e Zhang (1994), Aloi e Cherry (1996), Gregoriades et al. (2000), Mollet et al. (2007). The cells in a stirred tank are exposed multiple times to high levels of turbulent VEDR in the vicinity of the impeller due to the circulatory nature of the flow. Thus, the value of maximum turbulent VEDR that a cell can withstand would be substantially lower in a stirred tank than in a single-pass flow device, since the integrated exposure time is considerably longer. Clearly, both the residence time of a single pass and the number of exposures to high turbulent VEDR in the vicinity of the impeller must be considered when estimating cell damage in a stirred-tank reactor, or any other type of bioreactor.

To overcome the limitation of single pass, the Chalmers group (GODOY-SILVA et al., 2009) presented a new method in which a microfluidic device is joined in an external loop to a 2 L stirred tank bioreactor. This way the cells were subjected to high VEDR levels multiple times, though there is no confirmation that the same cell was subjected to high VEDR levels of the microfluidic device multiple times. Nonetheless, similar high levels of maximum VEDR were reported having a lethal effect on the cells as reported by Ma, Koelling e Chalmers (2002). In addition, Godoy-Silva et al. (2009) also addressed another problem of the biological response of cells to sub-lethal levels of hydrodynamic stress. They found that the maximum VEDR for the sub-lethal effects is around 100 times smaller than the lethal dose. Sub-lethal levels are known to induce apoptosis in cells (ALOI; CHERRY, 1995), reduction in the production of the recombinant protein (GODOY-SILVA; MOLLET; CHALMERS, 2009) and triggering the glycosylation shift of glicoproteins (GODOY-SILVA et al., 2009). Therefore, sub-lethal levels have to be taken into serious consideration to design a bioreactor with high productivity, reliability and operability for the cultivation of animal cells under strict guidelines implemented by regulatory agencies and required by the new cell lines.

Another important consideration requiring attention in a bioreactor is the necessity of sufficient oxygen supply for animal cell survival; though, aeration by means of bubbling air can result in cell damage due to rising and bursting of bubbles (TRAMPER et al., 1986). The viability and growth of cells in sparged reactors depend, amongst other factors, on the bubble size and the bubble frequency, which can be controlled by the gas flow rate or the superficial gas velocity (JOSHI; ELIAS; PATOLE, 1996). Joshi, Elias e Patole (1996), in agreement with Wu e Goosen (1995), suggested that the maximum cell damage occurs mainly in the region of bubble disengagement at the air-liquid interface. Various methods of oxygenation without the formation of bubbles have also been researched to avoid cell damage/death due to cell-bubble interactions, such as using gas–permeable membranes (KUNAS; PAPOUTSAKIS, 1990; SCHNEIDER et al., 1995; SANTIAGO; GIORDANO; SUAZO, 2011). A gas permeable membrane is essentially a long coiled gas-permeable tube placed within the bioreactor, with oxygen or air flowing within the tube, which allows oxygen to diffuse through the permeable wall (membrane) of the tube and into the culture medium. This approach allows enhanced mixing and homogeneity through increased agitation which cannot be achieved when oxygenating by bubbling; though, at much lower k_La, oxygen mass transfer, values in comparison to the bubbling systems. For instance, for a similar gas flow rate of 4 L/m and rotational speed pf 700 rpm with similar concentration of oxygen in the air of 21 % in a stirred tank, the oxygen mass transfer rate for bubbling was 66.1 hr^{-1} in comparison to the value for 3.3 hr^{-1} for the gas-permeable membrane (SINGH, 2011).

Summarizing, it can be said that the choice of bioreactor depends upon the cell type, and the possibility of scale-up of the chosen reactor type. At the same time, an oxygenation method should be available with a priority of not creating additional hydrodynamic stress to the cell cultures in addition to the necessary evil of agitation to sustain homogeneous mixture in a reactor. Hence, the ease of scale-up, bubble-free oxygenation and proven capability of culturing various animal cells in suspension have lead to the TVB as the chosen reactor for this study. As a consequence, a detailed hydrodynamic study of this reactor type is a basic necessity in order to obtain the parameters which will guide towards the choice of optimum operating conditions with respect to high productivity and reliability.

1.2 Understanding Hydrodynamics

In order to understand the hydrodynamics completely, a clear picture is required of all the different scales of fluid flow from the largest, Taylor's macro-scale which physically represents the mean size of large eddies, to the smallest, Kolmogorov's micro-scale, at which the kinetic energy is dissipated into heat. Taylor's macro-scale is limited by the physical boundaries of the flow, whereas, the Kolmogorov's micro-scale is determined by viscosity. Only by capturing accurately the smallest scales, an accurate prediction of the VEDR can be made in addition to the accurate estimation of any other flow parameter, and this still has not been achieved, either experimentally or numerically, for turbulent Reynolds numbers around 25,000. Higher the turbulent Reynolds number, the smaller the Kolmogorov scale becomes, implying that the amount of data that needs to be captured is humongous in order to reach the size of few μm, remembering that the Kolmogorov scale and the turbulent VEDR are inversely proportional to each other, $\eta = (\frac{\nu^3}{\epsilon})^{1/4}$. For example, Smith e Greenfield (1992) reported that they observed significant damage to cells in a stirred tank at a Reynolds number of 25,000 and rotational speed of 700 rpm, which based on (SINGH, 2011) estimations is equivalent of ≈ 38 m^2/s^3 maximum turbulent VEDR or ≈ 13 μm in terms of the Kolmogorov's micro-scale, assuming that the kinematic viscosity of culture media is similar to that of water. Analytical estimations of the VEDR are only valid for the laminar state, turbulent state requires a much more comprehensive estimation; thus, leaving the choice between the experimental and numerical methodologies for the estimation of VEDR.

1.2.1 Experimental method

Since early sixties, experimental methods have been shedding light on the flow structures and hydrodynamics in different fluid-flow configurations. In the early eighties and ninties, Smith e Townsend (1982) and Kobayashi et al. (1990) presented detailed experimental results of the mean and fluctuating velocities for a TVB using Pitot tubes and hot-wire anemometers. The biggest disadvantages of using these equipments were their intrusive nature and limited data in the boundary layers or near the walls in the case of TVB. Although, in recent years computational fluid dynamics (CFD) has become a more important tool for investigation, the experimental methods are still necessary in order to validate these numerical results. Mavros (2001) stated that among the various experimental techniques that are being practiced in recent years for flow visualization and analyzing hydrodynamics, particle image velocimetry (PIV) and laser Doppler anemometry (LDA) have become the predominant methods due to their relative easy-to-use techniques and non-intrusive nature. In the case of TVB, PIV has been the primarily used method (WERELEY; LUEPTOW, 1998; AKONUR; LUEPTOW, 2003; COUFORT; BOUYER; LINE, 2005; WANG; OLSEN; VIGIL, 2005; DUSTING; BALABANI, 2009; DENG et al., 2010), to examine principally the velocity and vortex structures.

Hout e Katz (2011) and Tokgoz et al. (2012) presented turbulence parameters, such as Reynolds stresses and VEDR, using the PIV method, but their spatial resolution was limited for turbulent Reynolds number. Due to limited spatial resolution, ranging from five to nine times the Kolmogorov scale, Hout e Katz (2011) observed severe underestimation as much as 55 % of the dissipation rate estimated assuming isotropy. Tokgoz et al. (2012) found that their tomographic PIV underestimated the mean dissipation, when comparing the PIV estimates with that of torque scaling, by 47 % and 97 % for shear Reynolds number of 3 800 and higher values, respectively. They worked with the spatial resolutions between 3 to 71 times that of Kolmogorov scale, thus also showing the importance of spatial resolution on the estimations of VEDR. In addition, they employed the large eddy PIV method, first implemented by Sheng, Meng e Fox (2000) and demonstrated more than three times increase in the mean dissipation rate values.

Delafosse et al. (2011) showed that the spatial resolution plays a strong influence on the estimation of VEDR when using the PIV technique in a stirred tank. They presented a study of 12 spatial resolutions ranging between 1 to 12 times the mean Kolmogorov scale, and confirmed that the spatial resolution equal to that of the Kolmogorov scale is required to accurately estimate the VEDR. However, they were able to achieve spatial resolution equivalent of Kolmogorov scale at their lowest rotational speed of 50 rpm equivalent of 13 000 Re number. They also observed that when they halved their spatial resolution, the estimation of VEDR increased by 220 %, in close agreement with the results of Baldi e Yianneskis (2004).

Reaching a certain value of spatial resolution depends directly upon the chosen interrogation cell size (ICS) and overlap ratio, apart from the camera and lens equipment. Tokgoz et al. (2012) showed improvement in the estimation of VEDR with each decrease in the ICS, and increase in the overlap value at a particular ICS. However, there are various other factors, such as time-step between the double framed image, particle size and concentration, and higher orders of the first derivative to estimate the gradients of the velocity vectors, which may also impact the VEDR. These aspects, as per author's knowledge, have not been presented before.

Secondary problem with the PIV studies is that the spatial resolutions available for 3D is bigger compared to the 2D PIV studies. However, 2D PIV suffers from another limitation apart from the spatial resolution. For a direct estimation of VEDR from its equation (SHARP; ADRIAN, 2001), twelve gradients are required to be calculated, all of which can be estimated with a 3D PIV methods at the expense of spatial resolution. Whereas, in the case of 2D PIV methods only five gradients can be estimated. Due to this limitation, the rest of the seven gradients are required to be estimated based on the isotropic turbulence assumptions (SHARP; ADRIAN, 2001).

On the technological front, there has been a steady evolution in the equipments and the softwares used to interpret the images. The resolution of cameras has increased from 1 M pixels in late nineties to 16 M pixels in present time. The computer memory and disk space has also increased in order to capture and store such high resolution images, and their treatment to capture the smallest scales; for example, a set of 2500 double frame images of 16 MPixel camera is equivalent of 75 Gbytes and its treatment to resolve upto 25 μm is equivalent of 500 Gbytes. At the same time, the algorithms to estimate the correlation vectors have also improved and became more efficient and reliable (STANISLAS et al., 2008).

One of the objectives of this study is to present a direct estimate of VEDR using a 2D PIV method, thereby presenting only five of the 12 gradients of a 3D equation of VEDR. The methods shown by Sharp e Adrian (2001) estimating the seven other gradients will also be included in this study. The 2D PIV method is used in order to capture the lowest possible spatial resolution with a 16 M pixel camera. A study will also be conducted to better understand the influence of not only the overlap ratio, and ICS but also the particle size and concentration, time-step and higher order gradients on the VEDR estimation.

1.2.2 Numerical method-CFD

Although, the experimental estimations are painstaking, cumbersome and require thorough attention, these are necessary in order to validate the numerical results. Still, the shear practicality and flexibility of numerical methods have shifted the weight towards computational side to study the hydrodynamics in more detail which may not be feasible with 2D PIV estimations. In addition, significant recent advances in the computational field has enabled the researchers to use the direct numerical simulation (DNS) model to examine the hydrodynamics at high Reynolds number in a simple geometry, such as TVB. Understanding the hydrodynamics of a reactor are necessary for its optimization and characterization. In a TVB, consisting of two concentric cylinders, flow can be generated by rotating one or both cylinders in co- or counter-current directions. The field of study in such a reactor is the gap-width, the distance between the inner and outer cylinder, which is of the order of only few centimeters for laboratory scale reactors. As a result, obtaining a mesh which is nearer to the smallest Kolmogorov scale in order to capture around 90 % of the eddies is within reach. Indeed, there has been a surge in the studies of the TVB using the DNS model in recent years (BILSON; BREMHORST, 2007; DONG, 2007; PIRRO; QUADRIO, 2008; DOUAIRE, 2010; BRAUCKMANN; ECKHARDT, 2013).

Bilson e Bremhorst (2007) showed a detailed analysis of velocity fluctuations, turbulent kinetic energy (TKE), Reynolds stress budget and one-dimensional energy spectra for a radius ratio, η, of 0.617 and an aspect ratio, Γ, of 4.58. The main focus of the DNS study of Dong (2007) was to demonstrate the effect of the variation in Reynolds number on the Gortler vortices and herringbone-like streaks that develop near the cylinder walls, and partly the statistical features of turbulence in TVB. Pirro e Quadrio (2008) explained the numerical method that they developed extending the work of Quadrio e Lichini (2002) to use the DNS model in fully turbulent regime at Reynolds number of 10500. After validating with numerical and experimental results, they discussed mean velocity and root mean square value of velocity fluctuations profiles. Their major observation was the identification of two distinct sources of fluctuations, namely: 1) curvature related large-scale vortices, and 2) small scale fluctuations produced by the wall turbulence cycle. The objective of using the DNS model by Douaire (2010) was to be able to explain the cell behavior with respect to the TVB hydrodynamics at different Reynolds number. They used the DNS model to estimate various volumetric distributions, such as that of dissipation, and to follow the trajectories of a Lagrangian particle in order to find out the how much dissipation and force a particle faces in the reactor. More recently, Brauckmann e Eckhardt (2013) presented detailed torque estimations and how they are influenced by the vortex heights in TVB for a radius ratio, η, of 0.71 using DNS model at various aspect ratios and shear Reynolds number up to 3×10^4.

Apart from the DNS model, the Reynolds averaged Navier-Stokes (RANS) based k-ϵ model (NASER, 1997; COUFORT; BOUYER; LINE, 2005; PAWAR; THORAT, 2012; FRIESS; PONCET; VIAZZO, 2013) and Reynolds Stress model (RSM) (COUFORT; BOUYER; LINE, 2005; PONCET; HADDADI; VIAZZO, 2011; PAWAR; THORAT, 2012; FRIESS; PONCET; VIAZZO, 2013), and the large eddy simulation (LES) model (CHUNG; SUNG, 2005; OGUIC; VIAZZO; PONCET, 2013; FRIESS; PONCET; VIAZZO, 2013) have also been used in numerical investigations of TVB. The RANS based models are well known for their under-estimation of turbulence parameters (HARTMANN et al., 2004; DELAFOSSE et al., 2008). The LES model's predictions of the turbulence quantities have been much better in the case of stirred tank (DERKSEN; AKKER, 1999; HARTMANN et al., 2004; DELAFOSSE et al., 2008) in comparison to the RANS based models. Though the mesh size used for the RANS model was much more courser in comparison to the mesh size used for the LES model (HARTMANN et al., 2004; DELAFOSSE et al., 2008), which could be one of the reasons behind the underestimation shown by the RANS based models. Study of Singh, Fletcher e J. (2011) in a stirred tank showed that improved mesh results in much better estimation of turbulence parameters by the RANS based models.

On the other hand, using the dynamic LES model in a TVB, Chung e Sung (2005) demonstrated a detailed validation of their numerical results, estimation of the anisotropy of the turbulent structures and probability density functions of the velocity fluctuations while focusing on the near-wall turbulent structures. Whereas, the aim of Oguic, Viazzo e Poncet (2013) was basically to validate their LES model based on their groups 2D compact fourth-order projection decomposition method presented by Abide e Viazzo (2005) and to present a brief study of anisotropy. Furthering on the research of Oguic, Viazzo e Poncet (2013), Friess, Poncet e Viazzo (2013) presented the LES-WALE (wall adapting local eddy) results of radial profiles of the rms velocities and the shear components of the Reynolds stress tensor along-with the axial and tangential velocity radial flow profiles. They also compared these LES-WALE results as a reference with a DES model and a RANS based RSM.

Considering these various studies, the objective of this study is to further the numerical research by: first, conducting a detailed validation of the DNS model with the 2D PIV estimations and; secondly, conducting a comprehensive comparison of different turbulence models for anisotropy, TKE and its terms, Reynolds stresses, and VEDR and its 12 terms in a TVB. In addition, a method on identification of vortex based on the study of Jeong e Hussain (1995) will be presented. Instead of the dynamic LES model, chosen by Chung e Sung (2005), the LES Smagorinsky and LES-WALE have been tested in this study. LES Smagorinsky has been the most commonly used LES model in case of stirred-tank reactor, though the impact of its C_S constant is also well known to have a significant effect on the turbulence quantities (DELAFOSSE et al., 2008). Based on the study of Delafosse et al. (2008), a value of 0.2 is chosen for the C_S constant in this study. The LES-WALE model is chosen because of its better numerical stability and zero damping functions in near-wall treatment Friess, Poncet e Viazzo (2013); Moreover, Weickert et al. (2010) showed that it fared much better than the LES Smagorinsky model. The dynamic model is not tested based on the suggestion of Weickert et al. (2010) that the variation in the LES constant both in time and space could lead to unstable numerical simulation. Apart from the DNS and LES models, some RANS based models, namely, k-ϵ, shear stress transport (SST), scale adaptive simulation (SAS)-SST and RSM, are also tested for the

TVB in this study. The mesh used for these RANS based models will be the same that will be used in the case of DNS and LES models in order to have a much direct comparison between these models.

1.3 Overall project

Although, the stirred tank and the airlift reactor are being used in the industry currently for culturing animal cells in reactors of 20,000 L capacity, these reactors are limited to a select few cell lines which can be cultured in a suspension and which are comparatively less shear-sensitive. For newer, more shear sensitive cell line and those cell lines requiring microcarriers (a support matrix used in bioreactors on which the adherent cells are cultured) a different bioreactor is required which has the possibility of providing oxygen in liquid phase, in order to reduce the hydrodynamic stress, and which can provide a environment with low shear but homogeneous in nature for culturing of the animal cells. The TVB fits this bill perfectly, as oxygen can be provided in liquid phase easily and culturing of various animal cell-lines with and without microcarriers has been effective. Hence, the main aim of the overall project is to asses the possibility of using the TVB as a bioreactor for culturing shear-sensitive animal cells at an industrial scale. In order to see the effectiveness of the TVB as a bioreactor, a couple of its geometrical features will also be studied using CFD. As the overall project has a vast scope, it has been divided into different subgroups:

a) A detailed hydrodynamic study of the TVB and its geometrical features: as has been mentioned till now, a good understanding of hydrodynamics of a reactor are a must in order to put the animal cell death/injury in picture.

b) Scale-up study of the TVB with animal cell culture: the scale - up study will lay the base for the TVB to be projected as the future industrial scale reactor for culturing animal cells.

c) Feasibility of culturing of different animal cell lines and a cell-line using microcarriers.

d) A multiphase numerical study of the TVB in order to access the direct impact of hydrodynamics on microcarriers and animal cells in the same conditions in which they are being cultivated in the TVB.

e) Finally, a general model to show the impact of hydrodynamics on the different animal cell lines tested in the TVB.

1.3.1 Main aim of this thesis

As the overall project is beyond the reach of one thesis due to limited time and resources in order to understand this complex industrial problem, this thesis has been conducted with an aim to understand and present the hydrodynamics of the TVB with regards to its feasibility as a bioreactor for cultivating animal cell lines of biotechnological interest. The hydrodynamics of the TVB will be studied both experimentally and numerically with an aim to reach the smallest scales that are feasible based on the available financial and technological resources. It is worth noting that the cost increases exponentially as we reach towards the smallest scales. Reaching the smallest scale is necessary for better estimation of the VEDR, which could be the ideal parameter to relate with the animal cell death (lethal impact) and/or injury (sub-lethal impact). Hence, the objectives of this thesis can be described as:

a) Experimental study of the TVB with the aim of validating a numerical model while achieving the smallest feasible spatial resolution to obtain the VEDR estimations closest to the Kolmogorov micro-scale, and assessing the limitations of this 2D-PIV method.

b) Reaching the smallest scales require extra care, therefore, special attention will be given towards the basic aspects, such as overlap ratio, ICS, time-step and higher order gradients, of the PIV in order to ascertain their influence on the estimation of the VEDR among other parameters such as fluctuating and mean velocity components.

c) The numerical study will be conducted with a CFD program named ANSYS-Fluent, and validated with the experimental results obtained with the PIV method.

d) Under the numerical methodology, the limitations and advantages of the different turbulence models will be evaluated, and the chosen turbulence models will be used to study the hydrodynamics in detail, especially the VEDR.

e) An application of the numerical model will also be presented to study the impact of changes in the geometrical configuration, namely off-bottom clearance area and outer cylinders bottom shape of a Taylor reactor on its flow structure and its employment as a bioreactor.

2 Experimental Method - PIV

A 2D Particle Image Velocimetry (PIV) system measures instantaneous velocity flow in a plane. The in-house built computer software program or the one provided by the providers of the PIV system shows the vectorial velocity profiles in real time. The principal behind the measurement is the simple relation that velocity = distance /time. In this system, a sufficient amount of particles of very small size of $\approx$ 10-20 μm, are dispersed in the fluid assuming that these particles will follow the fluid movement. These particles are illuminated by a laser in a chosen plane in synchronization with a camera to capture a double frame image. The movement of particles between these two frames divided by the time-step between these two frames generates the velocity flow profile which can be extracted and treated further to estimate the fluctuating components and the VEDR.

2.1 Description of case set-up

Generally, a TVB, consisting of two concentric cylinders, is characterized on the basis of the rotation of one or both of the cylinders, resulting in the fluid motion due to the: 1) rotation of only the inner cylinder; 2) co-current rotation of both cylinders; and 3) counter-current rotation of both cylinders. Each of these types can be further characterized on the basis of the radius ratios of both cylinders and aspect ratio of the equipment. Radius ratio, η_{rr}, is the ratio of the inner cylinder radius, r_i, to the outer cylinder radius, r_o, or $\eta_{rr} = r_i/r_o$ and aspect ratio, Γ, is the ratio of cylinder length, L, to gap width, $b = r_o - r_i$, and $\Gamma = L/b$. In addition, Taylor number and Reynolds number also play a significant role in the classification of reactors in relation to the turbulence and vortex structures that will be present.

The Table 2 presents the dimensions and geometrical characteristics of TVB used in the PIV study, as shown in the Figure 2. Water at room temperature was used as the working fluid. The analytical estimations for these rotational speeds, shown in Table 3, were made using the (WENDT, 1933)'s correlation for estimating dimensionless torque-G shown in Equation 2.1, as mentioned by (LATHROP; FINEBERG; SWINNEY, 1992). These analytical estimations serve as the global estimates for this TVB configuration.

$$G = \begin{cases} 1.45\frac{\eta_{rr}^{3/2}}{(1-\eta_{rr})^{7/4}}Re^{1.5} \quad for 4\times 10^2 < Re < 10^4 \\ 0.23\frac{\eta_{rr}^{3/2}}{(1-\eta_{rr})^{7/4}}Re^{1.7} \quad for 10^4 < Re < 10^5 \end{cases} \tag{2.1}$$

Tabela 2 – Dimensions and geometrical characteristics of the TVB used in the PIV system.

Parameters	Value (dimensions)
Inner cylinder radius, r_i	100 (mm)
Outer cylinder radius, r_o	115 (mm)
Length of the reactor, L	200 (mm)
Gap width or distance between inner and outer cylinder, b	15 (mm)
Off-bottom clearance(OBC) or the height at which inner cylinder is placed above the outer cylinder, c	0 (mm)
Radius ratio, $\eta=\frac{r_i}{r_o}$	0.87
Aspect ratio, $\Gamma=\frac{h}{b}$	13.3
Angular velocity, ω	3.14 to 11.94 (rad/s)
Rotational speed, N	30 to 114 (rpm)
Reynolds N$^{\underline{o}}$, Re= $\frac{r_i\omega(r_o-r_i)}{\nu}$	4700 to17900
Taylors N$^{\underline{o}}$, Ta= $\frac{r_i^{1/2}\omega(r_o-r_i)^{3/2}}{\nu}$	1825 to 6935

2.2 PIV set-up

The PIV system consists of a class IV Quantel Big Sky Laser (15 Hz and λ=532 nm), FlowSense EO 16 MPixel camera (4872 × 3248) provided by Dantec Dynamics using a 60mm objective having a diaphragm aperture of f/2.8 to f/32 and a synchronization system, shown in Figure 2. The black colored internal cylinder is made of PVC, and the transparent external cylinder is made of Plexiglas. The camera was placed on the top of the TVB to the capture the motion of particles in the X-Y plane. The XY plane is chosen in order to capture the radial flow structures and radial gradients, which are assumed to be the principal components of the VEDR in a TVB. Capturing these smallest possible scales with regard to the radial gradients for a better estimation of VEDR is the main reason for the usage of the 2D PIV measurements in the X-Y plane, instead of the 3D stereographic or tomographic PIV study which would have provided the out-of-plane motion but at the expense of the spatial resolution.

The first chosen location was dependent on the height at which the laser equipment can be located to illuminate the chosen X-Y plane. Once the reactor and the laser equipment were put into place in order to capture the closest feasible X-Y plane, the camera and lens were focused in that respective plane. Between the camera and the chosen X-Y plane lies the fluid above that plane, and the flat and transparent Plexiglas plate placed on the top of the reactor. As the Plexiglas plate is flat and the motion imparted by the inner rotating cylinder is purely tangential which spread radially towards the outer cylinder, the perspective error in order to capture the tangential and the radial velocity components is assumed to be negligible in this case.

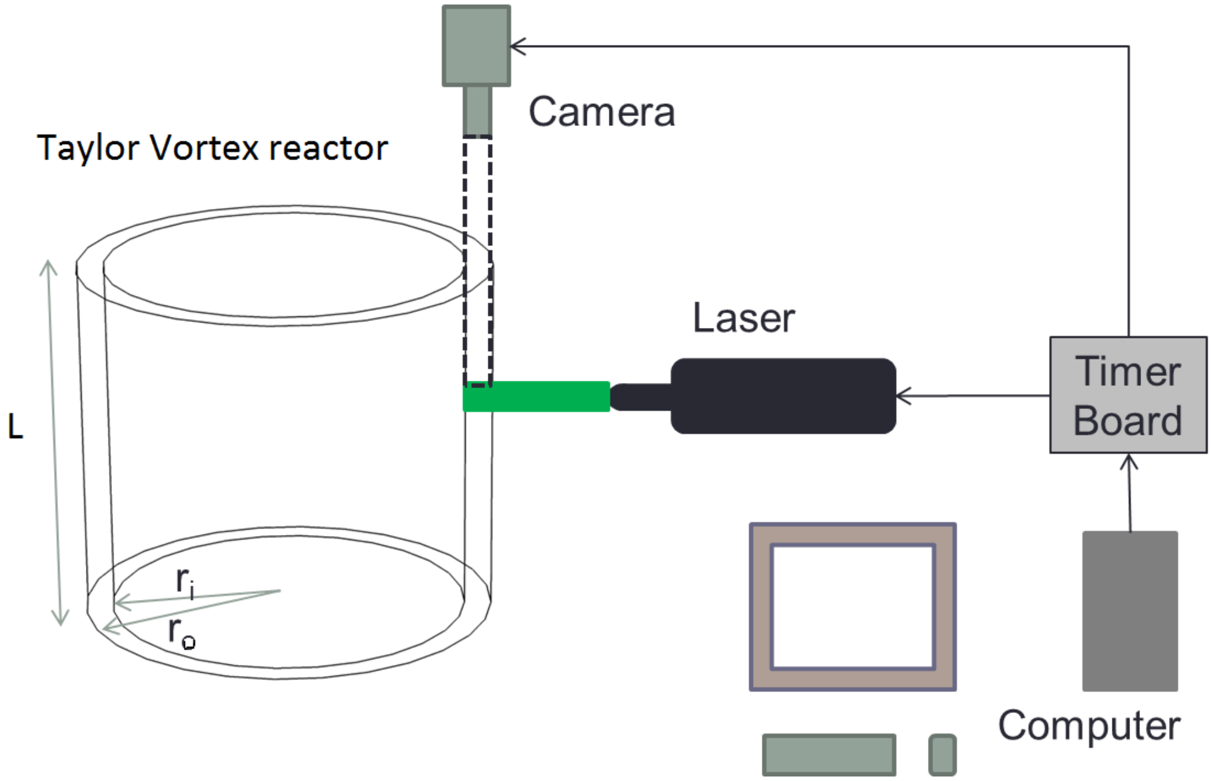

Figura 2 – PIV system consisting of the TVB, laser, camera, synchronization system and computer.

The focusing of the camera in the respective plane is the first step of calibration, which was achieved by using a quarter-circular flat plate of stainless steel with inner and outer radius one mm smaller than that of the inner and outer cylinders. The top of this plate was marked with horizontal and vertical lines one mm apart from each other forming a one mm square grid. The camera was focused on this plate and the images were saved in the computer program as calibration images. Then the second step for calibrating the images was conducted by computing a scale factor on the saved calibrated images. This scale factor was estimated by selecting two points on the saved images of the plate, and the known distance between the two points was provided. This procedure allowed the computer program to estimate the scale factor between the pixels and mm values along with the clarity of the images in that particular plane.

Each further chosen location was 10 mm downwards which lead to a small decrease in the spatial resolution for each further location. The five chosen horizontal locations are between Z_L= 0.725 ± 0.005 and 0.525 ± 0.005 with each approximately 10 mm apart from one another. Silver coated glass beads and fluorescent Rhodamine particles of 10 and 20 μm size, respectively, were used as seeding particles. A time-step size of 75, 75, 150, 200 and 300 μs was used for the 114, 90, 70, 50 and 30 rpm, respectively, with the laser sheet thickness of 1 mm. A total of 2500 image pairs were found to be more than sufficient for each ω at five different horizontal locations to achieve the statistical convergence of

Tabela 3 – Analytical estimations for the TVB used in the PIV system.

Parameters	Value (dimensions)				
	114 (rpm)	90	70	50	30
Moment, $\tau = G\rho\nu^2\text{h}$, where $G = 0.23\frac{\eta_{rr}^{3/2}}{1-\eta_{rr}}^{7/4} Re^{1.7}$, (WENDT, 1933)	0.022 (Nm)	0.015	0.01	0.006	0.003
Angular Velocity, ω	11.9 (rad/s)	9.4	7.3	5.2	3.1
Tip Speed, $r_i\omega$	1.19 (m/s)	0.94	0.73	0.52	0.31
Wall shear stress at inner wall, $\tau_{wi} = \tau/(2\pi r_i^2\text{h})$	1.78 (N/m^2)	1.19	0.78	0.46	0.21
Wall shear stress at outer wall, $\tau_{wo} = \tau/(2\pi r_o^2\text{h})$	1.35 (N/m^2)	0.9	0.59	0.35	0.16
Friction velocity at inner wall, $u_{\tau i} = \sqrt{\tau_{wi}/\rho}$	0.042 (m/s)	0.035	0.028	0.021	0.015
Friction velocity at outer wall, $u_{\tau o} = \sqrt{\tau_{wo}/\rho}$	0.037 (m/s)	0.03	0.024	0.019	0.013
$u_{\tau i}/r_i\omega$	0.035	0.037	0.038	0.04	0.048
Global power, P=$\tau\omega$	0.27 (Watts)	0.14	0.07	0.03	0.01
Average VEDR, $\langle\epsilon\rangle = P/(\rho\pi(r_o^2 - r_i^2)\text{h})$	0.132 (W/kg)	0.07	0.035	0.015	0.004
Average Kolmogorov's micro-scale, $\langle\eta\rangle = (\nu^3/\langle\epsilon\rangle)^{\frac{1}{4}}$	52.5 (μm)	61.6	73.0	90.5	124.5
Average Taylor's micro-scale, $\langle\Lambda\rangle = \sqrt{15\nu\overline{u_i^2}/\langle\epsilon\rangle}$	1.3 (mm)	1.4	1.5	1.7	1.9
VEDR at inner wall, $\epsilon_{innerwall} = u_{\tau i}^4/\nu$	3.172 m^2s^{-3}	1.415	0.602	0.211	0.046
VEDR at outer wall, $\epsilon_{outerwall} = u_{\tau o}^4/\nu$	1.814 m^2s^{-3}	0.809	0.344	0.121	0.027

the second order fluctuating velocity components, namely $u_r^{'2}$, $u_\theta^{'2}$ and $u_r^{'}u_\theta^{'}$, as shown in Figure 3.

The acquired data was processed with an image acquisition system provided by Dantec Dynamics, Dynamicstudio V4.0. The vector analysis was conducted using the adaptive correlation with overlapping windows ranging from 0 to 75 % and ICS ranging between 64 to 8 pixels squared for high resolution. The spurious vectors were removed using range validation, and then these were replaced by moving average validation using 3 or 5 neighboring cells, in most cases 3 neighboring cells were used. In total, less than 2.9, 3.5, 4, 7.7 and 6.7 % percent of spurious vectors were replaced at the $Z_L = 0.725$, 0.675, 0.625, 0.575 and 0.525 ± 0.005, respectively. The spatial resolutions based on these aspects for the horizontal plan located at $Z_L = 0.725 \pm 0.005$ are presented in the Table 4.

Tabela 4 – Different ICS and overlap windows tested at Z_L= 0.725 ± 0.005.

ICS	Overlap window	Spatial resolution in μm
64	0	546
32	0	273
	25	205
	50	136
	75	68
16	0	136
	25	102
	50	68
	75	34
8	0	68

2.3 Estimation of VEDR

The PIV measurements were taken in a horizontal plan in a location where U or u' = U_θ or u'_θ represents mean and fluctuating tangential component and V or v' = U_r or u'_r represents mean and fluctuating radial component of the velocity. In this context, y represents the radial directions and $\theta = tan^{-1}(y/x)$ represents the tangential direction, respectively, and were extracted as *.txt files from the image files using the Dantec Dynamic program Dynamicstudio V3.31. These txt files for the experimental results were treated with Matlab to create the gradients using the 2^{nd} order central differencing approximation of the first derivative, Equation 2.2, for the central elements. The boundary elements being only at the inner and outer wall due to the usage of the 2^{nd} order scheme were not considered for the VEDR estimation.

$$f'_i = \frac{f_{i+1} - f_{i-1}}{2h} + E, E \cong \frac{1}{6} h^2 (-f_i^3) \tag{2.2}$$

The gradients were estimated using the mean and fluctuating velocity components using the cylindrical coordinates (SUBRAMANIAN, 2015). The VEDR derived from the gradients of the mean and fluctuating velocity components are here-onwards termed as the VEDR of the mean flow kinetic energy (MFKE) and TKE, respectively. These two components of the VEDR are estimated directly from the Equations 2.3 and 2.4, albeit only five out of 12 gradients are estimated from the PIV measurements in the x-y plane, as

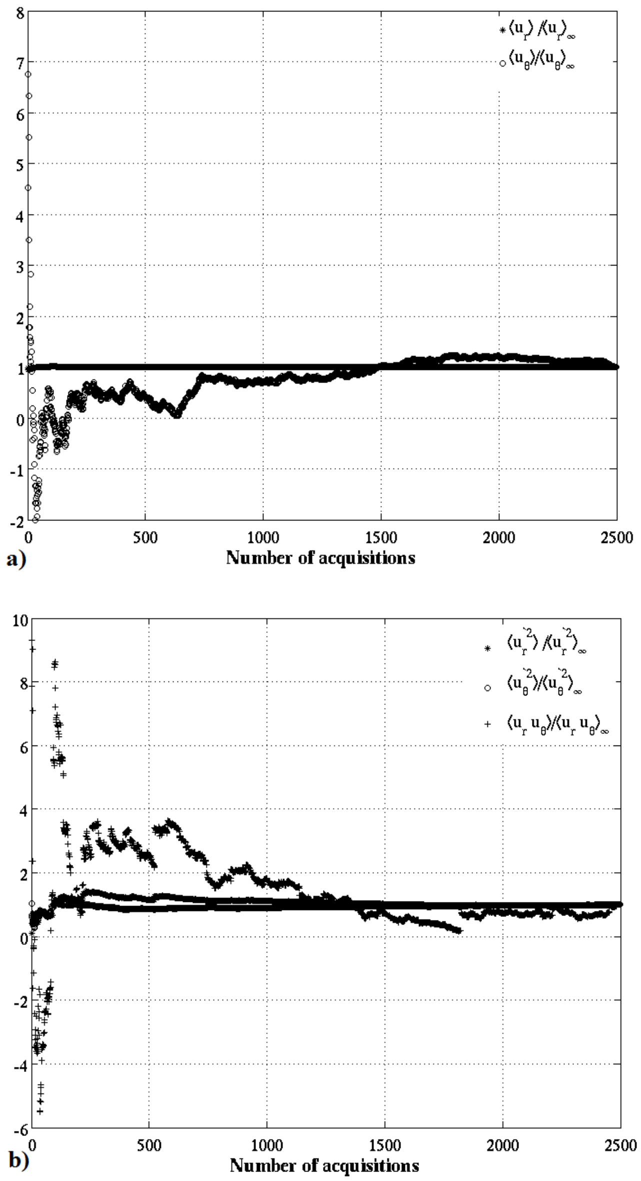

Figura 3 – Convergence statistics of moment of order one (a) and two (b) on a horizontal plane located at Z_L=0.725 and radially at R_b=0.082.

shown in Equations 2.5 and 2.6, respectively for the mean flow and turbulence components.

$$\begin{aligned}\epsilon_m = \nu \Bigg\{ & 2\left(\left(\frac{\partial \overline{U_r}}{\partial r}\right)^2 + \left(\frac{1}{r}\frac{\partial \overline{U_\theta}}{\partial \theta} + \frac{\overline{U_r}}{r}\right)^2 + \left(\frac{\partial \overline{U_z}}{\partial z}\right)^2\right) + \left(r\frac{\partial \overline{(U_\theta/r)}}{\partial r}\right)^2 \\ & + \left(\frac{1}{r}\frac{\partial \overline{U_r}}{\partial \theta}\right)^2 + \left(\frac{1}{r}\frac{\partial \overline{U_z}}{\partial \theta}\right)^2 + \left(\frac{\partial \overline{U_z}}{\partial r}\right)^2 + \left(\frac{\partial \overline{U_r}}{\partial z}\right)^2 + \left(\frac{\partial \overline{U_\theta}}{\partial z}\right)^2 \\ & + 2\left(\frac{\partial \overline{(U_\theta/r)}}{\partial r} \cdot \frac{\partial \overline{U_r}}{\partial \theta} + \frac{1}{r}\frac{\partial \overline{U_\theta}}{\partial z} \cdot \frac{\partial \overline{U_z}}{\partial \theta} + \frac{\partial \overline{U_r}}{\partial z} \cdot \frac{\partial \overline{U_z}}{\partial r}\right)\Bigg\}\end{aligned} \tag{2.3}$$

$$\begin{aligned}\epsilon_t = \nu \Bigg\{ 2 \left(\overline{\left(\frac{\partial u'_r}{\partial r}\right)^2} + \overline{\left(\frac{1}{r}\frac{\partial u'_\theta}{\partial \theta} + \frac{\overline{u'_r}}{r}\right)^2} + \overline{\left(\frac{\partial u'_z}{\partial z}\right)^2} \right) + \overline{\left(r\frac{\partial (u'_\theta/r)}{\partial r}\right)^2} \\ + \overline{\left(\frac{1}{r}\frac{\partial u'_r}{\partial \theta}\right)^2} + \overline{\left(\frac{1}{r}\frac{\partial u'_z}{\partial \theta}\right)^2} + \overline{\left(\frac{\partial u'_z}{\partial r}\right)^2} + \overline{\left(\frac{\partial u'_r}{\partial z}\right)^2} + \overline{\left(\frac{\partial u'_\theta}{\partial z}\right)^2} \\ +2 \left(\overline{\frac{\partial (u'_\theta/r)}{\partial r} \cdot \frac{\partial u'_r}{\partial \theta}} + \overline{\frac{1}{r}\frac{\partial u'_\theta}{\partial z} \cdot \frac{\partial u'_z}{\partial \theta}} + \overline{\frac{\partial u'_r}{\partial z} \cdot \frac{\partial u'_z}{\partial r}} \right) \Bigg\}\end{aligned} \tag{2.4}$$

$$\begin{aligned}\epsilon_m = \nu \Bigg(2 \left(\left(\frac{\partial \overline{U_r}}{\partial r}\right)^2 + \left(\frac{1}{r}\frac{\partial \overline{U_\theta}}{\partial \theta} + \frac{\overline{U_r}}{r}\right)^2 \right) + \left(r\frac{\partial \overline{(U_\theta/r)}}{\partial r}\right)^2 \\ + \left(\frac{1}{r}\frac{\partial \overline{U_r}}{\partial \theta}\right)^2 + 2\frac{\partial \overline{(U_\theta/r)}}{\partial r} \cdot \frac{\partial \overline{U_r}}{\partial \theta} \Bigg)\end{aligned} \tag{2.5}$$

$$\begin{aligned}\epsilon_t = \nu \Bigg(2 \left(\overline{\left(\frac{\partial u'_r}{\partial r}\right)^2} + \overline{\left(\frac{1}{r}\frac{\partial u'_\theta}{\partial \theta} + \frac{\overline{u'_r}}{r}\right)^2} \right) + \overline{\left(r\frac{\partial (u'_\theta/r)}{\partial r}\right)^2} \\ + \overline{\left(\frac{1}{r}\frac{\partial u'_r}{\partial \theta}\right)^2} + 2\overline{\frac{\partial (u'_\theta/r)}{\partial r} \cdot \frac{\partial u'_r}{\partial \theta}} \Bigg)\end{aligned} \tag{2.6}$$

2.4 Basic Aspects of PIV

Every basic choice in the utilization of PIV equipment has a significant impact on the estimation of the finer quantities, such as VEDR. To estimate accurately the smaller structures a very fine spatial resolution is required. The interesting aspect is that the actual spatial resolution is known after the treatment of data, meaning that the concentration of particles, size of particles and time-step between frames is decided by hit and trail method. In addition, all these basic aspects are inter-related to each other. This section shows the importance of these basic aspects in the estimation of the VEDR. All these aspects were studied with the 114 rpm rotational speed unless otherwise stated.

2.4.1 Concentration of particles

Figure 4 shows the concentration of particles in a horizontal plane in the TVB without a grid (4a) and with a 32 grid square (4b) at two different rotational rates of 114 rpm and 30 rpm. This figure presents two aspects related to the concentration of particles: firstly, variation in the concentration with the change in rotational speed; and secondly, variation in concentration with change in ICS. It can be seen that there are lesser number of particles in the 30 rpm frame (the one in the front) in comparison to the 114 rpm (the one behind) in both parts a) and b). The reason behind this is the gradual sedimentation of particles with each decrease in the rotational speed from 114 rpm to 30 rpm. An improvement in the concentration may be required in order to attain a fine spatial resolution as the rotational speed is decreased.

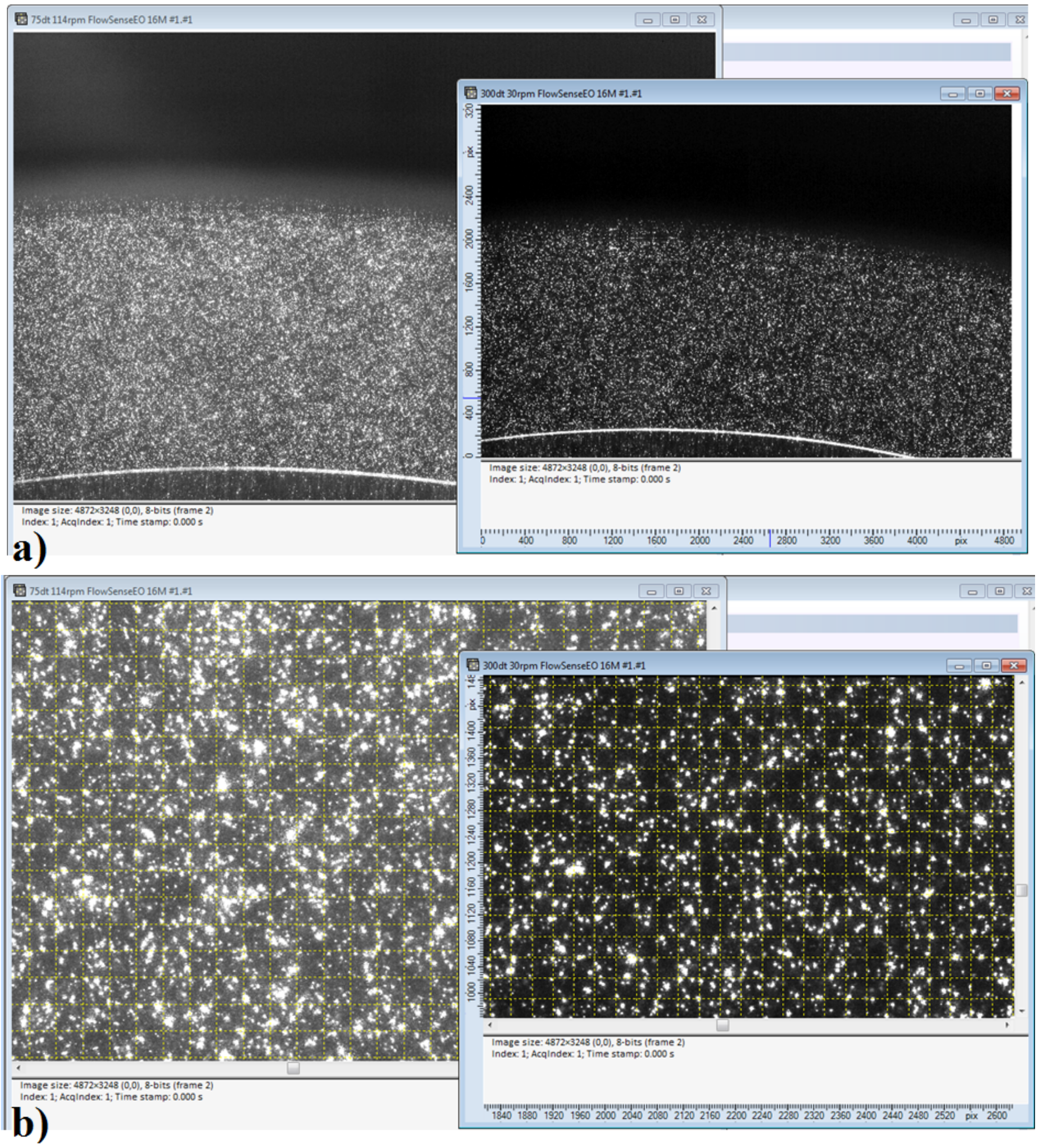
75dt 114rpm FlowSenseEO 16M #1.#1
300dt 30rpm FlowSenseEO 16M #1.#1
Image size: 4872×3248 (0,0), 8-bits (frame 2)
Index: 1; AcqIndex: 1; Time stamp: 0.000 s
a)
b)

Figura 4 – Concentration of particles in a horizontal plane in the TVB at two different rotational rates: 114 (the one behind) and 30 (the one in front) rpm without grid (a) and with a 32 square grid (b).

The choice of ICS value is directly related to the concentration of particles in the fluid. As mentioned earlier sedimentation leads to a decrease in the concentration or reduction in the number of particles in each square grid of 32 pixels with many empty grids as well. Empty grids generate spurious vectors which have to be replaced with the average of surrounding cells. This is one of the reasons behind the noise in the data; thus, poor concentration may lead to erroneous results, especially in the estimation of the smallest scales. If a smaller grid is chosen, say square grid of 16 pixels, then these empty grids will only increase requiring further substitution, in other words increasing noise in the data.

2.4.2 Size of particles

Figure 5 presents the influence of particle size on the tangential mean velocity components and its squared fluctuating velocity component located at $Z_h = 0.725 \pm 0.005$ using a time-step of 75 μs. Clearly the reduced particle size has not only improved the tangential mean velocity component but also has a significant impact on its squared fluctuating counterpart. Though there could be a slight difference of location of ± 1 mm between the two particle size estimations, a probable reason behind slightly different profile structures. Anyhow, in terms of the mean tangential velocity component, the estimations of the 10 μm particle size were completely identical for all four of the ICS values; whereas, for the 20 μm particle size the structures for the four ICS values had some slight differences and a little bit of noise as well. The noise becomes more pronounced for the 20 μm particle size in the estimation of the squared fluctuating tangential velocity component in addition to another problem of doubling of the magnitude with each decrease in the ICS value. The magnitude increases two times when the ICS value is decreased from 64 to 32 and from 32 to 16 and so on. This increase is not practical, and this lead to this study of understanding the influence of particle size on the estimation of the flow parameters.

Size of particle is important in order to attain the optimum concentration to attain a fine spatial resolution. The smallest available true spatial resolution is the one with overlap zero is 16 square grid leading to a spatial resolution of 136 μm (Table 4). An important point to note is that the 8 grid structure is actually adapted from the 16 grid structure; therefore, 16 square grid is considered as the smallest true spatial resolution available in this study. As per general guidelines, around 5 particles per square grid are considered an optimum concentration. Fitting five particles of the size of 20 μm in grid size of 136 μm is practically very difficult and may result in agglomeration of particles which will hinder further the estimation of smaller scales. Hence, based on this understanding the particle size was reduced from 20 μm to 10 μm, and a drastic improvement was seen in the estimations of squared fluctuating tangential velocity component (Figure 5b).

It can be seen that the magnitude variation between the 64, 32 and 16 square grids is very small with only slight improvements in magnitude and increase in the total number of data points. Moreover, there was very little noise in the data which in comparison to the estimations of the 20 μm is practically unnoticeable. The results of the ICS 8 square grid for the 10 μm particle size were considered unpractical in similarity with the results of the 32, 16 and 8 square grid for the 20 μm particle size. The 8 square grid has a spatial resolution of 68 μm, which implies that fitting five particles of 10 μm size in 68 μm will be a challenging proposition as in the case of the 20 μm particle size. Particles of size between 2-3 μm are required in order to achieve correct estimations for the 68 μm spatial resolution. However, due to limited time and financial resources it was not possible to use extremely costly particles of mean diameter of 2-3 μm.

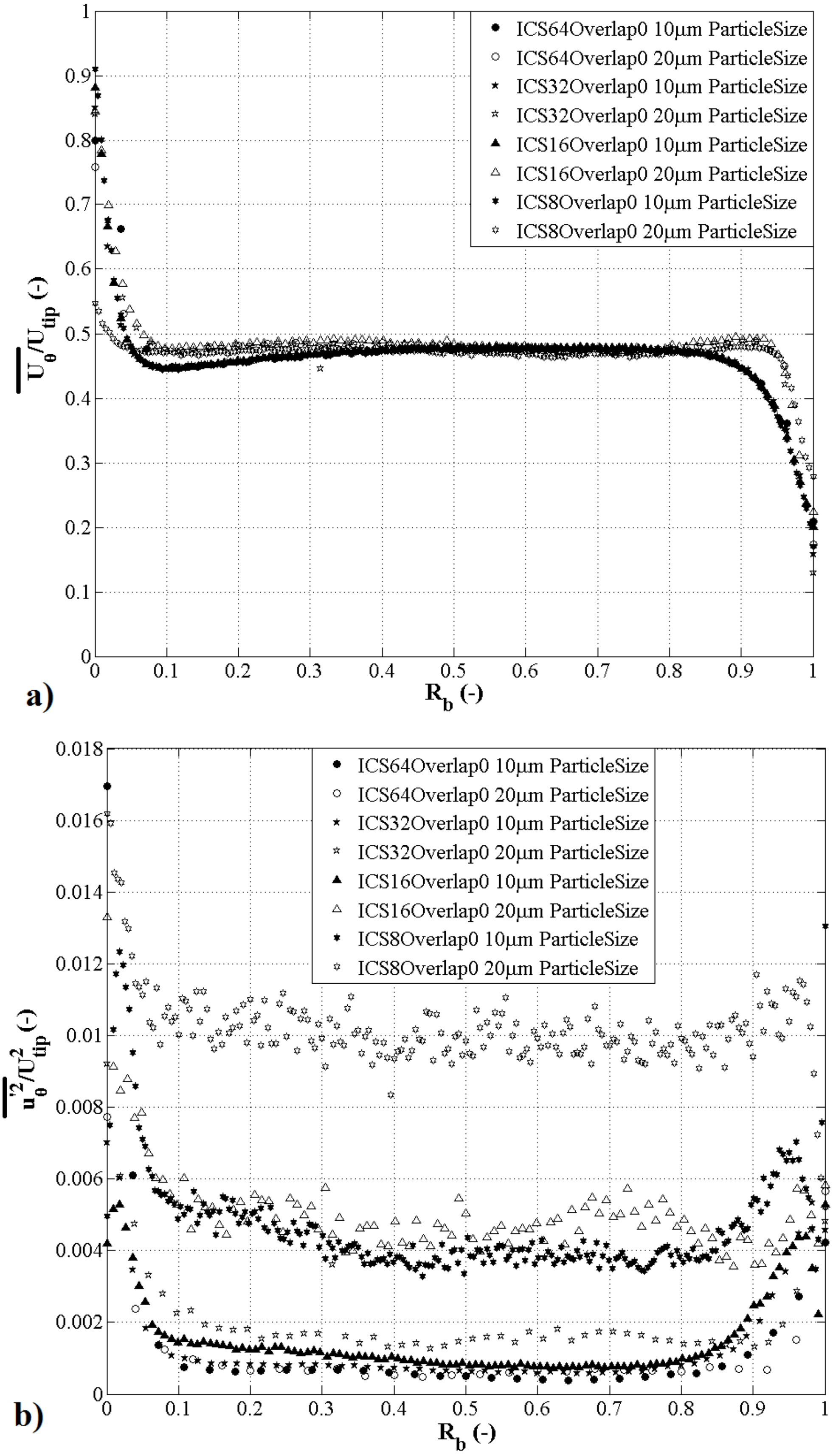

Figura 5 – Impact of particle size on the estimations of mean tangential velocity (a) and squared fluctuating velocity (b) for the horizontal plane located at $Z_h = 0.725 \pm 0.005$.

2.4.3 Time-step between frames

First of all, time-step is the difference in the time between a double frame image. A double frame image is necessary in order to estimate the movement of particles within that time-step from the first frame to the second. Depending on the fluid flow conditions and the chosen spatial resolution, the time-step should be small enough to capture the movement of particle from the first frame to the second. As per general guidelines, the movement of particle covering $1/4^{th}$ of the ICS is considered sufficient. However, when the time-step is very small of the order of 100 μs, it becomes necessary to choose time-step wisely. In this case, we studied four different time-steps within the range of 50 to 200 μs.

In the Figure 6, the influence of the time-step on the mean tangential velocity and squared fluctuating velocity component is shown. As in the case of the particle size, there is practically no influence of the time-step on the mean tangential velocity component. On the other hand, in the case of squared fluctuating tangential velocity component, the impact is significant on both the noise and magnitude value. With each decrease in the time-step from 50 towards 150 μs, the noise is reduced drastically and so does the magnitude. The results for the 150 and 200 μs are very similar with little noise.

These estimates of four different time-steps conducted with the 20 μm particle size were compared with the particle size of 10 μm using time-step of 75 μs, to compare with the better estimates obtained with the 10 μm particles. The estimations of the 10 μm particles were found to be very similar with the one using 150 μs time-step for the 20 μm particles. This suggests that the size of particle also plays a significant role in the determination of the time-step. The time-step size for the 20 μm particles is double that for the 10 μm particles to obtain valid results. It should be noted that the slight variation in the profile structure is most probably due to difference of location of ± 1mm between the profile structures for the two different particle sizes.

To study further this effect of the particle size on the time-step, Figure 7 presents the estimations of the dimensionless VEDR of mean flow kinetic energy for the two particles sizes located at $Z_h = 0.725 \pm 0.005$. In the x and y axis of the Figure 7, the shear velocity, $u_\tau i$, and the VEDR, $\epsilon_{innerwall}$, at the inner wall are the analytical estimations mentioned in the Table 3.

It can be seen that smaller the time-step is, higher the estimation of the VEDR becomes in the case of 20 μm particles. The squared fluctuating tangential velocity estimations for the 50 μs time-step were unpractical, and those estimations for the 150 and 200 μs time-step were of similar magnitude. However, this is not the case for the estimation of the VEDR where the 150 μ time-step estimations are higher in magnitude in comparison to those of the 200 μs time-step. On the other hand, the estimations of the 10 μm particles at 75 μs time-step are even better in the boundary layer area and the bulk

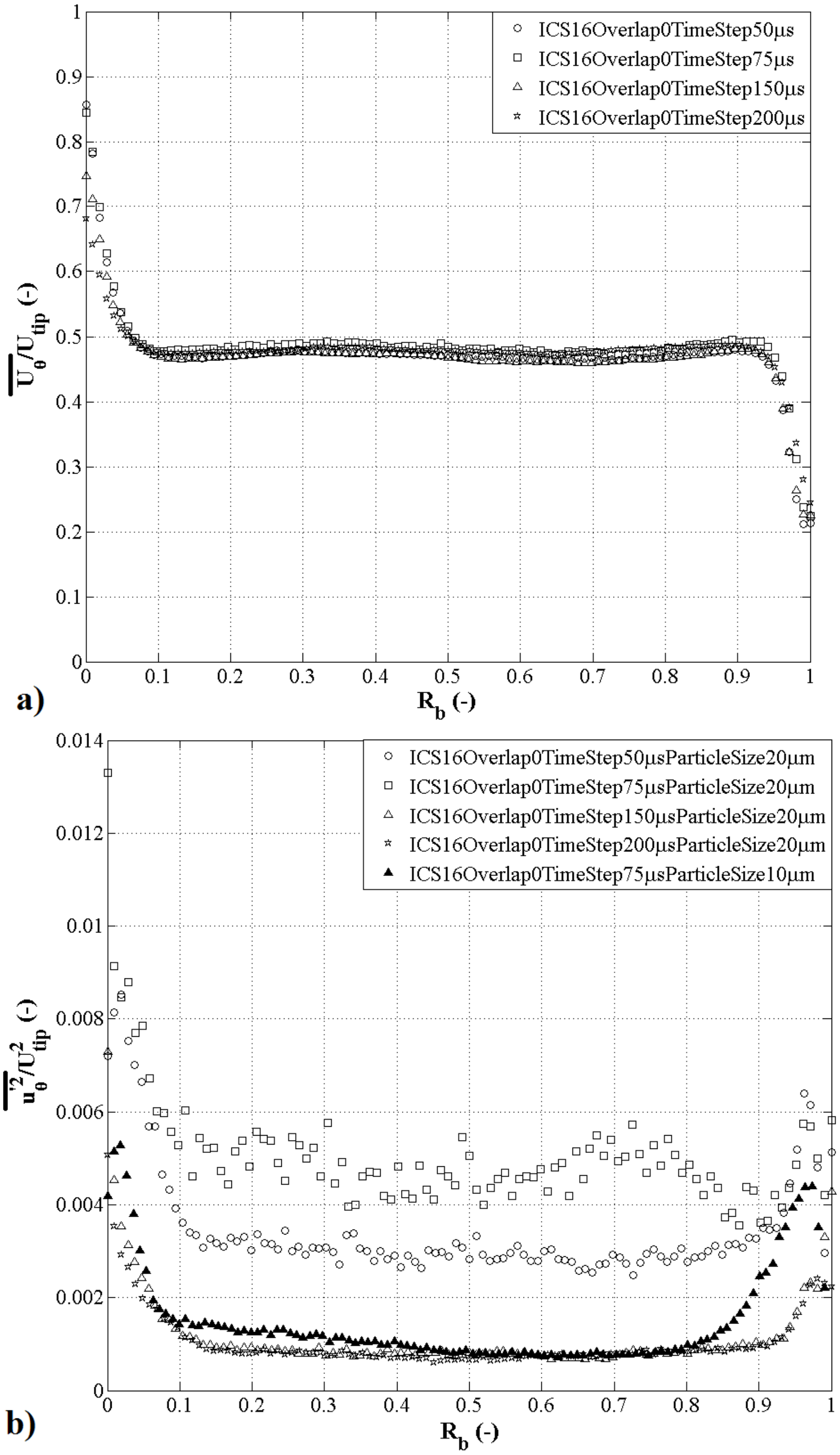

Figura 6 – Impact of time-step on the estimations of mean tangential velocity (a) and squared fluctuating velocity (b) for the horizontal plane located at $Z_h = 0.725 \pm 0.005$ using particle size of 20 μm.

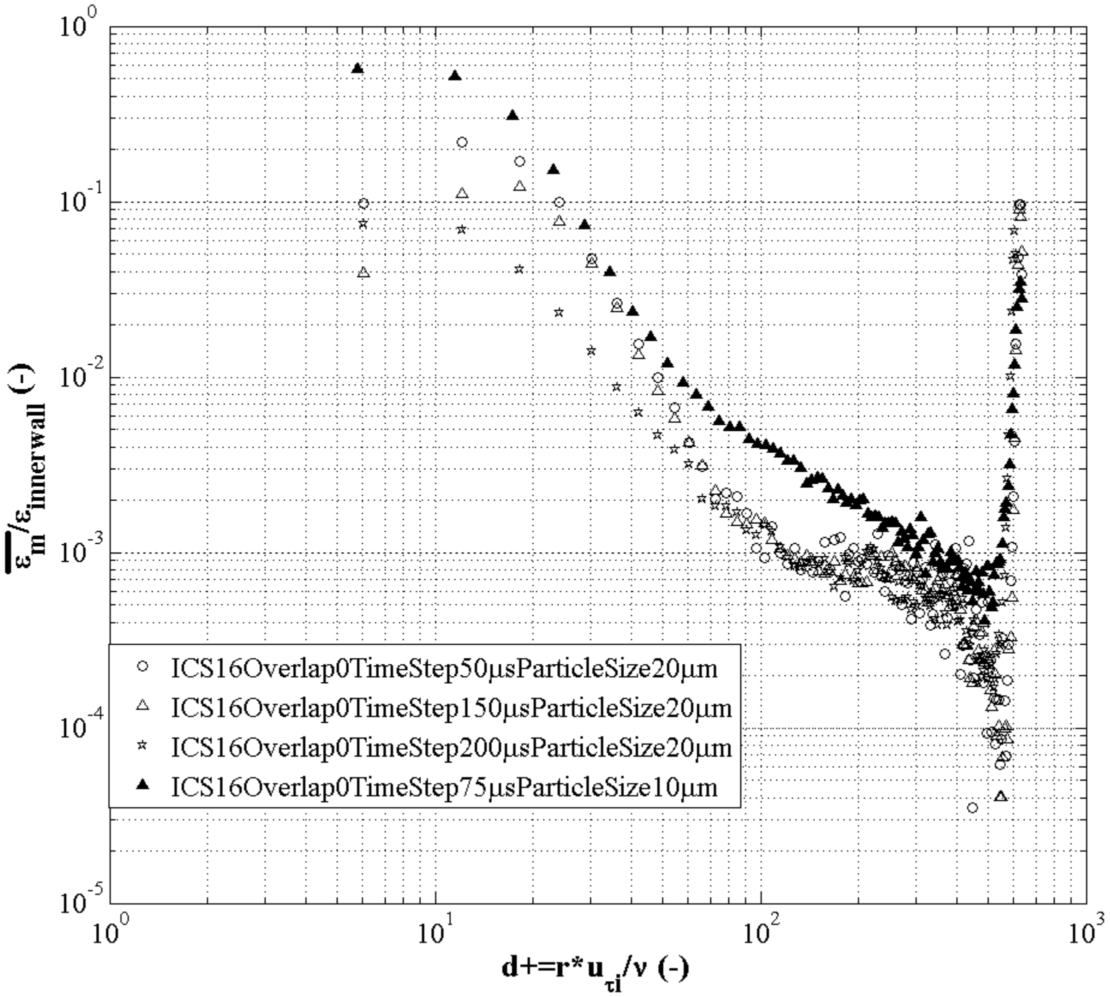

Figura 7 – Influence of the time-step and particle size on the VEDR of mean flow kinetic energy.

zone of the inner cylinder. This clearly demonstrates the need of the smaller time-step and particle size for improved predictions of not only the fluctuating velocity components but also the VEDR; thus, making the 10 μm particle size as the preferred choice for this study and 75 μs time-step for the 114 rpm rotational speed. Based on this rationale, time-step for the other rotational speeds was chosen.

2.4.4 Choosing overlap & ICS

The interrogation cell size (ICS) value is the initial grid structure in which the flow domain is divided to obtain the velocity vectors. Smaller the ICS value is, finer the grid structure becomes generating the smallest feasible spatial resolution. To estimate the velocity vectors, the double framed image is interposed on each other to observe the movement of particle from one frame to another. When interposing the two frames if no adjacent areas are used, then it is termed as the zero overlap ratio and the spatial resolution is equivalent to the basic grid structure of the ICS. However, if the adjacent area is used, usually between 25, 50 and 75 %, then the number of data points are increased for each increase in the adjacent area from 25 to 75 % leading to smaller spatial resolution for each increase in the overlap ratio. Contrary to the ICS value, higher the overlap ratio smaller the spatial resolution becomes; therefore, we see a spatial resolution of 68 μm at 32, 16 and 8 ICS with an overlap of 75, 50 and 0 respectively, as shown in the Table 4. It is important to note that the different overlap ratios use the same initial grid structure.

The 64 pixels square grid at zero overlap ratio is the coarsest grid with a spatial resolution of 546 μm with least number of data points. Although, the spatial resolution of 546 μm is more than two times finer than the Average Taylor's micro-scale of 1.3 mm, such fewer points leads to comparatively poor estimation of even the mean tangential velocity components near the inner and outer boundaries, as shown in Figure 8. A higher overlap ratio was not tested for the 64 pixels square grid due to the coarseness of the basic grid structure, and the objective of studying the smallest scales which would have been feasible only with smaller ICS values. Additionally, such fewer data points do not allow studying the boundary layer area in detail.

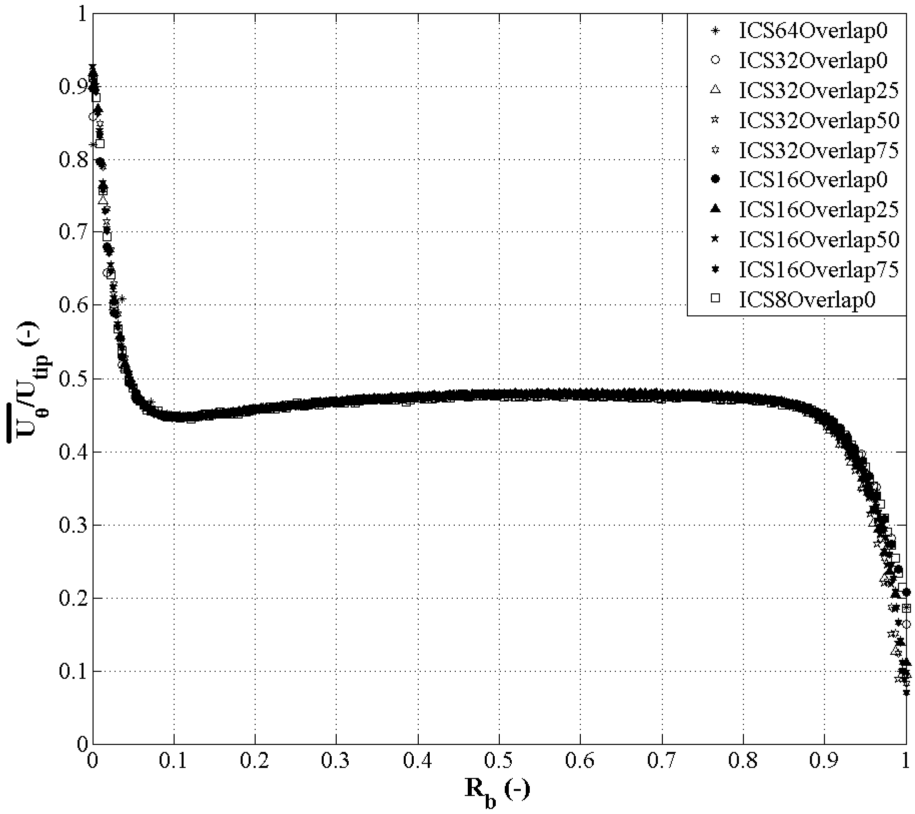

Figura 8 – Radial profile of mean tangential velocity at different overlap ratios and ICS values at $Z_L = 0.725 \pm 0.005$.

The results for the mean tangential velocity profile becomes independent of the ICS from 32 pixels squared onwards or 273 μm; in other words, at higher ICS values the flow structure may not be the actual representation while the lower ICS values will not provide any improvement in the estimation for the mean velocity components. If the estimations of the grid are independent, then the overlap ratio also should not influence the predictions of the mean tangential velocity component, which can be clearly seen in the Figure 8. The only advantage of using the overlap ratio for the estimation of the mean velocity component is to increase the number of data points in the boundary layer area, where lay the steepest gradients and could be beneficial in the prediction of the gradients of the mean flow components of the VEDR.

The estimation of the squared fluctuating tangential velocity component (Figure 9) also shows slight improvement in its estimation for the smaller ICS values and for higher overlap ratios in the boundary layer area. It should be noted that the estimations for the 8 ICS pixels square grid are considered inaccurate, hence not presented in the VEDR estimations. This inaccuracy arises due to the practical impossibility of achieving a good concentration of particles of the size10 μm per square grid of 68 μm. Resulting poor concentration generates many empty grids which are replaced by the average of surrounding particles and most of the grids with only one or two particles which in turn generates poor estimation of the turbulence with a lot of noise in the data. As per general guidelines, around 5 particles per square grid are considered an optimum concentration to generate a good velocity vector. Smaller particles of the size of 2-3 μm which could have been ideal for the 8 ICS square grid were not tested due to their extremely high cost. The experimentation with 20 μm particle size lead to discovery of this error, as can been seen in the Figure 5b. The estimations for the particle size 20 μm doubled for each decrease in the ICS value from 64 to 32 to 16 to 8 due to poor concentration of particles of even bigger size in similar spatial resolutions. Additionally, the results of the 16 ICS value were found to be slightly better than those of the 32 ICS value near the walls. The estimations of the 50 % overlap were very similar to those of the 75 % near the boundary layer, and with much less noise in the bulk zone.

In terms of the viscous dissipation of mean flow kinetic energy estimated from the gradients of the mean velocity components (Figure 10), an improvement can be seen in the estimation for both the overlap ratio and ICS value in the boundary layer area. An increase in the noise can be seen with increase in the overlap ratio for the 16 ICS with significant amount of noise for the overlap ratio of the 75 % in the bulk zone. The 16 ICS Overlap 75 have a spatial resolution of 34 μm, respectively, which is far too small for the particle size of 10 μm to have good concentration of particles, which consequently leads to this increased amount of noise in the estimation of the small magnitude values of the viscous dissipation of mean flow kinetic energy present in the bulk zone. The fluctuating tangential velocity component at 16 ICS Overlap 75 also presented significant amount of noise, as shown in Figure 9, which will only become worse for an even finer estimation of the VEDR; consequently, the 16 ICS Overlap 75 has not been presented for the viscous dissipation of turbulent kinetic energy estimated from the fluctuating velocity components.

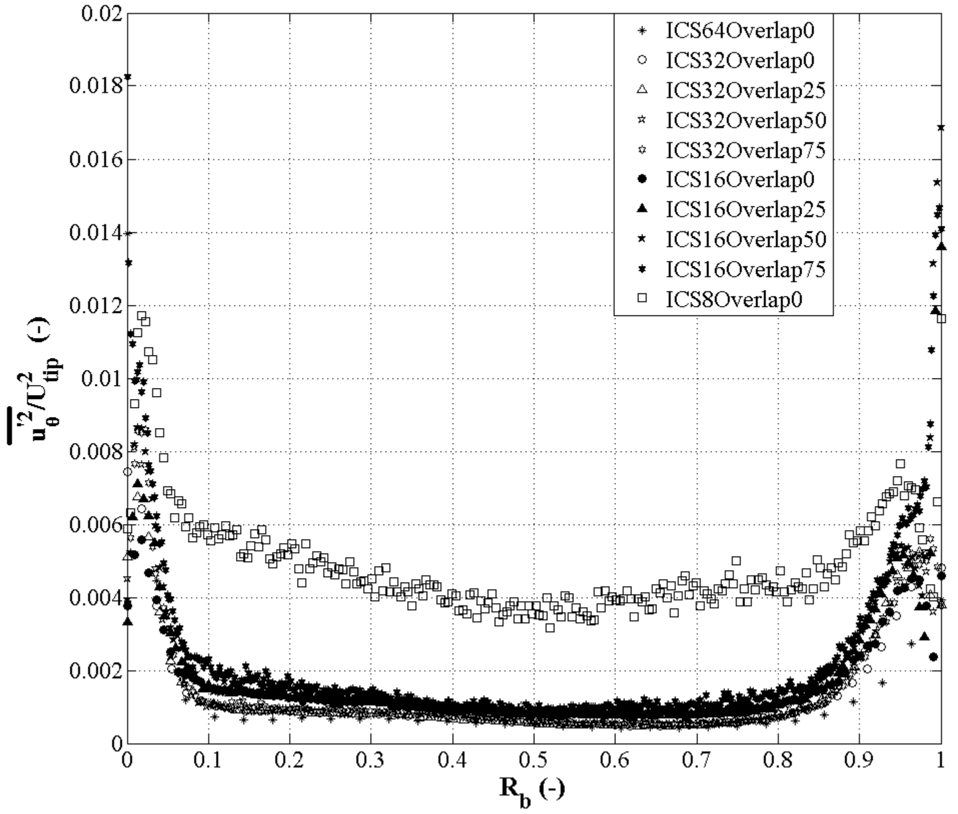

Figura 9 – Radial profile of squared fluctuating tangential velocity at different overlap ratios and ICS values at $Z_L = 0.725 \pm 0.005$.

Interestingly, the 16 ICS Overlap 50 and 32 ICS Overlap75 have a spatial resolution of 68 μm each, respectively, but the amount of noise is much less as can be seen in Figure 11. The less noise in the 32 ICS Overlap 75 in comparison to the 16 ICS Overlap 50 indicates that higher base grid structure helps in maintaining a better concentration of particles per square grid.

The prediction of viscous dissipation of turbulent kinetic energy (Figure 12) is higher for each reduction in the ICS value and increment in the overlap ratio. At the overlap ratio of zero, the magnitude increases by almost an order in the bulk zone for each decrease in the ICS value. While, for a constant ICS value, each increment in the overlap ratio predicts gradual increment in the magnitude of the viscous dissipation of turbulent kinetic energy through-out the reactor. This is the first instance where the increase in the overlap ratio has such a significant impact on the magnitude of the variable. It seems logical that with each decrease in the ICS value, smaller scales of turbulence are being captured.

Tokgoz et al. (2012) also observed similar observations of continual increase in their VEDR estimation for each decrease in the ICS or IW (interrogation window) as shown in Figure 13. It can be seen that with decrease by half in the IW values, i.e. from 160 to 80 to 40 IW, of the Tokgoz et al. (2012), the increase in the estimation of

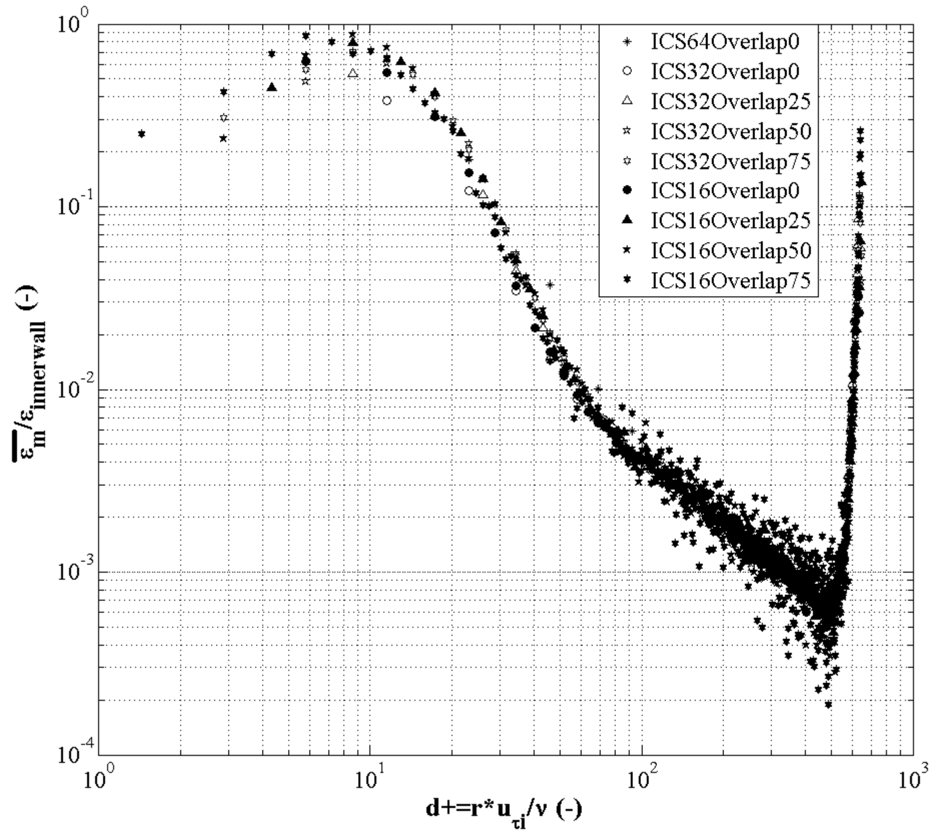

Figura 10 – Radial profile of the viscous dissipation of mean flow kinetic energy at different overlap ratios and ICS values at $Z_L = 0.725 \pm 0.005$.

VEDR is quite significant, in similar aspect of the results presented in this study. The difference is that their magnitude values are much lower due to their much courser spatial resolution (smallest resolution of 391 μm) for similar Reynolds number, and they used the instantaneous velocity components for the prediction of their VEDR. Such gradual increase generates another question if there is still under-prediction in the estimation of the viscous dissipation of turbulent kinetic energy. To resolve this question, the impact of the spatial resolution on the viscous dissipation of turbulent kinetic energy is presented in Figure 14. The data presented in the Figure 14 is shown in the Table 5.

First of all, it is important to understand the information that is being presented in the Figure 14 and Table 5. This data is presented only for one horizontal location because $\epsilon_{t,max}$ is different at each horizontal location and will generate significant amount of noise in the data. Ideally for the purpose of statistics, a mean value of the $\epsilon_{t,max}$ over the axial length should be considered for each and every rotational velocities at different ICS and overlap ratios, but is not possible in this case. Presently, only in the case of 16 ICS overlap 50, there is access to the mean value of the $\epsilon_{t,max}$ over the five horizontal locations and is equal to 0.66 which is very close to the value of 0.77 located at Z_L= 0.725 ± 0.005.

This work was derived from the work of Delafosse et al. (2011), where they presented similar data for the stirred rank reactor and used the variable ϵ_{mean}/N^3D^2 instead of

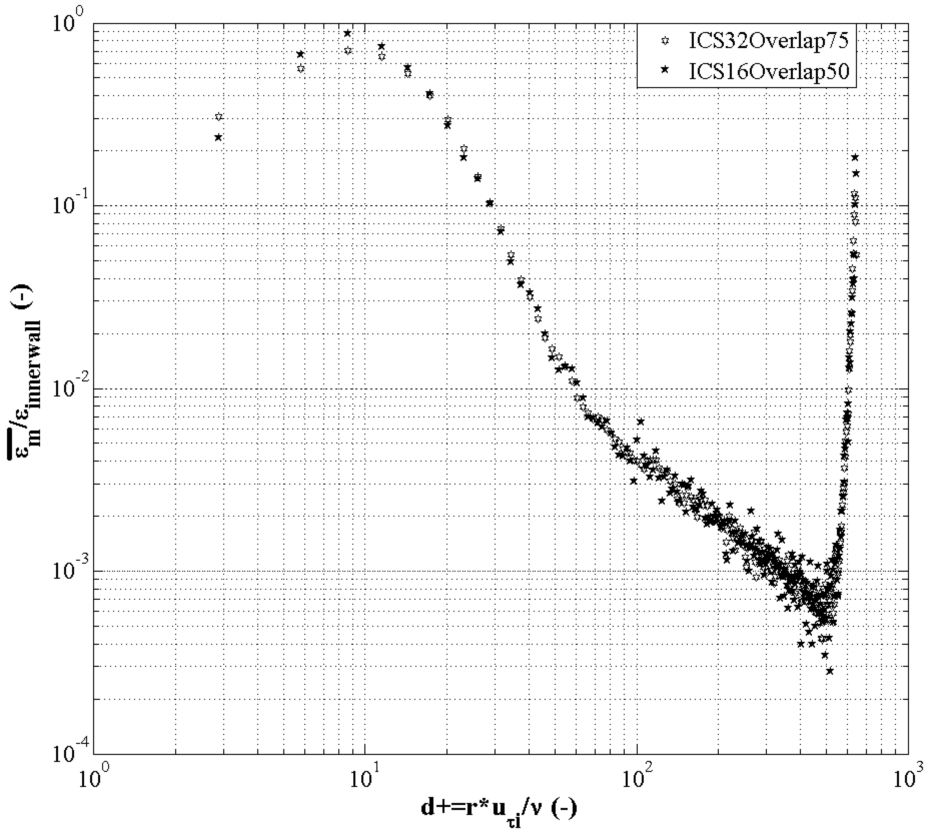

Figura 11 – Radial profile of the viscous dissipation of mean flow kinetic energy at different overlap ratios and ICS values at $Z_L = 0.725 \pm 0.005$.

Tabela 5 – Dimensionless Spatial resolution,$\delta/\langle\eta\rangle$, for different rotational velocities, ICS values and overlap ratios located at Z_L= 0.725 ± 0.005.

Rotational speed, rpm	ICS	Overlap window	$\delta/\langle\eta\rangle$	$\epsilon_{t,max}/\epsilon_{innerwall}$
114	64	0	10.4	0.012
	32	0	5.2	0.029
	16	0	2.6	0.1
	16	50	1.3	0.77
90	32	50	2.2	0.15
	16	50	1.1	0.71
70	32	50	1.87	0.25
	16	50	0.94	0.93
50	32	50	1.5	0.38
	16	50	0.75	1.57

$\epsilon_{t,max}/\epsilon_{innerwall}$. $\epsilon_{t,max}$ is used in this study because Delafosse et al. (2011) extracted the mean from the impeller discharge region where the dissipation rate is maximum and far greater the mean dissipation rate values. N^3D^2 represent the maximum value that can be achieved based on the tip of the impeller, and in similar aspect $\epsilon_{innerwall}$ is used which represent the maximum value that can be attained on the inner boundary in the TVB. Additionally, it is important to note that the $\epsilon_{innerwall}$ is a global average, so there will be regions in a Taylor vortex where the local value will be higher than this and other regions

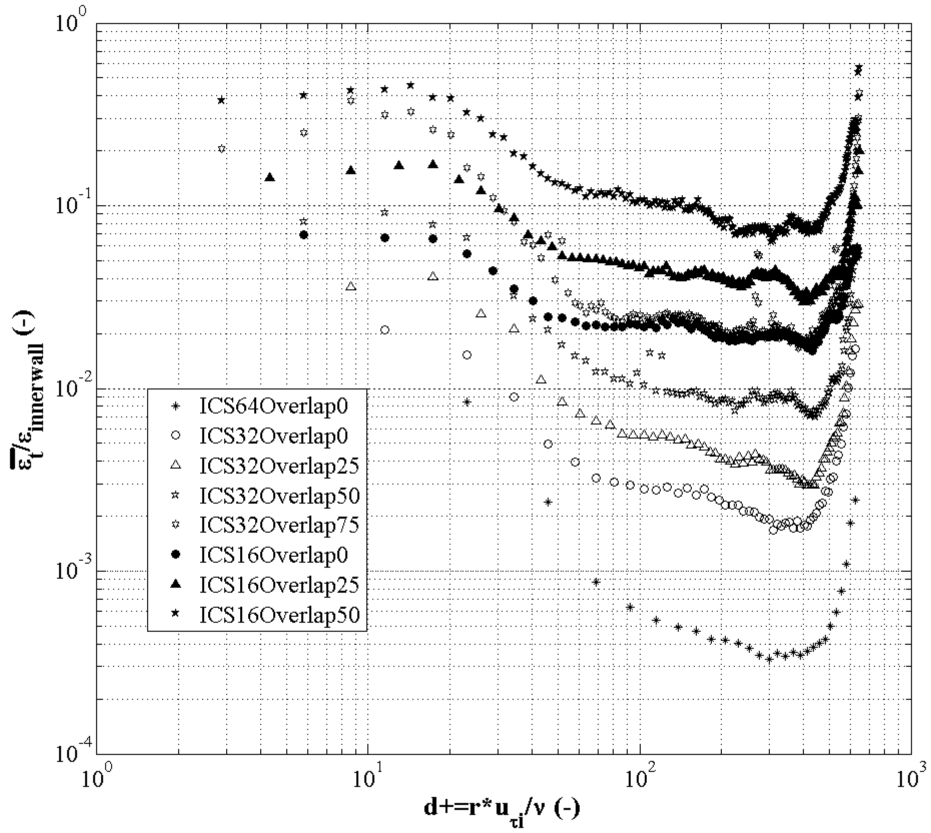

Figura 12 – Radial profile of the viscous dissipation of turbulent kinetic energy at different overlap ratios and ICS values at $Z_L = 0.725 \pm 0.005$.

where it will be lower.

Delafosse et al. (2011) described the evolution of the dissipation rate of the turbulent kinetic energy with respect to the dimensionless spatial resolution as a power law: $\epsilon_{mean}/N^3D^2 = a(\delta/\langle\eta\rangle)^{-b}$, where a = 0.69 and b = 1.15 for the stirred tank reactor. Based on this rudimentary study, a similar power law is obtained for this TVB as shown in Figure 14: $\epsilon_{t,max}/\epsilon_{innerwall} = a(\delta/\langle\eta\rangle)^{-b}$, where a = 0.84 and b = 1.93. In the Table 5, it can be seen that the dimensionless spatial resolution is around 1.3, 1.1, 0.94 and 0.75 for the rotational speeds of 114, 90, 70 and 50 rpm, respectively, but the $\epsilon_{t,max}/\epsilon_{innerwall}$ is more than one only in the case of the rotational speed of 50 rpm. Considering the case that there should be several locations where the local VEDR value will be higher than the global estimate, it can be confirmed that there is still some under-estimation of the viscous dissipation of turbulent kinetic energy at higher rotational speeds, especially the 114 rpm. In terms of the percentage of under-estimation, based on the study of Saarenrinne e Piirto (2000), who stated that the dissipation rate corresponds to 90 % of the exact value if the spatial resolution is around 2η, the present study must be under-estimating by less than 10%, considering the global average value of 52.5 μm for the Kolmogorov scale (Table 3). Further refinement in the size of particles and/or technological enhancements can shed further clarity on this subject.

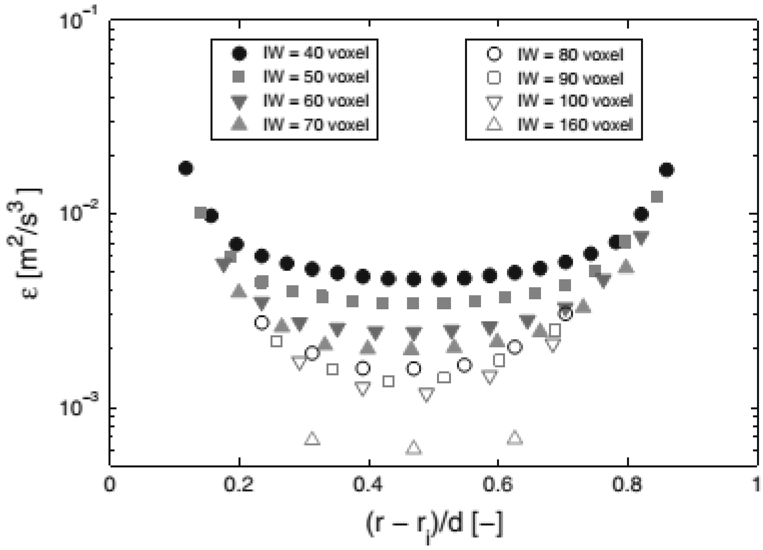

Figura 13 – Figure no 20 of Tokgoz et al. (2012) presenting dissipation rate estimations for changing interrogation window sizes (IW) for Re_s=14,000 with exact counter-rotation of cylinders. 75 % overalap ratio was used for all IWs.

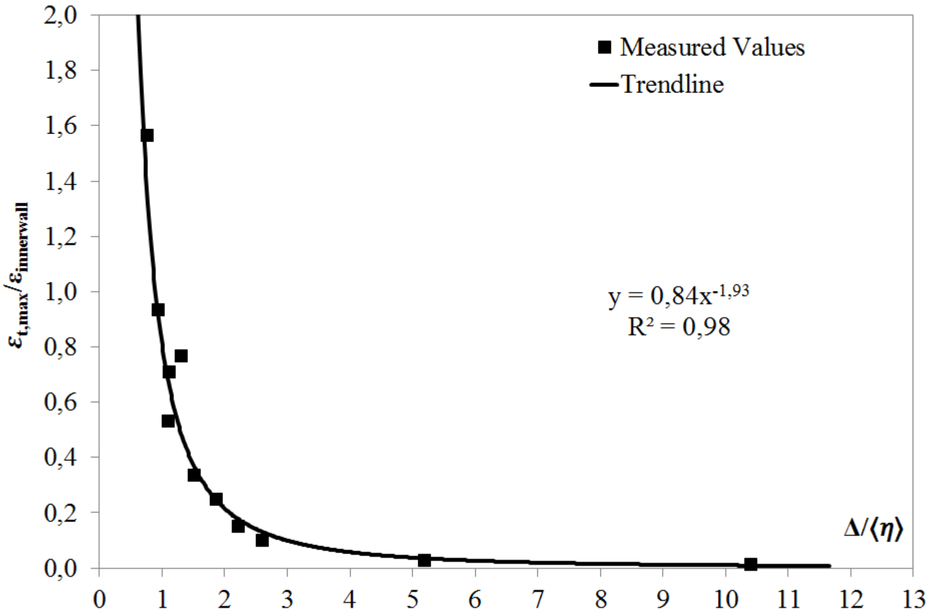

Figura 14 – Influence of the dimensionless spatial resolution of the maximum viscous dissipation of turbulent kinetic energy estimated at $Z_L = 0.725 \pm 0.005$ for different rotational speeds at different ICS and overlap ratios.

Overall, the 16 ICS square grid presented the best acceptable results among the four grids that were tested. For this grid structure, the 75 % overlap was found to present a fair amount of noise in the prediction of much finer quantities, i.e. the fluctuating tangential velocity component and the two components of the VEDR. Therefore, the 50 % overlap ratio was accepted as the chosen overlap ratio for the rest of this study. Similarly, 16 square grid was chosen as the ICS value for the rotational speed of 90, 70 and 50 rpm; whereas, for the rotational speed of 30 rpm the 32 square grid was found to be the optimum value.

2.5 Results and discussion

The results, until unless mentioned otherwise, are presented with the particles of size 10 μm at 16 ICS and 50 % overlap ratio.

2.5.1 Mean velocity flow field

The tangential and radial velocity profiles at five rotational velocities are presented in Figures 15, 16, 17, 18, 19, respectively. First of all, due to a technical problem the motor became unstable at values lower than 40 rpm for the rotational speed of 30 rpm at the horizontal locations of Z_L= 0.575 ± 0.005 and Z_L= 0.525 ± 0.005. Secondly, 114 rpm was the highest limit of the motor which is the one and only reason for choosing this value.

Kobayashi et al. (1990) presented these two components of the velocity in three regions of a Taylor-vortex in their experimental results, and observed similar flow structures. These three regions best describes the structure of a Taylor vortex pair, the extreme ends of the vortex pair, center of each vortex, and the center of the vortex pair. At the center of a vortex pair, termed as outward for describing its profile structure, the flow is moving from the inner rotating cylinder towards the outer stationary cylinder where it divides into two opposite vortexes of same size. When the flow reaches the extreme ends of each vortex pair, the flow starts diverging towards the inner rotating cylinder from the outer cylinder, hence termed as inward. Finally, each vortex of the pair has a center termed as center. The rest of profile structures lie between the outward and inward region but with profile structures similar to that of the center of vortex region, as observed by Kobayashi et al. (1990). It is very important to note that the results presented here may not necessarily show these three exact regions but the closest among the available five horizontal locations for the presented rotational velocities.

In the case of mean tangential velocity, the outward region is marked by the strongest flow profile and the weakest flow profile represents the inward region. The center of vortex region is represented by the flow profile with fairly constant flow in the bulk region, $R_b = 0.1$ to 0.9, with a magnitude of around 50 % of the tip velocity. The strength in the outward region is imparted by the rotating inner cylinder, while the weakness in the inward region is caused by the deceleration of the fluid by the outer wall ((KOBAYASHI et al., 1990)). In the bulk zone of the center of vortex region, the magnitude of the tangential velocity increases slightly but gradually moving from the inner cylinder towards the outer cylinder. Kobayashi et al. (1990) cited that the reason behind this is the phenomenon of uniformity in the circumferential velocity induced by convection of the secondary flow. This phenomenon states that the velocity profiles apart from the ones in the outward and inward region are very similar to the one in the center of vortex region which was also observed by Kobayashi et al. (1990). Overall, in the boundary regions there is sharp

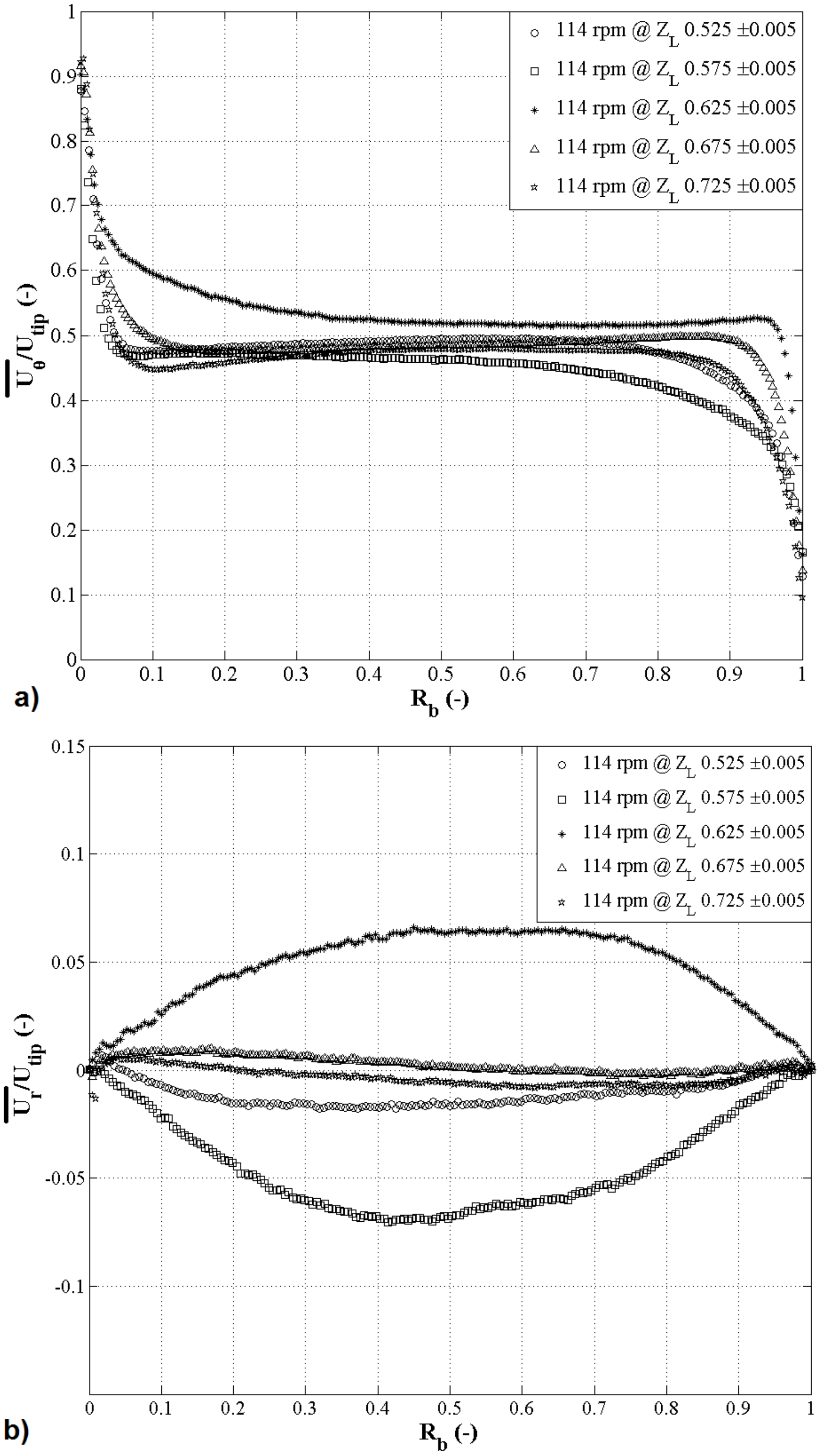

Figura 15 – The tangential (a) and radial (b) velocity flow profiles at 114 rpm.

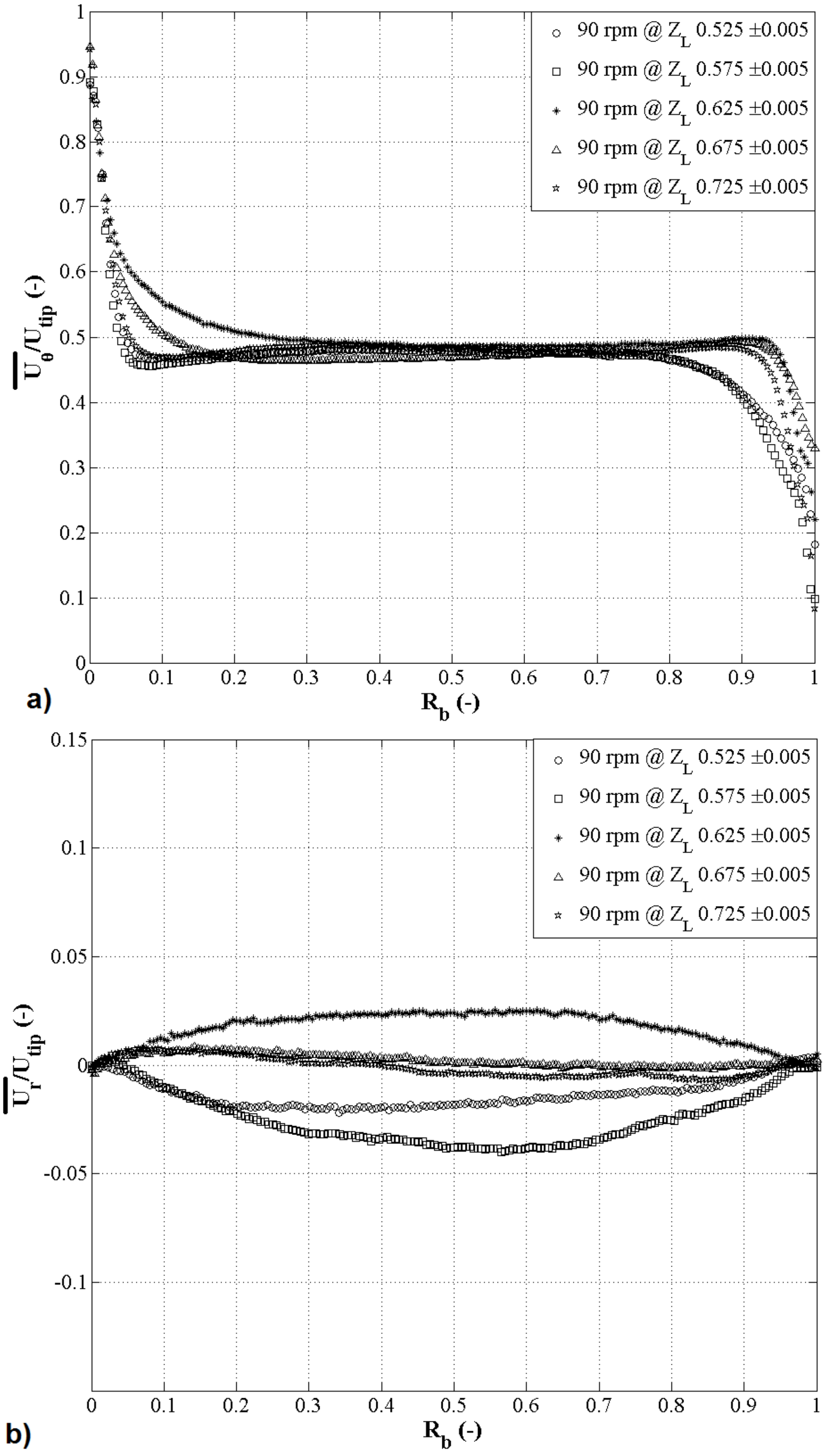

Figura 16 – The tangential (a) and radial (b) velocity flow profiles at 90 rpm.

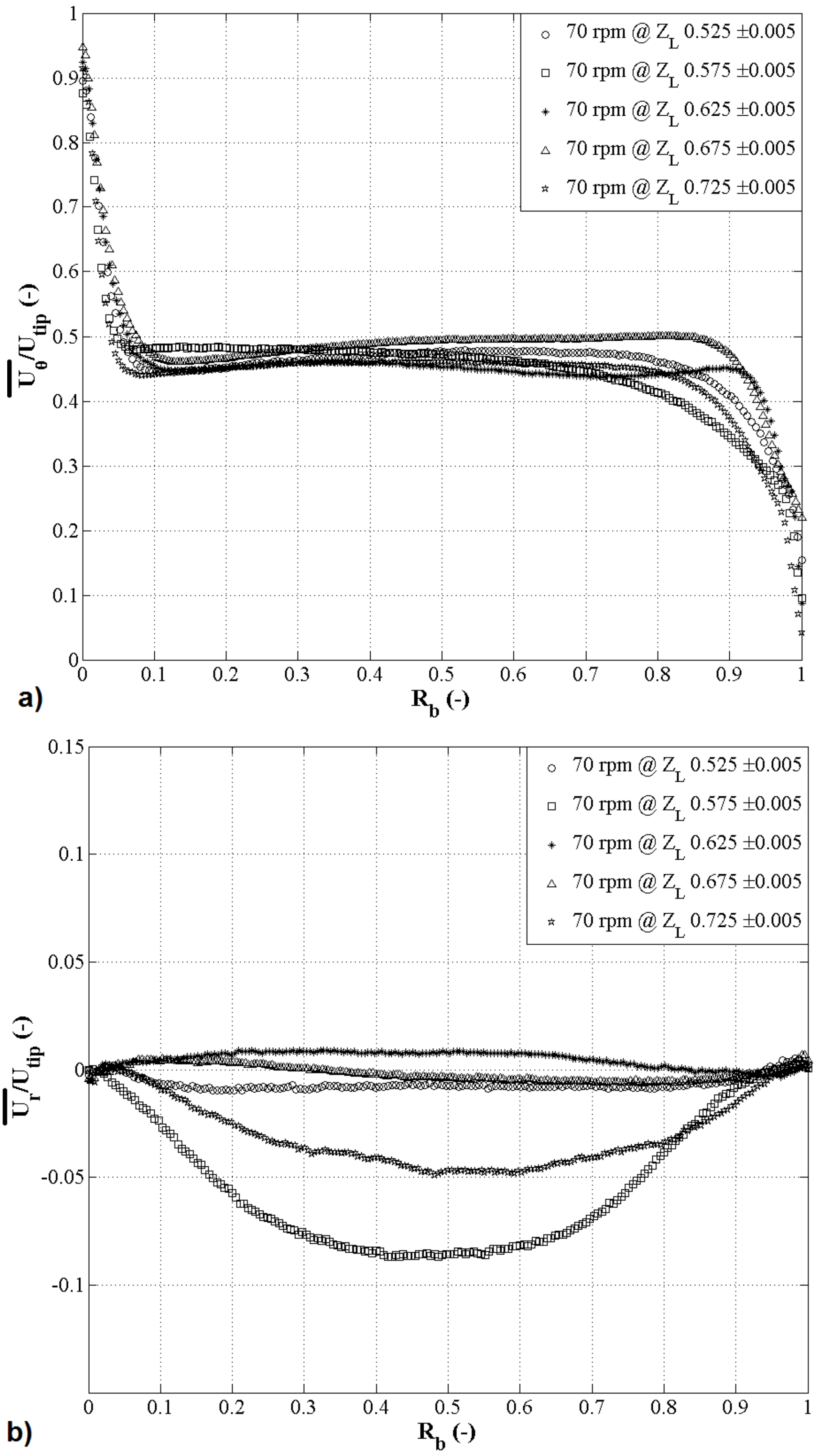

Figura 17 – The tangential (a) and radial (b) velocity flow profiles at 70 rpm.

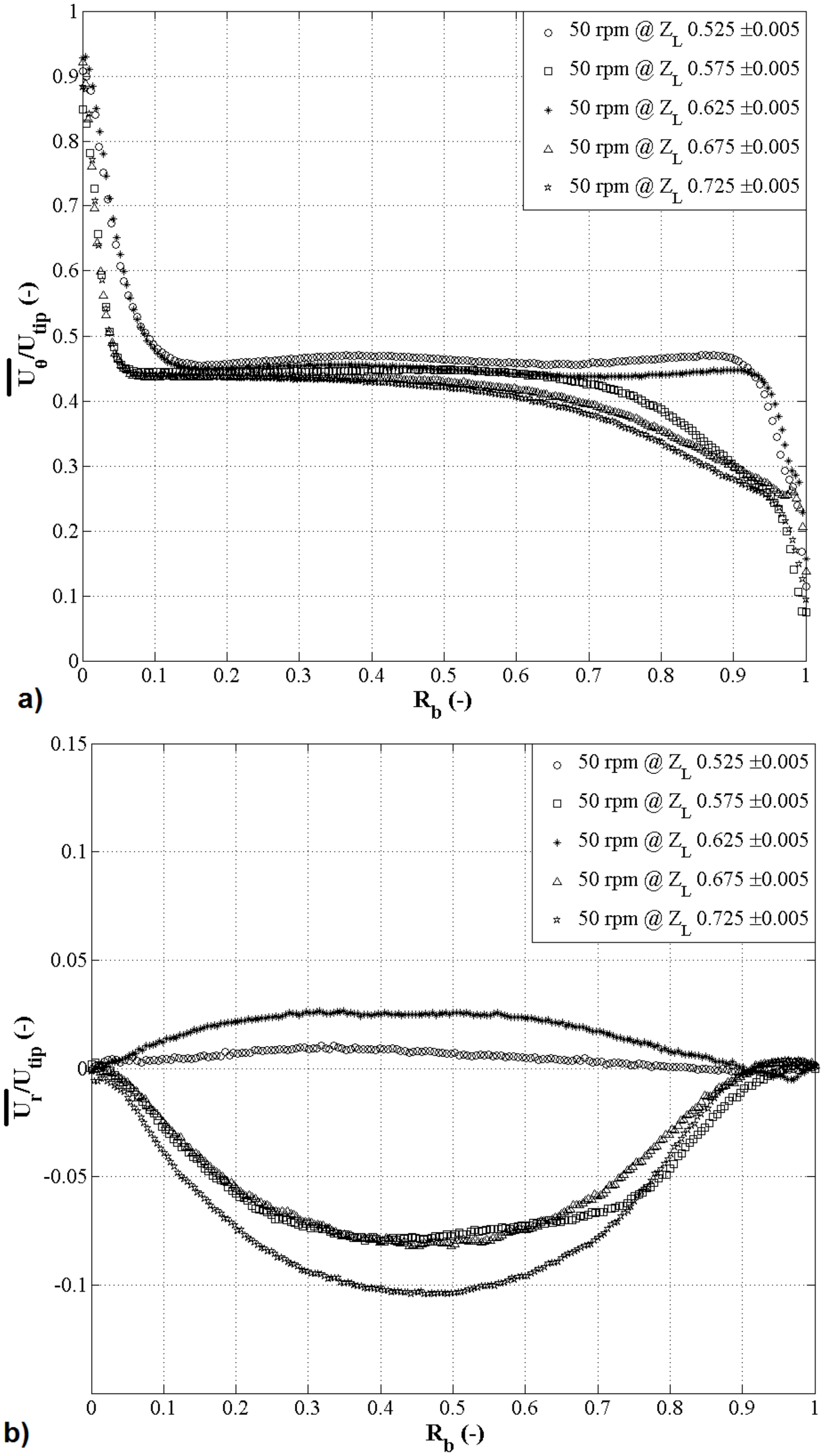

Figura 18 – The tangential (a) and radial (b) velocity flow profiles at 50 rpm.

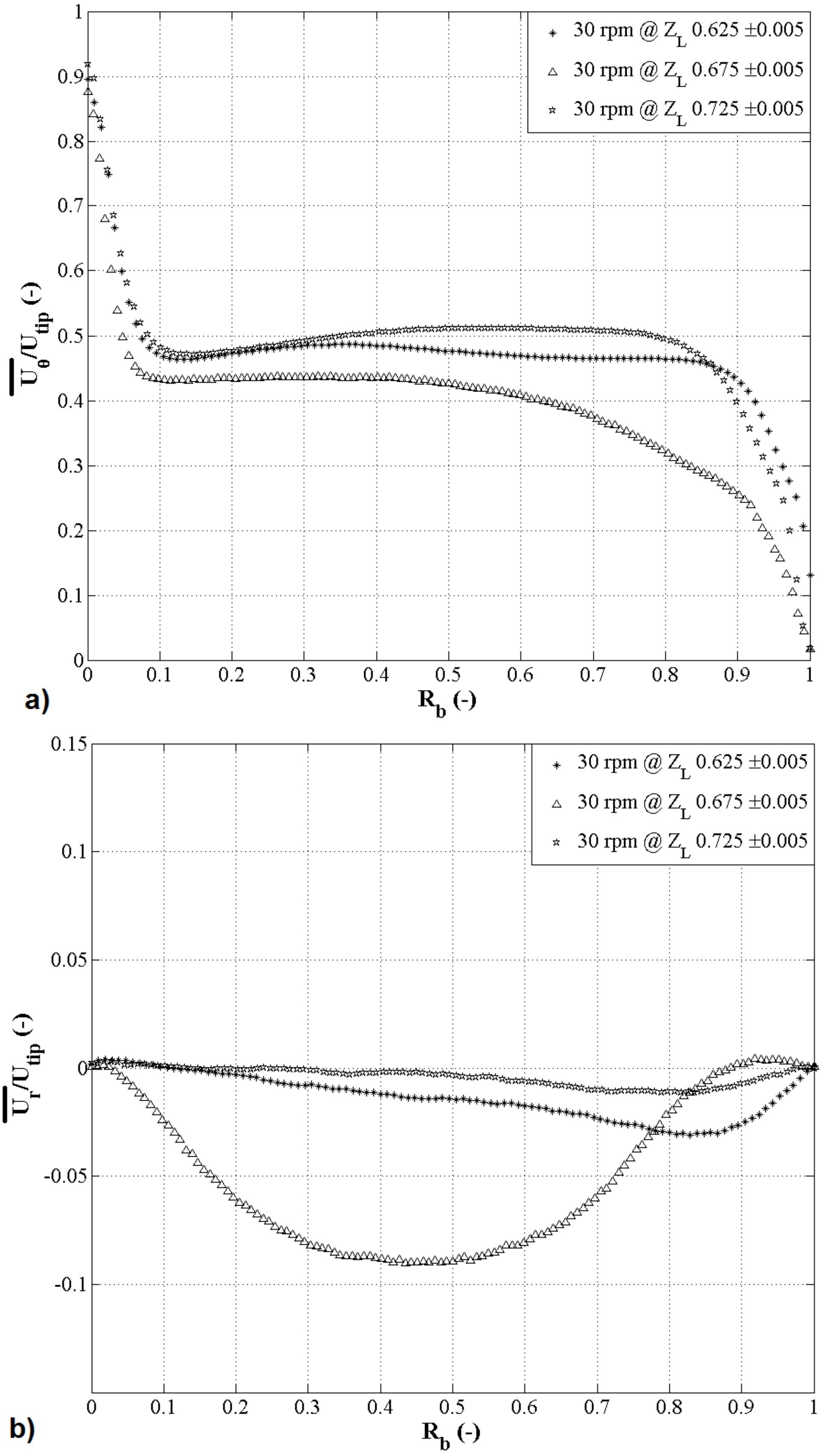

Figura 19 – The tangential (a) and radial b) velocity flow profiles at 30rpm.

decrease in the velocity, and in the bulk zone the flow remains in the vicinity of 0.5 magnitudes, i.e. 50 % of the tip velocity.

For the mean radial velocity, the outward and inward flow structures are opposite of each other represented by the upward and downward parabolic curves, respectively. While, in the center of the vortex region both of these profiles should cancel each other out and attain a zero magnitude. The center of the vortex region has been captured mostly well by all of the representing rotational velocities for both radial and tangential components of the velocity at the axial locations of $Z_L = 0.675$, 0.675, 0.675, 0.525 and 0.725 ± 0.005 for the rotational speeds of 114, 90, 70, 50 and 30 rpm, respectively. The best inward region profiles for these two components were obtained at the 30, 50 and 70 rpm, as shown in Figures 19b, 18b and 17b at axial locations of $Z_L = 0.675$, 0.725 and 0.625 ± 0.005, respectively; though, each at different horizontal locations, which clearly indicates variations in the height and location of the Taylor's vortexes with the variation in the rotational speed. On the other hand, the closest profile for the outward region was captured only at the rotational speed of 114 rpm (Figure 15a) at the axial height of $Z_L = 0.625 \pm 0.005$ with a distinct second at 90 rpm (Figure 16a) also for the axial location of $Z_L = 0.625 \pm 0.005$. This poor prediction of the outward region in comparison to the inward and center of vortex region lies in the fact that there are two inward and center of vortex regions for only one outward region for each Taylor-vortex pair. This lower probability for the outward region is considered the main reason behind the absence of this region for the rotational speeds of 30, 50 and 70 rpm (Figures 19a, 18a and 17a).

It is of great interest to note that the magnitude of the radial component of the velocity is only around 10 % of the tangential component (Figures 19b, 18b and 17b), in agreement with Kobayashi et al. (1990). Secondly, the steepest gradient of the tangential component velocity lie in the boundary layer area. This could imply that more than 80 % of the kinetic energy and its dissipation are represented only by the tangential component of the velocity in the boundary layer area. This aspect will be studied later on to understand the percentage impact of each of the five gradients on the VEDR. Another interesting observation is that the 80% of the cylinder width, the bulk zone, is represented by only 50 % of the magnitude of the flow with very little variation as far as the tangential component is concerned. This could turn out to be a significantly influential in terms of culturing animal cells because of similar flow conditions with very little gradients in the major part of the TVB.

2.5.2 Logarithmic velocity profiles

In a Taylor-Vortex reactor, the RANS equation in cylindrical coordinates can be written as in Equation 2.7. For a steady state and assuming that the axial velocity component is negligible and the tangential velocity component depends only on the radial position, the present case can be simplified to the Equation 2.8. In the center of vortex region, the radial velocity component, $\overline{U_r}$, is negligible, which further simplifies to the Equation 2.9, and which on expansion gives Equation 2.10. From the Equation 2.10, the total viscosity, i.e. the sum of molecular and turbulent, can be extracted as shown in Equation 2.11.

$$
\begin{aligned}
&\rho\left(\frac{\partial\overline{U_\theta}}{\partial t}+\frac{\partial\overline{U_rU_\theta}}{\partial r}+\frac{1}{r}\frac{\partial\overline{U_\theta}^2}{\partial\theta}+\frac{2\overline{U_rU_\theta}}{r}+\frac{\partial\overline{U_zU_\theta}}{\partial r}\right)\\
&=-\frac{1}{r}\frac{\partial\overline{P}}{\partial\theta}+\frac{1}{r^2}\frac{\partial r^2\overline{\tau_{\theta r}}}{\partial r}-\frac{1}{r}\frac{\partial\rho\overline{u_r'u_\theta'}}{\partial r}-\frac{2\rho\overline{u_r'u_\theta'}}{r}+\frac{1}{r}\frac{\partial(\overline{\tau_{\theta\theta}}-\rho\overline{u_\theta'^2})}{\partial\theta}+\frac{1}{r}\frac{\partial(\overline{\tau_{\theta z}}-\rho\overline{u_z'u_\theta'})}{\partial z}+\rho g_\theta\\
&=-\frac{1}{r}\frac{\partial\overline{P}}{\partial\theta}+\frac{1}{r^2}\frac{\partial r^2(\overline{\tau_{\theta r}}-\rho\overline{u_r'u_\theta'})}{\partial r}+\frac{1}{r}\frac{\partial(\overline{\tau_{\theta\theta}}-\rho\overline{u_\theta'^2})}{\partial\theta}+\frac{1}{r}\frac{\partial(\overline{\tau_{\theta z}}-\rho\overline{u_z'u_\theta'})}{\partial z}+\rho g_\theta
\end{aligned}
\tag{2.7}
$$

$$
\rho\frac{2\overline{U_rU_\theta}}{r}=\frac{1}{r^2}\frac{\partial r^2(\overline{\tau_{\theta r}}-\rho\overline{u_r'u_\theta'})}{\partial r}
\tag{2.8}
$$

$$
\begin{gathered}
\frac{\partial r^2(\overline{\tau_{\theta r}}-\rho\overline{u_r'u_\theta'})}{\partial r}=0, or\\
r^2(\overline{\tau_{\theta r}}-\rho\overline{u_r'u_\theta'})=r^2\tau_{r\theta}^{tot}=r_i^2\tau_{r_i\theta}^{tot}
\end{gathered}
\tag{2.9}
$$

$$
r^2(\nu+\nu^t)r\frac{\partial(\overline{U_\theta}/r)}{\partial r}=r_i^2u_{\tau i}^2
\tag{2.10}
$$

$$
1+\frac{\nu^t}{\nu}=\frac{r_i^2u_{\tau i}^2}{r^3\nu\frac{\partial\overline{U_\theta}/r}{\partial r}}
\tag{2.11}
$$

The profiles of this total viscosity at different rotational speeds is presented in Figure 20 in the center of vortex region. The limit of this simplified approach can be observed at the rotational speed of 30 rpm. It can be clearly seen that the data exhibit a similar trend which can be modeled by the Equation 2.12.

$$
1+\frac{\nu^t}{\nu}=\frac{((r^+-r_i^+)u_{\tau i}/\nu)^2}{10^2}
\tag{2.12}
$$

From the Equation 2.12, an analytical expression of the velocity can be derived by injecting the non-dimensional variable, $r^+=ru_{\tau i}/\nu$, $r_i^+=r_iu_{\tau i}/\nu$ and $U_\theta^+=\overline{U_\theta}/u_{\tau i}$ to obtain Equation 2.13. On integrating the Equation 2.13, a new equation for the mean velocity profile, Equation 2.14, is obtained with a constant C, where this constant C is found to be inversely proportional to r_i^+, as shown in Figure 21. In the Figure 21, it can be

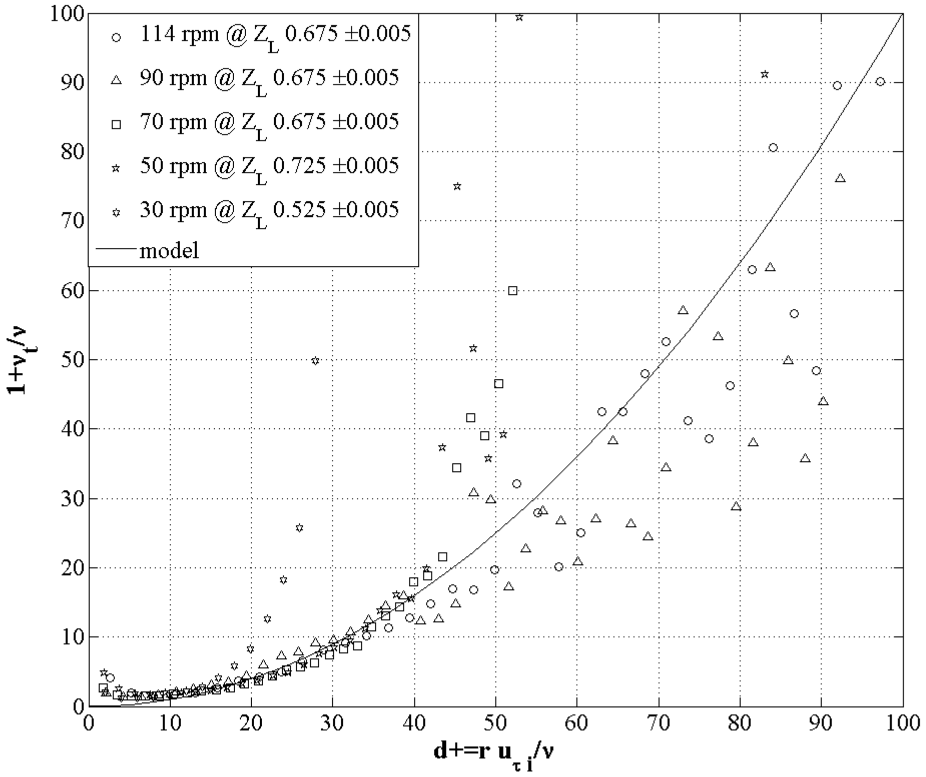

Figura 20 – The total viscosity at different rotational speeds in the center of vortex region.

seen that the constant C= $15/r_i^+$, which gives us the expression of velocity in the Equation 2.15.

$$\frac{\partial(\overline{U_\theta^+}/r^+)}{\partial r^+} = \frac{10^2 r_i^{+2}}{(r^+ - r_i^+)r^{+3}} \tag{2.13}$$

$$U_\theta^+ = \frac{50r^+}{r_i^{+2}}\left[\frac{r_i^+(-6r^{+2} + 3r_i^+ r^+ + r_i^{+2})}{(r^+ - r_i^+)r^{+2}} + 6log\frac{(}{r^+}r^+ - r_i^+)\right] + Cr^+ \tag{2.14}$$

$$U_\theta^+ = \frac{50r^+}{r_i^{+2}}\left[\frac{r_i^+(-6r^{+2} + 3r_i^+ r^+ + r_i^{+2})}{(r^+ - r_i^+)r^{+2}} + 6log\frac{(}{r^+}r^+ - r_i^+)\right] + \frac{15r^+}{r_i^+} \tag{2.15}$$

Based on the expression presented in Equation 2.15, the logarithmic profile of the velocity is presented in Figure 22 in the center of vortex region for the four rotational speeds. The rotational speed of 30 rpm is not presented because of its poor representation of the total viscosity in the Figure 20. Clearly it can be seen that in this case, the velocity structure clearly follows the new expression of log law after the viscous sub-layer. Most of the studies (BILSON; BREMHORST, 2007; HUISMAN et al., 2013; PONCET; VIAZZO; OGUIC, 2014) regarding the logarithmic law of the wall have used the classical expression

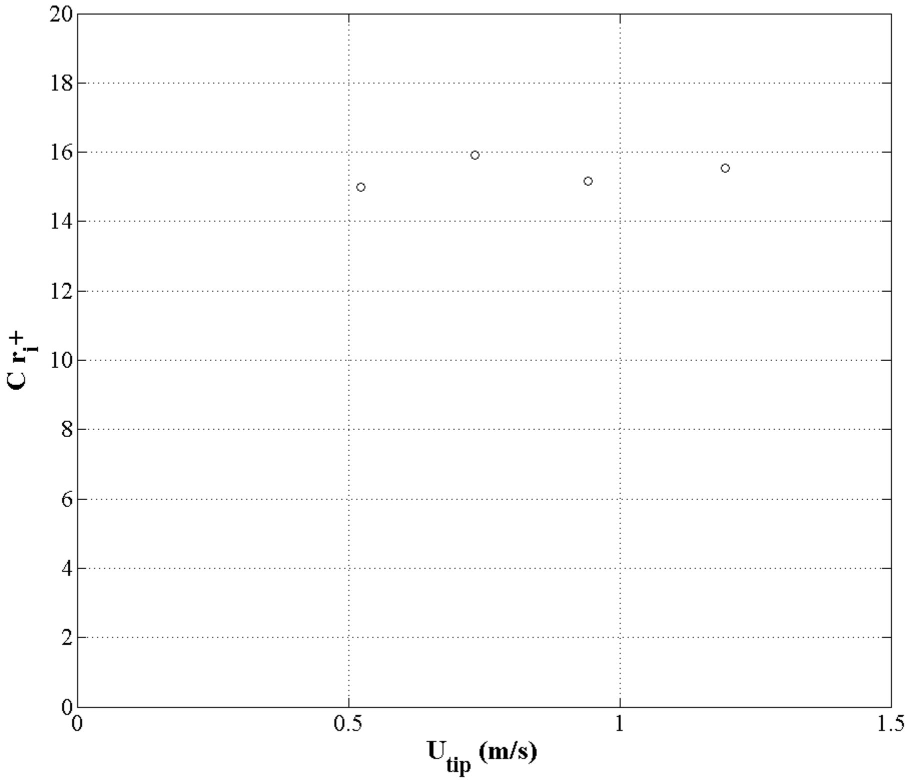

Figura 21 – The evaluation of the constant C presented in the Equation 2.14.

of the type $u^+ = 1/\kappa ln(d+) + B$. Near the walls in the viscous sub-layer till d+ =10, the velocity follows a profile of $u^+ = d+$, then there was huge buffer region till d+ =100, as mentioned by Poncet, Viazzo e Oguic (2014) and which can be observed in the study of Huisman et al. (2013). The classical expression of log-law was obeyed only after d+=100, which becomes negligible for the lower range of turbulent Reynolds no.

In the present case, the log-law is obeyed as soon as the viscous sub layer is finished at d+=10. With each increase in the Reynolds number, the new log-law is obeyed better. The application of this new law at even higher Reynolds numbers, the range used in the study of Huisman et al. (2013), can prove the worth of this law.

2.5.3 Reynolds stresses

2.5.3.1 Normal stress

In Figures 23, 24, 25, 26 and 27, the second order mean fluctuating components of the velocity also known as Reynolds normal stresses, namely $\overline{u_r'^2}$ and $\overline{u_\theta'^2}$ are presented for the five rotational velocities at five horizontal locations apart from the rotational speed of 30 rpm, for which only three horizontal locations were available. The profile structures of the Reynolds normal stresses, $\overline{u_\theta'^2}$ and , $\overline{u_r'^2}$, presented here qualitatively coincide well with those of the Kobayashi et al. (1990). However, the magnitudes of these stresses, $\overline{u_r'^2}$ and

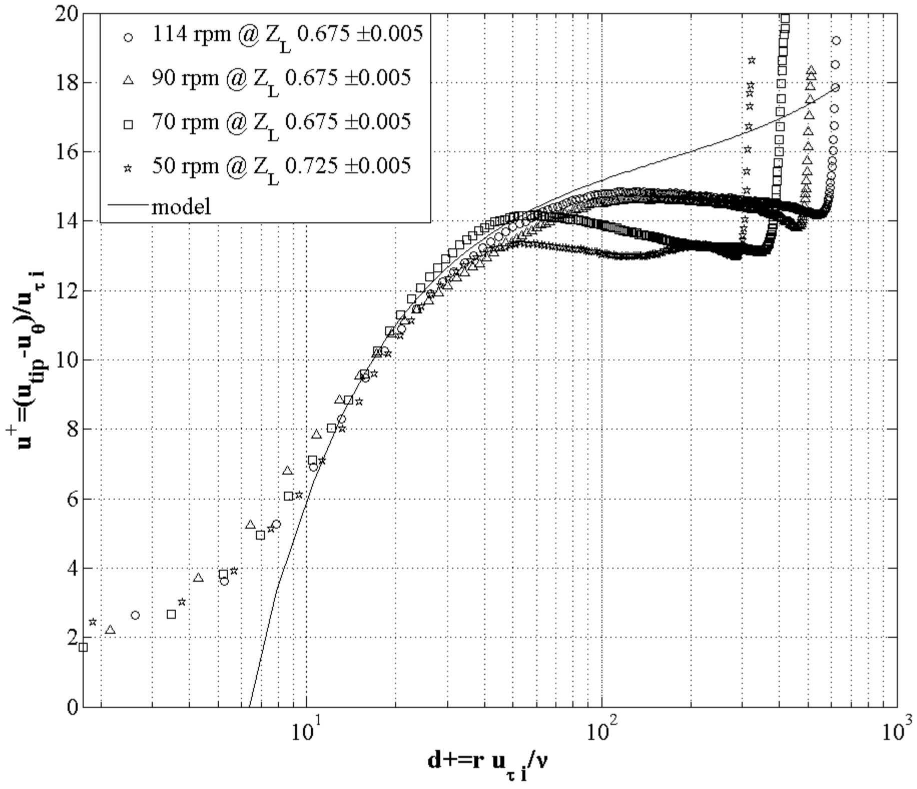

Figura 22 – The log-law profile of the velocity in the center of vortex region of the inner cylinder boundary layer.

$\overline{u_\theta'^2}$, in comparison with the results of Kobayashi et al. (1990) are significantly higher in the boundary layer and at-least double in the bulk zone.

The closest profile structures for the three regions, outward, inward and center of vortex region, can be observed only for 114 rpm rotational speed,as mentioned earlier. The basic difference between the profile structures for these three regions lie in the bulk zone for the normal tangential stress. In qualitative agreement with Kobayashi et al. (1990), the flow structure in the outward region is slanted decreasing gradually from the inner cylinder towards the outer cylinder and contrary in the inward region, i.e. gradually decreasing from the outer cylinder towards the inner cylinder. In the center of vortex region, the magnitude remains practically constant through-out the bulk zone. The profile structures of the center of vortex and inward regions can be seen in all of the rotational speeds (Figures 23a, 24a, 25a, 26a and 27a). The inner boundary layer of the normal tangential stress is marked by steep peaks near the wall; whereas, in the outer boundary layer the peaks are much smaller in comparison. This is the result of the fact that the maximum for the mean tangential velocity always lies on the inner cylinder with steep decreases in both boundary layers but with little variations in the bulk zone (Figure 15). Therefore, boundary layers are marked by steep gradients compared to the ones in the bulk zone.

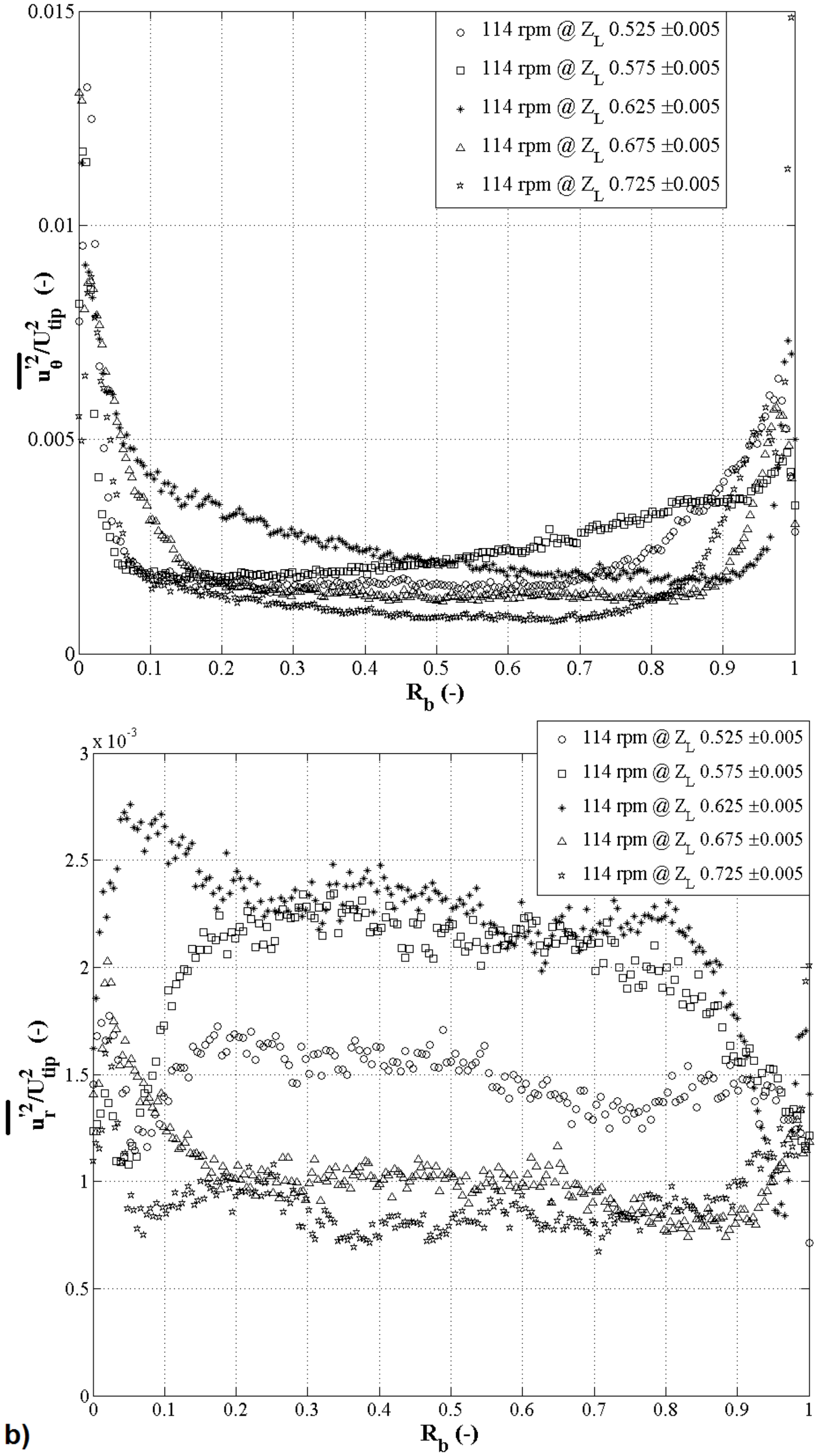

Figura 23 – The tangential (a) and radial (b) normal stress profiles at 114 rpm.

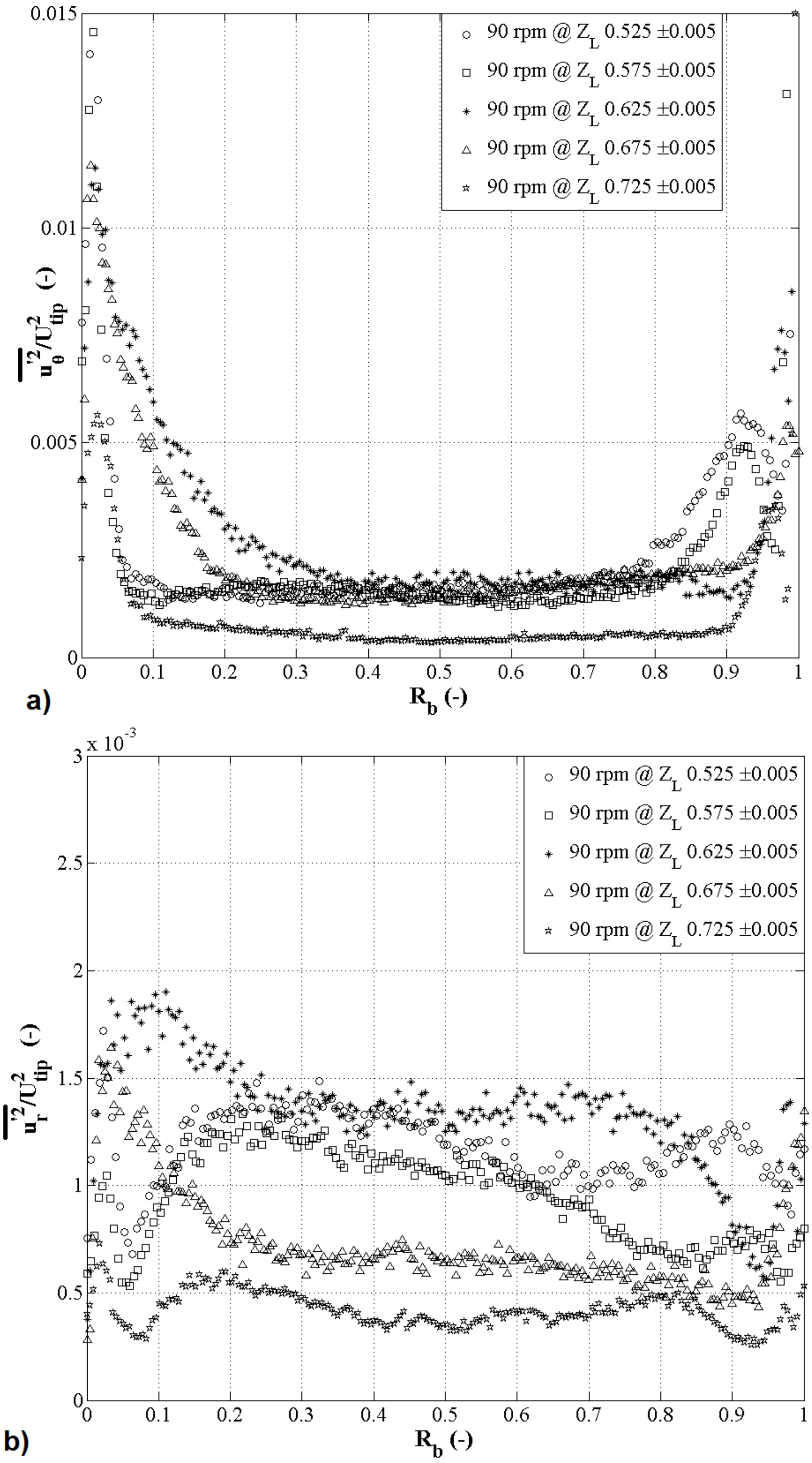

Figura 24 – The tangential (a) and radial (b) normal stress profiles at 90 rpm.

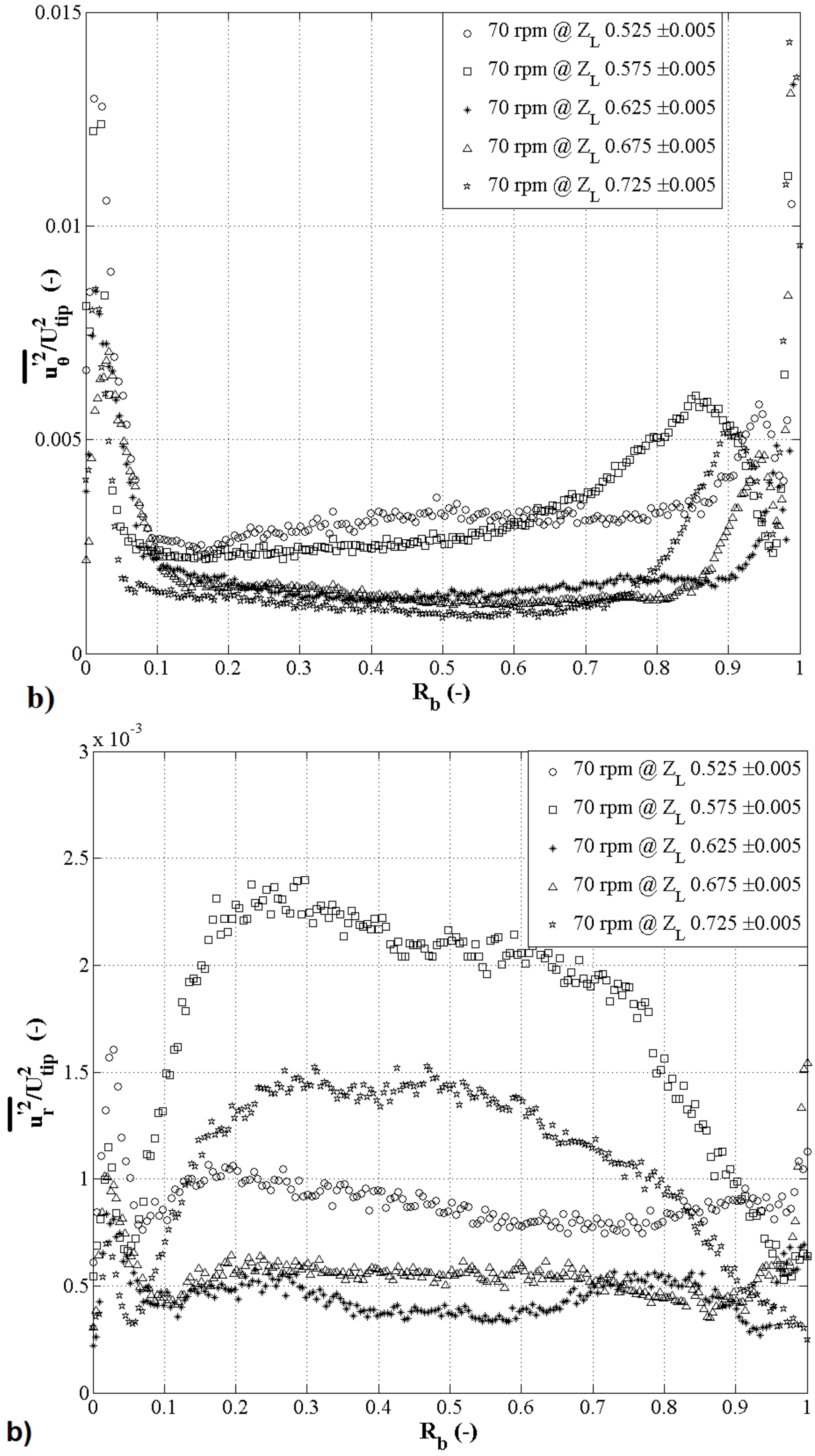

Figura 25 – The tangential (a) and radial (b) normal stress profiles at 70 rpm.

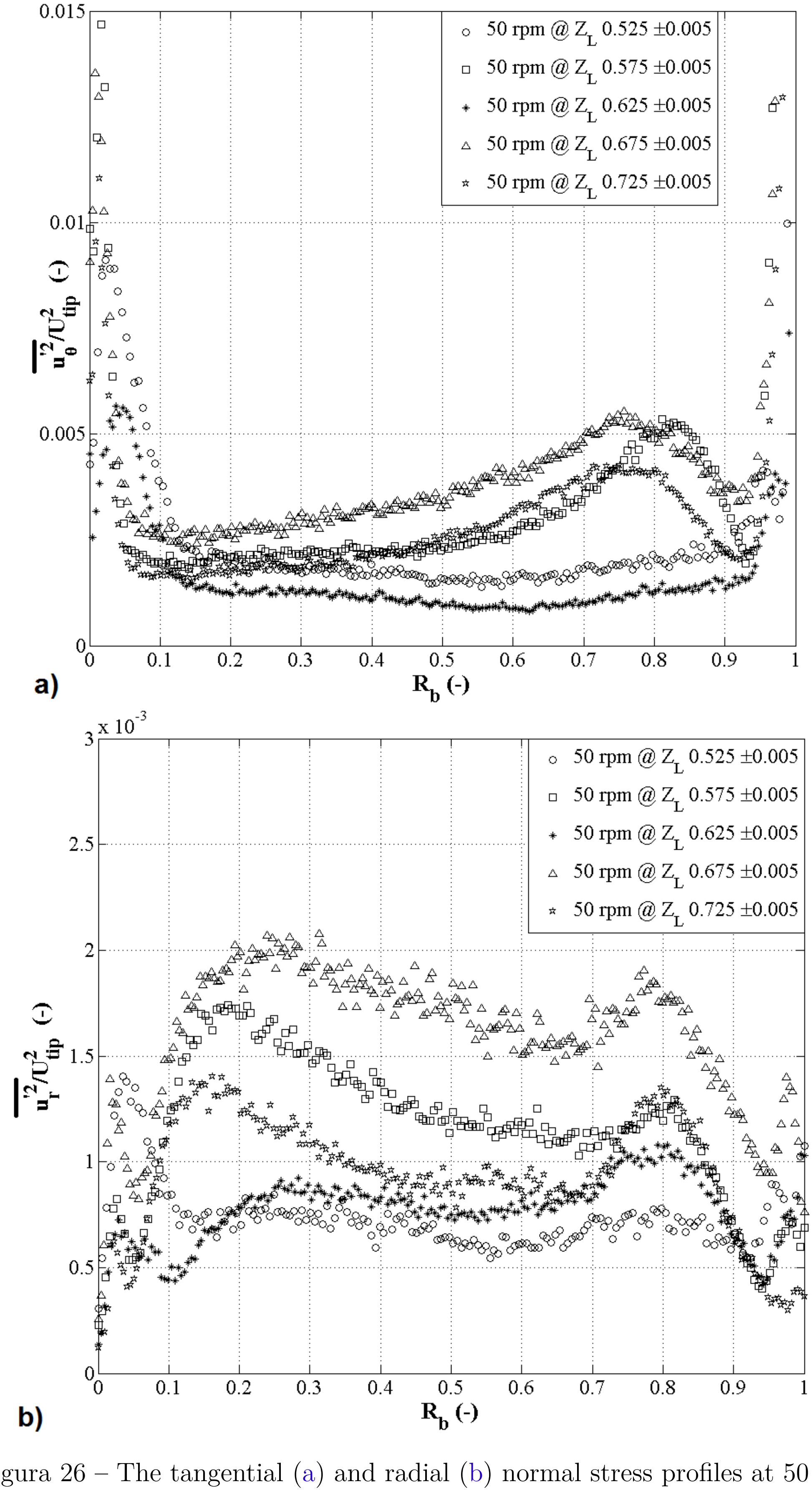

Figura 26 – The tangential (a) and radial (b) normal stress profiles at 50 rpm.

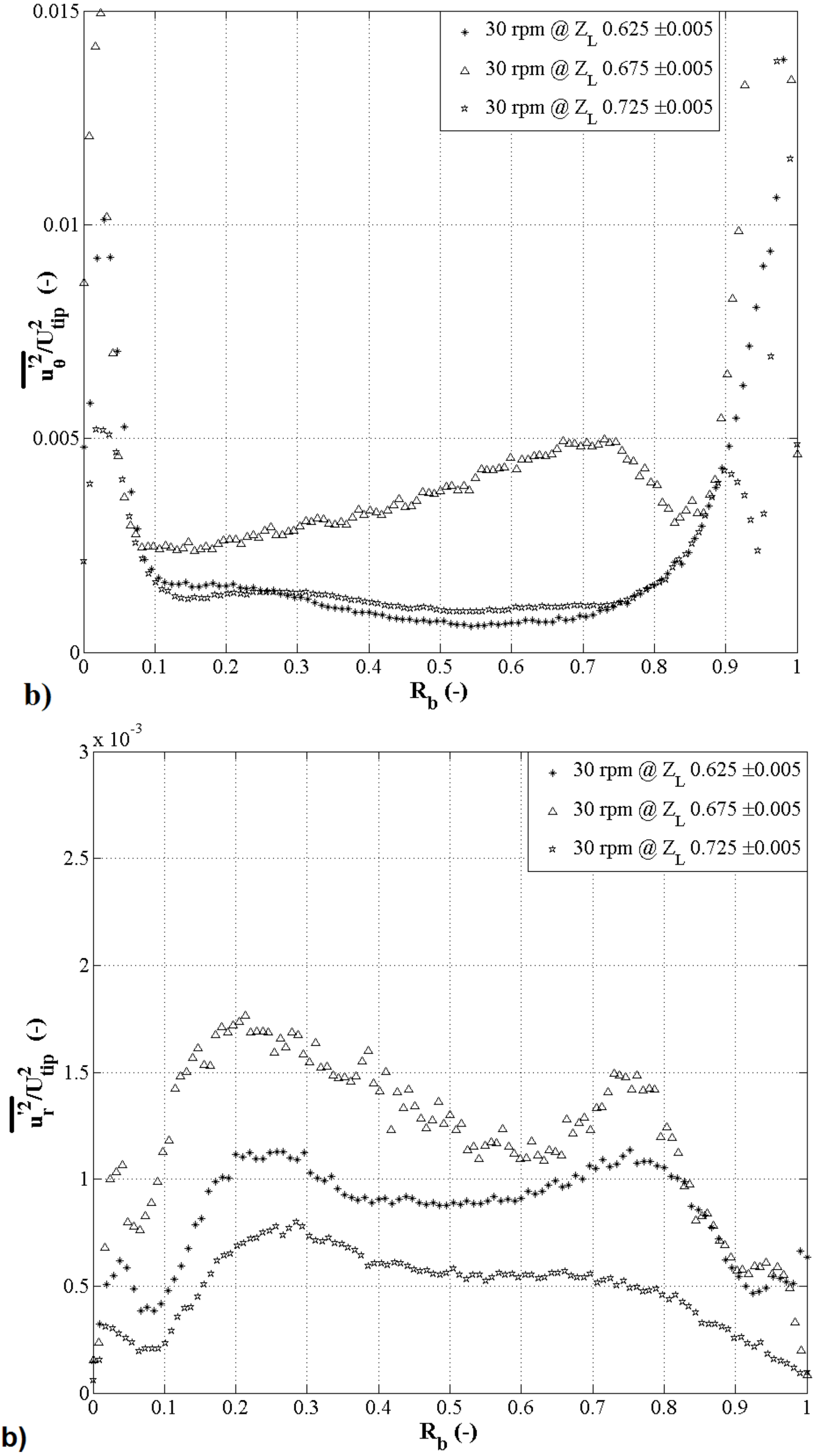

Figura 27 – The tangential (a) and radial b) normal stress profiles at 30rpm.

The magnitude of normal radial stress, equivalent of the minimum of the normal tangential stress, is very similar in the bulk zone and the boundary layer area in the three regions, the difference is minimal. The magnitude difference among the three regions is also small but highest for the outward and inward regions and near the lowest in the center of vortex region, in qualitative agreement with Kobayashi et al. (1990). The disparity with the results of the Kobayashi et al. (1990) lies in the magnitude values for these two squared fluctuating components. Kobayashi et al. (1990) observed that the maximum of the normal radial stress is around 60 % of the normal tangential stress with the maximum value for the normalized normal tangentital stress being 0.002, normalized with U_{tip}^2. While, in present study the maximum normalized normal tangential stress value is more than five times higher, also normalized with U_{tip}^2, and the maximum of normal radial stress is less than 20 % of the normal tangential stress.

Hout e Katz (2011) also presented these normal stress terms but for counter-rotating Taylor-Couette flow. It should be noted that they normalized the rms values of radial and tangential fluctuating velocities with the friction velocity instead of the tip velocity as in this case. Moreover, there range did not cover the boundary layer on the outer cylinder, and the location within the vortex at which these profiles are presented is not specified. For the normal tangential stress, they observed a similar structure as in the outward region, a peak near the inner boundary layer then gradual decrease towards outer cylinder in the bulk zone.

2.5.3.2 Shear Stress

Figures 28, 29a, 29b, 30a and 30b present the Reynolds shear stress, namely $\overline{u_r' u_\theta'}$, for the five rotational velocities at five horizontal locations apart from the rotational speed of 30 rpm, for which only three horizontal locations were available. Both the magnitude and the structure of the shear stress, $\overline{u_r' u_\theta'}$, is similar to the estimations of the Kobayashi et al. (1990), but of opposite sign. The opposite sign just implies that the location of extraction of data is different. The higher magnitude of the tangential component has a significant impact on the structure of the tangential-radial shear stress term. There is a peak near the inner wall and then a gradual decay towards the outer cylinder, similarly observed in Kobayashi et al. (1990) in the outward region. In the inward region, the peak is towards the outer cylinder with a gradual decay towards the inner cylinder, and in the center of vortex region this shear stress term is of near zero magnitude through-out the bulk zone.

This shear stress term was also presented by Hout e Katz (2011), and they normalized by using both the tip velocity and friction velocity at the inner cylinder. Looking at there Figure 13(a) for the shear stress term $\overline{u_r' u_\theta'}$ normalized by tip velocity, a similarity can be seen in the outward flow profile of the same term at 114 rpm (Figure 28). Among

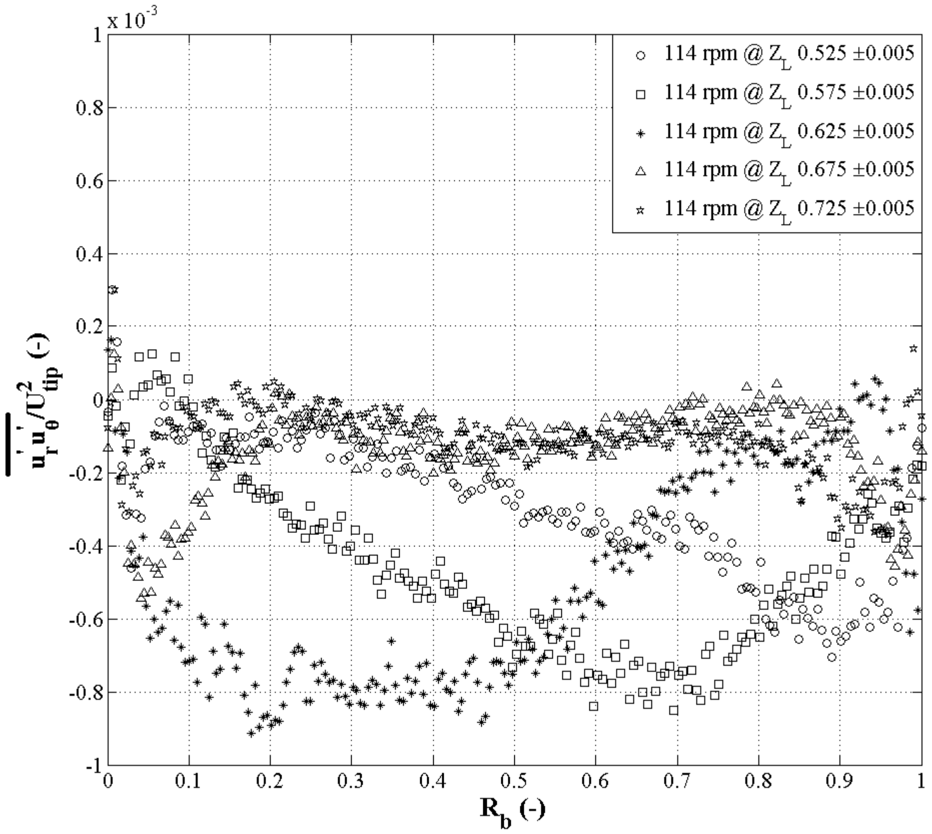

Figura 28 – The Reynolds shear stress, $\overline{u'_r u'_\theta}$, profiles at 114rpm.

the profiles for different rotational speeds, after 114 rpm only 90 rpm has these three regions distinguished. At all other rotational speeds, only center of vortex and inward region can be seen among the five horizontal locations. This is clearly a disadvantage of the experimental method with data available at very few locations in addition to the uncertainty of exact location of extraction of data.

2.5.4 Viscous energy dissipation rate

2.5.4.1 Composition of the VEDR

In the Figures 31 and 32, the five gradients of the VEDR estimation of the mean flow and turbulent kinetic energy, respectively, are presented for the horizontal location of Z_L= 0.725 ± 0.005. It can be clearly seen that the viscous dissipation of mean flow kinetic energy is mainly composed of only the $(\frac{\partial(\overline{U_\theta}/r)}{\partial r})^2$ gradient, while in the case of viscous dissipation of turbulent kinetic energy the gradient, $\overline{(\frac{\partial(u_\theta'/r)}{\partial r})^2}$, is the major contributor especially in the boundary layer area, and in the bulk zone its contribution is similar to the other gradient of the radial direction. Although, there are only five gradients instead of 12 for the complete estimation of VEDR, it is known that the axial velocity is also not very strong in the Taylor- Couette flow. The impact of axial flow on the VEDR could be considered to be similar to that of the radial flow, i.e. in the bulk zone and very little

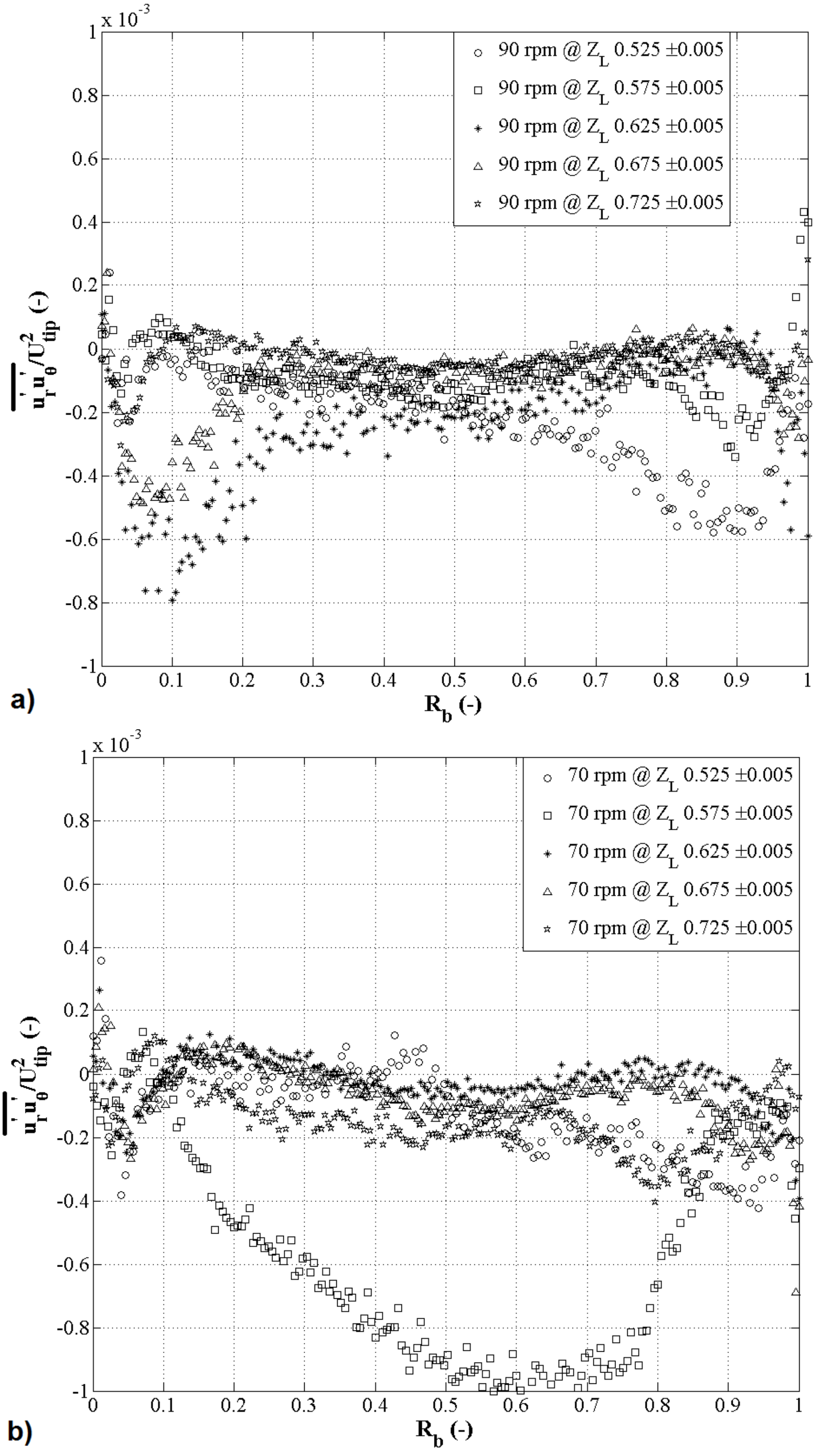

Figura 29 – The Reynolds shear stress, $\overline{u'_r u'_\theta}$, profiles at 90 (a) and 70 (b) rpm.

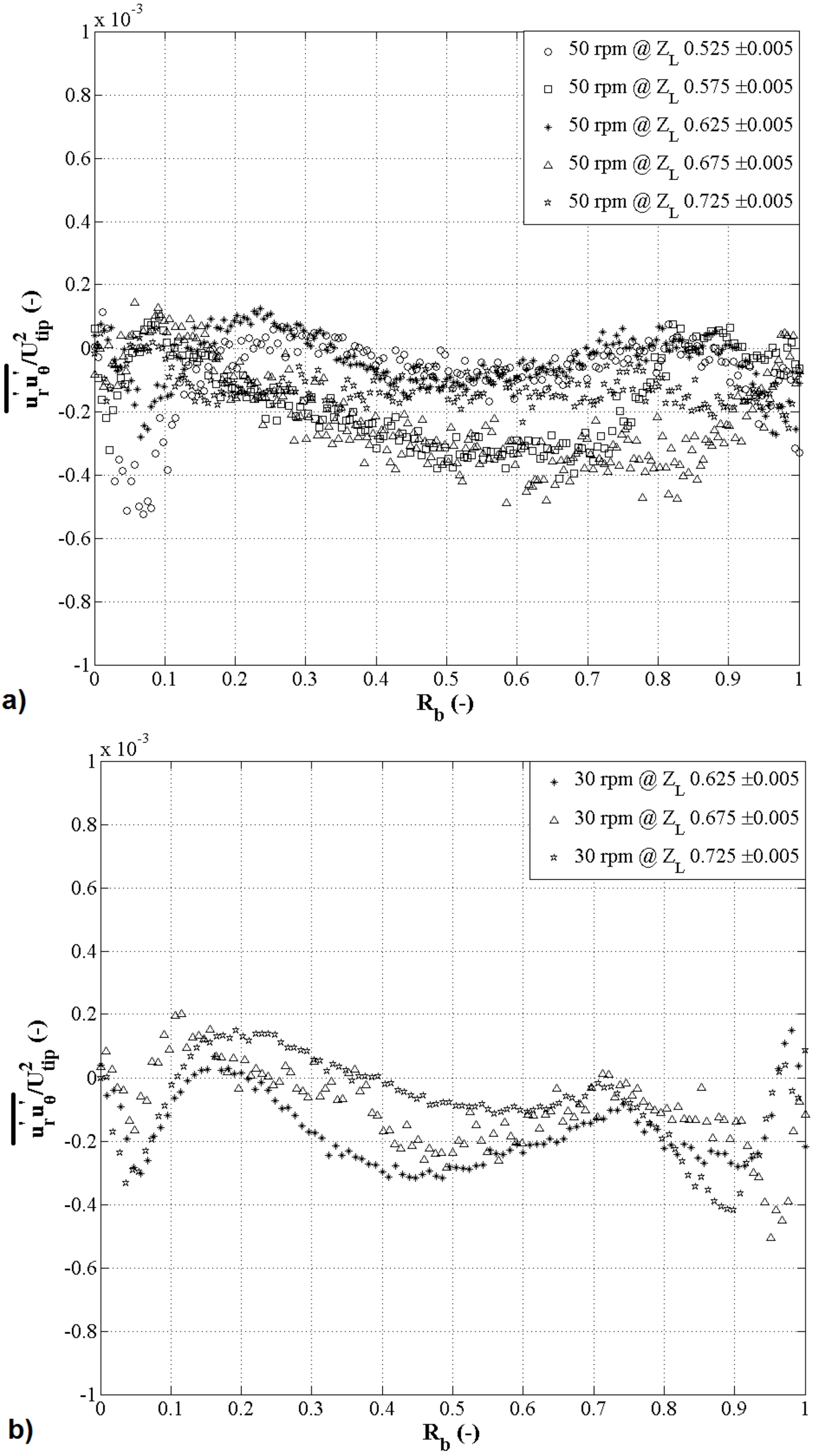

Figura 30 – The Reynolds shear stress, $\overline{u'_r u'_\theta}$, profiles at 50 (a) and 30 (b) rpm.

in the boundary layer. Thereby further enhancing the importance of the gradient of the tangential (both mean and fluctuating) velocity component in the radial direction in the estimation of the VEDR. In other words, capturing the propagation of the velocity in the radial direction is of utmost importance in order to estimate well the mean and turbulence components of the VEDR, especially in the boundary layer.

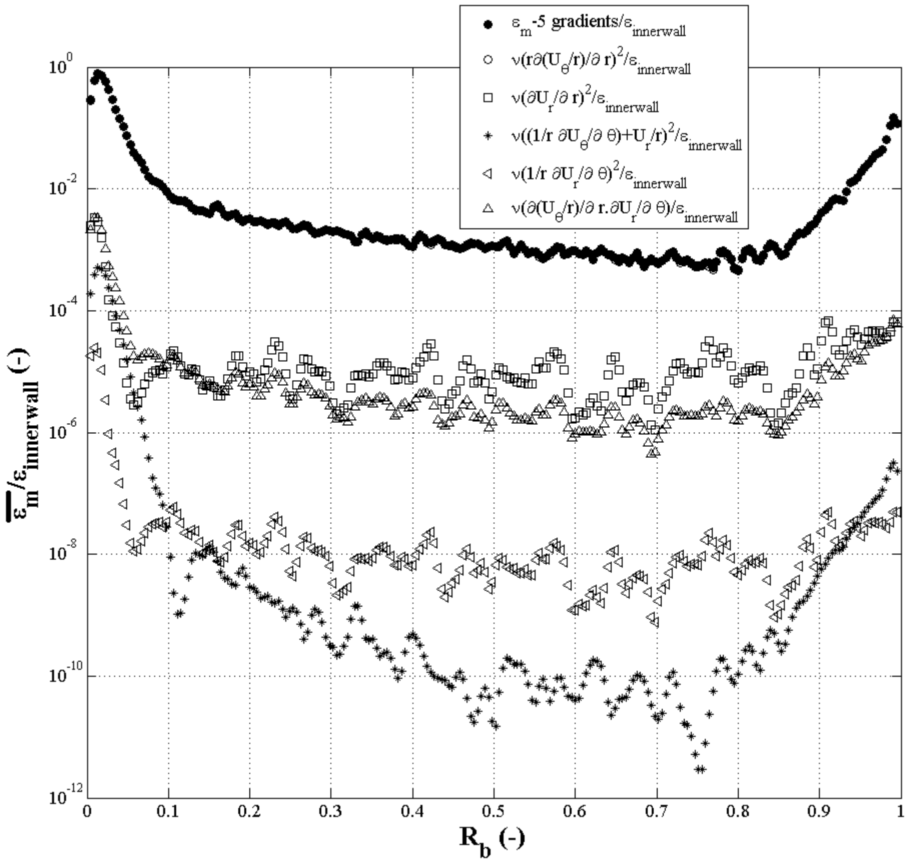

Figura 31 – The estimation of VEDR of mean flow kinetic energy and its 5 gradients at Z_L= 0.725 ± 0.005.

The estimation of the VEDR using the isotropic assumptions based on the work of Sharp e Adrian (2001) would imply that the $\overline{((\frac{\partial u'_{\theta}/r)}{\partial r})^2}$ gradient is used 3 times, and for the axi-symmetry assumption this gradient would be used two times. Hence, we could observe a direct impact on the estimation of VEDR using these assumptions leading to an estimate which is just a multiple factor of the one with only five gradients through-out the gap-width. Just because the estimation will be higher does not necessarily means that it will be the correct estimation. The composition of the VEDR of the mean flow and turbulent turbulent kinetic energy (Figures 31 and 32) showed that using an assumption based methodology which worked in the case of stirred tank (DELAFOSSE et al., 2011) may not be as successful in other geometries. Taylor-Couette is basically a tangential flow and radial flow is only about 10 % of the tangential flow. Axial flow should also be in the range of radial flow (KOBAYASHI et al., 1990). Therefore, for better estimation it is important to know the percentage composition of each of the 12 gradients on the VEDR,

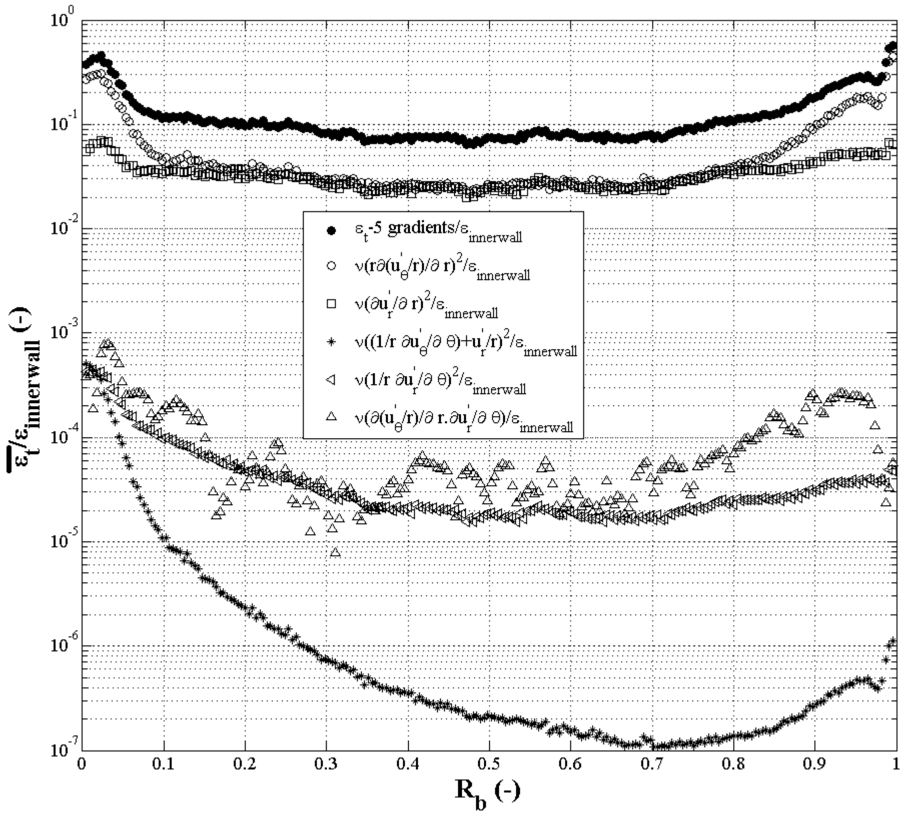

Figura 32 – The estimation of VEDR of turbulent kinetic energy and its 5 gradients at Z_L= 0.725 ± 0.005.

afterwards a newer and simpler equation can be created for 2D PIV results. Perhaps, this can be done numerically because experimentally the estimation of all 12 gradients while capturing the smallest scales is still out of reach as shown by Tokgoz et al. (2012).

There is another similarity between these two components of the VEDR, the magnitude of the gradient of radial fluctuating velocity component is same for both, radial and tangential, directions. This aspect of viscous dissipation of turbulent kinetic energy is more important as it confirms that the turbulence is not fully isotropic, and further confirmed by the fact that none of the isotropy ratios, K_{ijkl}, are equal to 1, as shown in Figure 33. The fully isotropic hypothesis implies that the following equations (2.16, 2.17 and 2.18) of the isotropic ratios (K_{ijkl}) are respected (DUCCI; YIANNESKIS, 2005; DELAFOSSE et al., 2011).

$$K_{jjjj} = \overline{\left(\frac{\partial u'_j}{\partial j}\right)^2} / \overline{\left(\frac{\partial u'_k}{\partial k}\right)^2} = 1 \tag{2.16}$$

$$K_{ijij} = \frac{1}{2}\overline{\left(\frac{\partial u'_i}{\partial j}\right)^2} / \overline{\left(\frac{\partial u'_k}{\partial k}\right)^2} = 1, i \neq j \tag{2.17}$$

$$K_{ijji} = -2\overline{\frac{\partial u_i'}{\partial j}\frac{\partial u_j'}{\partial i}} / \overline{\left(\frac{\partial u_k'}{\partial k}\right)^2} = 1, i \neq j \tag{2.18}$$

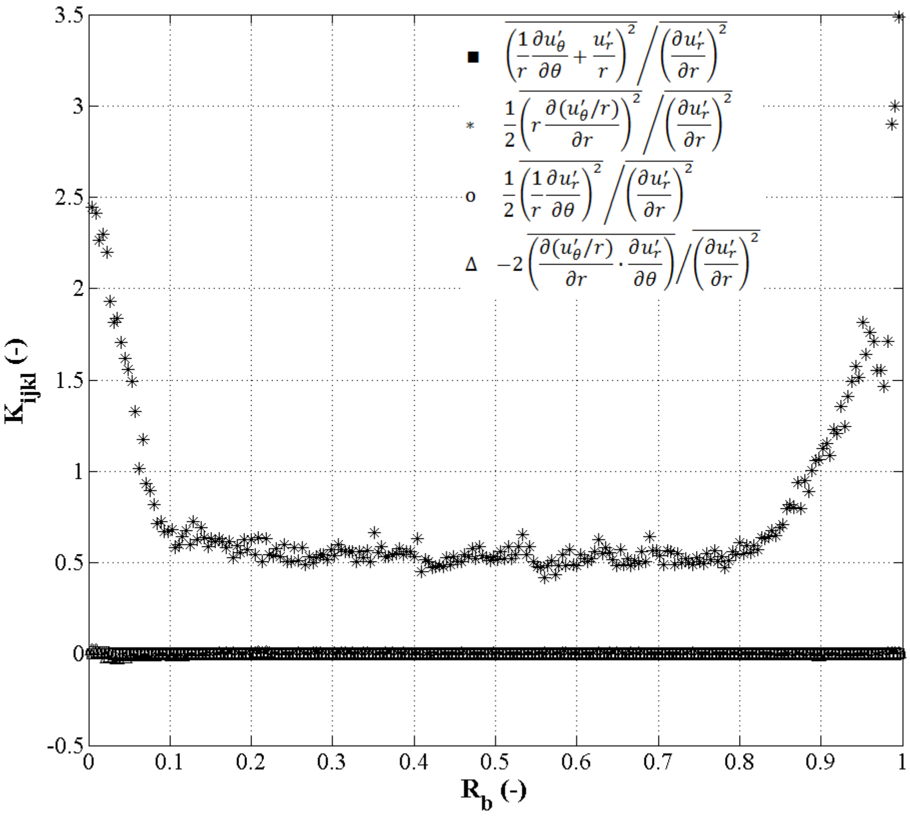

Figura 33 – Comparison of isotropy assumptions on radial profiles at Z_L= 0.725 ± 0.005.

It can be seen in the Figure 33 that none of these ratios exhibit values close to 1, in-fact most of the ratios exhibit values closer to zero. The cross product gradient, term K_{ijji}, and the ratio K_{jjjj} show the maximum departure from isotropy with a mean value of 0.0047 and 0.0003, respectively. Only one of the isotropy term K_{ijij} has a value of 0.5 in the bulk zone, the gradient of the tangential fluctuating velocity component in the radial direction; while, the other isotropy term K_{ijij} displayed departure from isotropy with a mean value of 0.0007.

As per authors knowledge, this kind of isotropic study has not been conducted before in the TVB. Though, in the stirred tank Sharp e Adrian (2001), Ducci e Yianneskis (2005), Delafosse et al. (2011) have presented work on these isotropy ratios, and there are some similarities with their work. Their cross product term also exhibited maximum deviation from the isotropy, and their term K_{ijij} also had a value of ≈ 0.5. The difference is that their K_{jjjj} ratio was closer to 1 in contradiction to this study. Additionally, Ducci e Yianneskis (2005) had access to the 9 mean squared gradients through their multi-point LDA study and Delafosse et al. (2011) conducted 2D-PIV study in three different planes in order to capture all of the gradients but in different locations and spatial resolutions.

The spatial resolution also has a significant impact on the K_{ijkl} ratios in complete agreement with Delafosse et al. (2011), as shown in the Figure 34. These averaged ratios were conducted on the horizontal plane located at Z_L= 0.725 ± 0.005 for the various ICS and overlap ratio mentioned in Table 4. At spatial resolutions far greater than the Kolmogorov scale, the averaged value of the K_{ijkl} ratios increases slightly, in similar observation of Delafosse et al. (2011). As mentioned by Delafosse et al. (2011), the reason behind this anomaly is that there are lesser number of data points at higher spatial resolutions which lead to comparatively higher average in comparison to the lower spatial resolutions.

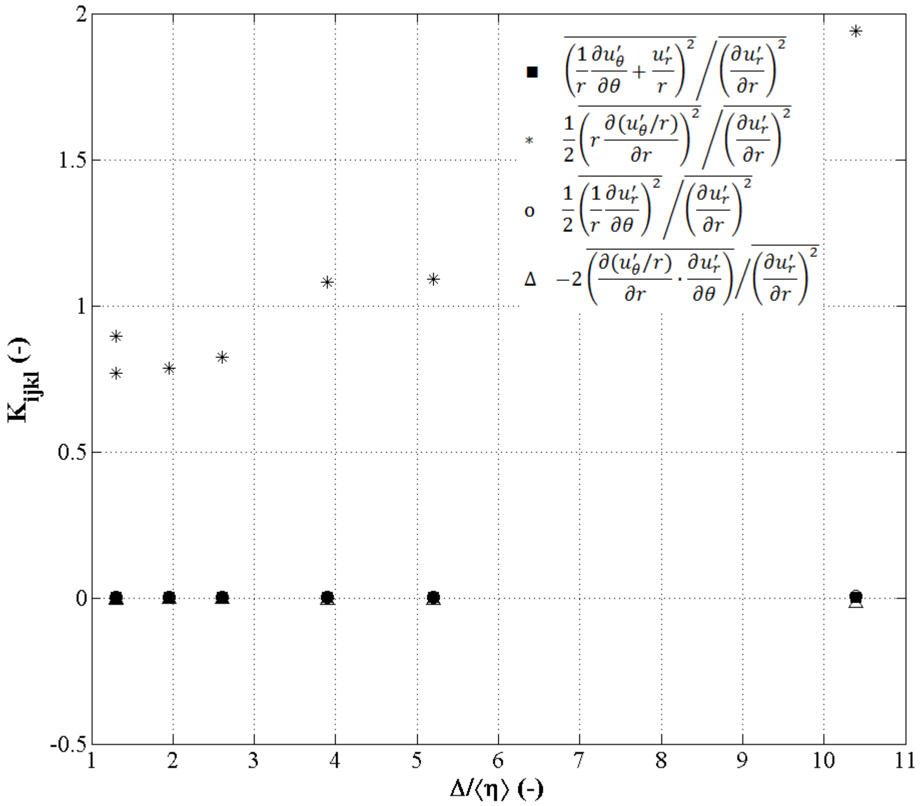

Figura 34 – Variation in the K_{ijkl} ratios influenced by the dimensionless spatial resolution for the radial profiles located at Z_L= 0.725 ± 0.005.

Another interesting observation is that there are two different values for the K_{ijkl} ratios at value near to 1 of the x-axis. These two different values for the same dimensionless spatial resolutions are for the 32 ICS Overlap 75 (higher value) and 16 ICS Overlap 50 (lower value). Although, the spatial resolution obtained is same through different overlap ratios, the higher base grid structure ICS of 32 is courser than the 16 ICS and therefore captures comparatively less information. This confirms further the importance of the ICS value in relation to the overlap ratio. Main aim of the overlap ratio is to increase the number of data points. True estimation comes from the base grid structure, which presently is hindered by both cost and technological development; for example, a camera with 32 or perhaps 64 Mpixels (higher cost), not available at the time the study was conducted, will provide access to double or quadruple amount of the information but will require particles of size 1 μm which are extremely costly.

The advantage of this study is that the whole of gap-width is covered and at different horizontal locations similar results were obtained (results not shown) in comparison to a stirred tank where only a small area near the impeller region is studied. On the other hand, the disadvantage is that only five gradients are available in this study; thus, the K_{ijkl} ratios are not known for the rest of the gradients. Perhaps, a validated numerical study with access to all 12 gradients can shed more light on this subject to provide more clarity on the anisotropy in a TVB.

2.5.4.2 EDR structure

The VEDR of the mean flow and turbulent kinetic energy is presented in Figures 35, 36a, 36b, 37a and 37b at the five different horizontal locations for the five rotational speeds, except at the rotational speed of 30 rpm where only three horizontal locations were available. In the x and y axis of these Figures, the friction velocity, u_τ, and $\epsilon_{innerwall}$ are estimated analytically from the dimensionless torque, G, estimations of the Wendt (1933) empirical correlation (Equation 2.1) cited in Lathrop, Fineberg e Swinney (1992), as shown in Table 3. It should be pointed out again that the noise in the bulk zone in VEDR estimations of very small magnitude values is due to poor concentration at higher overlap ratios. Choosing a zero overlap results in a lesser noise but also decrease substantially the number of data points available in the boundary layer (Figure 10).

The location of maxima is always very near to the wall, similarly observed by Tokgoz et al. (2012), Hout e Katz (2011) either to that of inner cylinder or outer cylinder depending upon the axial location in the Taylor-Vortex. In the outward region, the location of maxima is near the outer cylinder as shown for the rotational speed of 114 rpm at the axial location of $Z_L = 0.625 \pm 0.005$, and for the inward and center of vortex region the maxima is located near the inner cylinder, at the axial location of $Z_L = 0.575$ and 0.675 ± 0.005, respectively for the rotational speed of 114 rpm. Among the three presented regions, the viscous wall layer is weakest in the outward region because the magnitude of the tangential velocity is strongest in this region (Figure 15a); while, the deceleration of the fluid results in the increase in the viscous wall layer. It can be seen that among the three regions, VEDR is the most dominant near the inner wall with the overall maxima located near the inner wall.

McEligot et al. (2008) termed the VEDR of mean flow kinetic energy as direct dissipation and that of turbulent kinetic energy as turbulent or indirect dissipation. They presented the numerical results of the DNS model for these components in a channel flow and zero-pressure-gradient boundary layer. They found that the direct dissipation is the dominating component of the two near the wall. As the d+ increases, both the direct and

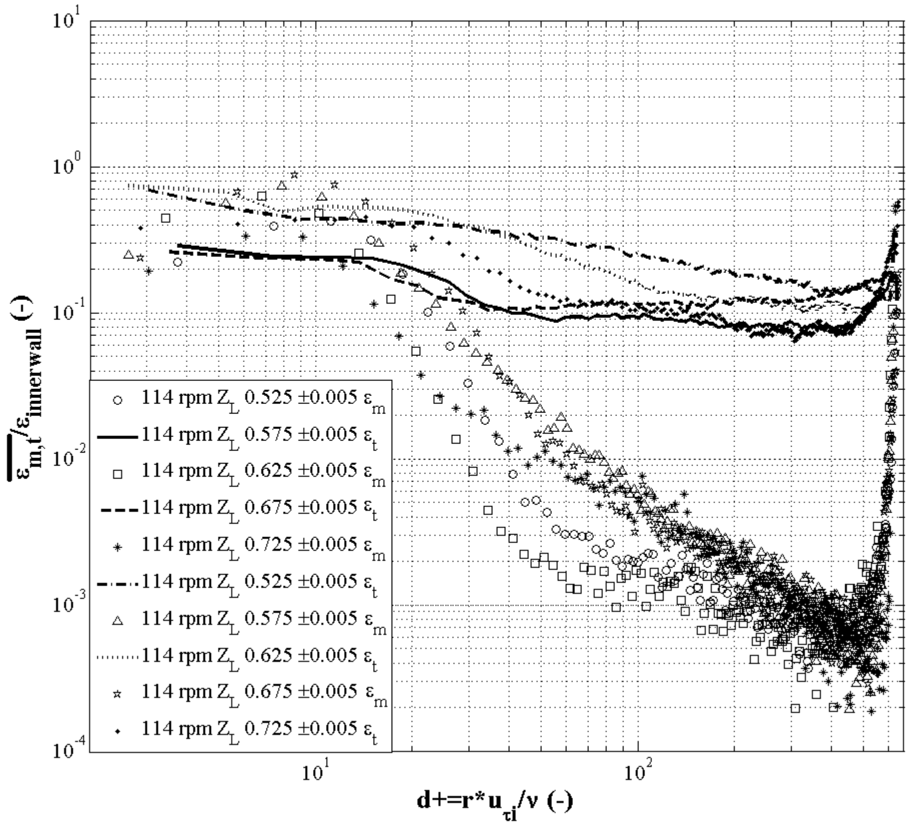

Figura 35 – The VEDR of the mean flow, ϵ_m, and turbulent, ϵ_t, kinetic energy at 114 rpm.

turbulent dissipation decreases with the reduction in the direct dissipation being much more drastic in comparison to the turbulence counterpart. Between d+ = 10 and 20, the magnitude of the direct and turbulent dissipation becomes equal, and with further increase in the d+ values the direct dissipation continues decreasing much more rapidly leading to the turbulence dissipation becoming the dominating component in the bulk zone.

Most of these aspects can be observed in the current estimations of these two components of the VEDR for the TVB for the five rotational speeds presented here. The only difference is that the direct dissipation is not dominating as estimated by them near the wall region, but only comparatively higher. Otherwise, increase in d+ results in decrease in both of these components of the VEDR with the decrease in the direct dissipation being more rapid in comparison to the turbulence one. Furthermore, the magnitude of the direct and turbulent dissipation becomes equal between the region d+=10 and 20, along with the progressive dominance of the dissipation of turbulent kinetic energy towards the bulk region, where turbulence component of the VEDR is at-least an order higher. In fact, in the bulk region, the direct or mean flow kinetic energy dissipation becomes practically negligible by reaching values less than 1 % of the maximum value in complete agreement with the results of McEligot et al. (2008).

Turbulence takes over completely in the bulk zone once the viscous wall layer becomes negligible around d+=30 for a classical zero-pressure gradient case, as mentioned

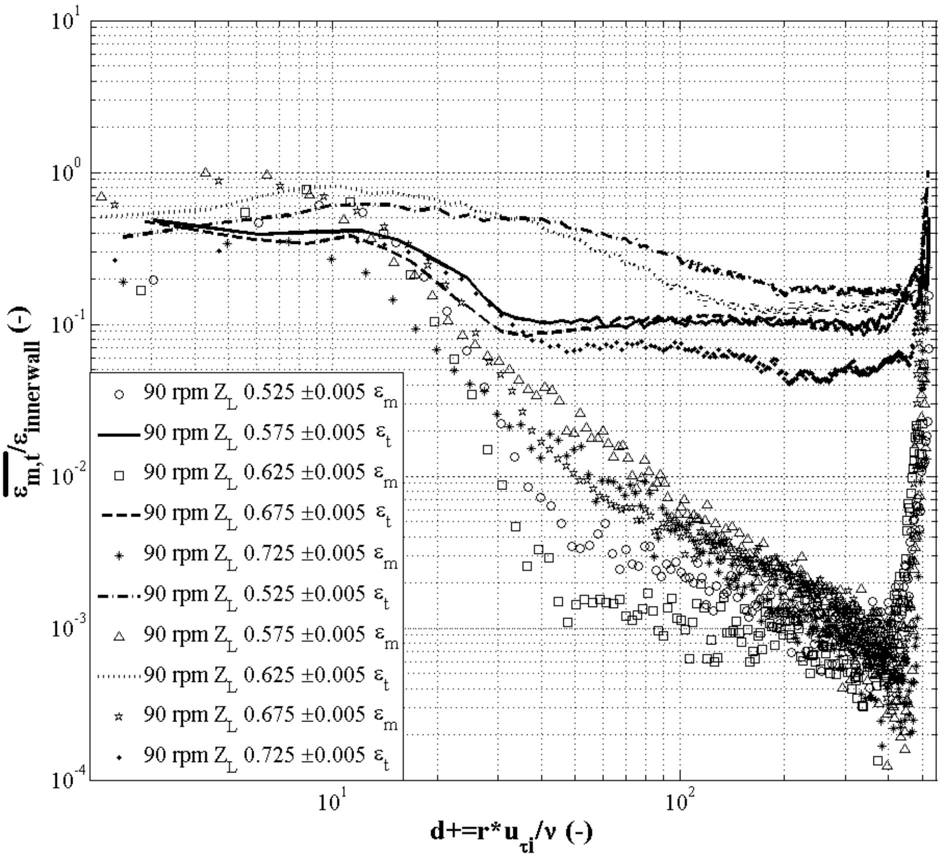

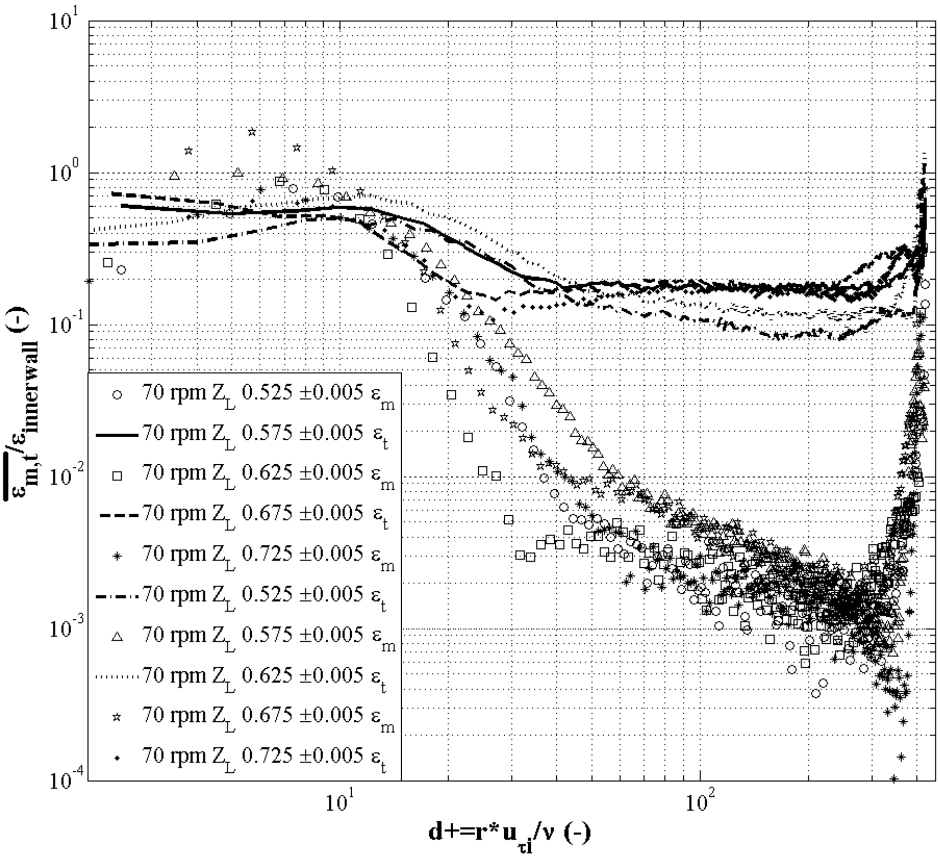

Figura 36 – The VEDR profiles of the mean flow, ϵ_m, and turbulent, ϵ_t, kinetic energy at 90 (a) and 70 (b) rpm.

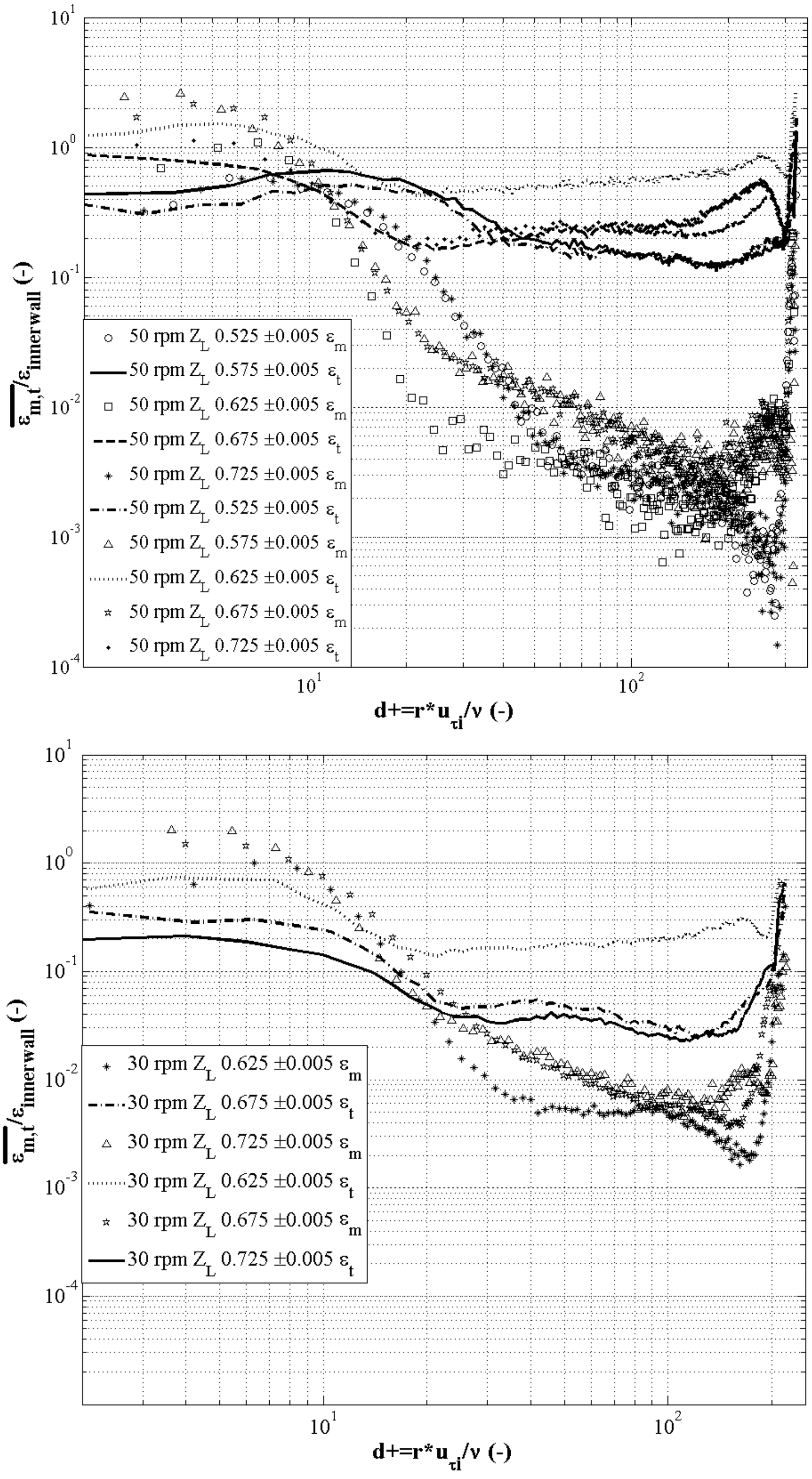

Figura 37 – The VEDR profiles of the mean flow, ϵ_m, and turbulent, ϵ_t, kinetic energy at 50 (a) and 30 (b) rpm.

by McEligot et al. (2008). They defined the viscous wall layer as the region with significant effects of viscosity which are not necessarily dominant and include the laminar and buffer sub-layers. The importance of this region lays in the fact that the largest gradients and greatest production of turbulence occur in this region besides being the region which provides major resistance to the momentum, mass and energy transfer (MCELIGOT et al., 2008). Additionally, it can be seen that the VEDR remains fairly constant in the viscous sublayer. These aspects of following the classical turbulence further strengthen the validity of these results.

It should be pointed out again that the noise in the bulk zone in VEDR estimation is due to the choice of higher overlap. Choosing a zero overlap results in a lesser noise but also decrease substantially the number of data points available in the boundary layer, and increases the under-estimation of the turbulence VEDR due to reduction in the spatial resolution, as can be seen in the Table5. In order to capture the smallest scales, the smallest feasible spatial resolution is chosen by accepting a certain amount of noise and keeping the validity of the results.

The profile structure of the VEDR for these five rotational speeds is very similar to that of the normal tangential stress (Figures 23a, 24a, 25a, 26a and 27a) at the three specified locations: outward, center and inward. First and foremost, boundary layers on both walls are marked by gradients with sharp decrease. The differentiation between the outward, center and inward region is decided by the location of the maxima, as explained earlier, and the flow structure in the bulk zone. In the bulk zone of the outward region, the flow manifests a gradual decrease from the inner cylinder towards the outer cylinder, and vice-versa for the inward region. This aspect further strengths the importance of capturing well the tangential gradient in the radial direction.

The dimensionless VEDR makes its profile appear to be of similar magnitude at different rotational velocities, especially in the center of vortex region which has best prediction among the three presented regions for these five rotational velocities. In this center of vortex region, the magnitude estimation of the VEDR is comparatively higher for the 30 rpm followed by 50, 70, 90 and 114 rpms. Similar effect can be seen in the inward and outward region as well. Moreover, the magnitude of the VEDR of mean flow and turbulent kinetic energy mostly stayed ≤ 1 for the rotational velocities of 114 and 90 rpms in the three presented regions. This implies that the maximum VEDR for these two components never goes above the global estimated value, whereas global estimate is the mean of all regions where there will certainly be maximum values higher than the global estimate, as demonstrated by the rotational velocities of 50 and 30 rpms. These two aspects further indicate that there is certainly some under-prediction at higher rotational velocities.

In order to use the TVB as a bio-reactor, the most important constraint will be to keep the VEDR within sub-lethal responses of a cell-line in order to achieve the desired results. Godoy-Silva, Mollet e Chalmers (2009) discovered that around 60 $W/kg = m^2s^{-3}$ maximum VEDR, the CHO cell line gave the sub lethal physiological responses that are critical to a bioprocess. CHO cell line is one of the most robust cell lines that exist in present time, but there are many cell lines which are much more sensitive and their sub-lethal response could be found at a much lower value.

In this study, as per global estimates of the VEDR, the maximum value of 3.17 was obtained located at the inner wall for the rotational speed of 114 rpm. The maximum value is only achieved in the viscous sub-layer very near to the wall where the cells may never reach due to the nature of the viscous layer of providing resistance to any kind of transfer. Away from the wall, the VEDR decreases rapidly and its magnitude is much smaller than 1 W/kg. The animal cells are bound to spend the maximum amount of time within a Taylor-vortex in the bulk zone, between R_b = 0.1 to 0.9, where the gradients are much smaller and hold similar magnitude, i.e., similar hydrodynamic conditions in the major part of the reactor. This is a big advantage for a Taylor reactor to be used a bioreactor for culturing animal cells.

2.5.5 Kolmogorov scale

In the Figure 38, the Kolmogorov scale, $\eta = (\nu^3/\epsilon)^{1/4}$ is presented for the five rotational speeds at the center of vortex region. The center of vortex region was chosen because this region was best characterized by all the presented rotational speeds. The Kolmogorov scale presented here is always smaller than the global Kolmogorov scale through-out the gap width, except for the rotational speed of 30 rpm, where the PIV estimated Kolmogorov scale was smaller only in boundary layer area.

The Kolmogorov scale has significant importance for the culturing of animal cells in bioreactors. Kunas e Papoutsakis (1990) observed increase in the cell damage due to the fluid hydrodynamic forces when the Kolmogorov eddy size approaches the cell size. They conducted these experiments in the absence of the bubbles to clarify that the damage is directly related to fluid hydrodynamic forces only. At the same time, there is no proof if there is any interaction between the cells and eddies or how the cells are damaged. Although, there may not be a direct relation with the Kolmogorov scale and a certain amount of turbulence might be necessary to ensure adequate mixing and mass transfer within the bioreactor, a significant amount of turbulence is known to damage the animal cells. Smith e Greenfield (1992) managed to culture the animal cells at a Reynolds No. of 25,000 in a tank stirred with Rushton turbine at a rotational speed of 600 rpm with estimated maximum and mean VEDR of 21.8 and 0.697 m^2s^{-3} (SINGH, 2011), respectively, corresponding to the minimum and mean Kolmogorov scale of 15 and 35 μm. Considering these aspects and that the animal cell size ranges between 10-15 μm,

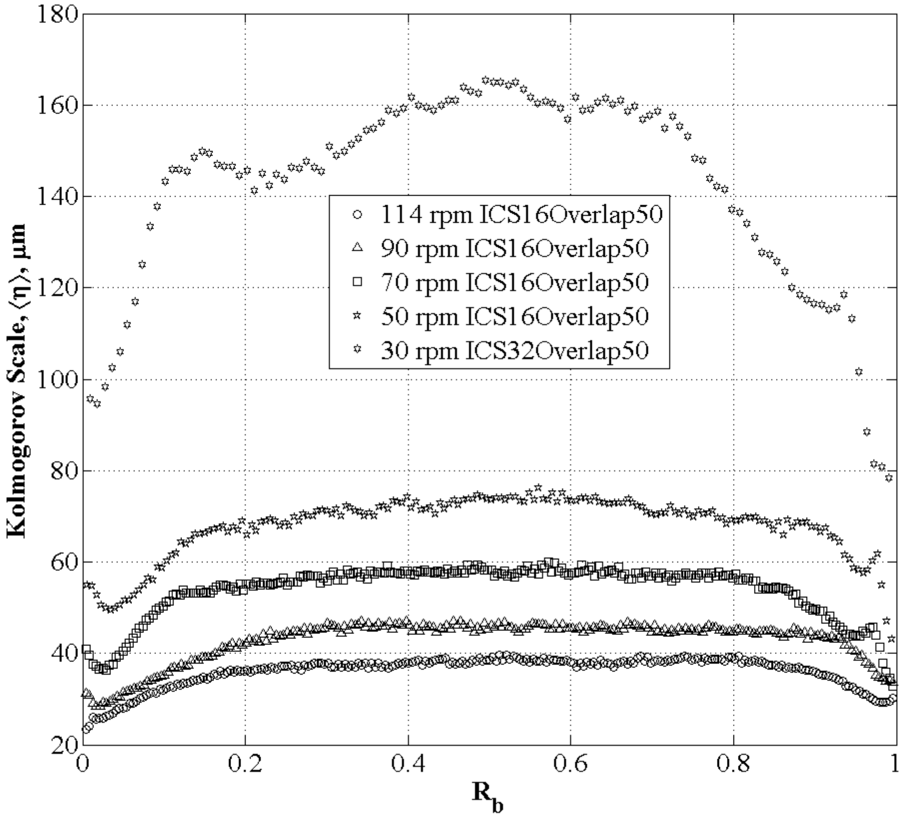

Figura 38 – The Kolmogorov scale for different rotational speeds at the center of vortex region.

the range of hydrodynamics that can be employed in a bio-reactor can be ascertained to avoid damage to animal cells in suspension provided an accurate estimation of VEDR is available because the Kolmogorov scale is inversely proportional to VEDR.

2.6 Conclusions

The main aim of this chapter was to present a direct VEDR estimation for the Taylor-Couette reactor at five different rotational velocities using only five of the twelve gradients required for a complete estimation. The composition of the five gradients of the VEDR of the mean flow and turbulent kinetic energy estimation was also presented. Apart from the VEDR estimation, mean radial and tangential velocity profiles, and their fluctuating counterparts are also presented in this study. In addition, a study was conducted to understand the impact of overlap ratio and ICS on the VEDR estimations, and mean and fluctuating velocity components.

The overlap study showed that overlap ratio does not ameliorate the estimations of the mean and fluctuating velocity components because the base grid structure, ICS, was able to capture these components, still the overlap ratio only increase the data yield for a particular ICS value. However, overlap ratios did improve on the VEDR estimations by capturing the smaller scales but at the expense of increased noise in the estimation of smaller magnitude values of the bulk zone. If there is a possibility of reaching the Kolmogorov scale with the ICS grid structure, then a zero overlap ratio could suffice.

Unlike the overlap ratio, ICS plays a significant role in the estimation of even the mean and fluctuating velocity components apart from the VEDR estimations. ICS value should be chosen depending upon the requirements of a particular study; for example, requirements of VEDR implies the usage of the smallest feasible ICS value which is equivalent of or closest to the Kolmogorov scale. If only mean flow is required than the ICS value should capture at-least the Taylor's micro-scale, but at the same time making sure that there are sufficient number of data points for a good estimation of the flow.

The magnitude of radial velocity component is only around 10 % of that of tangential component, and is nearly zero in the center of vortex region. In the outward and inward regions, the maximum is achieved towards the center of the gap-width forming a downward and upward U-like shapes for the outward and inward regions, respectively. In the case of tangential velocity component, the boundary regions are marked by sharp decreases and the bulk zone is characterized by a near constant flow structure in the vicinity of 50 % of the magnitude, while being strongest and weakest in the outward and inward regions, respectively. The strong tangential flow implies that it will have a significant contribution in the kinetic energy and its dissipation, and to capture its diffusion in the radial direction from the inner cylinder towards outer implies the requirement of very small mesh in this direction, especially near the walls where lies large gradients.

Similarly a steep decrease can be observed in the boundary layers of the normal tangential stress with little variation in the bulk zone in regards to the tangential component of the velocity. The center of the vortex region was best captured by the five presented rotational velocities, while the outward region was practically not captured by the 70, 50 and 30 rpm. The simple reason behind this could be the higher probability, as there are two centers of vortexes for each outward flow structure. The limited number of results that can be achieved due to practical reasons is one of the shortfalls of the experimental method. This limitation is one of the reasons for the popularity of numerical simulations, where data can be obtained anywhere within the geometry easily.

The VEDR of mean flow kinetic energy is mainly composed of the $(\frac{\partial(\overline{U_\theta}/r)}{\partial r})^2$ gradient, and the gradient, $\overline{(\frac{\partial(u'_\theta/r)}{\partial r})^2}$ is the major component of the turbulence VEDR especially in the boundary layer area. In addition, because of such a huge impact of only one gradient on the VEDR estimation, the application of isotropic and axi-symmetric assumptions is not valid in this case and leads to over-estimation. The dissipation of the mean flow kinetic energy was comparatively stronger in the boundary layer area, while the dissipation of turbulent kinetic energy was at-least an order higher than its mean flow counterpart in the bulk zone. The profile structures of these two components of VEDR in the three aforementioned regions for the five rotational velocities were observed to be very similar to the normal tangential stress again citing the significance of the tangential velocity component in the estimation of and turbulence VEDR. Knowing that this VEDR estimation is based on only five gradients, and considering that the axial velocity component has a similar impact as that of the radial velocity component, it becomes necessary to capture well the propagation of tangential velocity component in the radial direction, especially in the boundary layer for a better estimation of both components of VEDR.

These experiments were conducted with a view to validate numerical results, especially the VEDR estimations which contain the smallest scale. If the smallest scales of numerical results can be validated, than those results can be used with 100 % confidence leading to better designs and operating conditions. Therefore, the next chapter focuses on the validation of the numerical results with more attention towards the boundary layer area where lie the steep gradients. Another important aspect of the numerical simulations will be to estimate the VEDR using all the 12 gradients and presenting the compositions of those 12 gradients in order to better deduce an equation to estimate the VEDR from 2D PIV results.

3 Numerical Method and its Validation

All of these simulations were performed on a desktop with six-core and twelve-thread 3.5 GHz i7-3970X processor, and 64 GB of memory. All of the simulations were run using hpi based parallel processing with 4 cores. The CFD software Fluent of ANSYS-Fluent (2010) version 13.0.0 was used to perform the numerical simulations in the TVB used for the PIV estimations. The details of the TVB can be seen in the Table **??**, as shown in the Chapter 2.

In this section, firstly the basic numerical aspects used in the TVB model will be presented, along with a brief description of the turbulence models used in this study. Then the numerical model will be validated with the experimental results presented in the Chapter 2 at one of the PIV horizontal location for the rotational speed of 114 rpm. The analytical estimations for the TVB at 114 rpm can be found in the Table **??**, Chapter 2. Only the DNS model will be used for the validation of the numerical model.

3.1 Turbulence modelling

Turbulence, a time and space varying fluctuations in the flow field, is a phenomenon of three dimensional structures and unsteady nature made up of various scales, and characterized by Reynolds number. It is generated when the inertial forces overpower the viscous forces. Navier-Stokes equations for continuity, momentum and energy are used to describe both the laminar and turbulent flows. Present simulations are conducted in isothermal state, so the energy equation is not required here. In addition, it is assumed that the flow is incompressible, fluid is Newtonian and there are no external forces; thus, the Navier-Stokes equations for continuity (Equation 3.1) and momentum (Equation 3.2) become:

$$\frac{\partial u_i}{\partial x_i} = 0 \tag{3.1}$$

$$\frac{\partial u_i}{\partial t} + \frac{\partial (u_i u_j)}{\partial x_j} = -\frac{1}{\rho}\frac{\partial p}{\partial x_i} + \frac{\partial}{\partial x_j}\Big[\nu\Big(\frac{\partial u_i}{\partial x_j} + \frac{\partial u_j}{\partial x_i})\Big)\Big] \tag{3.2}$$

In order to solve all the spatial and temporal scales of the turbulence a direct numerical simulation (DNS) of the Navier-Stokes equations (3.1 and 3.2) has been conducted; though, to resolve all the scales the computational mesh must confirm to the smallest dissipative scales known as the Kolmogorov scale, given by, $\eta = (\frac{\nu^3}{\epsilon})^{1/4}$. If the computational mesh is not fine enough, a certain amount of information will be lost depending upon the coarseness of the mesh. The details of the computational mesh are discussed in the following section. Although, the DNS can resolve all the scales if the computational mesh is fine enough, it is known to be the most time and computational resource consuming model (BARTELS et al., 2002). Considering that the mesh may not be fine enough to resolve all the scales and in order to reduce the time and computational resource consumption, the LES turbulence models may be considered as a viable option.

LES model is based on the assumption that basically large eddies result in the transfer of the momentum, mass, energy and other passive scalars. Therefore, the governing equations of the LES model are obtained by spatially filtering over small-scales. Eddies with scale smaller than the filter are eliminated and are modeled with a sub grid scale (SGS) model. The SGS model describe the interaction between the resolved and unresolved scales (BAKKER; OSHINOWO, 2004).

The application of a filtered variable (Equation 3.3) for an LES model in the Navier-Stokes equation leads to new unknown quantities in the momentum Equation 3.4. The filtered variable is denoted by overbar, in the Equation 3.3, where D is the fluid domain and G is the filter function which determines the scale of the resolved eddies. In the Equation 3.4, τ_{ij} represents the SGS stresses and is the unknown quantity that arose out of the filtering process. In the Ansys Fluent, the SGS stresses τ_{ij} are correlated to the large-scale tensor S_{ij} (Equation 3.5) using eddy viscosity approach as shown in Equation 3.6.

$$\bar{f}(x) = \int_D f(x')G(x;x')dx' \tag{3.3}$$

$$\frac{\partial \bar{u}_i}{\partial t} + \frac{\partial(\bar{u}_i \bar{u}_j)}{\partial x_j} = -\frac{1}{\rho}\frac{\partial \bar{p}}{\partial x_i} + \frac{\partial}{\partial x_j}\left[\nu\left(\frac{\partial \bar{u}_i}{\partial x_j} + \frac{\partial \bar{u}_j}{\partial x_i}\right)\right] - \frac{\partial \tau_{ij}}{\partial x_j} \tag{3.4}$$

$$S_{ij} = \frac{1}{2}\left(\frac{\partial \bar{u}_i}{\partial x_j} + \frac{\partial \bar{u}_j}{\partial x_i}\right) \tag{3.5}$$

$$-\left(\tau_{ij} - \frac{\delta_{ij}}{3}\tau_{kk}\right) = 2\nu_{SGS}\bar{S_{ij}} \tag{3.6}$$

The ν_{SGS} is the subgrid scale eddy viscosity representing the smaller scales. There are various LES models available in the Fluent and each is differentiated from the other based on its definition of this SGS eddy viscosity. In this study, as mentioned earlier, two LES models are used, namely the Smagorinsky and wall adapting local eddy-viscosity (WALE) models. The Smagorinsky LES model describes this SGS eddy viscosity as shown in Equation 3.7, where $L_S = min(\kappa d, C_S\Delta)$ is the mixing length for SGS, where κ is the von Kárman constant, d is the distance to the closest wall, C_S=0.2 is the Smagorinsky constant and Δ is the local grid scale and computed as power 1/3 of the volume of the computational cell. In the case of the the WALE model, the SGS eddy viscosity is described in the Equation 3.8, where $L_S = min(\kappa d, C_W \Delta)$ with the $C_W = 0.325$ being the Wale constant.

$$\nu_{SGS,Smag} = L_S^2 |\bar{S}|, |\bar{S}| \equiv \sqrt{2\bar{S}_{ij}\bar{S}_{ij}} \tag{3.7}$$

$$\nu_{SGS,WALE} = L_S^2 \frac{(S_{ij}^d S_{ij}^d)^{3/2}}{(\bar{S}_{ij}\bar{S}_{ij})^{5/2} + (S_{ij}^d S_{ij}^d)^{5/4}}, \tag{3.8}$$

$$S_{ij}^d = 1/2(\bar{g}_{ij}^2 + \bar{g}_{ji}^2) - 1/3\delta_{ij}\bar{g}_{kk}^2, \bar{g}_{ij} = \partial \bar{u}_i / \partial x_j$$

Apart from the DNS and LES models, the four RANS based models, namely k-ϵ, SST, SAS-SST and RSM, used in this study are derived from Reynolds-averaging of the underlying Navier-Stokes equations (3.1 and 3.2) for an Newtonian fluid and incompressible flow. This process introduces Reynolds stresses, $-\rho\overline{u_i u_j}$, in the momentum Equation 3.9 that have to be modelled to form a closed system of equations. In the Equation 3.9, $p' = p + 2/3k$ is the modified pressure and $\nu_{eff} = \nu + \nu_t$, where ν_t is the turbulent viscosity that arose out of the averaging process and must be modelled. In the case of LES model, the filtration process introduced the SGS eddy viscosity representing the smaller scales which needed to be modeled. In the two equation RANS based model, turbulent viscosity is introduced based on the Boussinesq hypothesis, but the difference is that the turbulent viscosity represents all of the turbulent scales in contrast to only the small scales for the LES models. This approach of the RANS based models impact both the reliability of the modelled equations and the computational cost required to solve them.

$$\frac{\partial u_i}{\partial t} + \frac{\partial (u_i u_j)}{\partial x_j} = -\frac{1}{\rho}\frac{\partial p'}{\partial x_i} + \frac{\partial}{\partial x_j}\left[\nu_{eff}\left(\frac{\partial u_i}{\partial x_j} + \frac{\partial u_j}{\partial x_i})\right)\right] \tag{3.9}$$

In two-equation models, the Boussinesq hypothesis is used to model the unknown Reynolds stresses by assuming they can be approximated by the product of the mean strain rate multiplied by an isotropic turbulence viscosity. There are a variety of models that have been formulated but here we focus on just two of them. Firstly, the k-ϵ model, based on transport equations for the turbulent kinetic energy, k (Equation 3.10), and the turbulence energy dissipation rate, ϵ (Equation 3.11), is used in which the turbulent viscosity is described as $\nu_t = C_\mu k^2/\epsilon$. In these equations, $G_k = \nu_t S^2$ represents the generation of turbulent kinetic energy due to the mean velocity gradients, and the value for the model constants $C_{1\epsilon}$, $C_{2\epsilon}$, C_μ, σ_k and σ_ϵ is 1.44, 1.92, 0.09, 1.0 and 1.3, respectively. Whilst this model has known limitations, particularly its unsatisfactory performance in the near-wall region, it is still very widely used and also provides a good starting point to generate an initial flow field for more complicated models.

$$\frac{\partial k}{\partial t}+\frac{\partial (k u_i)}{\partial x_i}=\frac{\partial}{\partial x_j}\left[\left(\nu+\frac{\nu_t}{\sigma_k}\right)\frac{\partial k}{\partial x_j}\right]+G_k-\epsilon \tag{3.10}$$

$$\frac{\partial \epsilon}{\partial t}+\frac{\partial (\epsilon u_i)}{\partial x_i}=\frac{\partial}{\partial x_j}\left[\left(\nu+\frac{\nu_t}{\sigma_\epsilon}\right)\frac{\partial \epsilon}{\partial x_j}\right]+C_{1\epsilon}\frac{\epsilon}{\rho k}G_k-C_{2\epsilon}\frac{\epsilon^2}{k} \tag{3.11}$$

The k-ϵ model employs wall functions as the equations cannot be integrated to the wall. In order to address this problem, models in which the turbulence energy dissipation rate is replaced by the turbulence eddy frequency, ω_{tef}, have been derived. These behave well near the wall and allow the detailed behavior inside the boundary layer to be calculated. However, they perform poorly away from walls due to a problem with over-sensitivity to the free stream conditions. Menter (1994) blended the k-ϵ and k-ω models and added a turbulence production limiter in the calculation of the eddy viscosity (Equation 3.12) to produce the now widely used Shear Stress Transport (SST) model. It provides accurate predictions of the onset and the amount of flow separation under adverse pressure gradients (MENTER, 1994).

$$\nu_t=\frac{k}{\omega}\frac{1}{max\left[\frac{1}{a^*},\frac{SF_2}{\alpha_1\omega}\right]} \tag{3.12}$$

$$\frac{\partial k}{\partial t}+\frac{\partial (k u_i)}{\partial x_i}=\frac{\partial}{\partial x_j}\left[\left(\nu+\frac{\nu_t}{\sigma_{kSST}}\right)\frac{\partial k}{\partial x_j}\right]+min(G_k,0.9k\omega) \tag{3.13}$$

$$\frac{\partial \omega}{\partial t}+\frac{\partial (\omega u_i)}{\partial x_i}=\frac{\partial}{\partial x_j}\left[\left(\nu+\frac{\nu_t}{\sigma_{\omega SST}}\right)\frac{\partial \omega}{\partial x_j}\right]+\frac{min(G_k,0.9k\omega)a_\infty}{\nu_t}+\frac{2(1-F_1)}{\omega\sigma_{\omega,2}}\frac{\partial k}{\partial x_j}\frac{\partial \omega}{\partial x_j} \tag{3.14}$$

In the Equation 3.12, the S is the magnitude of strain rate, k represents the transport equation for the turbulent kinetic energy (Equation 3.13), ω represents the transport equation for the turbulence eddy frequency (Equation 3.14), a^* =1 for high Reynolds number, α_1 is a constant of value 0.31, and F_2 is a blending function (Equation 3.16), respectively. In the Equation 3.13, the $\sigma_{kSST}=1/(F_1/\sigma_{k,1}+(1-F_1)\sigma_{k,2})$ where F_1 is a blending function (Equation 3.15), $\sigma_{k,1}=1.176$ and $\sigma_{k,2}$=1.0. In the Equation 3.14, the $\sigma_{\omega SST}=1/(F_1/\sigma_{\omega,1}+(1-F_1)\sigma_{\omega,2})$ where $\sigma_{\omega,1}=2.0$ and $\sigma_{\omega,2}$=1.168, and a_∞ is defined in the Equation 3.17, where $\beta_{i,1}$=0.075, $\beta_{i,2}$=0.828, κ=0.41 and β^*_∞=0.09.

$$F_1=tanh\left(\left(min\left[max\left(\frac{\sqrt{k}}{0.09\omega y},\frac{500\mu}{\rho y^2\omega}\right),\frac{4\rho k}{\sigma_{\omega,2,D^+_\omega y^2}}\right]\right)^4\right), \tag{3.15}$$

$$D_\omega^+ = max\left[\frac{2\rho}{\omega\sigma_{\omega,2}}\frac{\partial k}{\partial x_j}\frac{\partial \omega}{\partial x_j}, 10^{-10}\right]$$

$$F_2 = tanh\left(\left(max\left[\frac{2\sqrt{k}}{0.09\omega y}, \frac{500\mu}{\rho y^2\omega}\right]\right)^2\right) \tag{3.16}$$

$$a_\infty = F_1\left(\frac{\beta_{i,1}}{\beta_\infty^*} - \frac{\kappa^2}{\sigma_{\omega,1}\sqrt{\beta_\infty^*}}\right) + (1-F_1)\left(\frac{\beta_{i,2}}{\beta_\infty^*} - \frac{\kappa^2}{\sigma_{\omega,2}\sqrt{\beta_\infty^*}}\right) \tag{3.17}$$

A key failing of unsteady two equation models is that they cause excessive damping of turbulence and thus do not resolve any of the details of the turbulence directly (MENTER, 2009). Menter e Egorov (2010) introduced the SAS-SST to overcome this deficiency. The SAS-SST model (SAS stands for Scale Adaptive Simulation) uses a turbulence length-scale, which induces "LES-like"behavior in unsteady regions of the flow field. By adjusting the turbulence length-scale to the directly resolved turbulent structures, the eddy viscosity is reduced to the level of the limiting LES model. In this way, the model does not dissipate directly-resolved turbulent structures as classical RANS would (MENTER; EGOROV, 2010; MENTER et al., 2010). This is obtained by the addition of Q_{SAS} (Equation 3.18) term in the transport equation for the turbulence eddy frequency (Equation 3.14) of the SST turbulence model, where L is the length scale of the modeled turbulence, L_{vk} is the von Karmen length scale, S is the scalar invariant of the strain rate tensor S_{ij}, and the constants η_2, C and σ_Φ are 3.51, 2 and 2/3, respectively.

$$Q_{SAS} = max\left[\eta_2\kappa S^2\left(\frac{L}{L_{vk}}\right)^2 - C\frac{2k}{\sigma_\Phi}max\left[\frac{1}{\omega^2}\frac{\partial \omega}{\partial x_j}\frac{\partial \omega}{\partial x_j}, \frac{1}{k^2}\frac{\partial k}{\partial x_j}\frac{\partial k}{\partial x_j}\right], 0\right] \tag{3.18}$$

Another drawback of eddy-viscosity RANS based models is the assumption of an isotropic turbulence viscosity, which limits the development of anisotropy in the Reynolds stresses. RSM remove this assumption and solve transport equations for each of the Reynolds stresses. The model is much more computationally intensive than two-equation models and suffers from poor convergence behaviour (AUBIN; FLETCHER; XUEREB, 2004). Just as there are many variants of the two equations models, there are a large number of Reynolds stress models that differ in their closure relationships, especially for the pressure-strain term. Here the linear pressure strain variant of the model, known as the Launder Reece Rodi - Isotropization of production (LRR-IP) (LAUNDER; REECE; RODI, 1975), is used.

The momentum equation for the RSM model (Equation 3.19) is similar to the one based on the Boussinesq hypothesis (Equation 3.9), but for the pressure term, $p'' = p + 2/3\mu\partial u_i/\partial x_k$ and the Reynolds stresses, $\overline{u_i u_j}$, which were replaced by the ν_t term. These stresses are modeled as shown in the Equation 3.20, where C_{S-RANS}=0.22, δ_{ij}, ϵ

P_{ij} and Φ_{ij} are the kronecker delta, VEDR of TKE, production term and pressure strain correlation, respectively. The production term and VEDR of TKE are represented by the Equations 3.21 and 3.22, and the pressure strain correlation, where $\Phi_{ij} = -(C_{1RSM}\rho(\overline{u_i u_k} - 2/3\delta_{ij}k)\epsilon/k + C_{2RSM}(P_{ij} - 2/6delta_{ij}P_{ij}))$ where $C_1 = 1.8$ and C_2=0.6. In the Equation 3.22, the $C_{1\epsilon RSM} = 1.45$, $C_{2\epsilon RSM}$ =1.9, $\sigma_{\epsilon RSM} = 1.1$

$$\frac{\partial u_i}{\partial t} + \frac{\partial (u_i u_j)}{\partial x_j} = -\frac{1}{\rho}\frac{\partial p''}{\partial x_i} + \frac{\partial}{\partial x_j}\left[\nu \left(\frac{\partial u_i}{\partial x_j} + \frac{\partial u_j}{\partial x_i})\right)\right] - \frac{\partial (\overline{u_i u_j})}{\partial x_j} \tag{3.19}$$

$$\frac{\partial (\overline{u_i u_j})}{\partial t} + \frac{\partial (u_k(\overline{u_i u_j})}{\partial x_k} - \frac{\partial}{\partial x_k}\left[\left(\nu + C_{S-RANS}\frac{k^2}{\epsilon}\right)\frac{\partial (\overline{u_i u_j})}{\partial x_j}\right] = P_{ij} - \frac{2}{3}\delta_{ij}\epsilon + \Phi_{ij} \tag{3.20}$$

$$P_{ij} = \overline{u_i u_k}\frac{\partial U_j}{\partial x_k} - \overline{u_j u_k}\frac{\partial U_i}{\partial x_k} \tag{3.21}$$

$$\frac{\partial \epsilon}{\partial t} + \frac{\partial (\epsilon u_k)}{\partial x_k} = \frac{\partial}{\partial x_k}\left[\left(\nu + \frac{\nu_t}{\sigma_{\epsilon RSM}}\right)\frac{\partial \epsilon}{\partial x_k}\right] + \frac{\epsilon}{\rho k}(\rho C_{1\epsilon RSM}(P_k + P_{\epsilon b}) - C_{2\epsilon RSM}\epsilon) \tag{3.22}$$

A key limitation of two-equation models is their insensitivity to streamline curvature and rotation, which is the main motivation for the use of Reynolds stress models. Recently, a modification to the two-equation models has been developed by Smirnov e Menter (2009) based on the work of Spalart e Shur (1997). This has shown considerable benefit in applications where highly swirling flows have been modelled. Singh, Fletcher e J. (2011) have shown that the addition of curvature correction to the turbulence models improves its predictions. In view of this study, curvature correction was applied to all of the two-equation turbulence models used in this study.

3.2 Numerical methodology

3.2.1 Geometry and Meshing aspects

Workbench was used to construct geometry and the sweep mesh which consists of the hexahedral nodes. In view of the intended use of the DNS and LES models, and multiple reference frame (MRF) technique in the modeling aspects, a full geometry was modeled containing only one body. However, in order to obtain better control over the radial mesh, the TVB geometry was designed as a semi-circle, as shown in Figure 39, and was later on duplicated to model the full geometry. MRF technique was used instead of the more sophisticated but time-consuming sliding grid technique because the fluid movement in the TVB is only due to the inner-rotating cylinder; thus, avoiding the usage of a inner and outer geometrical configuration required for the sliding grid interface.

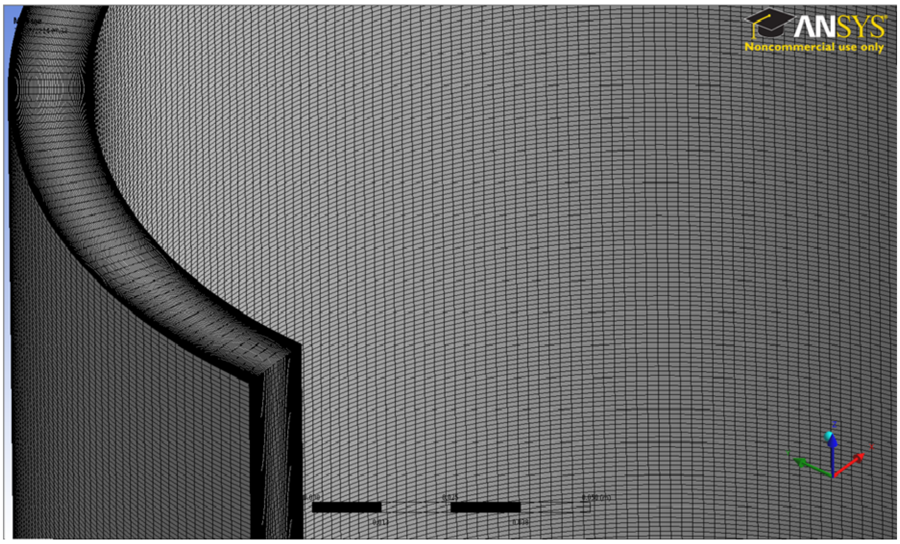

Figura 39 – Geometry and mesh of the TVB used in the PIV experiments.

Table 6 shows the different parameters that were varied and corresponding node and mesh sizes. Thee maximum aspect ratio value increased from 15.9 to 32.2 to 53.6 as the number of nodes were increased only in the radial direction in terms of radial divisions of 45 in Fine to 90 in Fine2X to 150 in Finer, respectively. Although, the aspect ratio increased significantly, the orthogonal quality remained the same for each mesh type with a value of 0.9999, where values close to 1 indicate good quality. Only the 3^{rd} Mesh name was tested for the DNS model, while all of these were tested for the LES-WALE model. In this grid-independence study, basically, the refinements in the mesh were done only in the radial direction because it is understood that the flow is radially transferred from the inner rotating cylinder to the outer cylinder, while the secondary vortices consisting of the radial and axial components of the velocity are only 10 % of the tangential component (KOBAYASHI et al., 1990). Thus, clearly citing the importance of a very fine grid in the radial direction in order to capture the smallest scales. Mesh in the radial direction was created in such a way that the nodes are smallest near the inner and outer walls and biggest in the center of the gap width. Figure 40 shows the impact of the refinements in the radial direction on the velocity flow field and TKE.

Tabela 6 – Mesh configurations used to model the TVB.

Mesh name	No of divisions			No of nodes	Mesh size			
	Z	X	Y	millions	Z	X min.	X max.	Y
					mm	μm	μm	mm
Fine	200	45	320	2.944	1	156	623	1.13
Fine2X	200	90	320	5.889	1	79	307	1.13
Finer	200	150	320	9.712	1	47	184	1.13

In terms of the global estimate of Taylor's micro-scale, $\langle \Lambda \rangle = 1.3$ mm (Table 3), all presented mesh types are sufficiently fine both near the walls and in the bulk zone to

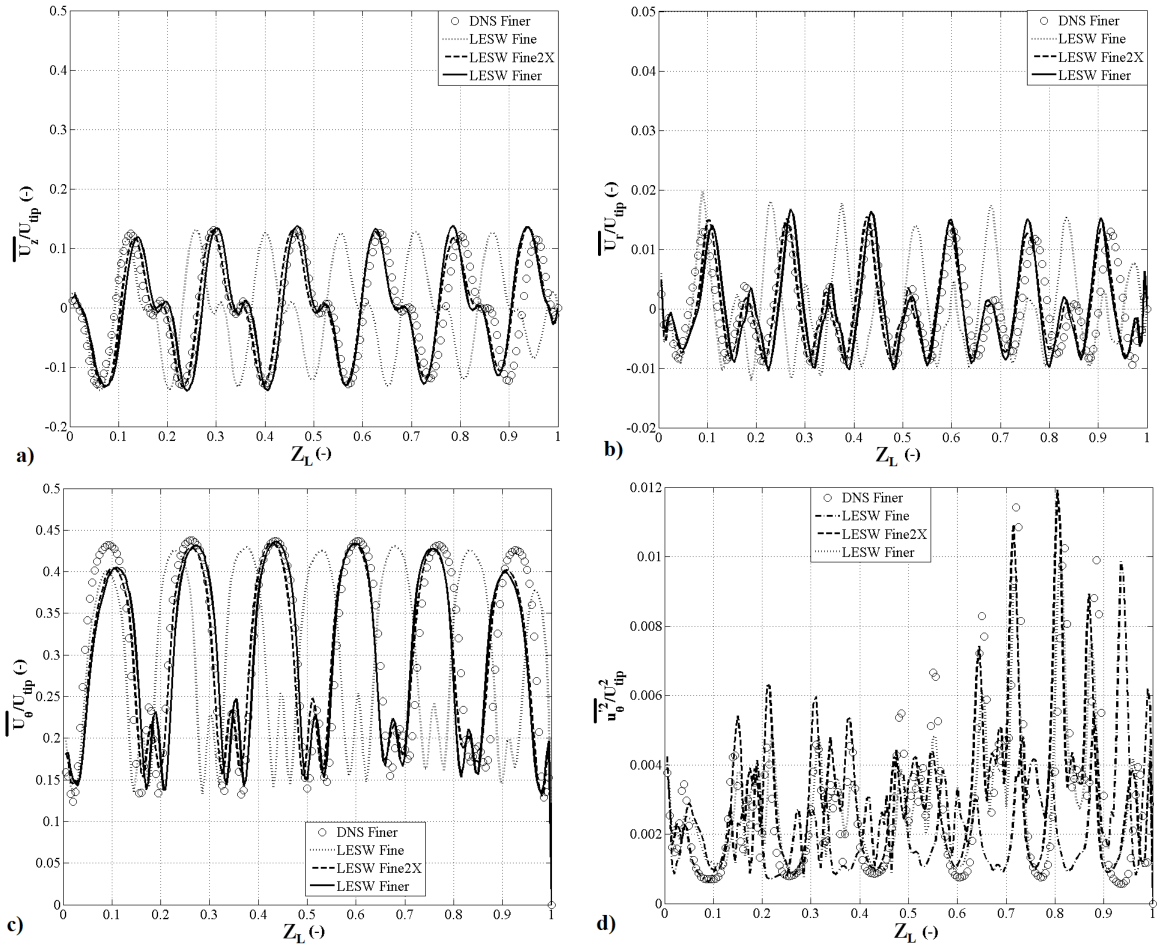

Figura 40 – Comparison of different grid sizes for the DNS and LES models of dimensionless mean axial velocity (a), radial velocity (b), tangential velocity (c) and mean square of fluctuating tangential velocity (d) axially at R_b=0.067. The legend is same in all figures.

capture the large-eddies defined by the Taylor's micro-scale. When a much courser grid (Fine grid with 2.9 million nodes) was used with the LES-WALE model, seven vortex pair appears instead of six vortex pairs for finer grids; considering that one vortex pair is represented by two crests and one trough. Among the Fine2X and Finer grid for the LES-WALE model, the three velocity components, radial, axial and tangential, are equally well predicted when compared with the DNS model using Finer grid. However, in the case of squared fluctuating tangential velocity the Fine2X grid comparatively over-predicts, thereby enhancing the choice of the finer grid LES-WALE model to be used in the rest of article for validation purposes and a much thorough comparison with the DNS model. In addition, the Finer grid must be capturing at-least 90 % of the dissipation rate near the boundary layer, especially considering the fact that nodes near the wall are ≈ 47 μm which is smaller than the global estimate of Kolmogorov scale, $\langle\eta\rangle$=52.5 μm (Table 3).

3.2.2 Pre-processing aspects

As mentioned in the previous section, the DNS, two LES models, namely Smagorinsky and WALE, and four RANS based models, namely, k-ϵ, SST, SAS-SST and RSM were used to estimate the flow and turbulence characteristics in the TVB. The Convergence criteria of 10^{-4}, which was achieved within a maximum of 40 iterations per time-step, for root mean square (RMS) scaled residuals was employed for the continuity, momentum and turbulence quantities. Double precision arithmetic was applied for all of the simulations. In order to collect the data, an xz-plane was created, and a certain number of variables, including velocity components and gradients, were chosen to be extracted at the end of each time-step in the text file format. The high resolution and second order backward Euler schemes were used to model the advection and transient terms, respectively, for all the equations.

3.2.3 Solver & Post-processing aspects

It took around 15 revolutions for the DNS and 5 revolutions for the LES models to achieve the moment stabilization, and 36 hours to complete one revolution for the DNS model and 24 hours to complete one revolution for the LES models. Once the moment stabilization was achieved, the data was collected for at-least 20 revolutions. The collected data was then treated using the Matlab program to process the results. As in the case of the experimental results, the statistical convergence of the second order fluctuating velocity components, namely $u_r'^2$, $u_\theta'^2$ and $u_r'^2 u_\theta'^2$ was also tested, and 20 revolutions or 7200 time-steps were found to be more than sufficient for an ensemble average.

3.2.4 Estimation of VEDR

The numerical results, the axial, radial and tangential velocity and direction components were extracted at each time step in the *.txt format. These txt files were treated with Matlab to create the gradients using the 2^{nd} order central differencing approximation of the first derivative, Equation 2.2, for the central elements. The boundary elements being only at the inner and outer wall due to the usage of the 2^{nd} order scheme were not considered for the VEDR estimation.

The gradients were estimated using the mean and fluctuating velocity components, as in the case of the PIV estimations and termed as the VEDR of mean flow and turbulent kinetic energy, respectively. These two components of VEDR are estimated directly from the Equations 2.3 and 2.4, respectively, in the case of DNS and LES models. Whereas, in the case of PIV measurements only five out of 12 gradients are estimated, as mentioned in Chapter 2, from the x-y plane for the VEDR of mean flow and turbulent kinetic energy, as shown in Equations 2.5 and 2.6, respectively.

3.3 Validation of the computational model

The validation of the numerical results was done at only one of the five available horizontal locations (Z_L=0.725 ± 0.005) of the PIV measurements. The comparison with the PIV data was conducted for the tangential and radial velocity components, the log-law profiles at the inner and outer boundary layers for the tangential component, squared fluctuating tangential velocity and the five available gradients of the VEDR of the mean flow and turbulent kinetic energy for the PIV measurements, as shown in Figures 41, 42,43 and 44. First of all, because the PIV location is not 100 % certain, the numerical horizontal location was chosen by observing a complete Taylor-Vortex pair and thereby choosing the most similar profile to that of the PIV measurement. The PIV profile lies in between the center of vortex and outward flow region of a Taylor-Vortex, but in close proximity to the center of vortex. The term center of vortex means as it says and the outward flow region means the region when the flow direction is at its strongest from the inner cylinder towards the outer cylinder, which is the center of a Taylor-vortex pair not to be confused with center of vortex. Each Taylor-vortex pair has one Outward flow, which lies in the center of this Taylor-vortex pair, two center of vortexes, in each vortex of the pair, and two inward flow regions, at each extremity of the pair. Secondly, considering that the numerical mesh spacing is of 1 mm in the axial direction, Figures 41a and 41b present data at two axial location for the numerical DNS model. Thirdly, the classical log-law is presented here and not the new law to validate the numerical results because the new law should be employed in the center of vortex region where the radial velocity component is practically negligible, and the chosen PIV height is nearer to the inward region instead of the center of vortex region. Finally, in the Figure 44 $\epsilon_{innerwall} = u_{\tau i}^4/\nu$, where $u_{\tau i} = \sqrt{\tau/(\rho 2\pi r_i^2 h)}$, is estimated using the DNS moment data.

The tangential velocity component (Figure 41a) is well predicted by the DNS model especially in the boundary layer; in addition, the difference between the axial heights is negligible which implies that this coarseness of mesh spacing in the axial direction has little impact on the tangential velocity component. In the bulk zone, between R_b=0.1 to 0.9, in agreement with Bilson e Bremhorst (2007), the numerical model does not accompany the phenomenon of small and steady increase through-out the bulk zone, as in the case of experimental results (SMITH; TOWNSEND, 1982; KOBAYASHI et al., 1990) and Figure (41a), but only till R_b=0.4. Kobayashi et al. (1990) stated that this phenomenon is because of uniformity in the circumferential velocity, in which the velocity profiles apart from the ones in the outward and inward region are very similar to the one in the center of vortex region, which in turn is caused by convection of the secondary flow. In-fact, none of the numerical studies (CHUNG; SUNG, 2005; BILSON; BREMHORST, 2007; PIRRO; QUADRIO, 2008; PONCET; HADDADI; VIAZZO, 2011; OGUIC; VIAZZO; PONCET, 2013; FRIESS; PONCET; VIAZZO, 2013) demonstrated the capability of

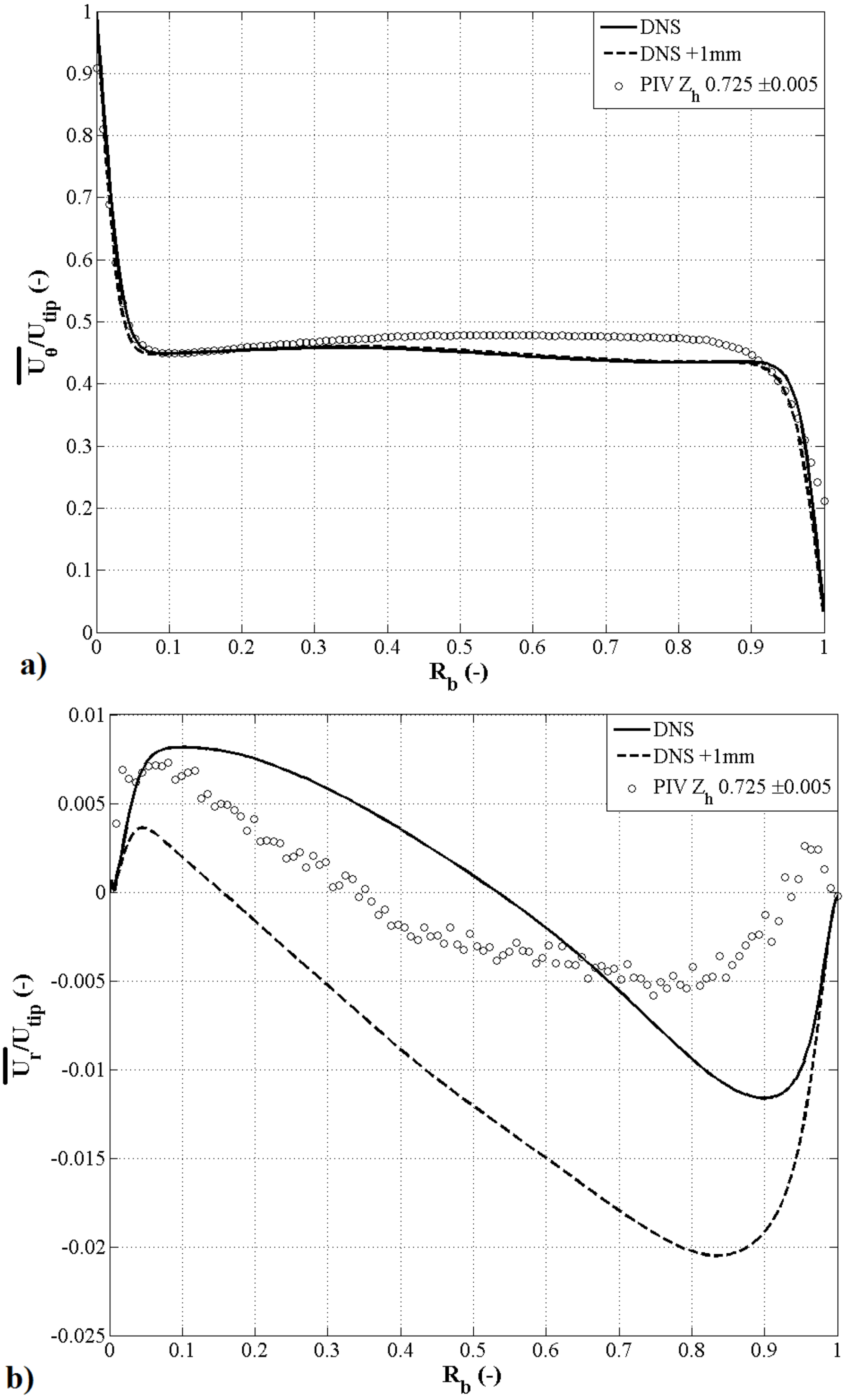

Figura 41 – Validation of the numerical DNS model with the PIV results of dimensionless mean tangential (a) and radial (b) velocity components.

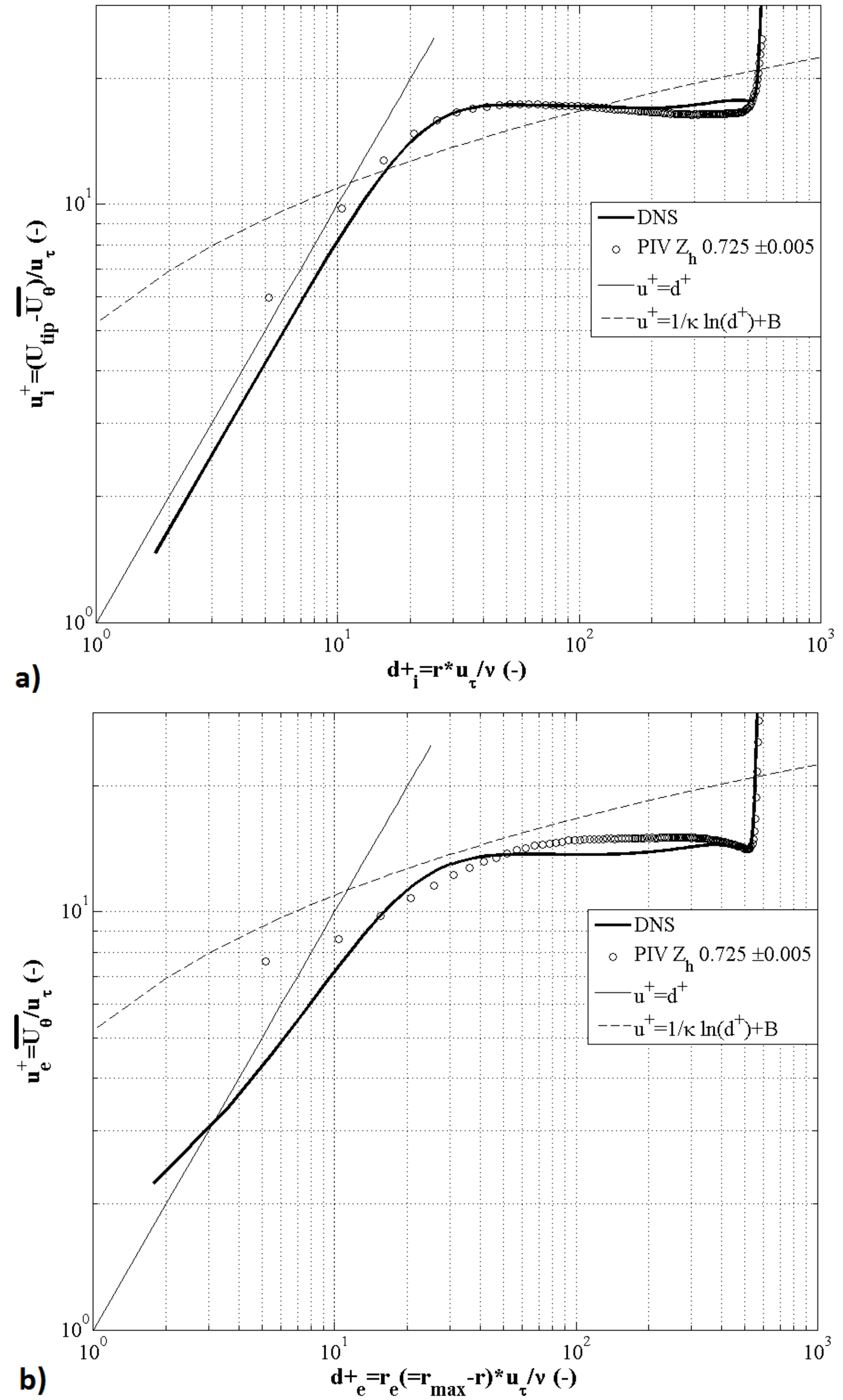

Figura 42 – Validation of the numerical DNS model with the PIV results of the log-law profiles for the tangential component at the inner (a) and outer (b) boundary layers. The $\kappa = 0.4$ and B $= 5.2$ is used in the log profile.

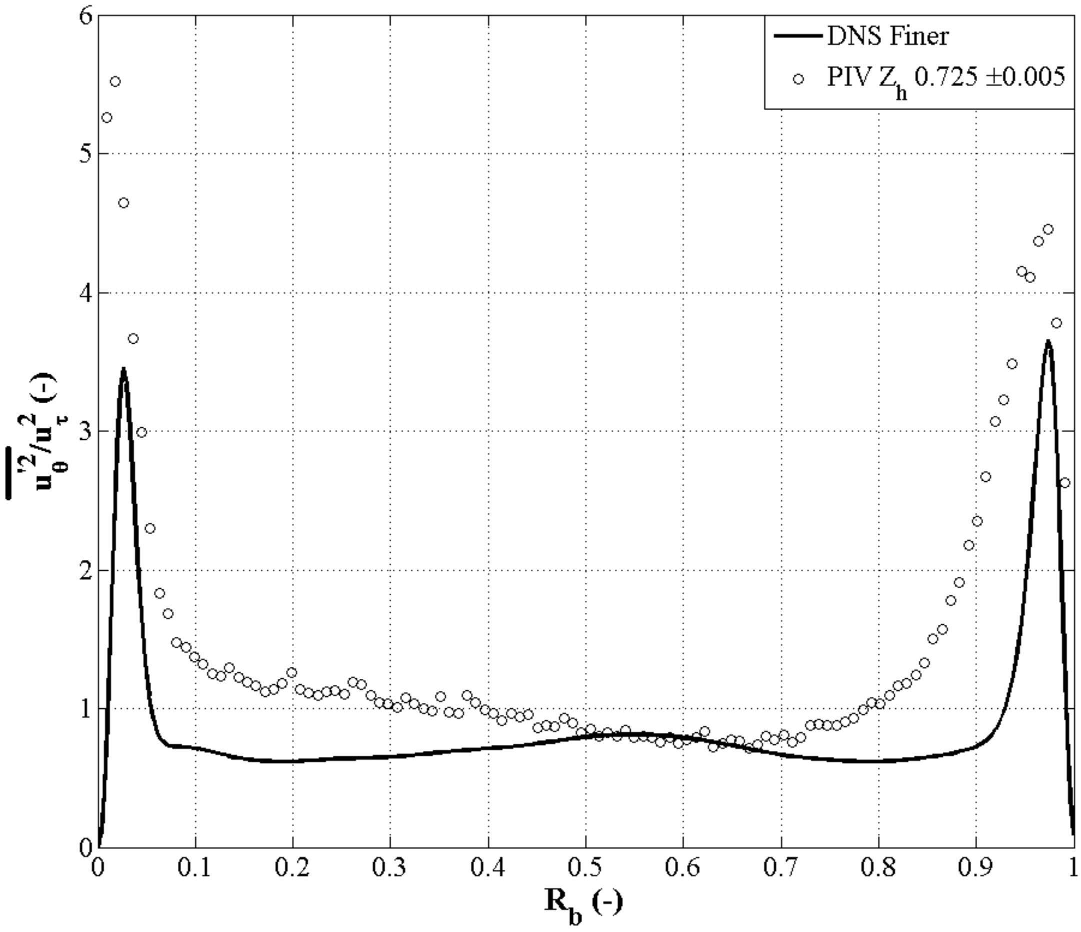

Figura 43 – Validation of the numerical DNS model with the PIV results of dimensionless mean squared fluctuating tangential velocity component.

the various numerical models to capture this phenomenon exhibited by experimental methods. In the case of the radial component, though the magnitude is less than 3 % of the tangential component and the shape is well predicted by the numerical model, the maximum difference between the two axial heights is approximately 25 %. In order to better capture the radial component reduction in the axial mesh size to 0.5 or perhaps to 0.25 mm is required, implying doubling or quadrupling, respectively, the total number of nodes, which is impractical presently to implement with the available computational resources and, in turn, time.

The log-law profiles for the inner (Figure 42a) and outer (Figure 42b) boundary layers shows different behavior from each other. Both inner and outer velocity profiles are normalized with appropriate u_τ, which is estimated from the global torque estimations of the numerical model, and for the PIV estimations, as there is no experimental torque data available, the DNS estimations are used. It should be remembered that u_τ is the average of the whole axial domain and not local, which can cause imperfect matching (HUISMAN et al., 2013). As mentioned by Huisman et al. (2013), the velocity profile follows u+=d+ in the viscous sub-layer (1<d+<10), which is evident from the numerical

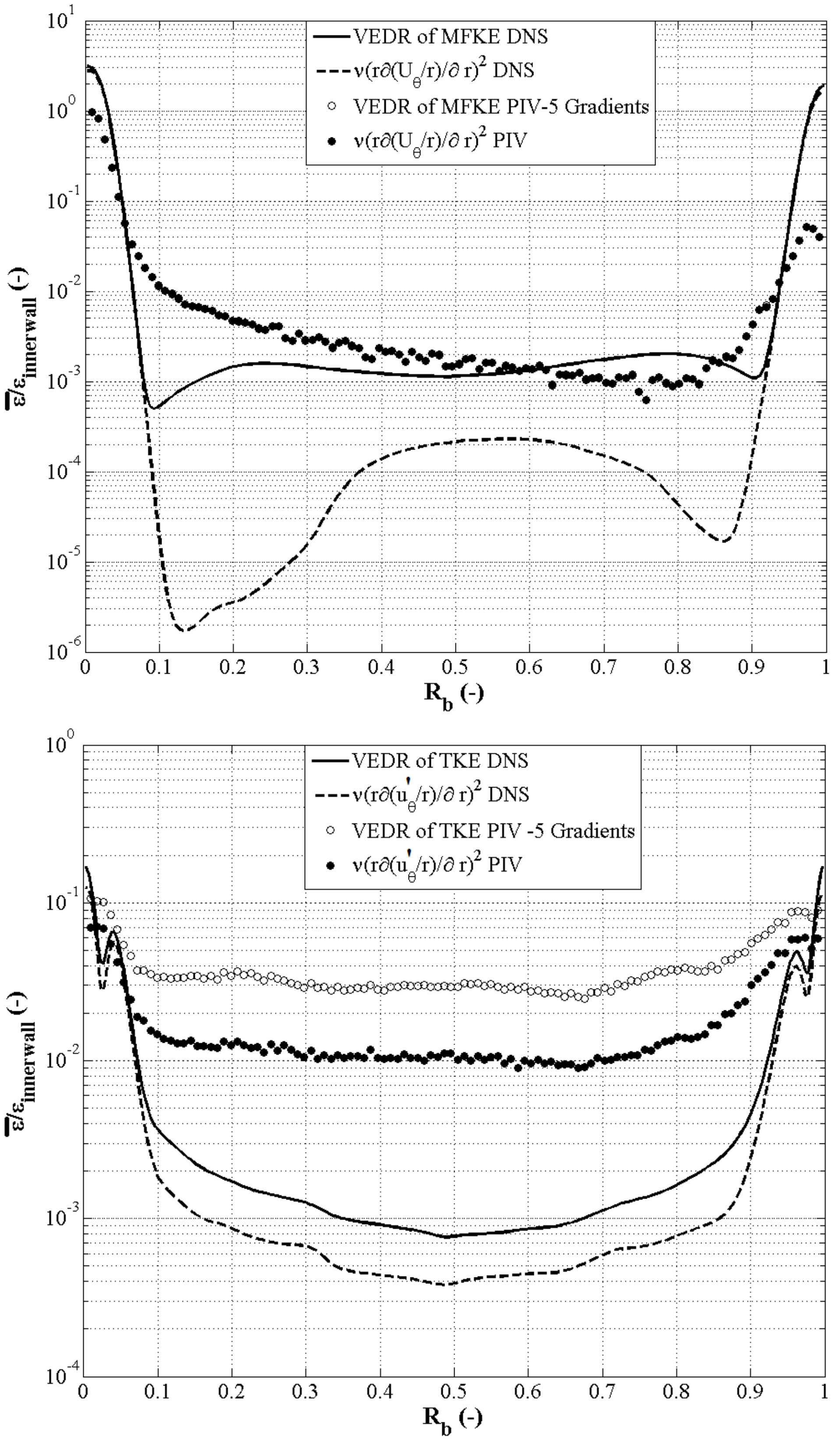

Figura 44 – Validation of the numerical DNS model with the PIV results of the VEDR of mean flow (a) and turbulence (b) kinetic energy.

and PIV estimations in the inner boundary layer. Viscous wall layer is much thicker in the inner boundary layer compared to the outer boundary layer, as the deviation from the u+=d+ profile for the outer boundary layer is quicker in comparison to the inner boundary layer, in accord with the observations of (BILSON; BREMHORST, 2007).

Proceeding towards the squared tangential velocity component (Figure 43), it can be observed that qualitatively the numerical model estimate it well. In the boundary layer of the inner cylinder, the DNS model estimates the maximum by around 60 % of the PIV; while, towards the boundary layer of the outer cylinder the estimation improves significantly in comparison to the inner wall. In the bulk zone, the estimation by the numerical model is much better compared to the boundary layer, but still comparatively under-predicting. Chung e Sung (2005), Poncet, Haddadi e Viazzo (2011), Oguic, Viazzo e Poncet (2013) also observed similar results in the validation of their numerical models in both the boundary layer and bulk zone.

For the VEDR of the mean flow kinetic energy (Figure 44a), it can be seen that the numerical model predicts the magnitude and the structure well in comparison with the experimental PIV estimations, especially in the boundary layer where the estimation is even comparatively higher. The VEDR decreases rapidly and remains practically in the vicinity of 0.001 through out the bulk zone for the DNS model; in contrast to the PIV method, where the VEDR decreases gradually from the inner wall towards the outer wall. It should be remembered that the PIV estimations are based on only five gradients in comparison to the 12 gradients for the DNS model; additionally, the spatial resolution of 136 μm remains constant through-out the grid structure for the PIV in comparison to the DNS model where the grid structure varies with least value being towards the walls (47 μm) and the highest being towards the center of the gap-width (184 μm). In the bulk zone, the spatial resolution of the DNS becomes coarser in comparison to the PIV, and evidently the estimations of the PIV method are slightly higher.

The impact of this varying grid structure can also be seen in the estimation of the $(r\partial(U_\theta/r)/\partial r)^2$ gradient, which can be seen as the principal component of the five-gradient viscous VEDR through-out the reactor for the PIV estimations. While, in the case of the DNS model, this gradient is the principal component in the boundary layer area only and in the bulk zone its over an order lower; implying that in the bulk zone, the gradients of the axial direction and velocity component must be of significant importance. These various aspects when joined together clearly indicates under-estimation of the VEDR of mean flow kinetic energy by the DNS model and that the mesh requires further refinements in the radial direction for a more accurate estimation of the VEDR.

The VEDR of turbulent kinetic energy (Figure 44b) also suffers significantly from the comparatively coarser grid structure in the bulk zone for the DNS model. The maximum near the wall is well predicted but the discrepancy increases towards the bulk zone, where the difference is more than 10 times. Although, the difference between the mesh structures of the DNS and PIV is just around 30 %, this significant under-estimation in the bulk zone of the VEDR of turbulent kinetic energy in comparison to the VEDR of mean flow kinetic energy is due to the fact that the magnitude of the VEDR of turbulent kinetic energy is practically an order higher in the bulk zone in comparison to the VEDR of mean flow kinetic energy. In addition, the increase in the VEDR nearer to the kolmogorov scale is much more drastic in comparison to away from the kolmogorov scale as it follows a power law of the type: $\epsilon/(normalisingfactor) = A(spatialresolution/GlobalKolmogorovscale)^{-B}$; where A and B are coefficients of the power law over the chosen area, as shown by Delafosse et al. (2011). They found that if the spatial resolution decreases by 50 %, the corresponding increase in the VEDR of turbulent kinetic energy is over 220 % for spatial resolution values approaching the global Kolmogorov scale.

In similar sense, the estimation of the VEDR of turbulent kinetic energy for the PIV measurements must be under-predicting as well, especially in the boundary layer area, considering the fact that the spatial resolution is of 136 μm in comparison to the global Kolmogorov scale of 52.5 μm. The global Kolmogorov scale value indicates that its value must be smaller in the boundary layer area and comparatively higher in the boundary layer area. This was the idea that was kept in the back of the mind when the varied radial mesh was created for the DNS model. This mesh structure definitely requires further refinements not only in the radial direction but also in the axial and tangential directions, which would mean something above 100 million nodes for this current configuration, impractical in the present case scenario due to limited computational resources.

In the case of the PIV, using a higher overlap ratio would have given a smaller spatial resolution, but this smaller spatial resolution is just the manipulation of the base structure in order to increase the number of data points, therefore does not represent the true picture of a smaller spatial resolution. Moreover, smaller spatial resolution of the order of 50 μm would require particles of much smaller size of 1-2 μm, which are extremely costly, to achieve good concentration of particles in the fluid for the corresponding grid structure. To avoid these details, the base overlap ratio of 0 % was employed in this study. Using a 32 Mpixels camera would have reduced the resolution by half but would also require smaller sized particles. This study presents the smallest spatial resolution for both the DNS and PIV study for the Reynolds number of 17900. Additionally, as per authors knowledge, validation of the numerical model based on this VEDR estimation has not been conducted before-hand for the TVB.

3.4 Conclusions

The main aim of this chapter was to validate the DNS model estimations with experimental PIV results within a certain degree of acceptance.A detailed description of the different turbulence models which are employed in this study is also presented. Additionally, the grid and time-step dependence aspects of the LES-WALE model are presented in comparison with the DNS model.

The grid structure was found to require improvements: firstly, in the axial grid as difference of 25 % in the magnitude between two values of the radial velocity components at two consecutive axial heights 1mm apart was observed; secondly, in the bulk zone because mesh size was found to be slightly on the courser side in the bulk zone in comparison to the Kolmogorov's micro-scale, and finally in the tangential direction as well due to grid spacing of only 1.96 cm. These enhancements may not be feasible on present day desktop computers, however considering the speed of advancements in the computational resources, a completely grid-independent mesh should be available with reduced time within a decade thereby reducing the limitations due to mesh attained here.

Although, the ideal scenario of 100 % concordance between the numerical and experimental study is not seen, the qualitative comparison between the two is completely acceptable, due to good prediction of the structure and shape of the flow within the TVB. Quantitatively, the mean velocity predictions of the DNS are in good agreement with the PIV data; whereas, the fluctuating components of the velocity and the VEDR of turbulent kinetic energy are underestimated with major under predictions being in the boundary layer area for the fluctuating components and in the bulk zone for the VEDR of mean flow and turbulent kinetic energy. Overall, these numerical results can be considered validated due to the clear evidence of good amount of concordance indicating that results are not hypothetical, especially the good qualitative comparison, between the numerical and experimental results.

4 Turbulence models

In this chapter the results of different turbulence models mentioned in the Chapter 3 are presented as a comparison with the DNS model. These results will be presented for the mean and fluctuating velocity components and their gradients which in turn generate the VEDR of mean flow and turbulent kinetic energy. In addition, the methods to estimate the anisotropy and vortex identification will be presented. Most of these results will be presented in three principal regions of the Taylor-Vortex: Outward, Center of Vortex and Inward.

4.1 Vortex identification

Figure 45 presents the Taylor's vortexes using the λ_2-definition method for identifying the vortex, first presented by Jeong e Hussain (1995), and a detailed presentation of one Taylor's vortex pair for the DNS model. The single vortex pair for the DNS model is located between z= 0.105 and 0.137 m which is equivalent of 34 mm or $\approx$ 2 times the size of gap width, and with clear representation of the two inward, one outward and two center of vortex flow profiles. The outward flow is located around 0.121 m with two inward flows located at the two extremities of the vortex pair, and the two center of vortexes being located around the middle of outward and inward flow profiles. The outward region is marked with strong flow moving from the inner cylinder towards the outer, and the vice-versa holds for the inward region.

Jeong e Hussain (1995) found that λ_2, the median of the three eigenvalues of $S^2 + \Omega^2$, correctly represented the geometry and topology of the vortex cores among four definitions for a large variety of flows. Escudie (2001) used this method to identify vortex in a tank stirred by Rushton turbine and also found that this approach is better to identify, characterize and measure the trajectory of a vortex in relation to other methods such as local pressure minimum and streamlines. Jeong e Hussain (1995) considered that the local pressure minimum caused by vortical motion can only be detected by $S^2 + \Omega^2$, and defined "a vortex core as a connected region with two negative eigenvalues of $S^2 + \Omega^2$". Assuming that the eigenvalues are λ_1, λ_2 and λ_3, and that $\lambda_1 \geqslant \lambda_2 \geqslant \lambda_3$, then the new definition implies that within the vortex $\lambda_2 < 0$. The details of this method can be seen in the original article of Jeong e Hussain (1995) and also in the PhD thesis of Escudie (2001).

The λ_2-definition method has been used to compare the different turbulencs models with the DNS model through Figures 46, 47 and 48. To keep the number of figures in check, the secondary vortex pair for other models has not been shown here. Instead, the λ_2-definition method will help in a better comparison of these secondary vortexes in terms

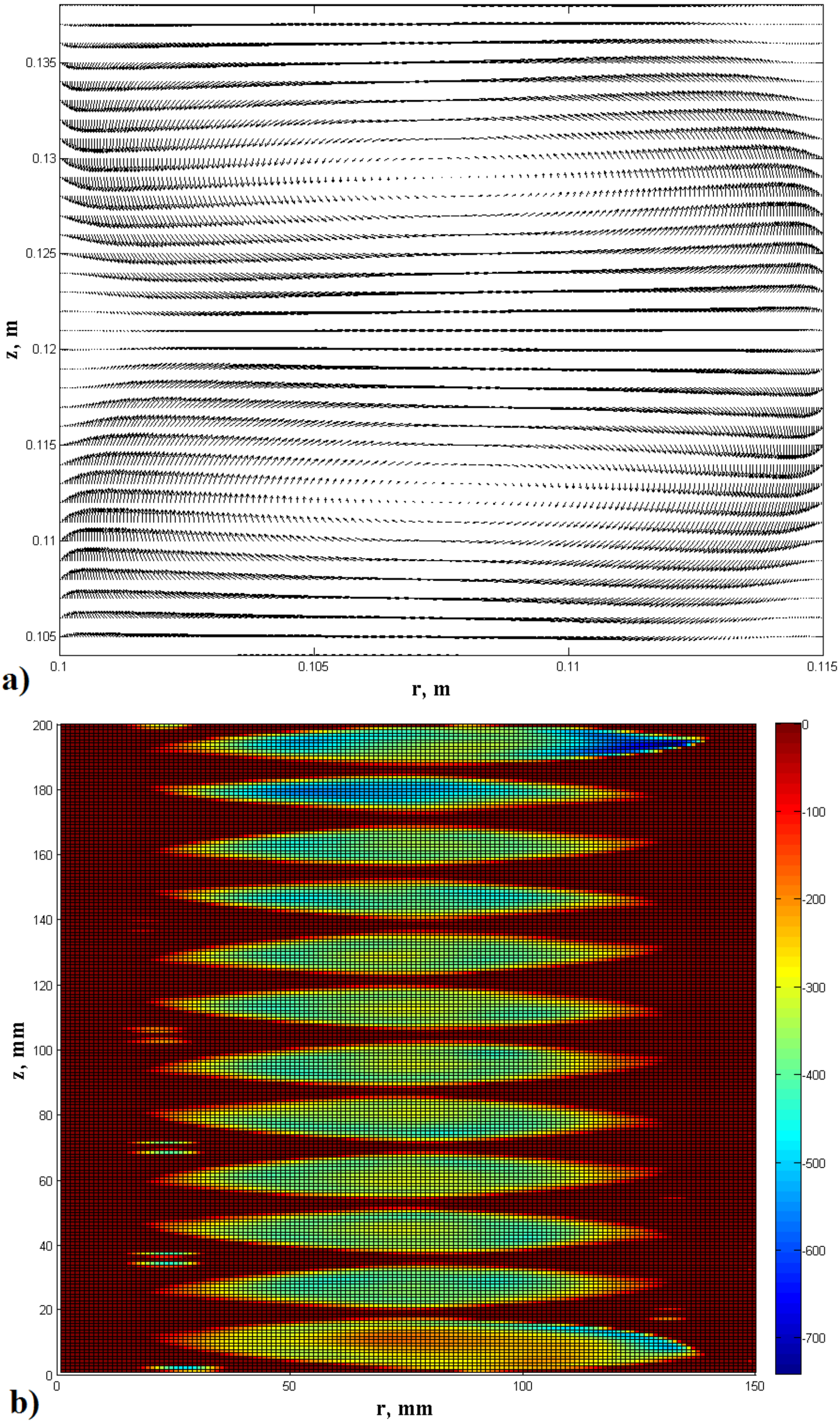

Figura 45 – Identification of the Taylor's vortexes through λ_2 (a) and a pair of secondary Taylor's vortexes (b) for the DNS model.

of their size and structure for the presented turbulence models.

For the DNS model, all vortexes but the ones on the bottom and top of cylinders are of similar size, here size refers to the value of λ_2, and structure. The vortexes on the top and bottom of the cylinders are opposite of each other in terms of the magnitude of λ_2; The one on the bottom is of the smallest magnitude whereas the one on the top has the highest magnitude among all of the vortexes. There are six pair of vortexes in the gap width of 15 mm and height of 200 mm, leading to approximately double the size of gap-width for each vortex pair.

The LES-WALE, k-ϵ, RSM and SAS-SST turbulence models also present six pair of vortexes; while, the LES-Smagorinsky and SST turbulence models presents 5 and 7 number of vortexes, respectively. This means that in comparison to the DNS model, the width of a Taylor vortex pair will be thicker for the LES-Smagorinsky model and thinner for the SST model. In-fact, for the LES-Smagorinsky model the width of each vortex pair is equivalent of 40 mm, where all vortex pairs are of practically same size (Figure 46b). In all other turbulence models, the size and structure of the top and bottom vortex pairs is different from the rest of the vortex pairs. The RSM turbulence model presents the worst comparison with the DNS model for the size, structure and magnitude values.

Apart from the top and bottom vortex pairs, the λ_2 magnitude value remains around 400 for the DNS and LES models. In the case of the k-ϵ, SST and RSM model, there is huge variation in the magnitude values most probably caused by the excessive damping of turbulence by the RANS based models (MENTER, 2009). An improvement can be seen in the SAS-SST model, where the turbulence length-scale is improved by adjusting it to the directly resolved turbulence structures (MENTER; EGOROV, 2005).

4.2 Mean velocity flow field

4.2.1 Tangential velocity

The tangential component of the mean velocity is presented in the Figures 49, 50 and 51 at or closest to the outward, center of vortex and inward regions of a Taylor-vortex for the different numerical models. Kobayashi et al. (1990) and Bilson e Bremhorst (2007) also presented these three components in the above mentioned regions of a Taylor-vortex in their experimental, using a Pitot tube, and numerical-DNS results, respectively, and observed similar flow structures. The tangential flow is at its strongest in the outward region where the rotating inner cylinder imparts momentum to the flow to move from the inner cylinder towards the stationary outer cylinder. Whereas, in the inward region the flow is at its weakest due to deceleration of the fluid in the outer wall where the fluid is transported by convection (KOBAYASHI et al., 1990).

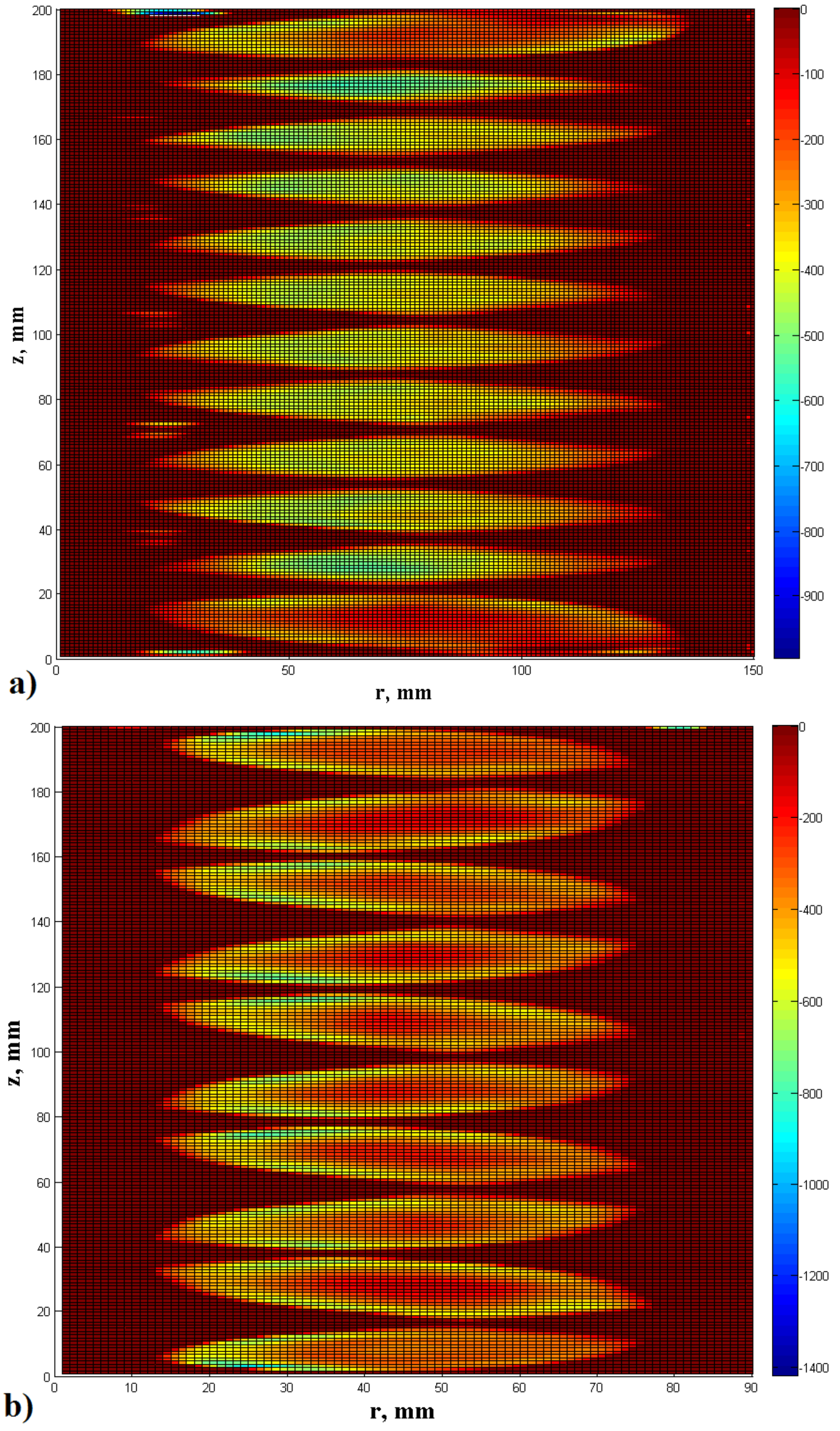

Figura 46 – Identification of the Taylor's vortexes through λ_2 for the LES-WALE (a), and LES-Smagorinsky (b) models.

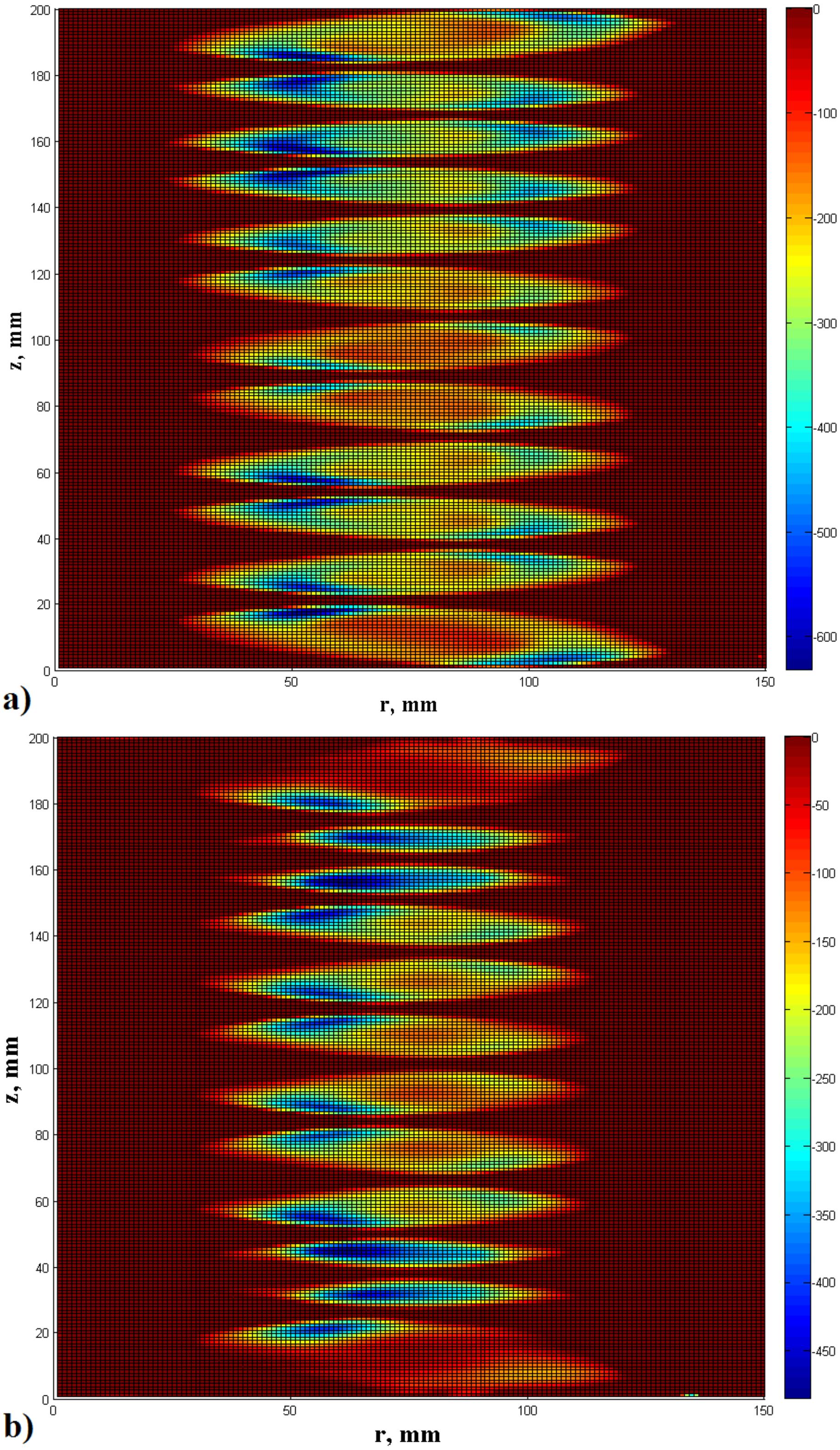

Figura 47 – Identification of the Taylor's vortexes through λ_2 for the k-ϵ (a) and RSM (b) models.

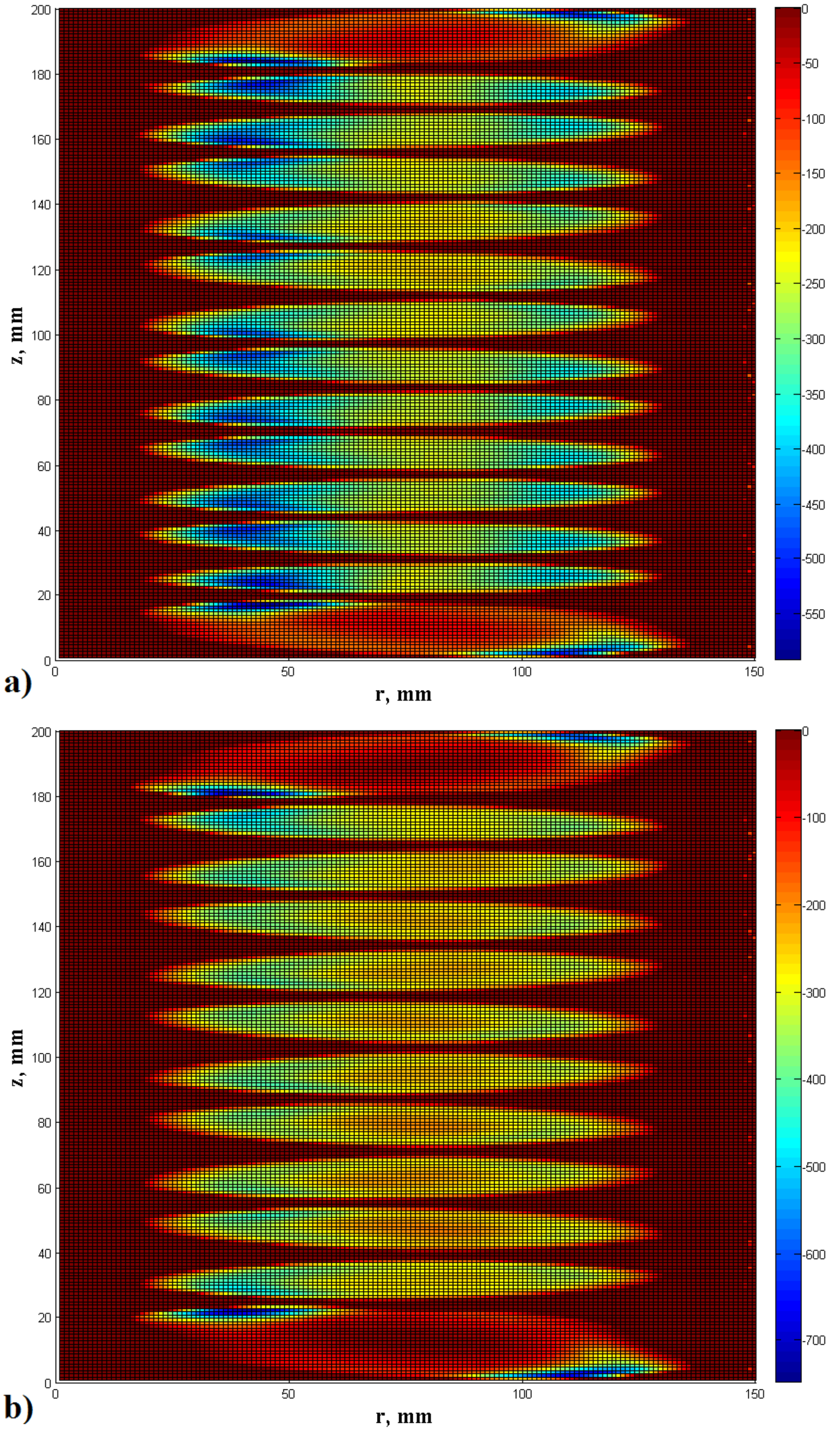

Figura 48 – Identification of the Taylor's vortexes through λ_2 for the SST (a), and SAS-SST (b) models.

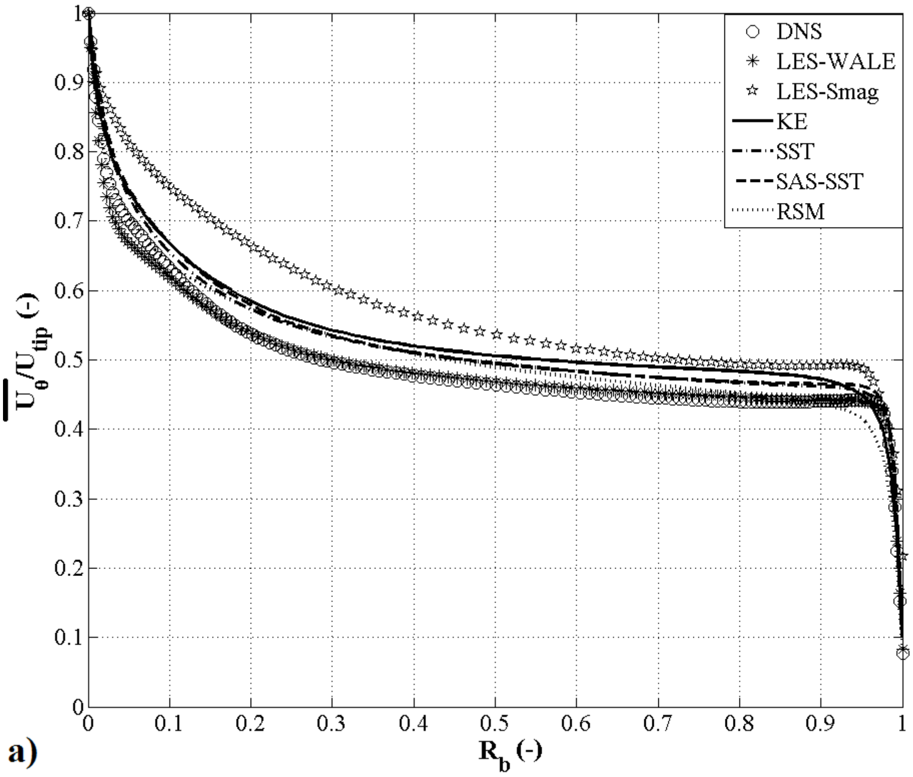

Figura 49 – Radial profiles of the tangential velocity component near the outward region of a Taylor vortex.

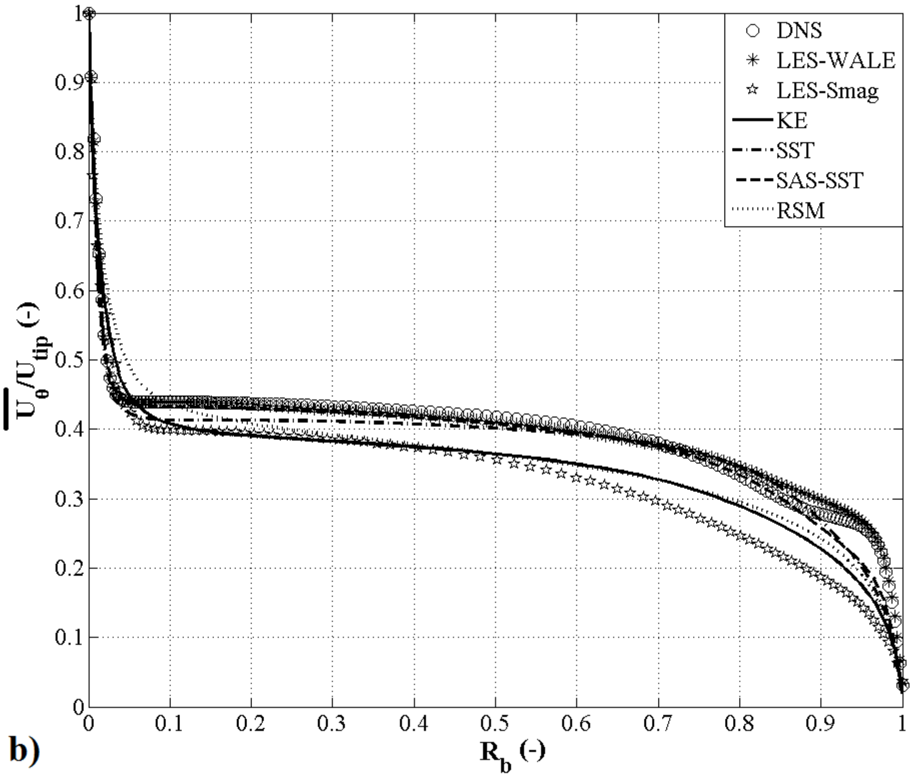

Figura 50 – Radial profiles of the tangential velocity component near the inward region of a Taylor vortex.

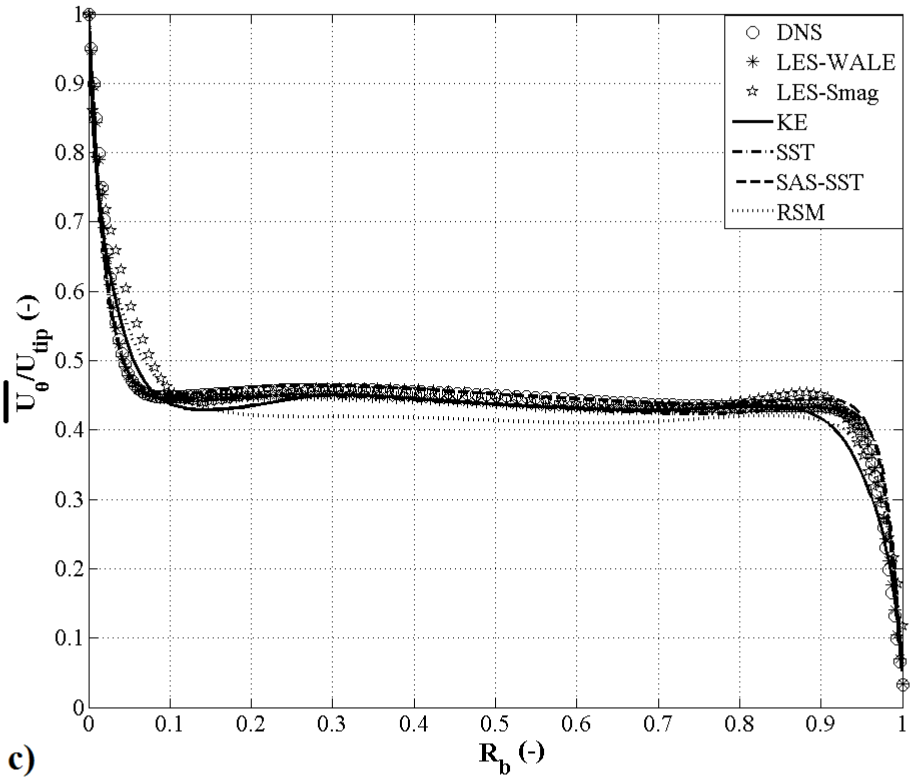

Figura 51 – Radial profiles of the tangential velocity component near the center of vortex region of a Taylor vortex.

An interesting point to observe is that the tangential component of the velocity is at-least 70 % of the total flow considering that the maxima for both axial and radial components is only around 15 % of the mean flow. The PIV experimental results in accord with Kobayashi et al. (1990) showed that both axial and radial components achieved a maximum of only around 10 % of the flow. Moreover, the steepest gradients for the tangential velocity lie in the boundary layer. This could imply that in the boundary layer more than 70 % of the kinetic energy and its dissipation must be represented by only the tangential component of the velocity and its gradients. Hence, for a better estimation of the kinetic energy and its dissipation requires finest grid structure on the radial direction to capture the propagation of tangential flow in-between the cylinders, especially in the boundary layers.

Among the different turbulence models, the worst comparison with the DNS model was for the LES-Smagorinsky model. It over-predicted the magnitude in the outward region and under-predicted in the inward region. In all the three regions, the LES-WALE model reproduced extremely well the profile structures and magnitudes estimated by the DNS model followed by the SAS-SST and SST model with very similar predictions. The predictions of the k-ϵ and RSM model were comparatively poor in the outward and inward region in comparison to the other RANS based models. In the center of vortex region where all turbulence models predicted similar structures, the RSM model was comparatively under-predictive in the bulk zone.

The radial profile of the tangential component showed that within 80 % of the gap-width between $R_b = 0.1$ to 0.9, the magnitude of the velocity is constant at around 50 %. This aspect is of great consequence because in the case of animal cell cultures, the cell lines within the TVB will spend most of the time in the vicinity of these values of similar and weak magnitude, and only a fraction of its times will be spent near the high gradients located near the wall. Additionally, the viscous layers in the region of high gradients near the wall will further propel the cell cultures towards the bulk zone having uniform flow.

4.2.2 Radial velocity

The radial component of the mean velocity is presented in the Figures 52, 53 and 54 at or closest to the outward, center of vortex and inward regions of a Taylor-vortex for the different numerical models. Kobayashi et al. (1990) observed that the axial and radial velocity components achieved a maximum of only around 10 % of the mean flow, whereas in this study and in Bilson e Bremhorst (2007)'s work a maximum of approximately 15 % for these two components is achieved. The radial velocity achieves this maximum in parabolic shapes in the outward, in the upward direction, and inward regions, in the downward direction. The upward and downward parabolic shapes of the radial velocity are due to opposite direction of flow in the outward and inward region, respectively. In the outward region, the flow is from the inner cylinder towards outer and vice-versa in the inward region.

As in the case of the tangential velocity, the estimations of the LES-Smagorinsky models were over-predictive in comparison to the rest of the models in the outward and inward region. While, the RSM models estimations were under-predictive in these two regions. The LES-WALE model captured extremely well the flow structure exhibited by the DNS model followed by the SAS-SST, SST and k-ϵ models. In the center of vortex region, the radial velocity is near zero for all the turbulence models.

4.2.3 Axial velocity

In the Figures 55, 56 and 57, the axial component of the mean velocity is presented at or closest to the outward, center of vortex and inward regions of a Taylor-vortex for the different numerical models. It should be noted that the structure of the axial velocity is opposite to that presented in the research work of Kobayashi et al. (1990). The reason is that the single vortex from which the data is represented in these results is from the vortex with anti-clockwise rotation, whereas the data was taken from the vortex rotating in clockwise direction by Kobayashi et al. (1990). The rotation direction of the vortex can be judged by the shape of the axial velocity in the center of vortex region, as explained by

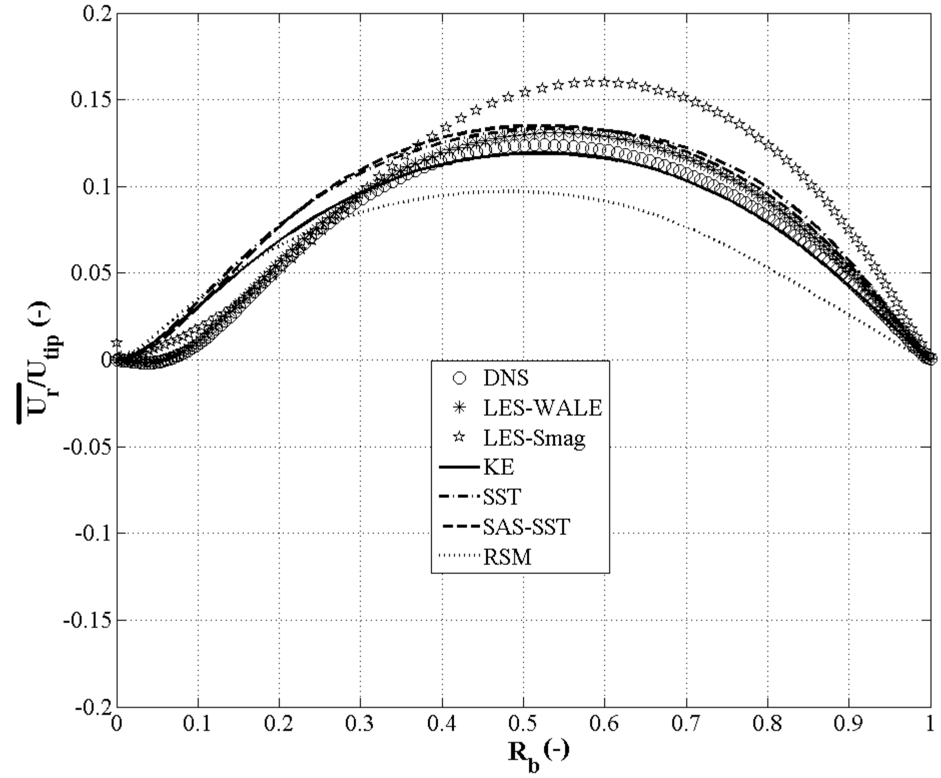

Figura 52 – Radial profiles of the radial velocity component near the outward region of a Taylor vortex.

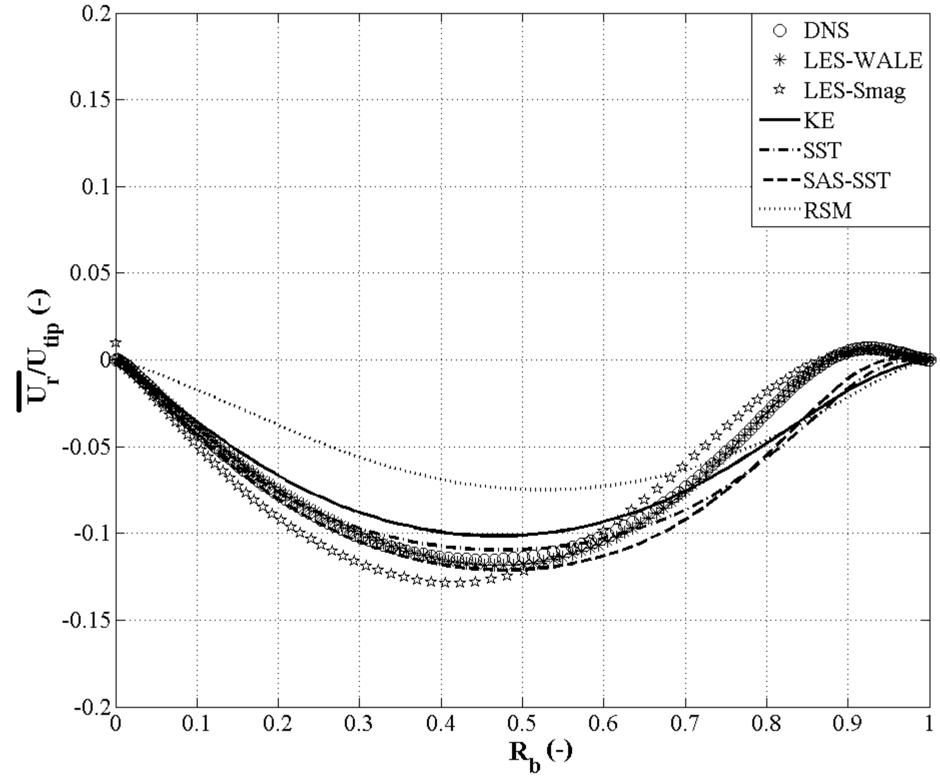

Figura 53 – Radial profiles of the radial velocity component near the inward region of a Taylor vortex.

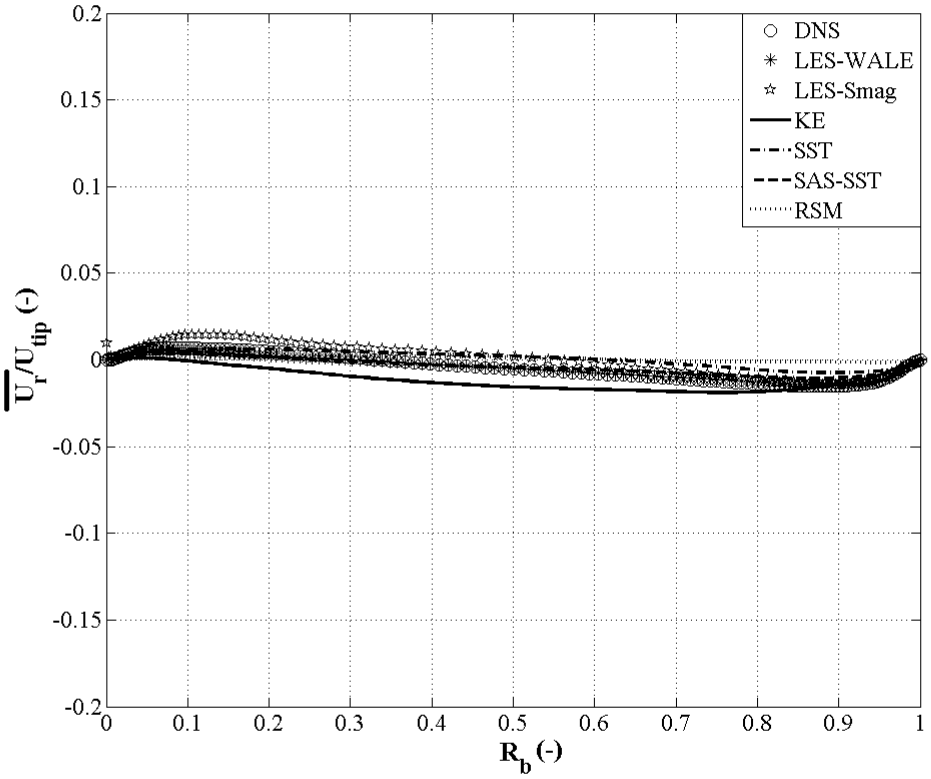

Figura 54 – Radial profiles of the radial velocity component near the center of vortex region of a Taylor vortex.

Kobayashi et al. (1990). In the axial velocity flow, the maximas lie near the walls, one of positive magnitude and another negative, in the center of vortex region, and in the bulk zone there is a linear distribution slanting from the positive to the negative maxima. If the positive maxima lies near the inner cylinder, then the rotation is clockwise otherwise its anti-clockwise. In complete agreement with Kobayashi et al. (1990) and Bilson e Bremhorst (2007), the axial velocity is nearly zero in both the outward and inward regions.

As the axial velocity is near zero in the outward and inward region, all turbulence models estimations were similar. The small differences between these models for the small magnitude values is most probable due to the poor grid structure of 1 mm in the axial direction. The LES-Smagorinsky model was over-predicting in the center of vortex region, while the RSM model was under-predicting. Again the LES-WALE model best captured the DNS estimations followed by the SAS-SST, SST and k-ϵ model.

4.2.4 Log law profiles of tangential velocity

In order to better understand the boundary layer, the classical log-law profiles for the inner (Figure 58a) and outer (Figure 58b) boundary layers are presented for the mean of the whole axial domain of the tangential velocity component. Both inner and outer velocity profiles are normalized with appropriate u_τ, which is estimated from the global torque estimations of each respective numerical model. As mentioned in Chapter 3, it

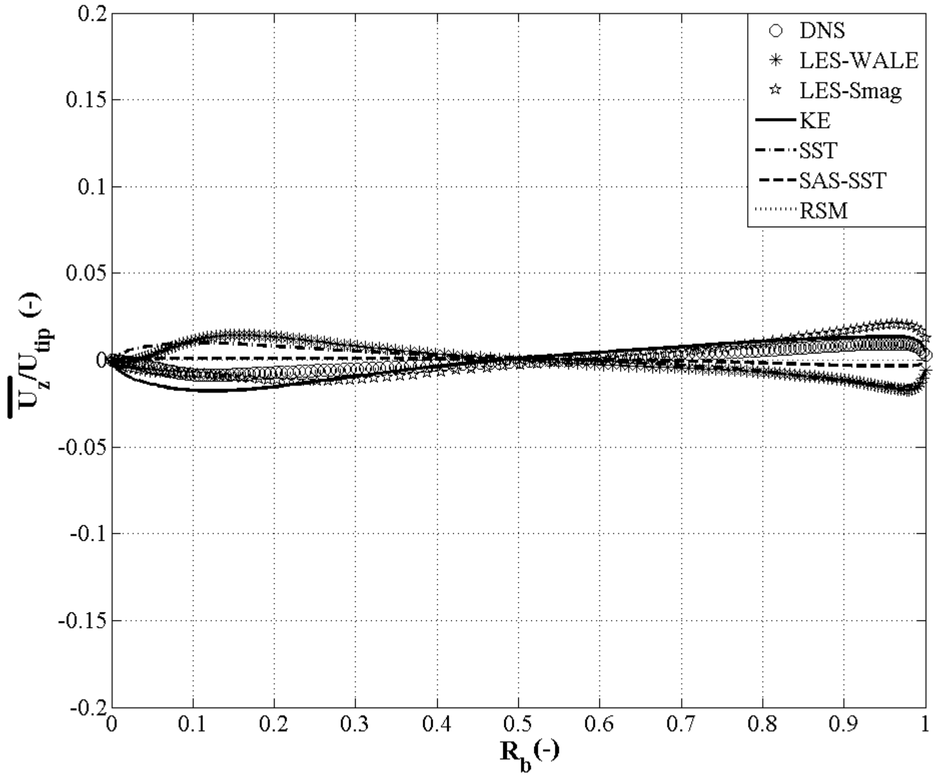

Figura 55 – Radial profiles of the axial velocity component near the outward region of a Taylor vortex.

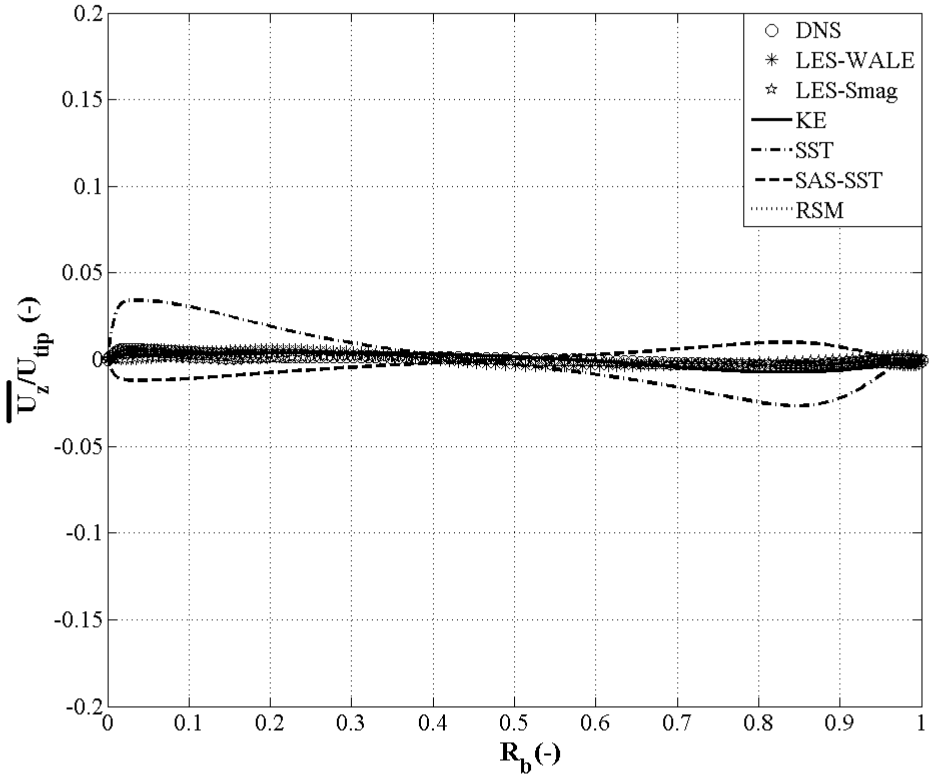

Figura 56 – Radial profiles of the axial velocity component near the inward region of a Taylor vortex.

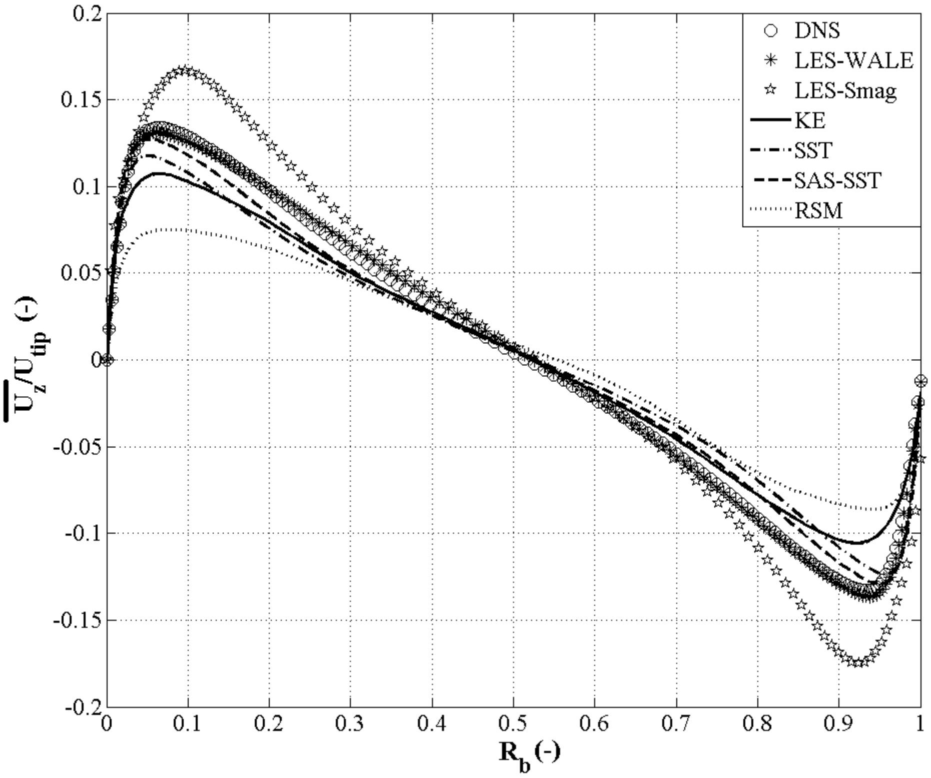

Figura 57 – Radial profiles of the axial velocity component near the center of vortex region of a Taylor vortex.

should be remembered that u_τ is the average of the whole axial domain and not local, which can cause imperfect matching (HUISMAN et al., 2013). As mentioned by Huisman et al. (2013), the velocity profile follows u+=d+ in the viscous sub-layer (1<d+<10), which is evident from the numerical estimations in the inner boundary layer. Viscous wall layer is much thicker in the inner boundary layer compared to the outer boundary layer, as the deviation from the u+=d+ profile for the outer boundary layer is quicker in comparison to the inner boundary layer, in accord with the observations of (BILSON; BREMHORST, 2007).

Among the different turbulence models, the estimations of the LES-WALE model were exactly the same as those of the DNS model in both the inner and outer boundary layers. The SAS-SST and SST model estimations were very similar and closely followed the DNS predictions, especially in the outer boundary layer area. The estimations of the k-ϵ, RSM and LES-Smagorinsky models were similar to each other but very different to those of the DNS model for both the magnitude and structure. The main reason behind such poor estimations for these three models is the over-estimation of the torque not only in comparison to the DNS model but also in comparison with the analytical estimations of the Wendt (1933). This aspect will be discussed in more detail in the power estimation section.

The classical log-law profile structure for the three regions is presented in the Figure

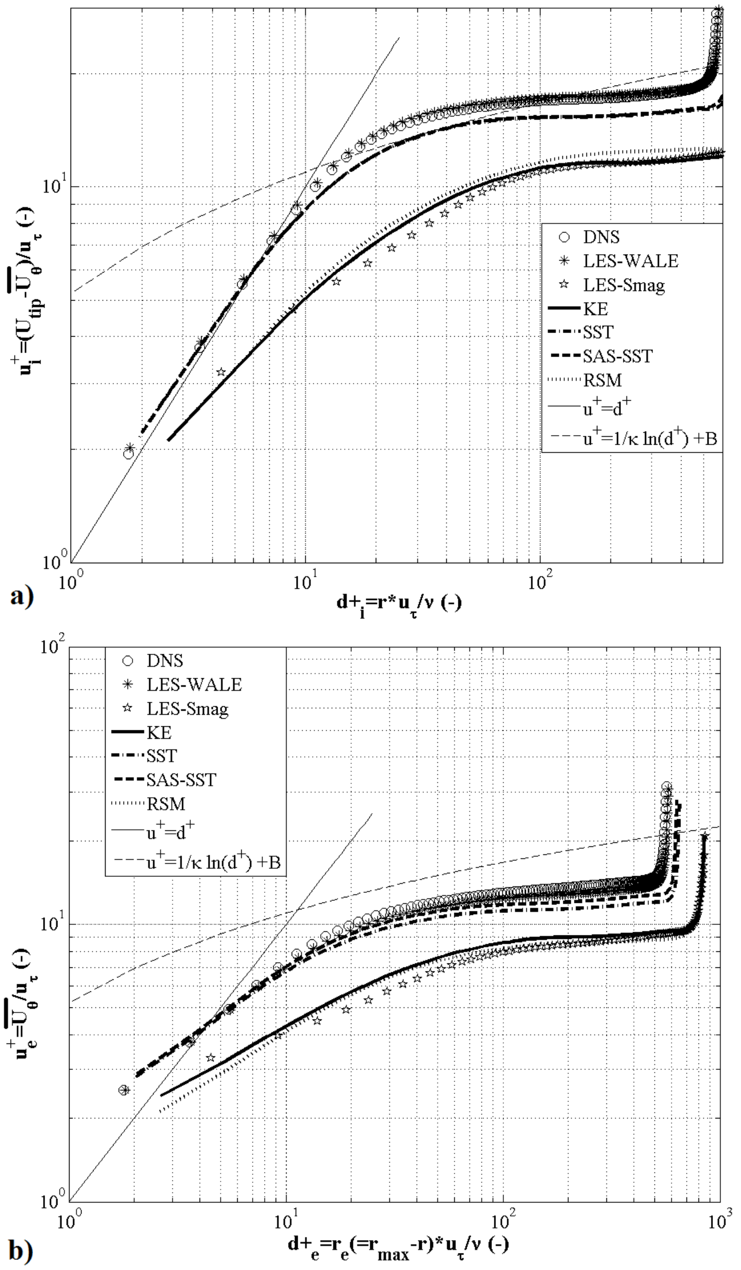

Figura 58 – Radial profiles of the log-law profiles of the axial mean of tangential velocity component for the inner (a) and outer (b) walls for the different turbulence models.

59 only for the DNS model to reduce the number of figures. Clearly in all regions and in both boundary layers, the velocity profile exhibits similar structure to that of u+=d+ at-least in the viscous sub-layer. The thickness of this layer behaves differently in different regions. The axially averaged profile resembles more closely to the center of vortex region, which provides further proof to the observation of (KOBAYASHI et al., 1990) that flow structures in a Taylor's vortex are mostly, apart from the ones in the outward and inward region, similar to the center of vortex region profile, which he cited as the phenomenon of uniformity in the circumferential velocity caused by the convection of the secondary flow. The outward region structure acquire a near parallel structure to the log-law profile in the inner boundary layer around d+>20; whereas, the inward region does the same in the outer boundary layer. This can be explained by the fact that the velocity flow is strongest in the outward region towards the inner cylinder thus leading to small viscous sub-layer. Similarly, a small viscous sub-layer is seen in the outer boundary layer for the inward region where the velocity flow is strongest near the outer cylinder.

4.3 Normal stresses

Figures 60, 61, 62, 63, 64, 65, 66, 67 and 68 present the radial profiles of the three fluctuating velocity components, tangential, radial and axial, near the outward, center of vortex and inward region of the Taylor vortex, respectively. These fluctuating components are presented in various formats in different studies, such as root mean square (rms) velocity fluctuations (CHUNG; SUNG, 2005; HOUT; KATZ, 2011; TOKGOZ et al., 2012; FRIESS; PONCET; VIAZZO, 2013), Reynolds stress tensor components (PONCET; HADDADI; VIAZZO, 2011; VIAZZO et al., 2012; OGUIC; VIAZZO; PONCET, 2013), and squared velocity fluctuations this study and (KOBAYASHI et al., 1990; BILSON; BREMHORST, 2007). Please note that though Kobayashi et al. (1990) presented the data as squared velocity fluctuations, they termed these as turbulence normal stress components. Furthermore, only Kobayashi et al. (1990) mentioned the regions of the Taylor-vortex at which the data was presented. In any case, a qualitative comparison with other studies can still be considered useful.

In the case of fluctuating tangential velocity, the flow structure of the tangential velocity is at its strongest in the outward region, in agreement with Kobayashi et al. (1990). In the inward region, the structure is opposite in nature to that in the outward region, i.e. stronger near the outer wall and decreasing progressively towards the inner wall through-out the bulk zone, though the magnitudes are relatively weaker. There are two local maximas of which one is near and the other further away from inner cylinder boundary, R_b=0.14, and the one towards the outer cylinder boundary is very close to the wall, in rapport with Kobayashi et al. (1990). Whereas, in the inward region the structure is opposite but with comparatively lower magnitude with one local maxima closer to

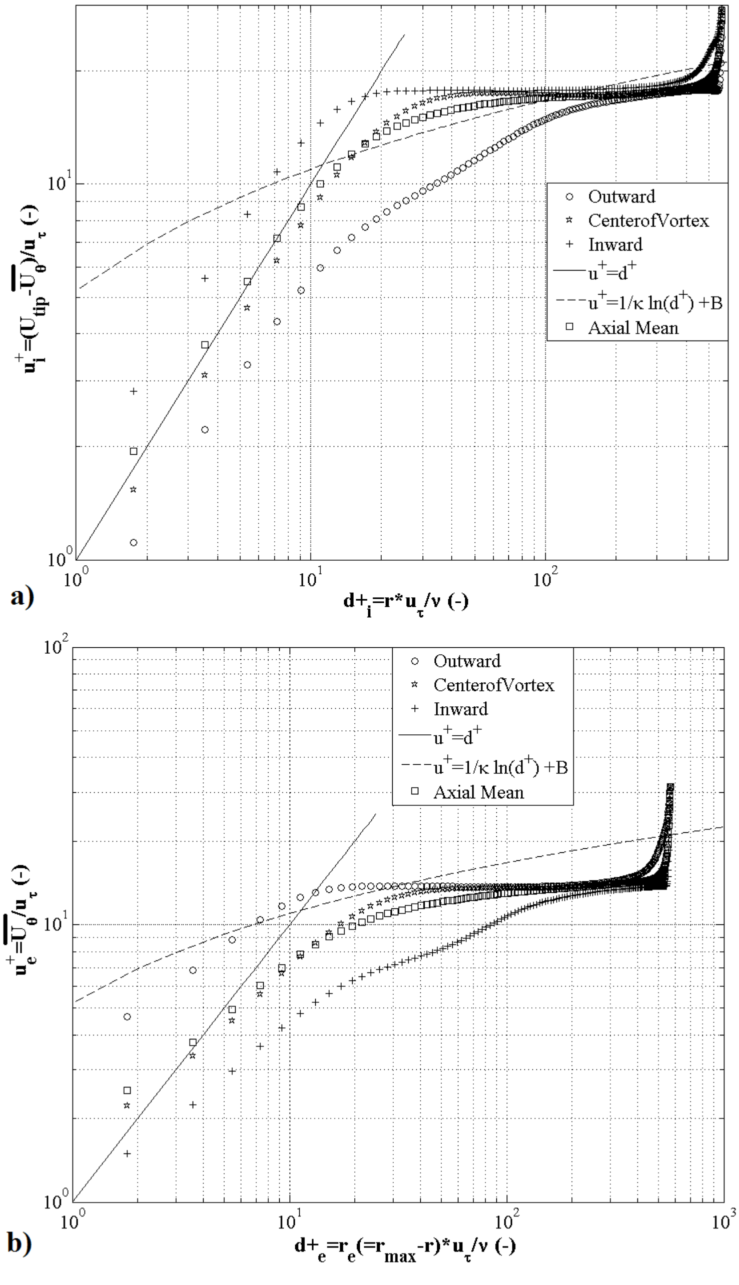

Figura 59 – Radial profiles of the log-law profiles for the inner (a) and outer (b) walls near the outward, center of vortex and inward regions of a Taylor vortex for the DNS model only.

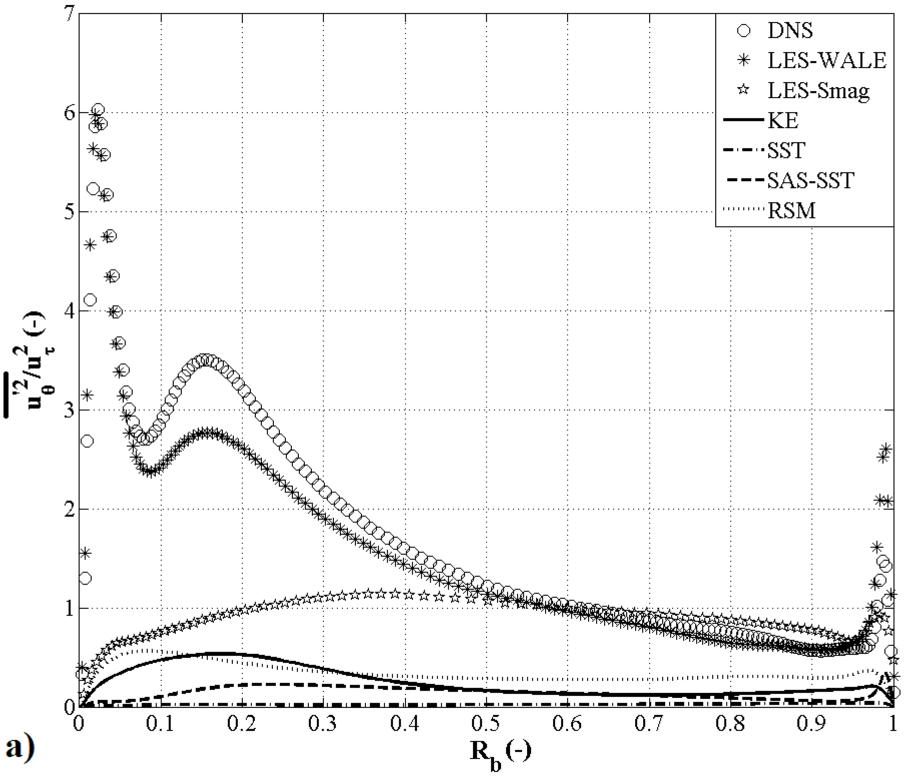

Figura 60 – Radial profiles of the tangential velocity component near the outward region of a Taylor vortex.

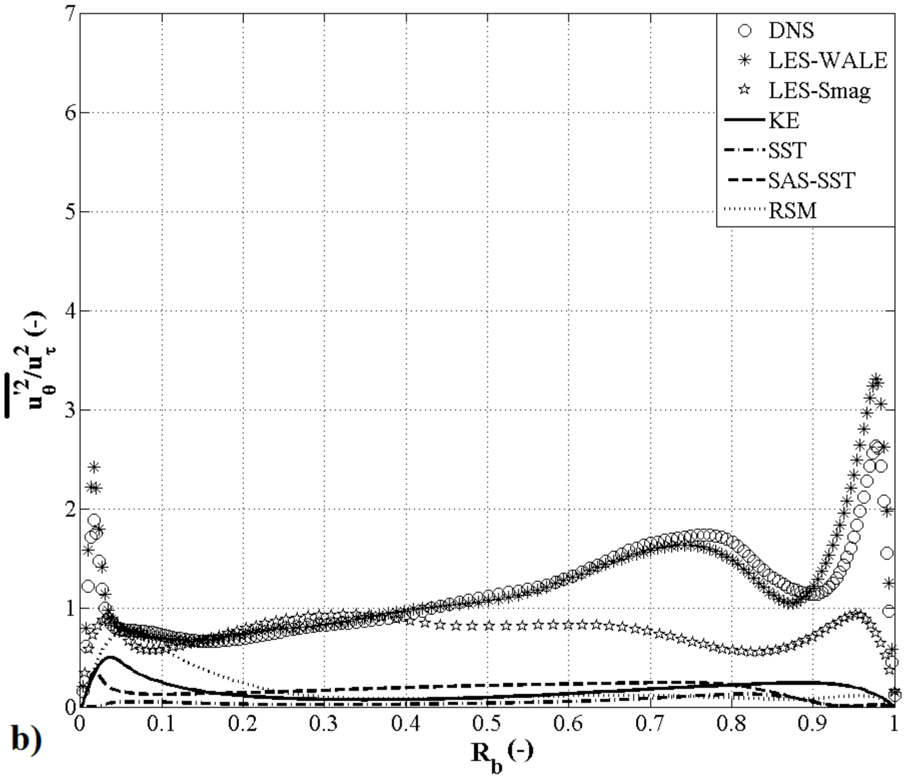

Figura 61 – Radial profiles of the tangential velocity component near the inward region of a Taylor vortex.

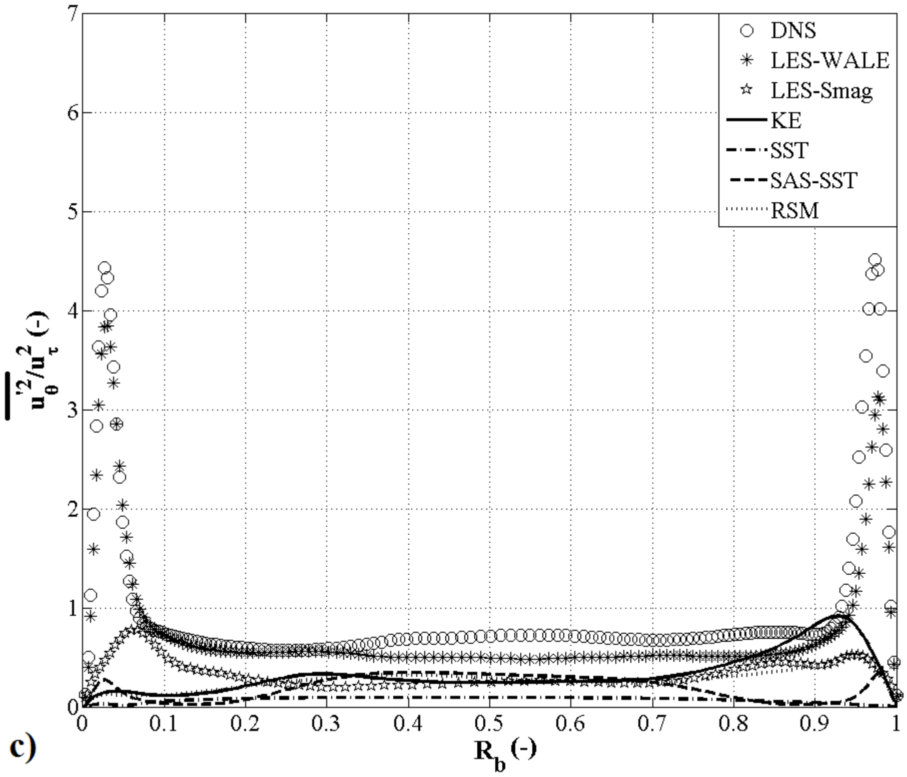

Figura 62 – Radial profiles of the tangential velocity component near the center of vortex region of a Taylor vortex.

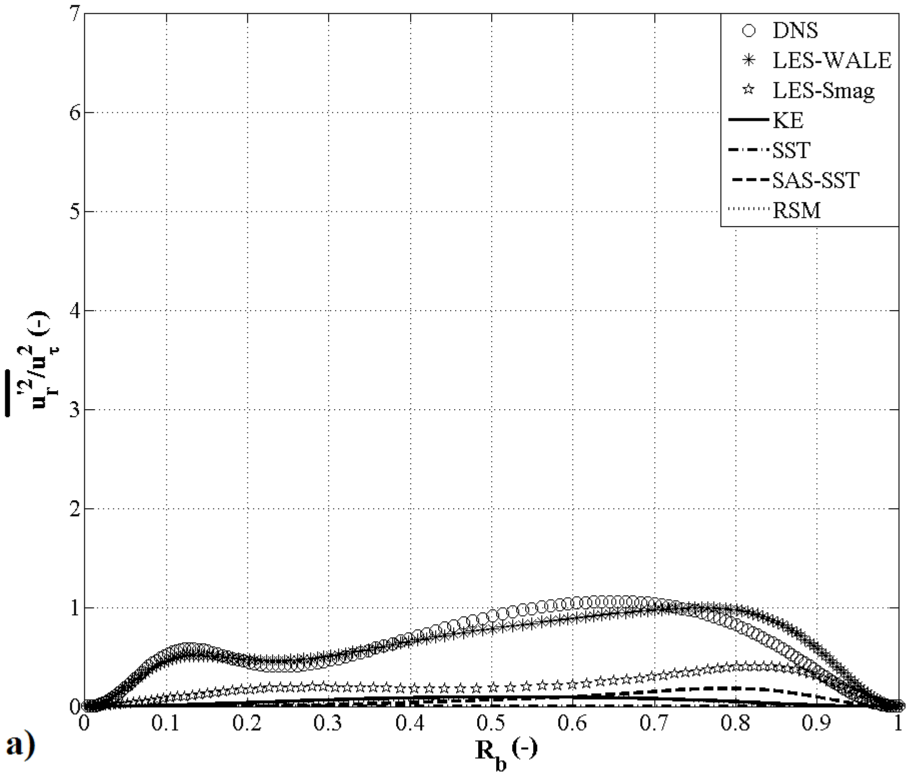

Figura 63 – Radial profiles of the radial velocity component near the outward region of a Taylor vortex.

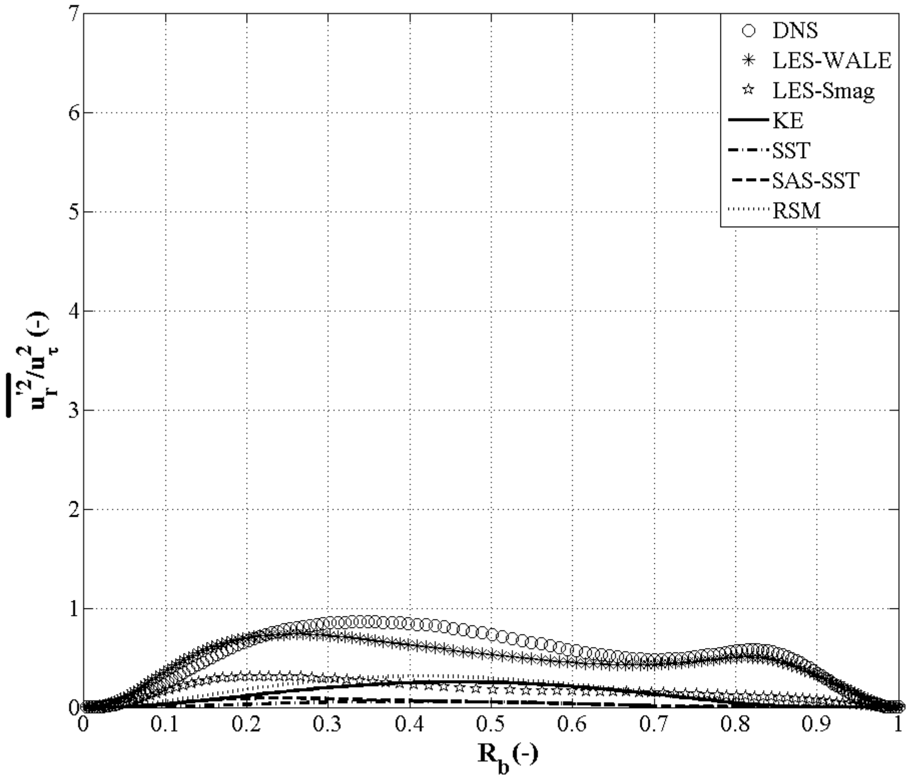

Figura 64 – Radial profiles of the radial velocity component near the inward region of a Taylor vortex.

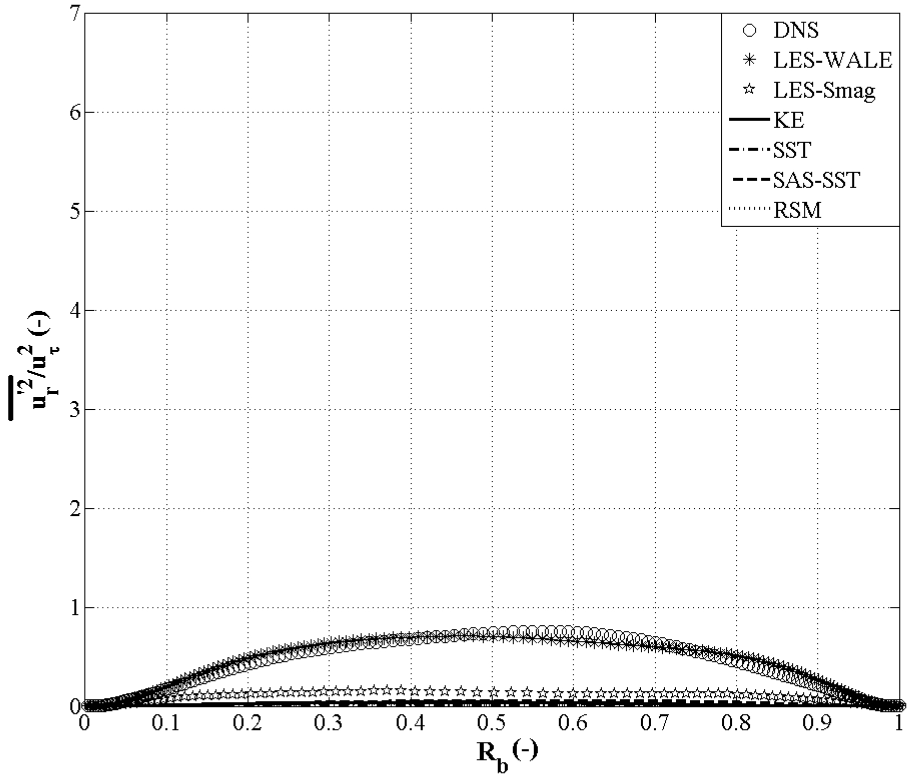

Figura 65 – Radial profiles of the radial velocity component near the center of vortex region of a Taylor vortex.

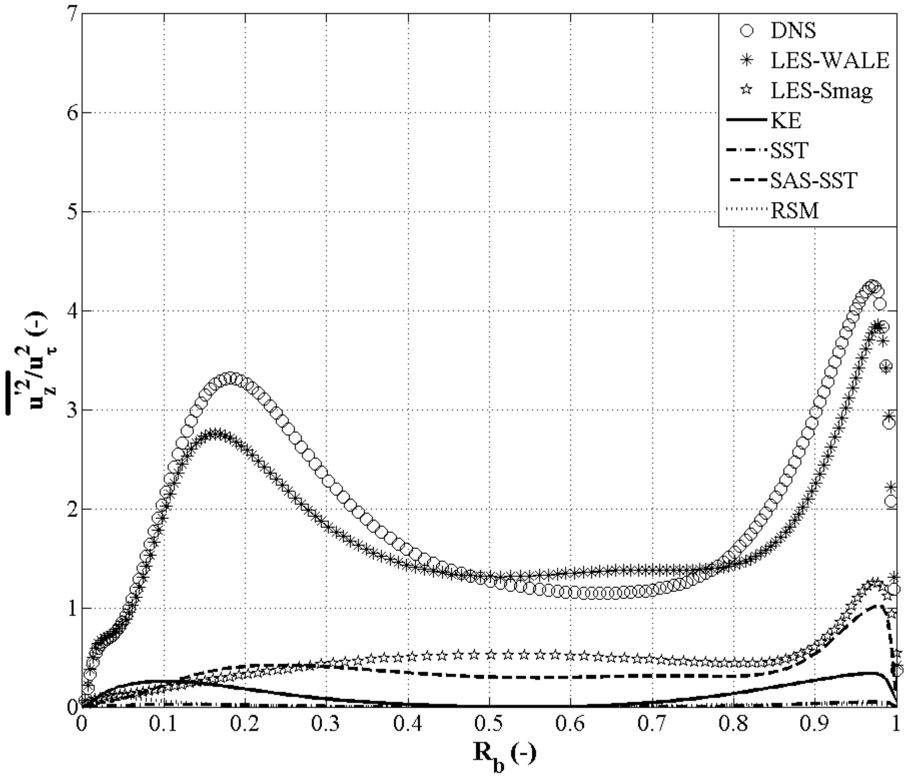

Figura 66 – Radial profiles of the axial velocity component near the outward region of a Taylor vortex.

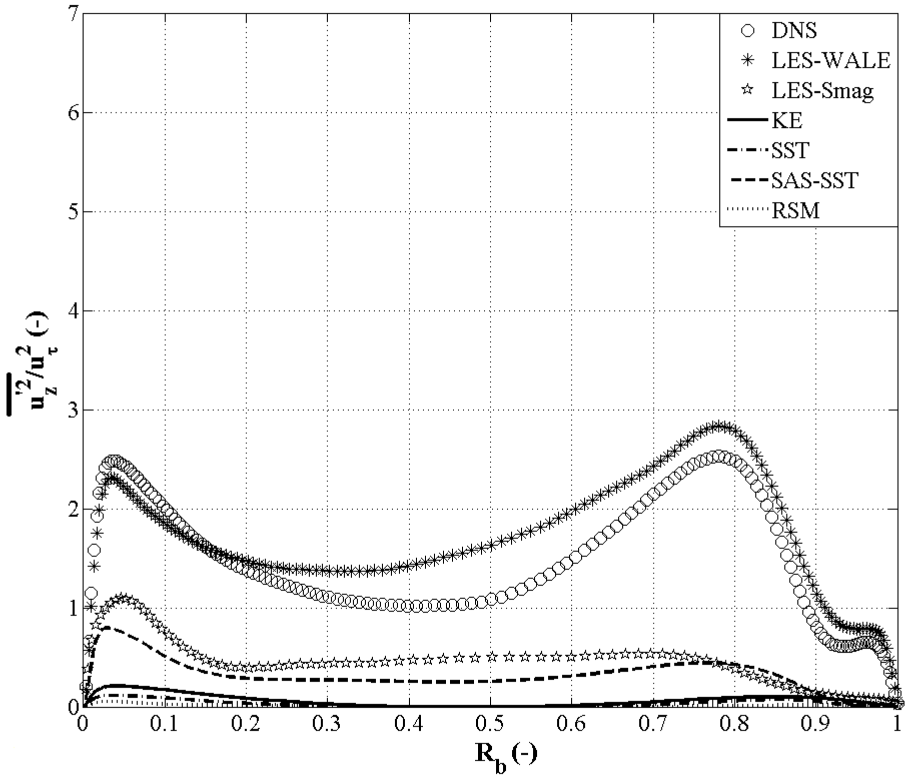

Figura 67 – Radial profiles of the axial velocity component near the inward region of a Taylor vortex.

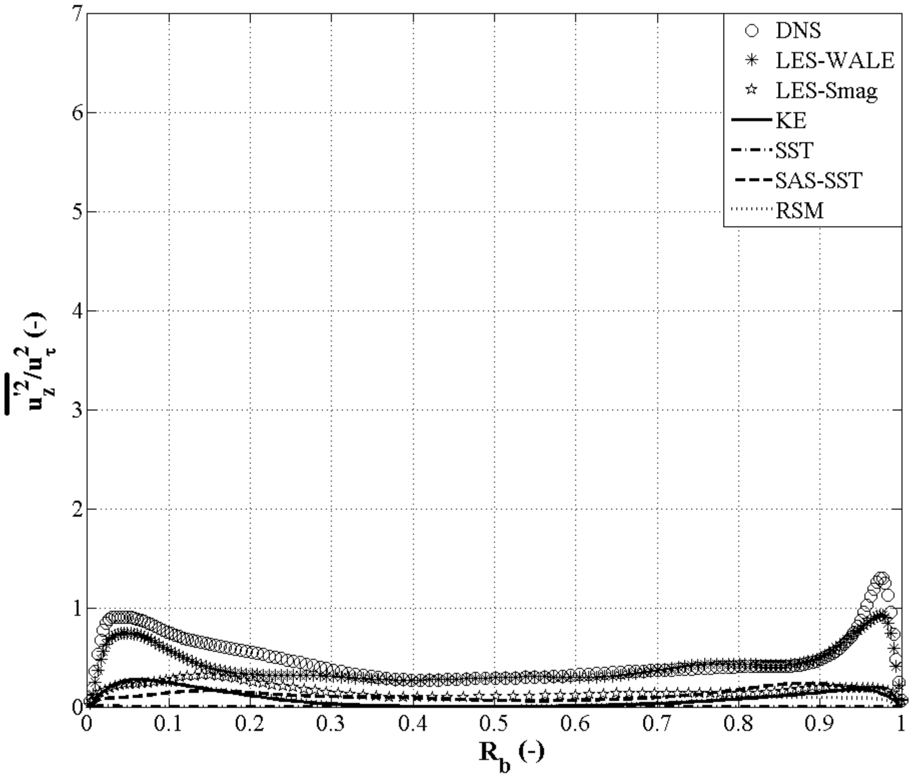

Figura 68 – Radial profiles of the axial velocity component near the center of vortex region of a Taylor vortex.

the inner cylinder boundary, while two local maximas lie in the boundary layer of outer cylinder of which one is next to the wall and other at R_b=0.8, also in consistence with the results of Kobayashi et al. (1990). In the center of vortex region, the maximas lie very near to the boundary with sharp decrease in the boundary layer area and near constant magnitude in the bulk zone, and in the boundary layer the disparity in the magnitude of the maximas near the wall is very little in comparison to the outward and inward regions.

The radial fluctuating component is the weakest of the three, in agreement with the experimental and numerical results of Kobayashi et al. (1990), Chung e Sung (2005), Bilson e Bremhorst (2007), Poncet, Haddadi e Viazzo (2011), Friess, Poncet e Viazzo (2013), with the maxima around one-third and one-seventh of the axial and tangential components, respectively. In all three regions, outward, center of vortex and inward, both numerical models predict similar magnitudes and flow structures. In the center of vortex region, the flow has a curved shape with the maxima lying in the middle of the gap-width, as in the case of mean radial velocity. Whereas, the inward and outward regions also have curved but opposite flow structure with two local maximas at R_b≈0.25 and 0.15 at the inner wall and 0.85 and 0.75 at the outer wall, respectively.

In the case of fluctuating axial velocity, the maxima lie further away from inner cylinder boundary, R_b=0.16, but closer to the other boundary for outward region, in rapport with Kobayashi et al. (1990). Whereas, in the inward region the structure is opposite but comparatively weaker with the maxima closer to the inner cylinder boundary, but at R_b=0.8 for outer cylinder, also in consistence with the results of Kobayashi et al. (1990). In the center of vortex region, both the structure and magnitude are predicted of similar order by both numerical models. The maximas lie very near to the boundary with gradual decrease from the boundaries towards the center of the bulk zone. Though the Chung e Sung (2005) have not mentioned the region of extraction of results, their root mean square (RMS) axial velocity fluctuations were of similar structure as that of the center of vortex region with the maxima lying very close to the boundary and the minima, having a magnitude of 50% of the maxima, lying in the middle of the gap-width.

It is interesting to note that the flow in the outward region is always comparatively stronger compared to the one obtained in the inward and center of vortex region, and in case of fluctuating tangential velocity the maxima is two times higher. Kobayashi et al. (1990) surmised that the most probable reason behind the comparatively weaker flow in the inward and center of vortex region is due to the viscous forces causing deceleration of the fluid on the wall. Secondly, the flow structure of the fluctuating axial velocity is very similar to that of the fluctuating tangential velocity in the bulk region, also observed in Kobayashi et al. (1990), Chung e Sung (2005), Bilson e Bremhorst (2007), Friess, Poncet e Viazzo (2013). Kobayashi et al. (1990) said that the reason behind this similarity relates to the energy redistribution from $u_\theta'^2$ through the pressure rate-of-strain correlation and also due to small production of $u_z'^2$.

The LES-WALE models predicts equally well the shape and location of the maximas estimated by the DNS model in all three regions for the three components of the TKE, but the magnitude of the flow has some very small disparities both near and away from the walls. The other LES model was under-predicting these turbulence parameters significantly but captured the flow structure to a certain extent. In the case of the mean flow components the LES-Smagorinsky model was over-estimating, and in the case of the fluctuating velocity components which represents the turbulence are under-predicted. All the RANS based models were severely under-predicting and the worst being the SST turbulence model. The SAS-SST model captured the normal axial stress in close similarity to that of the LES-Smagorinsky model, but not the other two normal stresses where it was under-predicting even more. The RSM and k-ϵ were slightly better than the SAS-SST model for the estimation of the tangential normal stress, but poorer in the estimation of normal axial stress; while, in the estimations of the normal radial stress there is little difference among these three models.

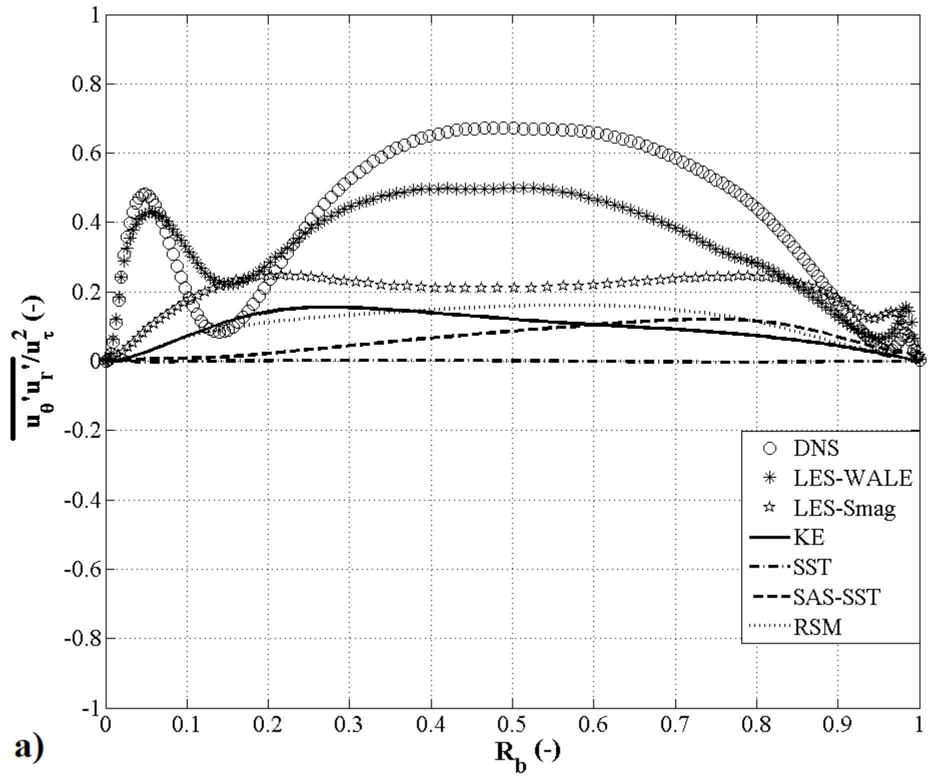

Figura 69 – Radial profiles of the tangential velocity component near the outward region of a Taylor vortex.

4.4 Reynolds shear stresses

In Figures 69, 70, 71, 72, 73, 74, 75, 76 and 77, the radial profiles of the three Reynolds shear stresses, $\overline{u_r' u_\theta'}$, $\overline{u_r' u_z'}$ and $\overline{u_\theta' u_z'}$, are presented near the outward, center of vortex and inward region of the Taylor vortex. Unlike the squared fluctuating components, these have been unanimously named as the Reynolds shear stresses (KOBAYASHI et al., 1990; CHUNG; SUNG, 2005; BILSON; BREMHORST, 2007; HOUT; KATZ, 2011; PONCET; HADDADI; VIAZZO, 2011; FRIESS; PONCET; VIAZZO, 2013). Once more only Kobayashi et al. (1990) mentioned the regions of the Taylor-vortex at which the data was presented; nonetheless, a qualitative comparison with other studies is still valid.

The Reynolds shear stress $\overline{u_\theta' u_r'}$ is stronger in the bulk zone in all the three regions in comparison to the boundary layer. In contradiction to the experimental estimations of the Kobayashi et al. (1990), who predict a profile similar to that of the fluctuating tangential component in these regions, the bulk zone follows the profile structure of the fluctuating radial component in these regions. It can be seen that the fluctuating radial component is nearly zero in the boundary layer and attains a magnitude in the vicinity of the tangential component in the bulk zone, which is most probably the reason behind stronger magnitude in the bulk zone in comparison to the boundary layer area.

The magnitude and structure of the Reynolds shear stress $\overline{u_r' u_z'}$ has a very significant

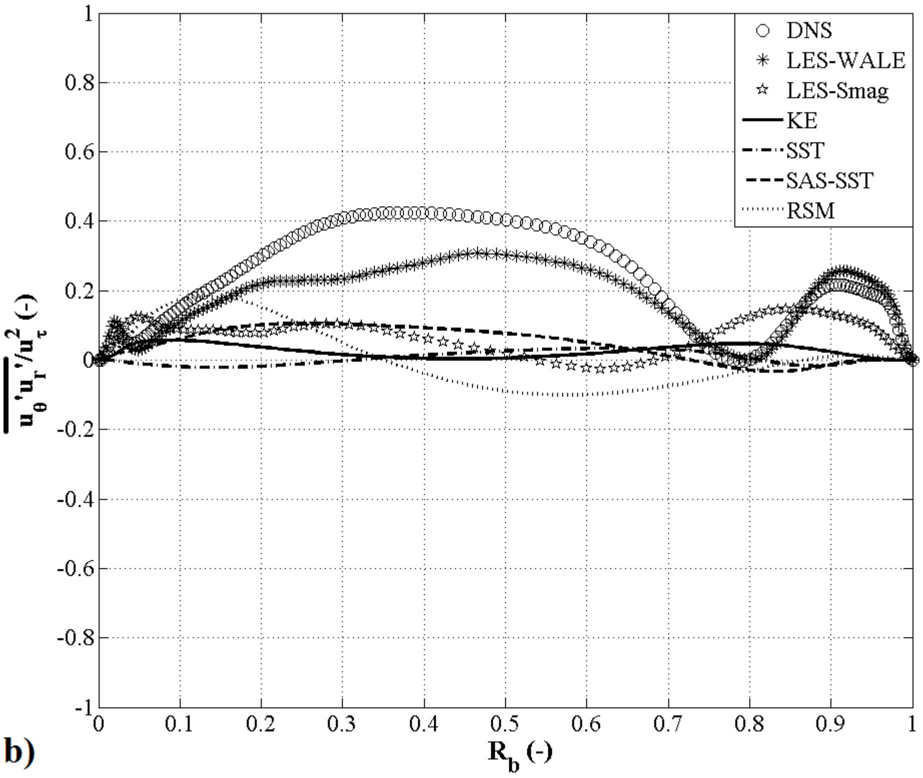

Figura 70 – Radial profiles of the tangential velocity component near the inward region of a Taylor vortex.

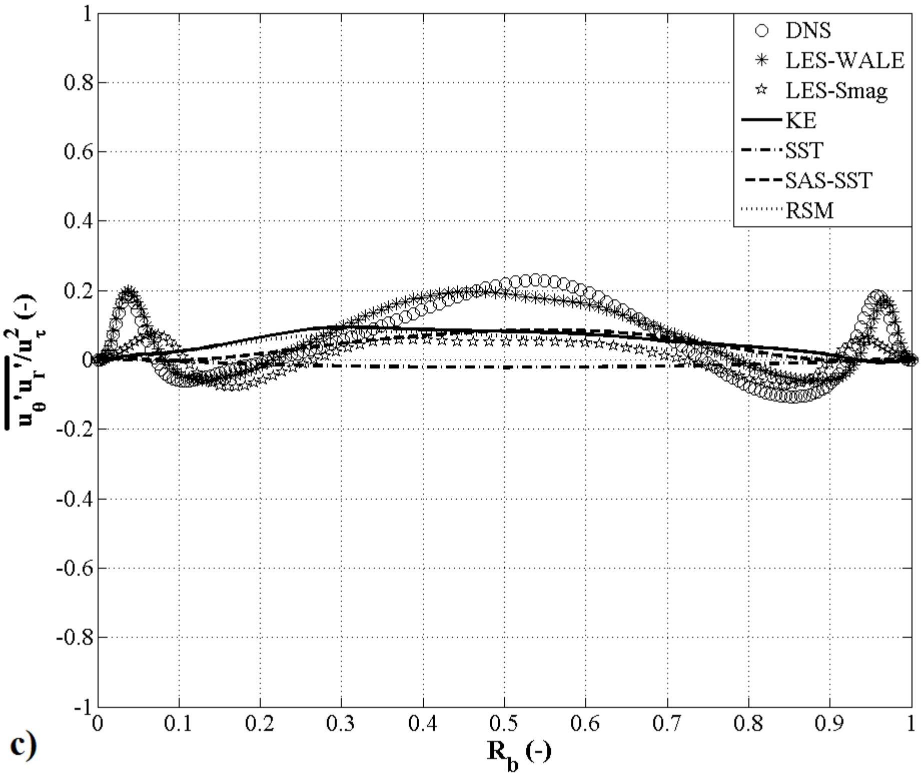

Figura 71 – Radial profiles of the tangential velocity component near the center of vortex region of a Taylor vortex.

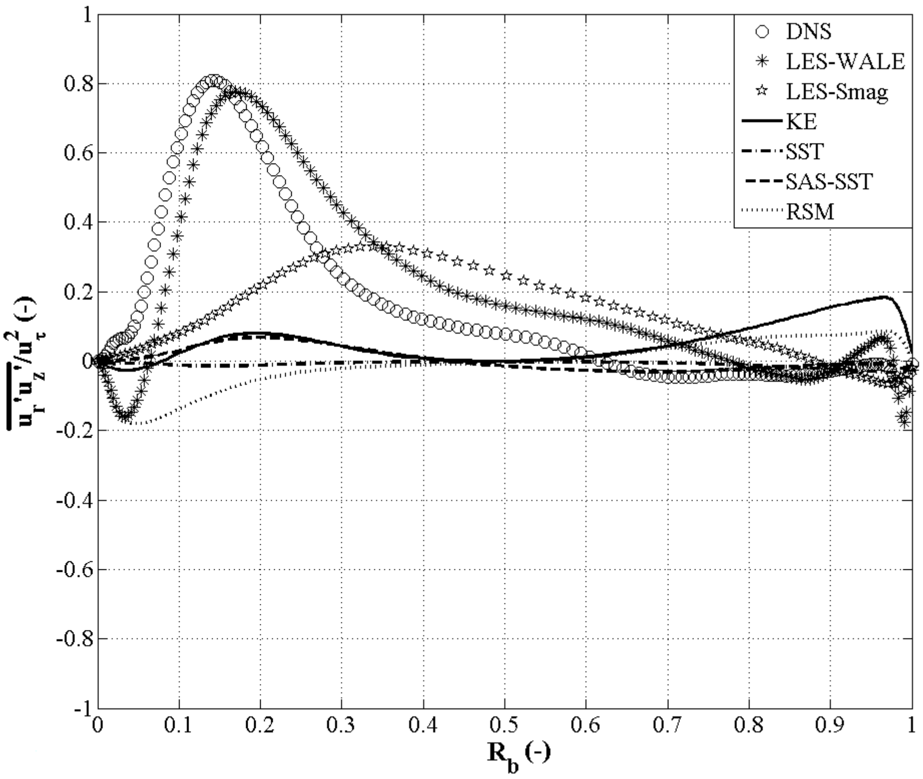

Figura 72 – Radial profiles of the radial velocity component near the outward region of a Taylor vortex.

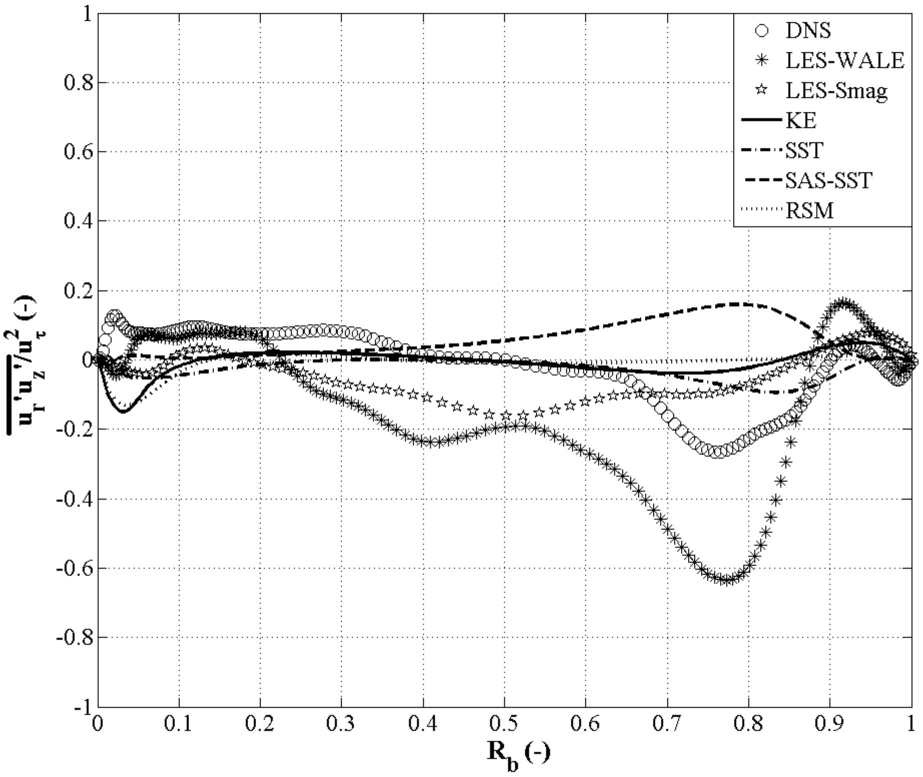

Figura 73 – Radial profiles of the radial velocity component near the inward region of a Taylor vortex.

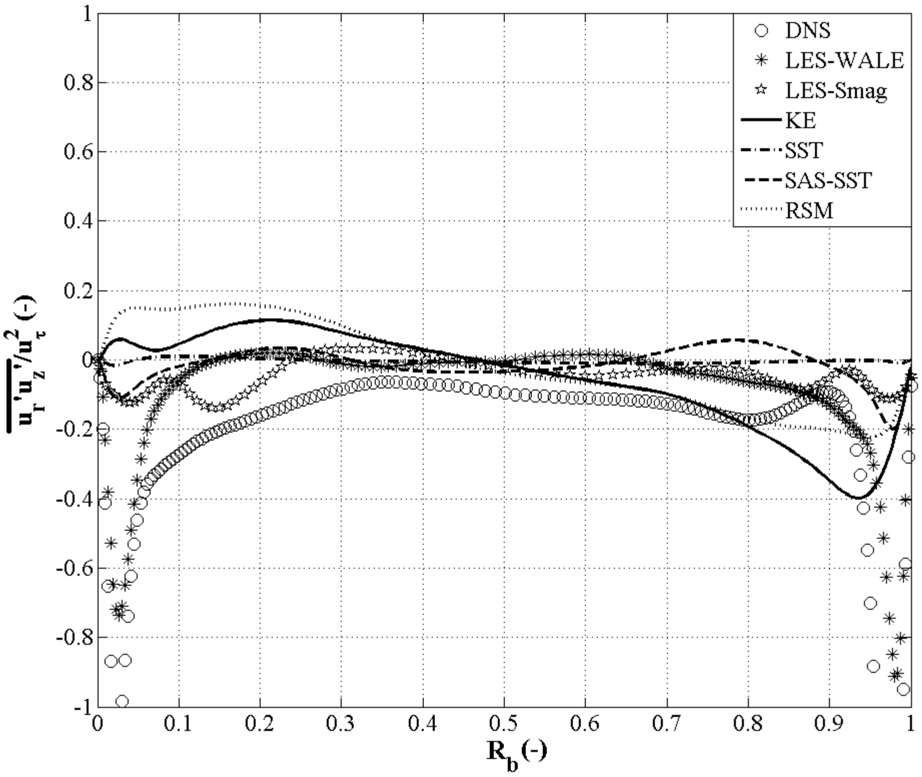

Figura 74 – Radial profiles of the radial velocity component near the center of vortex region of a Taylor vortex.

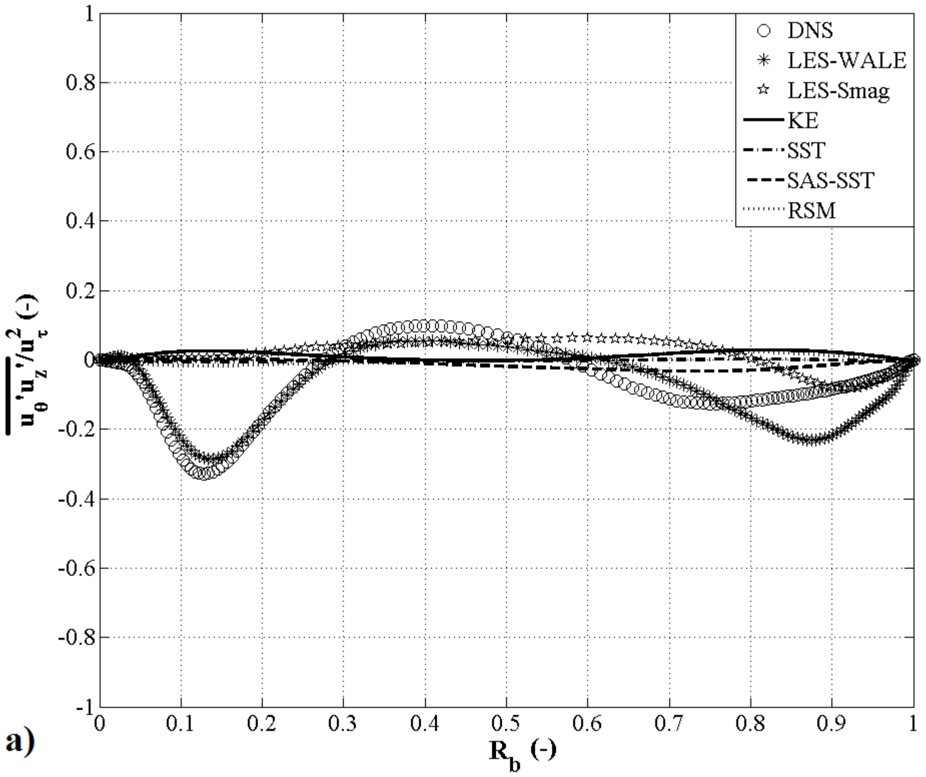

Figura 75 – Radial profiles of the axial velocity component near the outward region of a Taylor vortex.

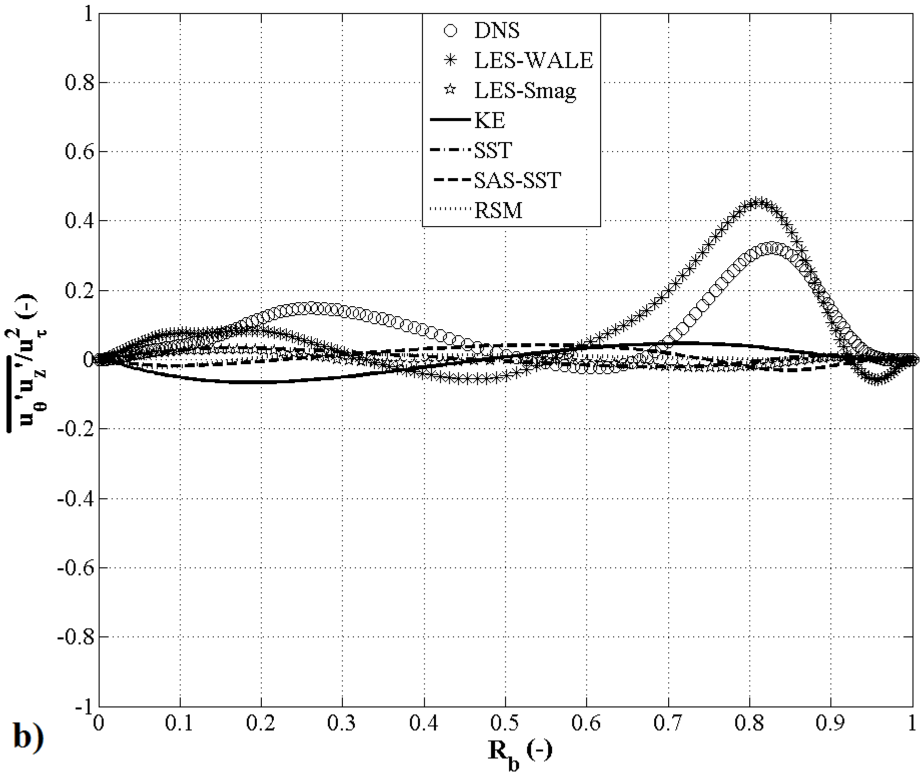

Figura 76 – Radial profiles of the axial velocity component near the inward region of a Taylor vortex.

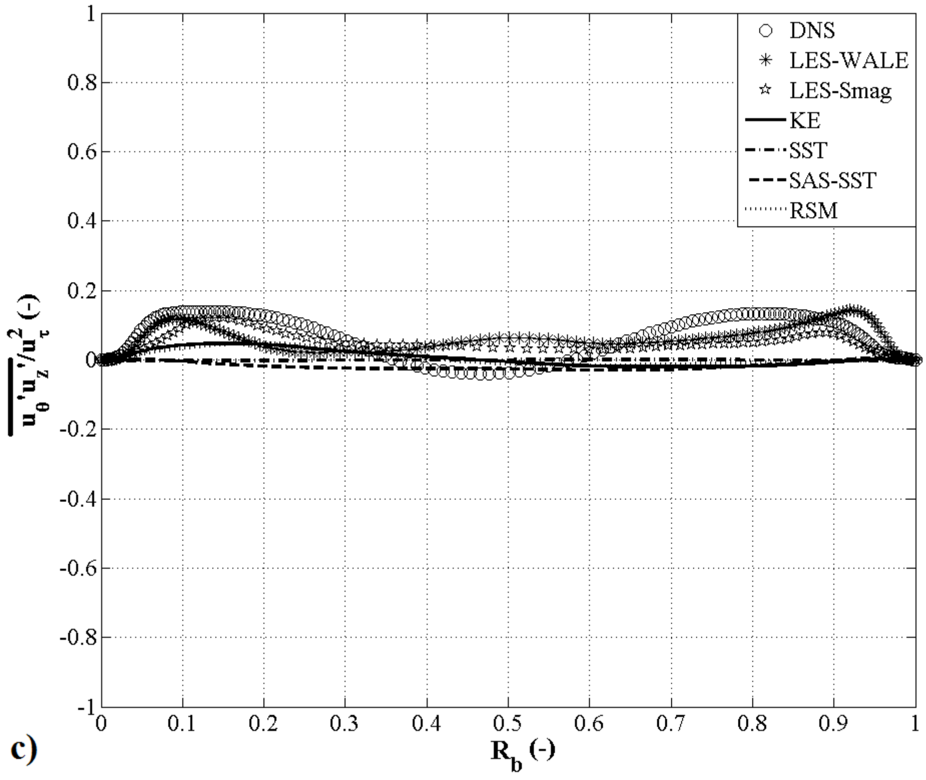

Figura 77 – Radial profiles of the axial velocity component near the center of vortex region of a Taylor vortex.

imprint of the fluctuating axial component in all the three regions, but the sign is due to the radial component. In the outward region, the magnitude is mostly of +ive sign with the maxima near the inner cylinder wall and gradually reaching the zero magnitude towards the outer wall; while, in the inward region its opposite with the sign being -ive and maxima towards the outer wall. In the center of vortex region, there are two maximas of similar magnitude and -ive sign near each cylinder wall.

The third Reynolds shear stress $\overline{u'_\theta u'_z}$ is the weakest of the three shear stresses in all three regions. Being a mixture of tangential and axial fluctuating velocity components, this shear stress has two local maximas near each cylindrical wall. In the outward region, the maxima is stronger near the inner boundary; on the contrary, the maxima is towards outer boundary are in the inward region. Whereas, in the center of vortex region both local maximas are of similar magnitude.

The numerical models of the Chung e Sung (2005), Poncet, Haddadi e Viazzo (2011), Friess, Poncet e Viazzo (2013) for the Reynolds shear stresses $\overline{u'_r u'_z}$ and $\overline{u'_\theta u'_z}$ estimated a profile structure similar to that of the mean axial component of the velocity in the center of vortex region (Figure 57). Whereas, for the Reynolds shear stress $\overline{u'_r u'_\theta}$, the LES models of the Chung e Sung (2005), Friess, Poncet e Viazzo (2013) predicts a sort of inverted U-shape which is slanting from the inner cylinder toward the outer through-out the bulk zone. First of all, it should be noted that the exact region of extraction of data has not been specified, nor has been specified if these results are the mean of the whole axial height. If the mean of the whole axial height is taken then for the Reynolds shear stress $\overline{u'_r u'_z}$ a profile similar to the ones predicted by these researcher is obtained but not in the case of the Reynolds shear stress $\overline{u'_\theta u'_z}$. Secondly, the present results predict a upward parabola for the Reynolds shear stress $\overline{u'_r u'_\theta}$ only in the bulk zone with two small peaks in the boundary layer area in the outward region. If the mean of the whole axial height is taken, then the prediction becomes a inverted V-shape in the bulk zone with two small peaks in the boundary layer. Please note that the mean of the whole axial heights are not shown here.

Overall, the LES-WALE model reproduces very well the estimation of the DNS model, especially the structure, with slight discrepancies in the magnitude estimations. The SST model predicted near zero magnitude estimations in all three regions for the three shear stresses and is the poorest of the RANS based model presented here for these turbulence parameters. The LES-Smagorinsky model captured the shape of the flow to a certain extent but the magnitude was well under-predicted. The other three RANS based models were equally poor in capturing both the shape of the flow and its magnitude but still better then then SST model.

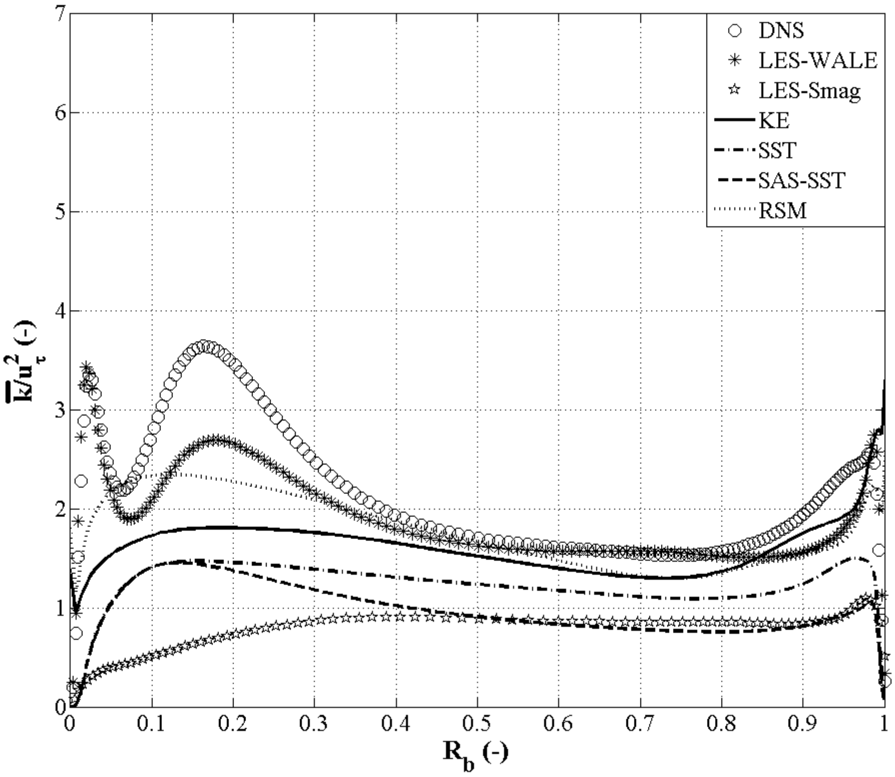

Figura 78 – Radial profiles of the turbulent kinetic energy near the outward region of a Taylor vortex.

4.5 Turbulent kinetic energy

The Figures 78, 79 and 80 present the TKE near the outward, inward and center of vortex regions of the Taylor vortex. In the case of the RANS based models, the modeled TKE is presented and not the one estimated from the normal stresses. There is a significant difference between the modeled TKE and the one obtained after the treatment of the velocity data set, as can be seen in Figure 81. This substantial difference is due to the fact that the Reynolds averaging process reduces the turbulence content in the velocity and therefore requires the modeling of the turbulent kinetic energy. This should be the main reason behind the under-estimation of the Reynolds normal and shear stresses which are estimated from the velocity data set for the RANS based models.

The TKE profile bears a very close resemblance with the profiles of the tangential and axial fluctuating velocity components, especially the tangential component being the strongest of the three. The radial component being the weakest of the three fluctuating components has virtually no similarity with the TKE profile. In the boundary layer, the dominant factor is the tangential component leading to sharp peaks near the walls in all the three regions. In the bulk zone, though the axial component is slightly stronger than the tangential component, both these components have similar flow structures; hence the striking resemblance to both these components is evident.

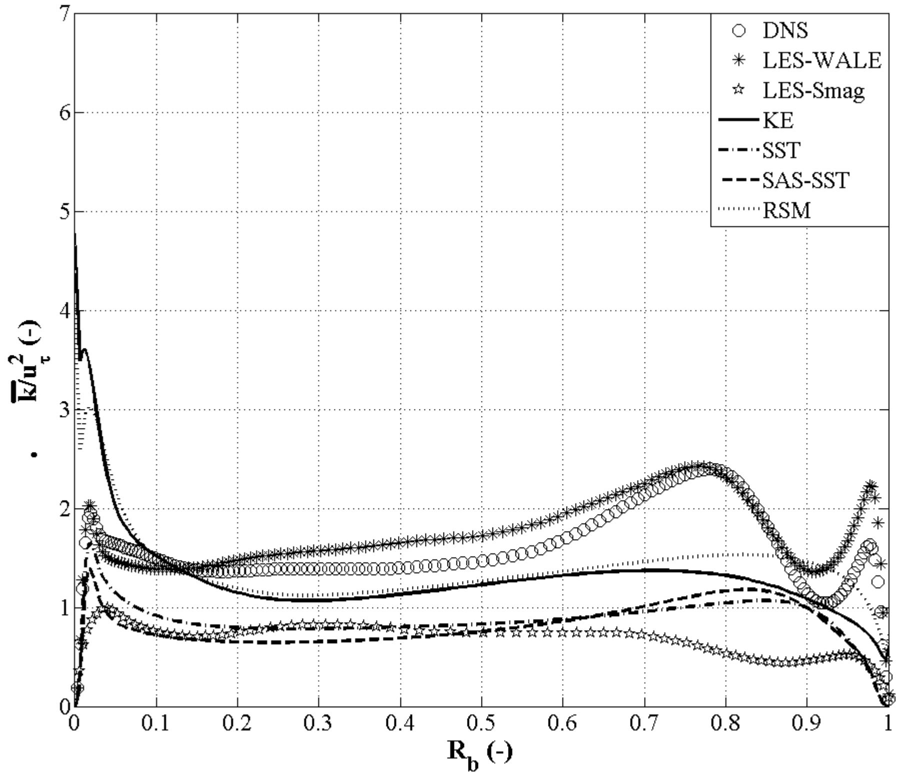

Figura 79 – Radial profiles of the turbulent kinetic energy near the inward region of a Taylor vortex.

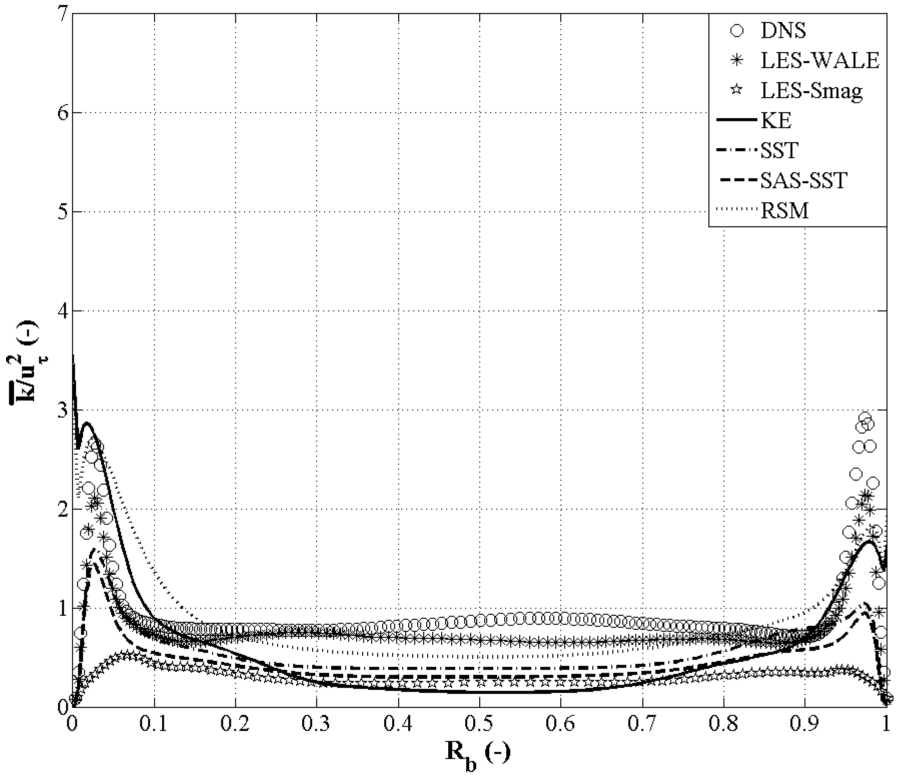

Figura 80 – Radial profiles of the turbulent kinetic energy near the center of vortex region of a Taylor vortex.

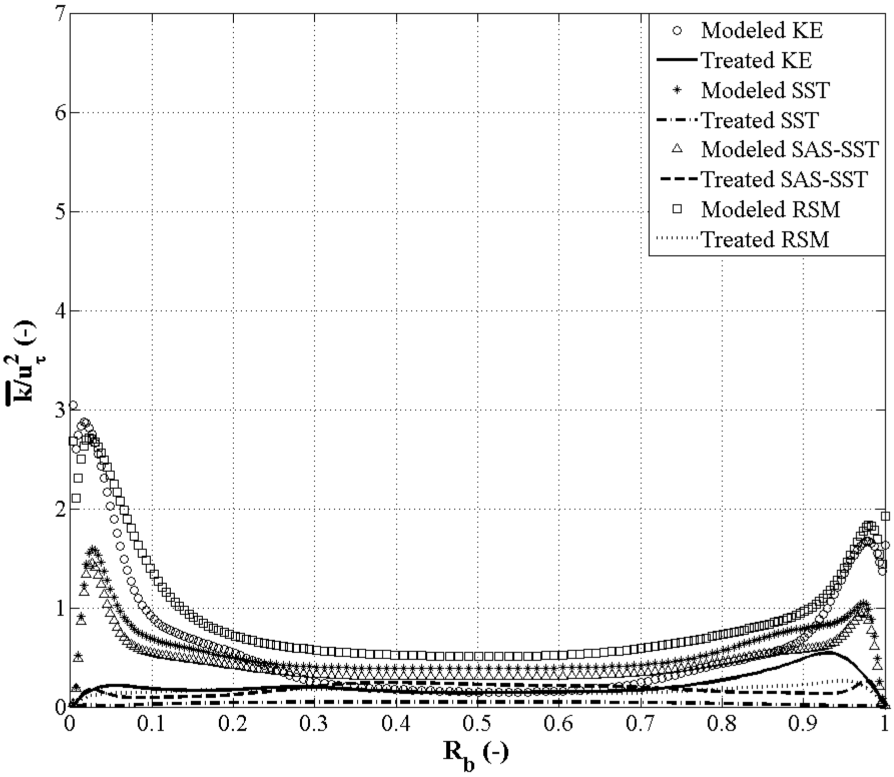

Figura 81 – Comparison of the modeled turbulent kinetic energy with the one estimated from the velocity data in the center of vortex region of a Taylor vortex.

The LES-Smagorinsky model presented the poorest estimation of the TKE in comparison with the predictions of the DNS model. It under-predicts significantly the magnitude in all three regions, and does not capture well the flow structure either in all three regions. The LES-WALE model, on the other hand, captures extremely well both the flow structure and the magnitude estimated by the DNS model in all three regions. All the RANS based models estimations of the flow structure were similar to each other. They were not able to capture the two local maximas near the inner wall in the outward region and near the outer wall in the inward region, but were able to predict the structure much better in the center of vortex region. In terms of the magnitude, the estimations of the $k-\epsilon$ and the RSM model were similar and comparatively better than the SST and SAS-SST models.

4.6 Anisotropy

In Figure 82, a small study of anisotropy near the walls and in the three prominent regions of a Taylor vortex, outward, center of vortex and inward regions, is presented through Lumley-Newmann and AG graphs of the invariant maps for the Reynolds stress tensors only for the DNS model. This anisotropy study has been conducted with the DNS model only because of very poor estimations of the Reynolds normal and shear stresses by

RANS based models and the LES-Smagorinsky model, and very similar estimations of the LES-WALE model. Method of Lumley e Newman (1977) is the most popular one to characterize flow anisotropy in the TVB (CHUNG; SUNG, 2005; PONCET; HADDADI; VIAZZO, 2011; OGUIC; VIAZZO; PONCET, 2013; PONCET; VIAZZO; OGUIC, 2014) through the Reynolds stress anisotropy tensor b_{ij}, Equation 4.1: where k and δ_{ij} represent the average turbulent kinetic energy and the kronecker delta tensor, respectively. The first invariant of the tensor b_{ij} is the trace of the tensor and zero by construction. The second and third invariants for the tensor b_{ij} are defined in Chung e Sung (2005) as: II=$\frac{1}{2}b_{ij}b_{ji}$ and III=$\frac{1}{3}b_{ij}b_{jk}b_{ki}$. Hence, the anisotropy can be characterized by the invariants II and III in a triangle elaborated by Lumley e Newman (1977).

$$b_{ij} = \overline{u_i^{'}u_j^{'}} - \frac{2k\delta_{ij}}{3} \tag{4.1}$$

Apart from using the invariants II-III, the invariants of the axi-symmetry (A) and bi-dimensionality (G) may also be used, where G=1/9+(III-II)/8 and $A = -(III/6)/(II/6)^{3/2} = \pm 1$ in terms of the invariants II-III as explained by Escudie (2001). As stated by Escudie (2001), these two invariants, G and A, possess much more physical significance to understand the anisotropy in comparison with the invariants II-III, and these are represented in a rectangle instead of a triangle. In this case, the state of isotropic turbulence is achieved when the value of the invariant G is near or equal to its maximum value of 1/9 irrespective of the value of the invariant A. The invariants A and G allow the quantification of the disparity of the measuring data with respect to axi-symmetry and bidimensionality, thus isotropy as well.

The numerical results are in coherence with the realizability diagram of Lumley as they remain within the region delimited by the two axi-symmetric limits and one bidimensional limit. Furthermore, Figures 82a and 82b confirm that closer to the cylindrical walls the turbulence is mainly bi-dimensional or two-component, in complete agreement with Chung e Sung (2005), Oguic, Viazzo e Poncet (2013) and Poncet, Viazzo e Oguic (2014). Bidimensional state near boundaries is in complete agreement with the VEDR estimations where the gradients of the tangential co-ordinate were practically negligible in the boundary layer area. In addition, as more than 80 % of the VEDR was formed by only one gradient near the walls, we can observe a large concentration of points towards the monodimensional state on the bidimensional limit (82b), also observed by Poncet, Haddadi e Viazzo (2011).

In the bulk zone, Chung e Sung (2005) and Poncet, Haddadi e Viazzo (2011) stated that the turbulence is almost isotropic, which is further confirmed by the Oguic, Viazzo e Poncet (2013). However, it can be seen in Figures 82c and 82d that the turbulence tends towards isotropic state depending upon region of the Taylor-vortex in which it is located. In the outward and inward region, the turbulence tends towards the axi-symmetry limit and

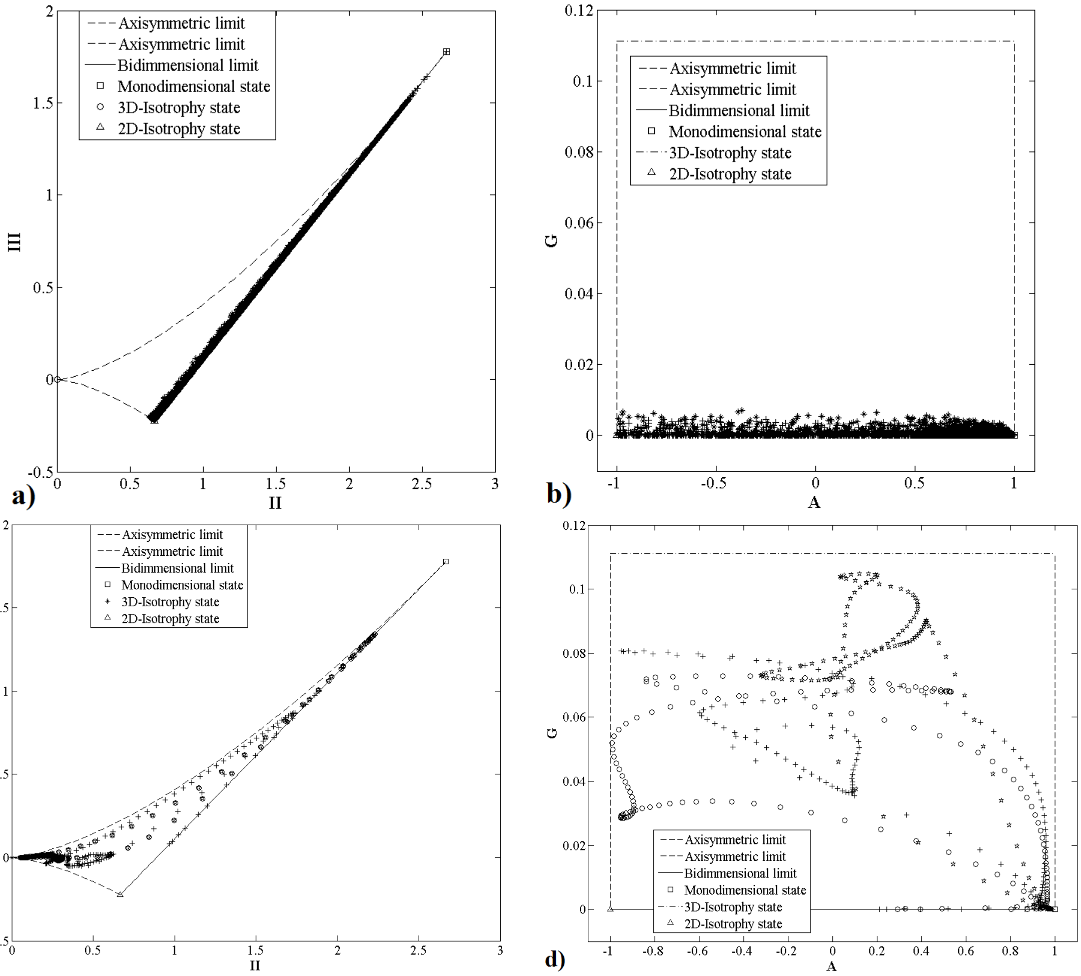

Figura 82 – Presentation of anisotropy through Lumley-Newmann and AG graphs axially near the walls, a) and b), and radially at the outward, center of vortex and inward regions of Taylor vortex, c) and d) respectively, for the DNS model. Note: in part a) and b) * represent the data near the inner and outer boundaries, while in c) and d) o, + and pentagram represent the outward, center of vortex and inward regions, respectively.

only in the center of vortex region that the turbulence tends towards the isotropic state. In other words, the turbulence fluctuates between the axi-symmetry limit and isotropic state in the bulk zone of a Taylor-vortex pair.

4.7 Viscous energy dissipation rate

4.7.1 Composition of VEDR

In Figure 83 the composition of the twelve gradients is shown for the estimation of VEDR of the mean flow and turbulent kinetic energy for the DNS model. It can be seen that the major component near and away from the walls for both components of the VEDR is the gradient of the tangential velocity component in the radial direction: $(\frac{\partial(\overline{U}_\theta/r)}{\partial r})^2$ for the VEDR of the mean flow kinetic energy and $\overline{(\frac{\partial(u_\theta'/r)}{\partial r})^2}$ for the VEDR of the turbulent kinetic energy. In combination with the other two gradients of the radial direction, i.e. $(\frac{\partial(\overline{U_r})}{\partial r})^2$ and $(\frac{\partial(\overline{U_z})}{\partial r})^2$, these account for at-least 90 % of the VEDR of mean flow and turbulent kinetic energy, respectively, through-out the reactor. These three gradients of the radial direction practically constitute the VEDR of turbulent kinetic energy with the rest of the gradients being closer to lower than one-millionth of the $\epsilon_{innerwall}$. The three gradients of the axial and tangential direction account for the less than 10^{-4} and 10^{-3} of the $\epsilon_{innerwall}$ for the turbulence and mean flow kinetic energy, respectively, through-out the reactor. The three cross product gradients accounts for less than 10^{-5} of the $\epsilon_{innerwall}$ for both components of the VEDR.

Sharp e Adrian (2001) presented equations based on the statistical isotropy or axi-symmetry to capture the out-of-plane gradients for the 2D-PIV measurements. In these equations, an arithmetic mean of the in-plane gradients is taken into consideration to account for the out-of-plane gradients. Keeping in view the impact of radial gradients on the VEDR, such methodology will generate over-estimation of the VEDR in the case of a TVB. Therefore, in-order to achieve a good estimation of at-least the maximum and average VEDR, the gradients of the radial co-ordinate have to be well captured. The three well captured radial gradients can provide a good estimation of the VEDR, especially near the wall where lies the maximum VEDR and which will lead to a better averaged VEDR as well. However, from the numerical 3d point of view, care still has to be taken when constructing the grid in the axial and tangential direction in order to keep a good aspect ratio and orthogonal quality.

However, it should be remembered that the grid structure in the tangential and axial directions are more than 10 and 5 times coarser near the boundary layer and bulk zone, respectively, in comparison with the radial direction. In comparison with the five gradient PIV estimation of the VEDR (Figure 44), it was observed that even the finer grid structure in the radial direction presented significant amount of under-estimation for the VEDR of turbulent kinetic energy in the bulk zone. It could mean that such poor magnitude values of the gradients in the axial and tangential direction could also be due to the coarser grid structure in these directions. In fact, the composition of the five gradients of PIV estimation of turbulence VEDR show that the magnitude of the radial velocity component in the tangential direction is exactly the same as that in the radial direction, Figure 32. The PIV estimation of the VEDR of mean flow kinetic energy component presented similar results, Figure 31. In the DNS estimation, the structure for the radial velocity component in the tangential, radial and axial direction for both mean flow and turbulent kinetic energy VEDR is similar, but the magnitude is much smaller.

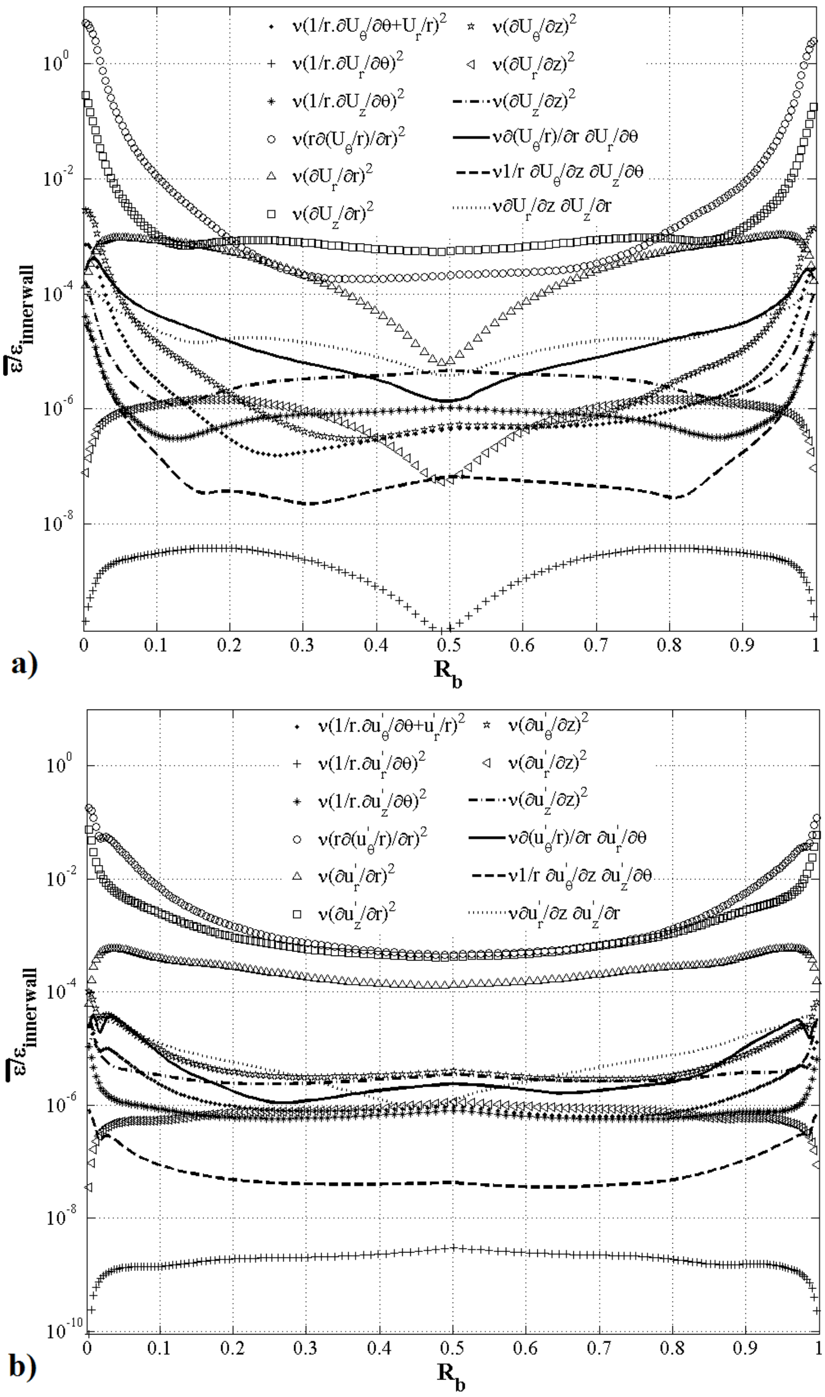

Figura 83 – The twelve gradients of the VEDR of mean flow (a) and turbulent (b) kinetic energy for the DNS model.

4.7.2 Structure of VEDR

Figure 84 presents the VEDR of the mean flow and turbulent kinetic energy of the DNS model in the outward, center of vortex and inward regions. The estimations are presented in a loglog profile to study the details of the inner cylinder's boundary layer. In the x and y axis of this Figures, the friction velocity, u_τ, and $\epsilon_{innerwall}$ are estimated from the DNS data as mentioned earlier. In the case of the RANS based model, only the VEDR of turbulent kinetic energy is modeled and that of mean flow kinetic energy is unavailable. As in the case of TKE, there is a considerable difference between the modeled VEDR of TKE and the one estimated after the treatment of velocity data set through the equations of the VEDR, with the treated data under-predicting by more than an order. Please note that the figure comparing the modeled and treated VEDR of TKE is not presented here. The modeled data of VEDR of TKE for the RSM model was also unavailable. These are the main reasons that the three regions are presented with the DNS model only.

The location of maxima is always very near to the wall, similarly observed by Tokgoz et al. (2012), Hout e Katz (2011) either to that of inner cylinder or outer cylinder depending upon the axial location in the Taylor-Vortex. In the outward region, the location of maxima is near the outer cylinder and for the inward and center of vortex region the maxima is located near the inner cylinder The decrease for both these components is very steep in the boundary layer, though it should be noted that the magnitude of the mean flow kinetic energy component is around an order higher than the turbulence component in this area. Whereas, in the bulk zone, this decrease in the viscous component is steeper in comparison to the turbulence component.

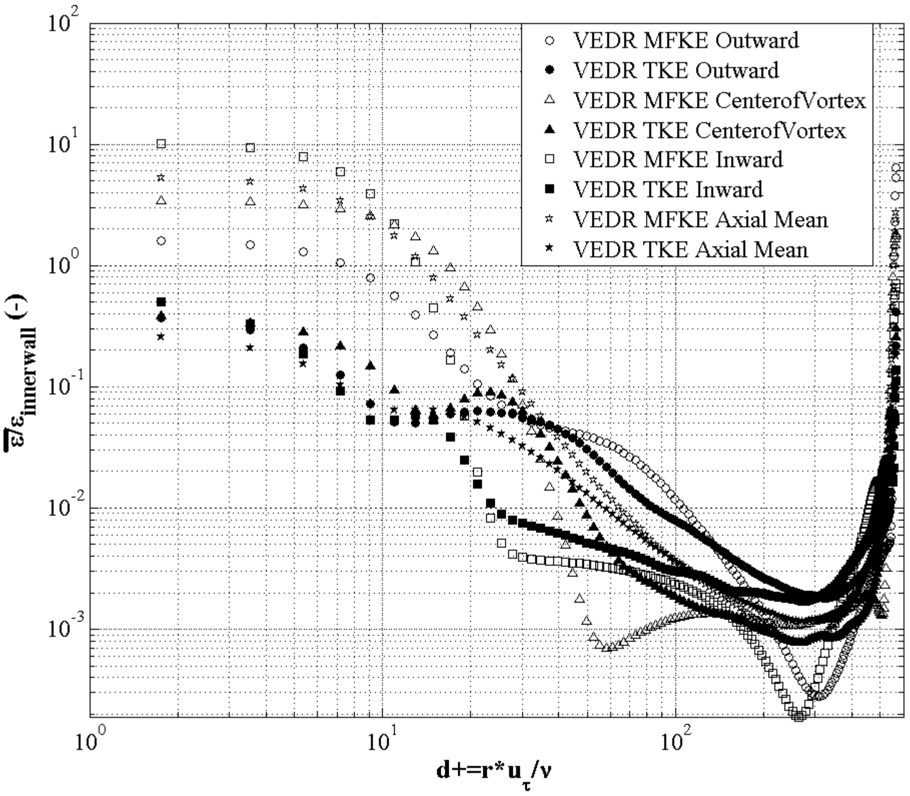

Figura 84 – The estimation of the VEDR of mean flow and turbulent kinetic energy of the DNS model in the outward, center of vortex and inward regions .

McEligot et al. (2008) termed the VEDR of mean flow kinetic energy as direct dissipation and that of turbulent kinetic energy as turbulent or indirect dissipation. They presented the numerical results of the DNS model for these components in a channel flow and zero-pressure-gradient boundary layer. They found that the direct dissipation is the dominating component of the two near the wall. As the d+ increases, both the direct and turbulent dissipation decreases with the reduction in the direct dissipation being much more drastic in comparison to the turbulence counterpart. Between d+ = 10 and 20, the magnitude of the direct and turbulent dissipation becomes equal, and with further increase in the d+ values the direct dissipation continues decreasing much more rapidly leading to the turbulence dissipation becoming the dominating component in the bulk zone.

Most of these aspects can be observed in the current estimations of these two components of the VEDR for the TVB. The direct dissipation is the dominating near the wall, and increase in d+ results in decrease in both of these components of the VEDR with the decrease in the direct dissipation being more rapid in comparison to the turbulence one. Furthermore, the magnitude of the direct and turbulent dissipation becomes equal between the region d+=10 and 30, with the dissipation of turbulent kinetic energy becoming the stronger component towards the bulk region, where turbulence component of the VEDR is at-least an order higher in the outward and inward regions. In fact, in the bulk region, the direct or mean flow kinetic energy dissipation becomes practically negligible by reaching values less than 0.1 % of the maximum value in complete agreement with the results of McEligot et al. (2008).

Turbulence takes over completely in the bulk zone once the viscous wall layer becomes negligible around d+=30 for a classical zero-pressure gradient case, as mentioned by McEligot et al. (2008). They defined the viscous wall layer as the region with significant effects of viscosity which are not necessarily dominant and include the laminar and buffer sub-layers. The importance of this region lays in the fact that the largest gradients and greatest production of turbulence occur in this region besides being the region which provides major resistance to the momentum, mass and energy transfer (MCELIGOT et al., 2008). Additionally, it can be seen that the VEDR remains fairly constant in the viscous sublayer. These aspects of following the classical turbulence further strengthen the validity of these results.

The only discordance with the predictions of the McEligot et al. (2008) is that the turbulence component of VEDR is not as strong as it should be. The most probable reason behind this disparity is that the mesh is comparatively courser in the middle of the gap-width, 184 μm, in comparison to the nodes on the wall, 47 μm. The Kolmogorov scale estimations in comparison with the mesh size, presented in Figure 85, confirm the requirement of further enhancement in the radial mesh to capture 100 % of the eddies. The Kolmogorov scale was estimated from the mean of all axial heights of the mean VEDR of turbulent kinetic energy for the PIV and DNS model. The PIV estimations of the Kolmogorov scale confirm that the radial mesh is around 3 times coarser in the center of gap-width. This should be the main factor behind such poor estimation of the VEDR of turbulent kinetic energy which is the stronger component in the bulk zone where the radial mesh is poorest.

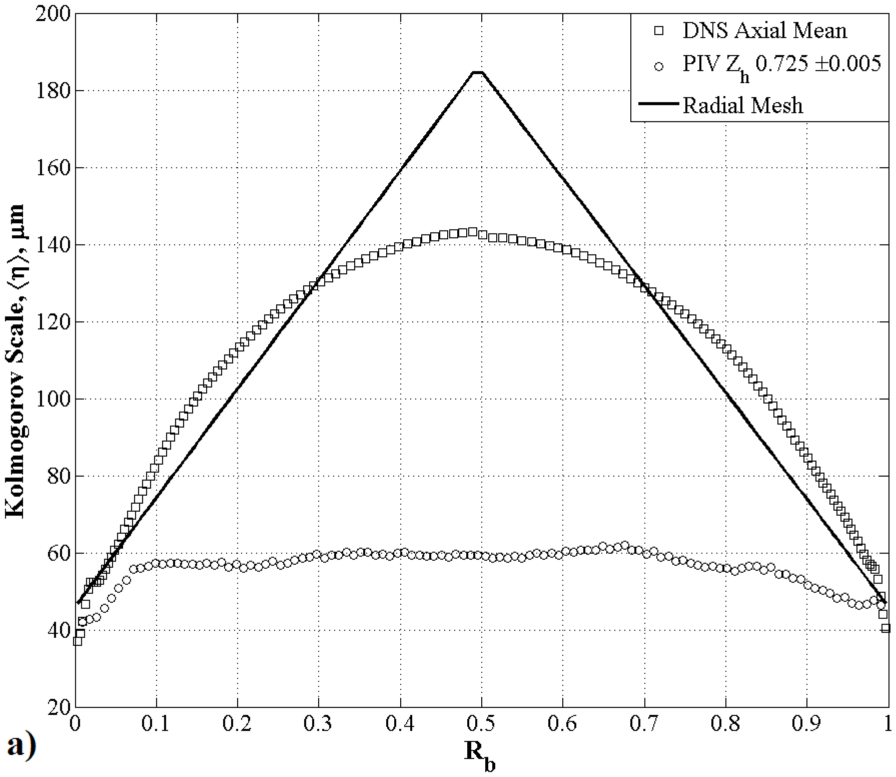

Figura 85 – The Kolmogorov estimations of the DNS model calculated through the VEDR of turbulent kinetic energy for the respective model and the mesh size.

The comparison of different turbulence models is shown in Figure 86 for the mean of all the axial profiles. It should be noted that in order to dimensionlize the y axis, the $\epsilon_{innerwall} = u_{\tau i}^4/nu$ is different for each turbulence model because the friction velocity, $u_{\tau i}$ of each respective model is considered. In addition, the estimations of the sub-grid scale model are not included in the LES models.

The estimations of the LES-WALE model were very similar to the DNS model and with a slightly higher magnitude in the bulk zone. The predictions of the LES-Smagorisnky model were the poorest among the turbulence models presented in this study. The estimations of the RANS based models were mostly on the higher side magnitude both in the bulk zone and boundary layer area. Only the SST model comparatively under-predicted in the boundary layer area in comparison to the DNS model. The predictions of the SAS-SST model were an order higher than the DNS model in the bulk zone.

The estimations of the LES-WALE model could be improved with the addition of the sub-grid scale predictions to reduce the under-prediction of VEDR of TKE in the bulk zone. However, in the case of the LES-Smagorinsky model, the under-prediction is already more than an order and the sub-grid scale prediction can not improve those drastically. In order to understand the reason behind the higher estimation of the RANS based models in

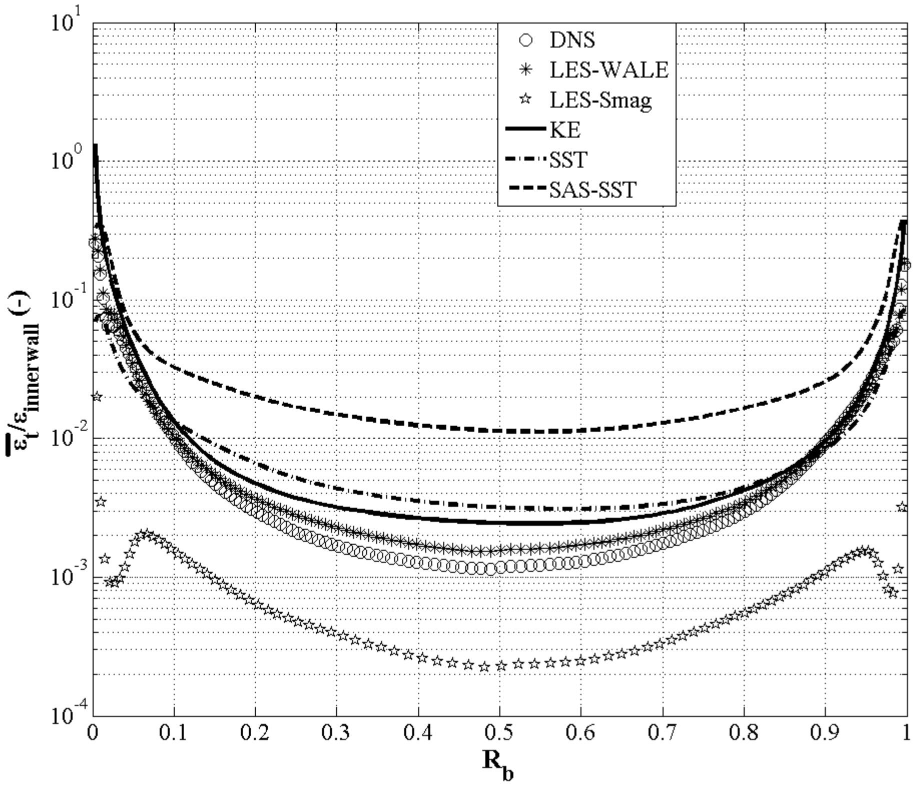

Figura 86 – The estimation of the VEDR of TKE for the different turbulence model for axial mean of all the radial profiles.

comparison to the DNS model, it is important to remember that the DNS model actually calculates the eddies while the RANS based models use a transport equation to estimate the VEDR of TKE. This makes the predictions of the DNS model much more sensitive and dependent on the grid structure in comparison to the RANS based models. The better predictions of the SAS-SST model in the bulk zone are most probably due to the induction of the "LES-like"behavior in unsteady regions of the flow field away from the wall. Near the walls, the SAS-SST model behave like an SST model because of the usage of SST wall functions.

4.7.3 Power Estimation

The power estimation was conducted for the numerical model using the torque, P=$\tau\omega$, and volume integral of the VEDR methods, P=$\underset{v}{\iiint}\rho\epsilon \mathrm{d}v$, as shown in Table 7. An analytical estimation of torque based power is also presented based on the wendt's correlation cited in Lathrop, Fineberg e Swinney (1992). The Numerical estimation of the DNS model is around 15 % lower in comparison to the analytical estimation based on the Wendt's correlation (WENDT, 1933). The numerical estimation of power based on torque was ≈ 19 % higher in comparison to the power estimated from the volume integral of VEDR method for the DNS model. Higher torque based power in comparison to the VEDR method clearly indicates under-estimation of the VEDR by around 20 %. The under-estimation is not that poor because the maximum is well predicted by the DNS model while the lower magnitude values of the bulk zone are not well estimated.

Tabela 7 – Torque and Power estimations in TVB through numerical and analytical methods.

Method	Torque (Nm)	Power-Torque (Watts)	Power-VEDR (Watts)
Numerical - DNS	0.0188	0.23	0.184
Numerical - LES-WALE	0.0199	0.24	0.188
Numerical - LES-Smagorinsky	0.042	0.5	0.21
Numerical - k-ϵ	0.041	0.49	0.597
Numerical - SST	0.025	0.3	0.092
Numerical - SAS-SST	0.0237	0.28	0.084
Numerical - RSM	0.041	0.49	0.503
Analytical - Wendt	0.022	0.27	

The predictions of the LES-WALE model are very similar to those of the DNS model for both the torque and volume integral of the VEDR methods, with the difference between these models being around 1 %. The LES-Smagorinsky and two RANS based models, $k-\epsilon$ and RSM, overestimate the torque based power by over 80 % in comparison with the analytical estimations. The SAS-SST model was more in tune with the analytical estimations with the difference being less than 6 % on the higher side; while, the SST model estimations were around 11 % higher than the analytical estimations. However, the difference between the torque and volume integral of VEDR based power was much more pronounced in the RANS based models and the LES-Smagorinsky model.

4.8 Conclusions

The main aim of this chapter was to discuss the hydrodynamics of TVB with respect to the mean velocity gradients and different turbulence parameters; such as, anisotropy, TKE and its terms, VEDR and its 12 terms, power estimation and identification of a vortex, and the effectiveness of different turbulence models for these parameters. These aspects are presented around three different locations of a Taylor vortex: outward, center of vortex and inward regions.

The anisotropy study conducted by the DNS model revealed that apart from coherence with the realizability diagram of Lumley-Newman, the prevalent state near inner and outer wall boundaries is bidimensional but towards the monodimensional state in complete accordance with literature. In the bulk zone, it was observed that the turbulence tends towards axi-symmetry in the outward and inward region and towards isotropic state in the center of vortex region; in other words, the turbulence oscillates between axi-symmetry and isotropic state in the middle of the gap-width in a Taylor-Vortex.

The division of VEDR into its mean flow and turbulent kinetic energy counterparts shed light on their behavior in the Taylor-Vortex flow. The mean flow component is higher by an order near the wall, while in the bulk zone the turbulence component is comparatively stronger. An important aspect of this study is the composition of the 12 gradients for the estimation of the VEDR. These compositions clearly showed that the three second-order radial gradients alone accounted for at-least 90 % of the VEDR of mean flow and turbulent kinetic energy through-out the reactor. While, the cross-product gradients and the gradients of the tangential direction were found to have negligible impact. The power estimations showed that the under-estimation of the VEDR is around 20 %.

Among the different turbulence models, only the LES-WALE model captured well the estimations of the DNS model for all the parameters presented here. The two-equation based models estimations were better than the RSM and the LES-Smagorinsky model for the mean velocity components. Whereas, for the Reynolds normal and shear stresses, the predictions of all of the RANS based models and the LES-Smagorinsky model were poor in comparison to the DNS model due to the Reynolds averaging process for the RANS models which dampens the turbulence content, and most probably the C_S constant for the LES-Smagorinsky model. The modeled TKE and its dissipation of the RANS model was improved magnitude wise but could not capture well the structure of these parameters. Overall, among the RANS based models, the SAS-SST model performed much better because the usage of von Karmen length-scale adjusts the local scales in the unsteady region away from walls and reduces the damping of the turbulence content.

5 An application of CFD

5.1 Problem description

The interest in culturing animal cells has increased significantly in the last 20 years due to the need of large-scale production of monoclonal antibodies, hormones, vaccines, recombinant proteins and, more recently, the production of specialized cells for applications in tissue engineering and cell therapy Agarwal (2013), Heathman et al. (2015), Mason et al. (2012). Accordingly, a wide variety of cell lines have been cultivated in the reliable, well known and easy to scale-up stirred tank bioreactor with a design adapted from the fermenters used for microbial cultures (STANBURY; WHITAKER; HALL, 1995).

However, in order to cultivate the animal cells in stirred tank bioreactor, some fine adjustments in the geometrical design of the fermenters were required to reduce the damage of cells due to shear stress, heat and contamination (STANBURY; WHITAKER; HALL, 1995). In the design one of the most important but controversial item is the bottom geometry of the tank, which as per these authors should be hemispherical or concave to ensure better mixing at lower impeller rotational speed. On the contrary, Lydersen, D'Elia e Nelson (1994a) stated that this requirement is not acceptable since there is no firm evidence to support this belief in addition to the fact that several stirred tank bioreactors with flat bottom have worked well in commercial applications and with the benefit of 50 % lower cost of the tank. Lubiniecki (1990) and Lydersen, D'Elia e Nelson (1994b) advocate the use of concave bottom, considering the usage of flat bottom to be inappropriate because of formation of stagnant regions in the bottom corners which can cause particle accumulation. In the case of animal cell culture, sedimentation problems can hinder the operation of the bioreactor during the cell adhesion process and during the actual cultivation by forming aggregates because of the large size of the particles (cells, cells clusters and microcarriers) (IBRAHIM; NIENOW, 2004).

A study conducted by Chaudacek (1985) showed that the accumulation of high density solids, such as silica, in flat bottom tanks can be eliminated by using axial impellers and implementing modifications in the geometry of the tank. Ibrahim e Nienow (2004) applied this reasoning to low density solids, such as microcarriers, and validated the geometry modification principle using rounded corners in the bottom of the tank and a conical indentation in the region under the impeller. Although, stirred tank is the first bioreactor type for culturing animal cells from laboratory scale to industrial scale, it was not until the study of Ibrahim e Nienow (2004) that there was a better definition of technical criteria demonstrating an advantage of modified bottom with respect to the flat bottom for bioprocesses. Considering the lack of information for bioreactors to culture animal cells with different geometrical conditions, carrying out studies in this direction becomes extremely interesting and necessary since the geometry modifications can greatly influence the bioprocess efficiency.

As a result of such studies, in laboratory scale bioreactors to culture animal cells, in general practice, the outer cylinder usually has a curved geometry on the bottom. The three well-known industrial suppliers of the stirred tank laboratory scale bioreactors, New Brunsswick, Infors HT and Applikon biotechnology, have curved (dished outwards) geometry of the outer cylinder. However, the demand of newer and more shear sensitive cell cultures, especially the ones using microcarriers, require newer bioreactor types that generate milder hydrodynamic forces in comparison to the stirred tank (JAIN; KUMAR, 2008). The Taylor bioreactor due to lower and uniform distribution of shear is fast becoming a strong candidate to replace the traditional stirred tank in the cultivation of animal cells by presenting a lower and more uniform shear (O'CONNOR et al., 2002; HAUT et al., 2003; CURRAN; BLACK, 2004; CURRAN; BLACK, 2005; GONG et al., 2006; TANZEGLOCK, 2008; SANTIAGO; GIORDANO; SUAZO, 2011; ZHU et al., 2010).

However, in the case of Taylor bioreactor, there is empirical evidence of accumulation of particles at the bottom of the bioreactor which hinders the process of cell adhesion and proliferation. Considering the lack of information for bioreactors using the Taylor vortex principle to culture animal cells with different geometrical conditions, carrying out studies in this direction becomes extremely important and necessary since the geometry modifications can greatly influence the bioprocess efficiency. Consequently, the shape of the outer cylinder and the height at which the inner cylinder is placed above the outer cylinder, or off-bottom clearance-obc, are considered as parameters which can lead to stagnant zones in a Taylor bioreactor. For example, if the inner cylinder is placed too high, there could be stagnant zones in the bottom of the tank because with only inner rotating cylinder tangential velocity has the biggest impact on the flow structures, thus implying that in the off-bottom clearance area there may not be sufficient amount of mixing due to weak axial flow.

However, as far as the authors are aware, the off-bottom clearance and shapes of the outer cylinder's base have not been investigated for Taylor reactor, but are of significant practical importance especially in the case of using it as a bioreactor for culture of anchorage dependent cells on microcarriers. Therefore, the main purpose of this chapter is to elucidate a favorable geometry for the particle suspension in a Taylor bioreactor at energy dissipation rates that are lower to those considered sub-lethal for the cells by providing an analysis of the flow structures and identifying the locations where the stagnation may occur using a computational fluid dynamics (CFD) validated model. Best practice numerical methods are employed, and due attention is paid to find a proper grid and time-step independence mesh. The SST turbulence model is employed in this study considering its more accurate prediction of the magnitude and location of the maxima of TKE and VEDR of TKE in a stirred vessel in comparison to the k-ϵ, SST, RSM and SAS-SST turbulence models (SINGH; FLETCHER; J., 2011). The DNS and LES models are not considered in this study due to the considerable requirements of time and computational resources for these models. The numerical model will be validated by comparison with the PIV and numerical study presented by Coufort (2004) and Coufort, Bouyer e Line (2005) on the grounds of similar radius ratio of 0.87 and 0.84 (this study), consideration of only inner cylinder rotation and similar Reynolds number of 10995 and 12000 (this study).

5.2 Computational model

5.2.1 Description of case set-up

In this study, a different configuration of the TVB was chosen in comparison to the one studied in the Chapter 2, 3 and 4. The dimensions and the geometrical characteristics of this TVB can be found in Table 8. This TVB is based on the one used by Santiago, Giordano e Suazo (2011). The rotational speed of 3.33 rps was chosen in order to have the Reynolds number closer to the fully turbulent Reynolds number (Re_T) of 13,000 (LATHROP; FINEBERG; SWINNEY, 1992) for the TVB, and in order to validate with PIV and numerical study presented by Coufort (2004) and Coufort, Bouyer e Line (2005) which was conducted at a Re number of $\approx$ 11,000. Being a single phase simulation, only water at a temperature of 20º was used as the working fluid.

Tabela 8 – Dimensions and geometrical characteristics of the TVB used for studying the different geometrical structures.

Parameters (dimensions)	Value
Inner cylinder radius, r_i (mm)	54.4
Outer cylinder radius, r_o (mm)	65
Length of the outer cylinder, L (mm)	210
Gap width, b (mm)	10.6
Off-bottom clearance, c (mm)	0, 5, 10, 15
Radius ratio, η	0.84
Aspect ratio, Γ	19.8
Rotational speed, ω (rps)	3.33
Reynolds number, Re	12,077
Taylors number, Ta	5331

Three different bottom shapes of the outer cylinder were tested: flat, dished and dished inwards, as shown in Figure 87. The geometries flat bottom and dished bottom are commonly used shapes in laboratory scale reactors; while, dished inwards shape was tested based on the idea that with this configuration type accumulation of animal cells in the middle of the bottom of the reactor could be reduced. In terms of the off-bottom clearances, c, four different values were tested, 0, 5, 10 and 15 mm, with only the flat bottom geometry of the outer cylinder. Both the dished outwards and inwards geometries of the outer cylinder had an off-bottom clearance of 15 mm. In total, six different geometries were tested: four for flat-bottom at c = 0, 5, 10 and 15 mm, and one each for dished and dished inwards at 15 mm c.

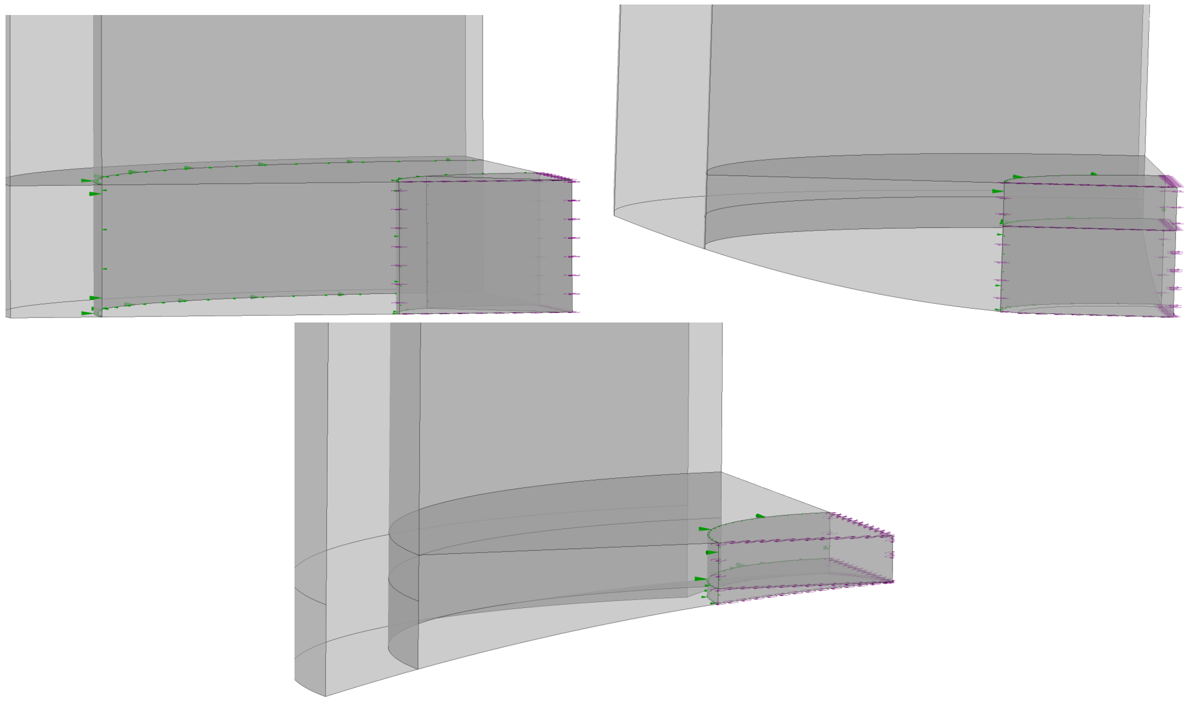

Figura 87 – Three different shapes of the outer bottom cylinder at 15 mm off-bottom clearance and 1.968×10^6, 2.24×10^6 and 2.22×10^6 node meshes, respectively, for each geometry. Green and purple markers signify interface area and periodic boundaries respectively. Please note that not all interface areas and periodic boundaries are shown here.

The geometry for each of these six test cases was divided into multiple sections: three for flat bottom geometries and four for the other two cases. The idea behind this multiple geometry was to accommodate sliding-mesh technique and implement sweep mesh on the inner and outer surfaces. Because of the impossibility of implementing the sweep mesh in the complete off-bottom clearance area, another small section was created in the off-bottom clearance area. Moreover, in the two geometries with curved surfaces on the bottom of the outer cylinder, another section was created covering the curved surfaces again in view of the implementation of the sweep mesh in the gap-width area. The top of the TVB is considered as symmetry because when working with animal cells the top is a free surface. Furthermore, due to the symmetrical flow conditions in the TVB and to reduce the computational effort, only 25 % of the geometry was modeled using cyclic symmetry.

5.2.2 Turbulence modeling

In this study, an unsteady-Reynolds averaged Navier-Stokes based SST turbulence model is used. The equations used for this model can be found in version 13.0 of ANSYS-Fluent (2010). The SST turbulence model was developed by Menter (1994), and the curvature correction that is used with the SST turbulence model is a recent development of Smirnov e Menter (2009). The curvature correction sensitizes the SST turbulence model to streamline curvature and rotation, thus correcting a key limitation of two-equation turbulence models. This curvature correction clearly improved the predictions of the SST turbulence model in a tank stirred with Rushton turbine, as shown by Singh, Fletcher e J. (2011). In addition, Poncet, Haddadi e Viazzo (2011) stated that in the core region the turbulence is almost isotropic, thereby confirming the usage of a two-equation turbulence model which assumes isotropic turbulence.

Although, these simulations were carried out with a geometrical mesh having a radial mesh value of 80 μm or in other words very close to the Kolmogorov scale, the DNS or LES models were not tested due to limited availability of computational resources and time. A DNS or LES model would have required simulating a full-scale geometry instead of one-fourth geometry being used in this case, thereby increasing the computational effort by four times. In addition, it is known that DNS and LES models requires collection of large-amount of simulated time-steps to achieve statistical averaging of data (HARTMANN; DERKSEN; AKKER, 2004). Considering the number of geometries tested, it became impractical to use either DNS or LES because of this limitation of time and computational resources.

5.2.3 Computational mesh and time-step

Simulations for grid and time-step independence study were carried out using the sliding mesh technique by separating the gap width area into two parts: one stationary outer part and second rotating inner part. Table 9 shows the different parameters that were varied and corresponding mesh sizes. The mesh was refined by adjusting the axial (H), radial (L) and angular (W) directions, so that the impact of the respective refinements can be observed in the consideration of a grid independent mesh. As one can understand that the major impact of rotation in the TVB is on the radial direction, the radial refinement has been the most studied in this grid independent mesh test. Figure 88 shows the impact of the refinements in the radial, axial and angular directions on the velocity flow field. In Figure 88, $U_{tip} = r_i\omega$ is the tip velocity and R_b = r (radial location)/b(gap-width) is the dimensionless radial coordinate.

As can be seen in Figure 88a, while looking at the comparison between Fine2L, Fine2LW and 2Fine, and between Fine3L and Fine3L2W, there is practically no improvement in the velocity flow field when the mesh is refined in the axial and angular directions, Tabela 9 – Grid independence study with the flat-bottom TVB at 5 mm off-bottom clearance.

Mesh name	No of divisions				No of nodes
	Axial	Radial		Angular	millions
		Gap-width	Rest		
Fine	210	24	108	102	0.638
Fine2L	210	48	216	102	1.225
Fine2LW	210	48	216	204	2.400
2Fine	420	48	216	204	4.718
Fine3L	210	72	324	102	1.807
Fine3L2W	210	72	324	204	3.548
Fine4L	210	96	432	102	2.393
Fine5L	210	120	540	102	2.800

even though the number of nodes have increased from 1.2 (Fine2L) to 4.7 (2Fine) millions. Whereas, an increase in the radial direction brings a significant impact on the maximum value and flow profile near the boundaries, for an increase of only around 0.6 million, i.e. from 1.2 (Fine2L) to 1.8 (Fine3L) millions. This is a result of the rotating inner cylinder generating, mainly, tangential-velocity which is spread through the radial direction in the gap-width.

In terms of the grid independence, Table 10 presents the average percentage difference between different mesh types for the mean velocity at different axial and radial locations. It can be seen that there has been a certain improvement in the results with each increment in the mesh in the radial direction. Moreover, the radial mean velocity flow profiles are very similar between Fine4L and Fine5L as shown in Figure 88b. As a result grid independence can be confirmed, and the mesh type Fine4L has been chosen for the rest of the study based on the percentage difference and qualitative analysis of the velocity flow profiles.

It can also be seen in the Figure 88b that there is little improvement in the accuracy when time-step is reduced from 1^o resolution to 0.5^o resolution using the same mesh, Fine4L, and the SST turbulence model. In addition, the average percentage difference between these two time-steps was less than 0.6 % for the mean velocity at different radial and axial locations, as shown in the Table 10. Therefore, it can be confirmed that time-step independence has been achieved with 1^o resolution for the SST turbulence model, and all further simulations were conducted with the time-step of 1^o resolution.

5.2.4 Sliding mesh or MRF technique

In the case of stirred tank, sliding mesh has proven itself to be better at estimating flow field and turbulence parameters (BRUCATO et al., 1998; LUO et al., 1993; YEOH et al., 2004; YEOH; PAPADAKIS; YIANNESKIS, 2004) in comparison to the MRF technique.

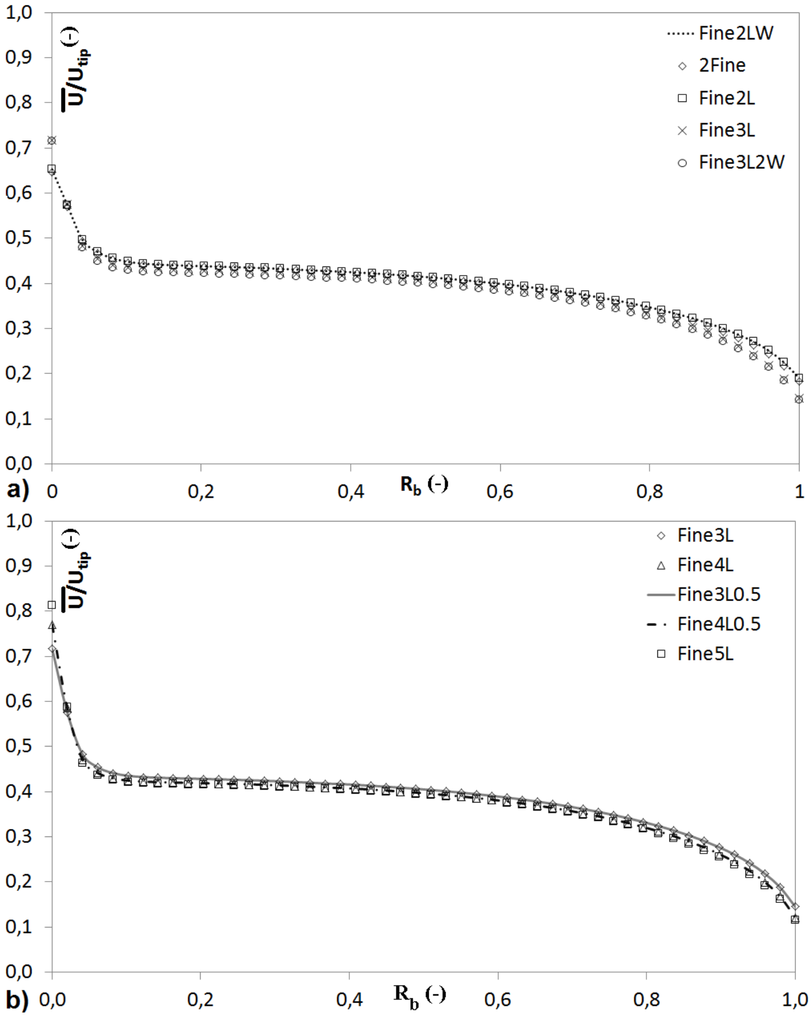

Figura 88 – Radial flow profiles of the mean velocity for the mesh and time-step independence study in the TVB with 5 mm off-bottom clearance and flat bottom at Z_L=0.57.

Tabela 10 – Mean percentage difference of the mean velocity between different meshes.

Location	2L-3L	3L-4L	4L-5L	4L1º-0.5º
Radially at Z_L=0.48	2.1	2.4	1.4	0.1
Radially at Z_L=0.57	2.7	2.2	0.8	0.1
Axially at R_b=0.009	9.7	5.8	3.8	0.3
Axially at R_b=0.047	1.8	1.5	0.9	0.1
Axially at R_b=0.094	2.1	1.8	1.6	0.6

Based on this aspect and due to personal experience of working with sliding grid (with stirred tank), the grid and time-step independence study was conducted using the sliding mesh technique. However, most of the simulations conducted in the TVB have been done using the MRF technique (COUFORT; BOUYER; LINE, 2005; HWANG; YANG, 2004; PAWAR; THORAT, 2012; PONCET; HADDADI; VIAZZO, 2011; SOBOLICK et al., 2011; WANG; VIGIL; FOX, 2005). Therefore, it became imperative to find the effectiveness of these two techniques in a TVB. Figure 89 shows the mean velocity comparison between these two methods using 4L mesh type for MRF and 4L and 5L Mesh types for SM techniques, respectively. The difference between these meshes is that the radial mesh value is of around 76, 80 and 63 μm for the 4L MRF, and 4L and 5L SM mesh types, respectively, near the inner and outer boundary walls.

It can be clearly seen in the Figure 89 that the results of the MRF technique are as good as the sliding mesh in the case of TVB. This disparity between the stirred tank and TVB should be the consequence of a simpler TVB geometry where there is only a rotating wall that is creating the flow, and which does not require a more sophisticated sliding mesh technique for improved estimations. Moreover, the sliding mesh technique is comparatively more expensive on the computational front in comparison to the MRF method. The simulation time to complete one revolution with 1^o resolution in time-step was around 35 hours for the Fine4L SM with 2.393 million node mesh, and 16 hours for the Fine4L MRF with 2.31 million node mesh. It should also be noted that the geometrical configuration for MRF technique does not require inner and outer geometries, thus geometry creation is comparatively simpler and easier. Therefore, in order to reduce computational expense, the rest of the simulations are conducted with the MRF technique using the Fine 4L MRF mesh type with 1^o resolution in time-step.

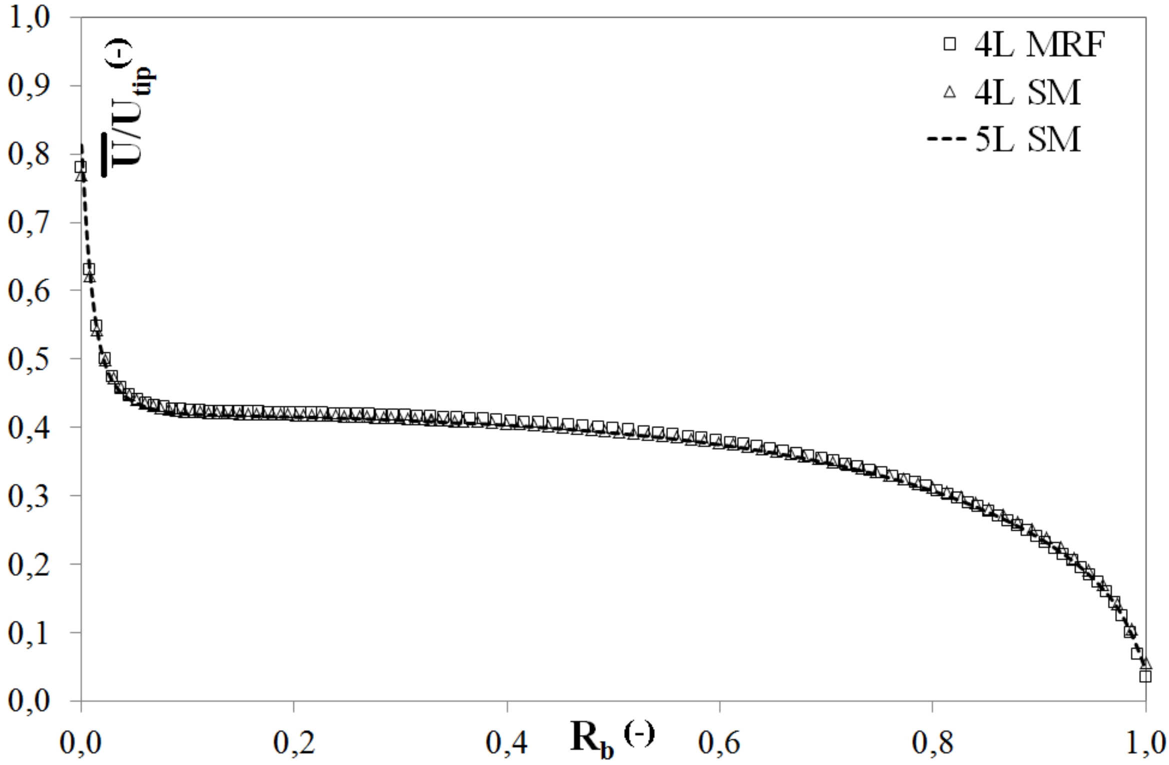

Figura 89 – Mean velocity comparisons between the sliding mesh and MRF techniques in the TVB with 5 mm off-bottom clearance and flat bottom at Z_L=0.57.

5.2.5 Computational aspects

The high resolution and second order backward Euler schemes were used to model the advection terms and transient terms, respectively, for all the equations. The Convergence criteria of 10^{-5}, which was achieved within a maximum of 5 iterations per time-step, for RMS scaled residuals was employed for the continuity, momentum and turbulence quantities. Double precision arithmetic was applied for all of the simulations. Once a pseudo steady state was achieved, the transient data was collected for only one more revolution since the acquired data would have been a repeat for each further revolution. It took around 7 revolutions to reach the pseudo steady state for each tested grid. All of these simulations were performed on a desktop with eight-core 3.2 GHz processor and 32 GB of memory. Most of the simulations were run using hpi based parallel processing with 4 cores.

5.3 Validation of the computational model

As explained earlier, the numerical results are validated by comparison with the PIV velocity results of the Coufort (2004) on the grounds of similar radius ratio of 0.87 and 0.84 (this study) and the consideration of only inner cylinder rotation, even though the aspect ratio is, 13.3 and 19.8 (this study), different. It is important to note that the velocity flow profile data presented in their study was for 70 rpm and Re= 10995 in comparison to the 200 rpm and Re=12000 in this study in order to compare similar flow conditions. Because of having similar geometrical and flow configurations, qualitative and quantitative comparisons should be considered valid. Figure 90 shows that both qualitatively and quantitatively the comparison of flow structure for the tangential velocity component is well depicted by the SST turbulence model in this study. The SST turbulence model not only predicts well the velocity flow structure and its magnitude in the boundary layer but also away from the walls in the center of the gap-width. Hwang e Yang (2004) validated their numerical results with the velocity data set of Wereley e Lueptow (1999).

Further validation is done by estimating torque numerically and empirically using the correlation of Wendt (1933) to compare the Power number obtained through these two methods. The Power number, N_P, was calculated using the Equation 5.1 used by Coufort (2004) and Douaire et al. (2010), where P represents power, b represents gap-width, ρ represents density, V represents volume of the reactor, ω represents the rotational speed and r_i represents inner cylinder radius. In both cases, the Power number is of 1.4×10^{-3}. For a Reynolds number of approximately 11000, similar to this study, Coufort (2004) also observed a Power number of 1.4×10^{-3}.

$$N_P = \frac{Pb}{\rho V \omega^3 r_i^3} \tag{5.1}$$

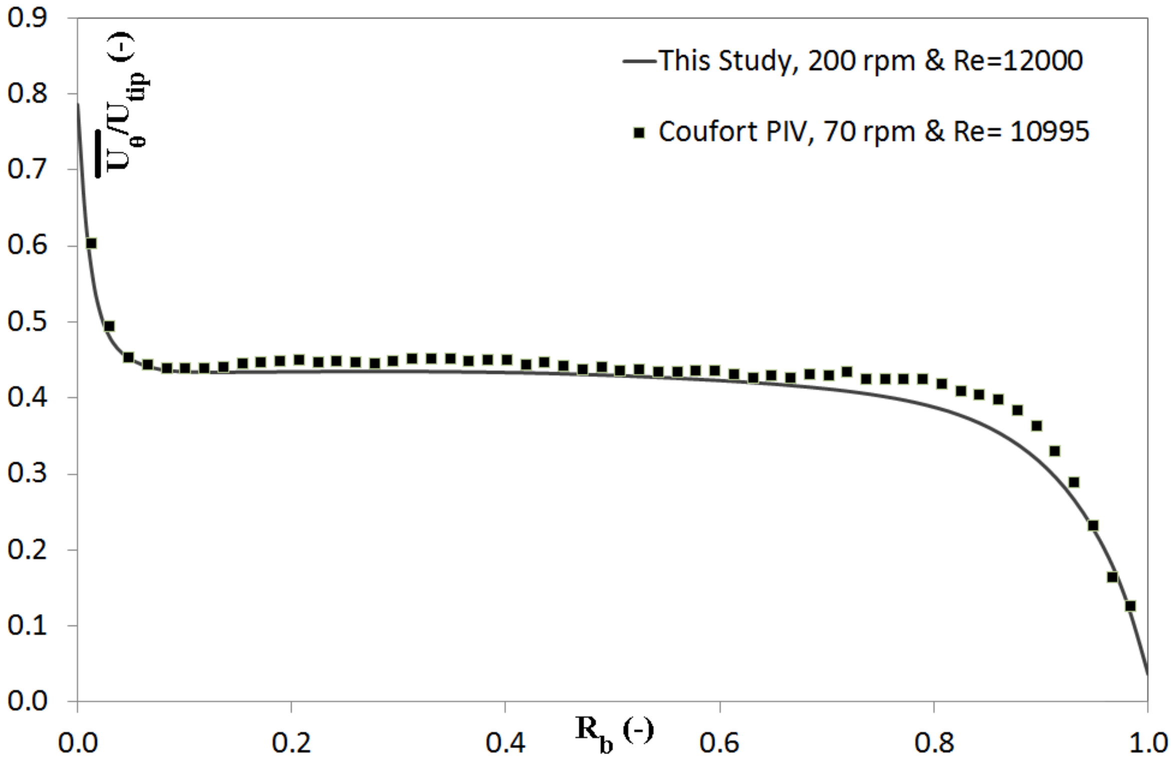

Figura 90 – Comparison of numerical tangential velocity results with the PIV results of (COUFORT; BOUYER; LINE, 2005).

5.4 Results and discussion

5.4.1 Mean velocity flow field

Figure 91 shows the velocity and its three components for an axial profile located at R_b=0.009. It clearly shows that the tangential component of the velocity is its main component. Radial component is completely negligible, while the axial component is less than 5 % of the total. Hence, here onwards only the velocity is presented which is basically composed of its tangential component.

Figure 92 presents the Taylor vortex structure through a vector profile, and Figure 93 presents the mean velocity flow profiles dimensionalized by the tip velocity, $r_i\omega$, along various dimensionless axial (Figure 93a) and radial (Figure 93b) locations marked in the legend section of the figures. In Figure 93a, the dimensionless mean velocity profiles are demonstrated at five different axial locations, from Z_L = 0.471 to 0.519, covering one pair of the Taylor-Vortex. The line with square markers represents the outward flow, and the triangle markers represent the two inward flows at the end of a Taylor-Vortex pair. A pair of Taylor-Vortex was found to be equivalent of 21 mm of axial distance, thus implying that the height of one Taylor-Vortex pair is equivalent of one-tenth of the height of the reactor, in the center of the reactor. It also shows that the height of one vortex pair is approximately double the size of gap-width. As observed by Coufort (2004) in her

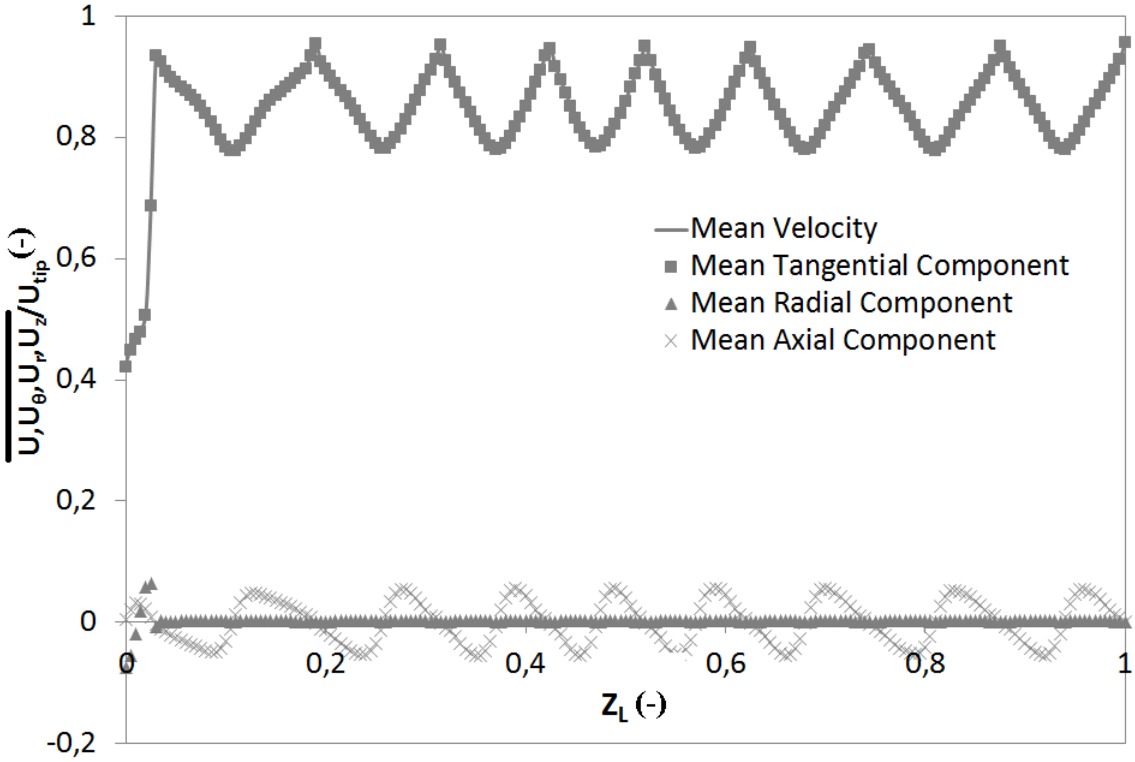

Figura 91 – Velocity and its three components in an axial profile located at R_b=0.009.

experimental PIV study, the radial velocity profiles, apart from the ones with markers, correspond to around 50 % of the velocity flow field in the 80 %, i.e. between R_b = 0.1 to 0.9 of the reactor in the gap-width.

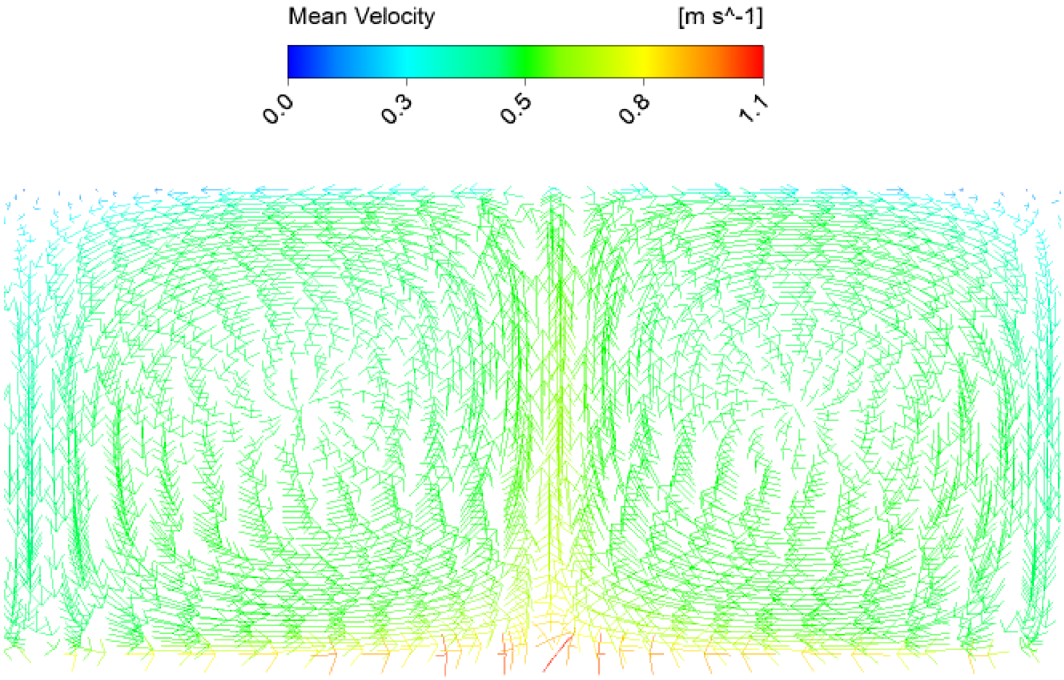

Figura 92 – Vector profile of the secondary vortex.

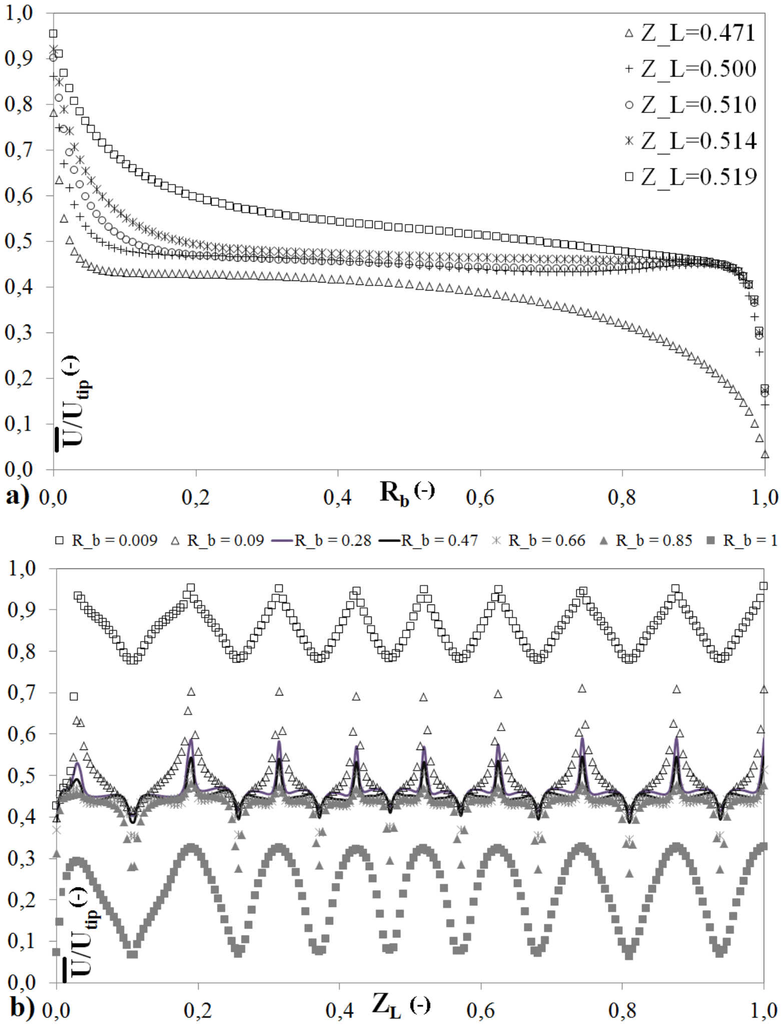

Figura 93 – Dimensionless mean velocity at various radial (a) and axial positions (b).

The vector profile (Figure 92) shows three important regions of a secondary vortex. First one can be termed as the outward region due to the direction of flow moving outwards from the inner cylinder towards the outer cylinder. It lie in the center of a Taylor vortex pair and is marked by the highest magnitude of the velocity. In this region, the inner rotating cylinder imparts momentum to the flow as it moves from the inner cylinder towards the outer; therefore, this region has the highest magnitude of the velocity, as can be seen in the radial flow profiles of the tangential velocity component (Figure 93b). The magnitude of the velocity decreases gradually as it moves from the inner towards the outer cylinder.

The second important region of a Taylor vortex pair is the center of the vortex region. There are two such regions for each the Taylor-vortex pair, one in the each opposing vortex. The importance of this region lies in the fact that the velocity profiles apart from the ones in the outward and inward region are very similar to this one, as can be seen in the radial (93b) profiles of the tangential velocity component. Kobayashi et al. (1990) termed this similarity as the uniformity in the circumferential velocity and stated that it is caused by convection of the secondary flow.

The third one is termed as the inward region because of the movement of flow is from the outer cylinder towards the inner cylinder. It is marked by the two extremities of the Taylor vortex pair and represents the weakest magnitude of the flow in a Taylor-vortex pair. Both the color map of the secondary vortex and the radial flow profile confirms that the velocity magnitude is the weakest in the inward region. It is due to the deceleration of the fluid in the outer wall where the fluid is transported by convection (KOBAYASHI et al., 1990).

Furthermore, in the axial profile of the mean velocity (Figure 93b), it can be seen that there are nine peaks in each of the axial mean velocity profile located at different radial locations from $R_b = 0.009$ to 1 . Each peak is related to the center of each Taylor-Vortex pair, or the outward flow, where the magnitude of velocity is the highest, as can be seen in the vector profile showing the Taylor-Vortex structure (Figure 92). As the width for each peak increases towards the top and bottom of the reactor, it can be affirmed that the width of the vortex is the shortest in the center of the reactor.

5.4.2 Outer cylinder's bottom shapes

Figure 94 presents vector profiles of the mean velocity for the different shapes of the outer cylinder's base. It can be seen that the dished outward and inward surfaces impact significantly the secondary vortex structure of the reactor towards the bottom. The Taylor-vortex pair which is nearer to the bottom of the reactor for Flat surfaces is pushed up for the dished surfaces. The location of first pair of Taylor-Vortex for these three different bottom surfaces is around 0.08, 0.15 and 0.23 Z_L for flat, dished outward and dished inward surfaces types, respectively. For both dished surfaces before the formation of the Taylor vortex pair, a single vortex is formed and which is much longer for the dished inwards surface in comparison to the dished outwards, as can be seen in Figures 94a and 94b. The axial profiles of velocity (Figure 95b) further confirms the formation of this single vortex and that the profiles for these three different shapes join up around $Z_L = 0.3$ from bottom, in other words, the flow structure attains similar magnitude in the rest of the axial length.

It can be seen that the dished surfaces impacts significantly the magnitude of the velocity towards the bottom of the reactor. The velocity is below 20 % of the tip velocity for $R_b < 0.4$ for dished surfaces in comparison to $R_b < 0.13$ for the flat surface, as shown in the radial velocity flow profile located at 1 mm below the inner cylinder (Figure 95a). Furthermore, for dished surfaces the velocity magnitude remains below 30 % in 70 % of the area below the inner cylinder and never attains a velocity magnitude value above 40 %. Thereby, indicating that the dead-zone, where mixing will not be efficient, is larger for dished surfaces, a pattern which can also be noticed in Figure 94.

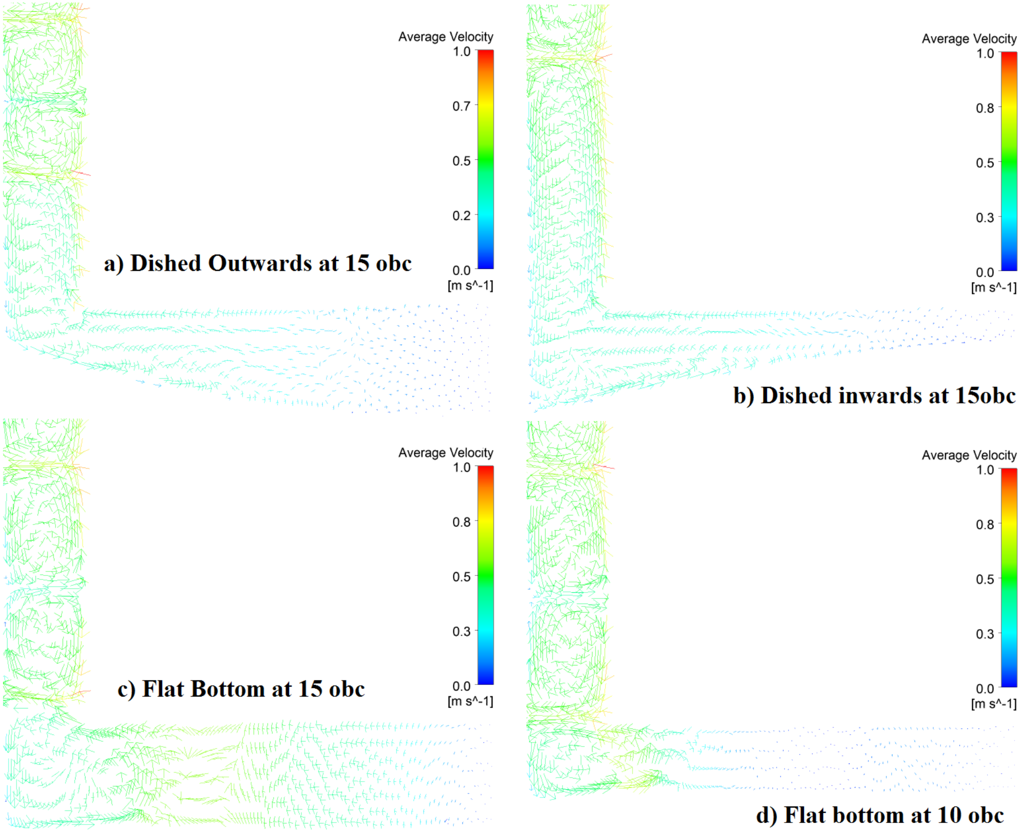
a) Dished Outwards at 15 obc

b) Dished inwards at 15obc

c) Flat Bottom at 15 obc

d) Flat bottom at 10 obc

Figura 94 – Mean velocity vectors for different shapes and off-bottom clearance areas.

Such poor magnitude values of the velocity clearly confirm the empirical observations of accumulation of particles in the bottom of reactor for the dished outwards bottom structure. This aspect will demand the usage of higher rotational velocities to pick up particles settled at the bottom of reactor for these shapes. Usage of high rotational speeds could be detrimental to growth of animal cell cultures which are highly sensitive to the hydrodynamics of the fluid. The dished outwards shape which was found to be beneficial in the case of stirred tank reactor is clearly a disruptive factor in the case of Taylor reactor. In contrast to the stirred tank, the flat bottom offers a significant advantage over the dished surfaces, especially at lower off-bottom clearance areas.

5.4.3 Off-bottom clearance

In contrast to the dished bottom surfaces, where the impact of the geometry is adversely effective up-to a certain height in the gap-width area, the off-bottom clearance area does not interfere in the flow structures of the gap-width area. As soon as the off-bottom clearance height is finished, similar flow structures with similar magnitudes develop in the gap-width area instantly, as represented by the Figures 94c and 94d. However, the off-bottom clearance area has a very big disadvantage of completely zero velocity magnitude values in the center of the obc region for all geometry types presented here. Higher the off-bottom clearance height will be, larger the volume will be with weak velocity

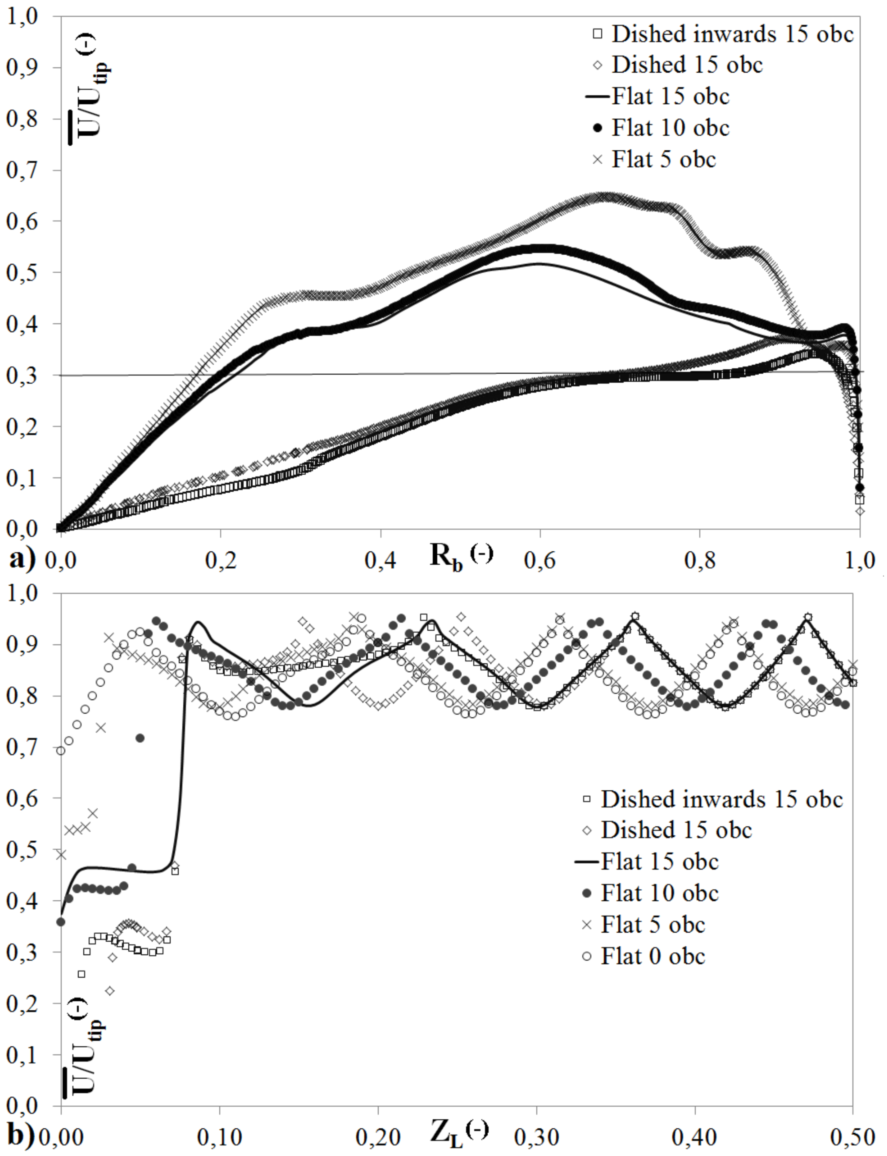

Figura 95 – Dimensionless mean velocity at different radial (a) and axial (b) positions for different geometry types.

magnitude values which lead towards the dead-zone area located in the middle of the off-bottom clearance area (94c and 94d.

The flow structure in the gap-width is generated due to the inner rotating cylinder, and is mainly tangential in nature. The axial flow is of secondary nature only, and is not strong enough to sustain flow in the off-bottom clearance area. Unless there is a change in the geometry to help generate flow in the off-bottom clearance area, it will be important to keep it to a minimum height possible. Considering the high sensitivity of the animal cell lines and that the animal cell cultures are generally operated in batch operation mode, one possible change in the geometry could be the influx of axial flow through recirculation to generate some movement in the off-bottom clearance area. However, the idea of recirculation of the fluid requires significant amount of experimental and numerical study, and it is out of scope of this study.

5.4.4 Viscous energy dissipation rate(VEDR)

In order to use the TVB as a bioreactor, the most important constraint will be to keep the VEDR within sub lethal responses of a cell line in order to achieve the desired results. Godoy-Silva et al. (2009) discovered that when the CHO (Chinese Hamster Ovary) cell line was cultured in suspension in a stirred tank bioreactor around a maximum VEDR value of 60 W/kg = $m^2 s^{-3}$, caused sub lethal physiological responses that can be considered critical to a bioprocess. CHO cell line is one of the most robust cell lines used by industries in present time, but there are many cell lines, especially the ones requiring microcarriers, which are much more sensitive and their sub lethal response should be found at a much lower value (MOLLET et al., 2004). Figure 96 depicts the response of animal cell cultures to different hydrodynamic conditions in a bioreactor. This figure was adapted from the study of Godoy-Silva et al. (2009), so for further information please consult their article.

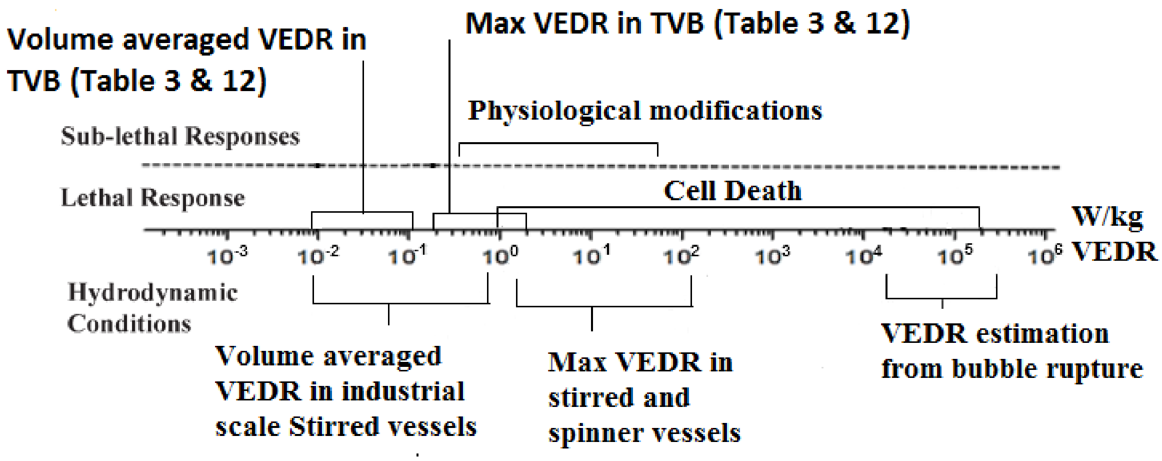
Volume averaged VEDR in TVB (Table 3 & 12)
Max VEDR in TVB (Table 3 & 12)
Physiological modifications
Sub-lethal Responses
Lethal Response
Cell Death
W/kg
VEDR
10^{-3}
10^{-2}
10^{-1}
10^{0}
10^{1}
10^{2}
10^{3}
10^{4}
10^{5}
10^{6}
Hydrodynamic Conditions
Volume averaged VEDR in industrial scale Stirred vessels
Max VEDR in stirred and spinner vessels
VEDR estimation from bubble rupture

Figura 96 – VEDR values for different hydrodynamic conditions in bioreactors and regions of lethal and sub-lethal impacts on cell lines. Adapted from Godoy-Silva et al. (2009).

Ibrahim e Nienow (2004) suggested a volume average VEDR value of 0.001 W/kg to be considered as a base line for culturing cells on microcarriers in stirred vessels. However, Kaiser et al. (2013) and Hewitt et al. (2011) have successfully cultured mesenchymal stem cells at volume averaged VEDR values of 0.0021 and 0.0034 W/kg in spinner flasks, a kind of stirred vessel. Santiago, Giordano e Suazo (2011) have successfully cultured CHO-K1 cells on microcarriers in a Taylor reactor at 50 rpm for a Reynolds no 3660 and volume average VEDR of 0.0037 W/kg. Mollet et al. (2004) advocated a more discriminative criterion of adopting the local VEDR instead of volume averaged VEDR due to large difference between these two values in some vessels such as spinner flasks, where the difference between the maximum and volume average VEDR is more than 100 times (CROUGHAN; HAMEL; WANG, 1986; HEWITT et al., 2011). This could mean that the extremely high local values in the impeller regions of stirred vessel should also be considered as an important factor as the cell damage could be due to these high local values in the impeller region instead of the small values of the volume averaged VEDR. Moreover, when culturing cells on microcarriers the size of microcarriers also play a relevant role because Croughan, Hamel e Wang (1986) and Hewitt et al. (2011) found that milder hydrodynamic forces were required for cells cultures on microcarriers in comparison to the suspension cultures.

In Table 11, the analytical estimations based on the Wendt (1933)' s empirical correlation (Equation 2.1) to estimate torque are presented alongside the numerical estimations of the torque for the SST turbulence model. The numerical estimations of torque and its derivatives are in complete sync with the analytical estimations. As per global estimates of the VEDR, the maximum value of 3.9 W/kg was obtained located at the inner wall for the rotational speed of 200 rpm. Based on the analytical estimations at 150, 100, 50 and 30 rpm, the maximum and mean VEDR value would be of 1.5 and 0.09, 0.45 and 0.033, 0.06 and 0.006, and 0.01 and 0.002 W/kg, respectively, as shown in Table 12. The range 30 to 200 rpm covers the Reynols number (Re) regions from transition to fully turbulent (Re_T), and allow a comparison with other geometries for similar value of Re/Re_T ratio.

Tabela 11 – Analytical and numerical estimations of the Taylor reactor at 200 rpm.

Parameters	Value (Dimensions)	
	Analytical	Numerical
Moment, τ	0.0077(Nm)	0.0077
Wall shear stress at inner wall, $\tau_{wi} = \tau/(2\pi r_i^2 \mathrm{h})$	1.96 (N/m^2)	1.96
Friction velocity at inner wall, $u_{\tau i} = \sqrt{\tau_{wi}/\rho}$	0.044 (m/s)	0.044
Max VEDR at inner wall, $\epsilon_{innerwall} = u_{\tau i}^4/\nu$	3.86 ($m^2 s^{-3}$)	3.88
Global power, P=$\tau\omega$	0.16 (Watts)	0.16
Average VEDR, $\langle\epsilon\rangle = P/(\rho\pi(r_o^2 - r_i^2)\mathrm{h})$	0.192 (W/kg)	0.193
Average Kolmogorov's micro-scale, $\langle\eta\rangle = (\nu^3/\langle\epsilon\rangle)^{\frac{1}{4}}$	47.7 (μm)	47.7

Tabela 12 – Summary of VEDR and Kolmogorov micro-scales for different geometrical conditions.

Group	Geometry	Rotational velocity	Reynold's No.		VEDR Max/Mean	Kolmogorov Min/Mean
		rpm	(-)	Re/Re_T	W/kg	μm
This study	TVB	200	12077	0.93	3.88/0.193	23/48
		150	9058	0.70	1.51/0.09	29/58
		100	6039	0.46	0.45/0.033	39/74
		50	3019	0.23	0.06/0.006	65/115
		30	1812	0.14	0.01/0.002	95/158
Kaiser et al. (2013)	Spinner	105	3014	0.15	0.58/0.004	38/133
		50	1435	0.07	0.062/0.0006	66/228
Hewitt et al. (2011)	Spinner	50	1690	0.08	(-)/0.0034	(-)/131

In order to compare the data with a different geometry type Re/Re_T ratio will be used as the criteria based on the study of Lathrop, Fineberg e Swinney (1992). Here Re_T is the Reynolds number related to fully turbulent Reynolds number, and its value for stirred vessels is known to be 2×10^4 and in the case of Taylor reactor Lathrop, Fineberg e Swinney (1992) have shown that $Re_T = 1.3 \times 10^4$. First of all, the impeller rotational speed is not used because it becomes irrelevant for different scales and geometry types. Reynolds number is relevant for the different scales of the same geometry, but when the geometry is changed the significance of Reynolds number also changes as Re_T values are different for different geometry types: the Re_T values for stirred vessels, Taylor-Couette reactor, pipe flow and flat plate are 2×10^4, 1.3×10^4, 2.3×10^4 and 3.2×10^5, respectively (LATHROP; FINEBERG; SWINNEY, 1992). Therefore, for a better comparison between different geometry types, the Re/Re_T ratio presents the option of comparing similar turbulence flow conditions.

For similar Re/Re_T ratio of ≈ 0.14 in comparison with the spinner vessel of Kaiser et al. (2013), the max and mean VEDRs are around 50 and 2 times lower. In comparison with the spinner vessel study of Hewitt et al. (2011), at a slightly higher Re/Re_T value of 0.14 the mean VEDR is practically half the value. In addition, the difference between the maximum and mean value for the spinner vessel is more than 100 times, as mentioned earlier, in comparison to around 10 times for the Taylor reactor. This clearly indicates that the flow is less uniform in spinner vessels in comparison to the Taylor reactor.

In a Taylor reactor, it is important to note that the maximum value is only achieved in the viscous sub-layer very near to the wall where the cells may never reach due to the nature of the viscous layer of providing resistance to any kind of transfer. Away from the wall, the VEDR decreases extremely rapidly and its magnitude is much smaller than the maximum value (COUFORT; BOUYER; LINE, 2005; TOKGOZ et al., 2012; HOUT; KATZ, 2011). It can be further confirmed by the fact that the volume average VEDR, $\langle\epsilon\rangle$, was found to be 0.193 based on numerical simulations (Table 11). The animal cells are bound to spend the maximum amount of time within a Taylor-vortex in the bulk zone, between Rb = 0.1 to 0.9, where the gradients are much smaller and have similar magnitude (COUFORT; BOUYER; LINE, 2005; TOKGOZ et al., 2012; HOUT; KATZ, 2011), i.e., similar hydrodynamic conditions in the major part of the reactor. This is a significant advantage for a Taylor reactor to be used as a bioreactor for culturing animal cells in comparison to the spinner vessel where the probability of cells reaching the high gradient region near the impellers is high and the fluid flow conditions are less uniform. These aspects clearly demonstrate the possibility of using the Taylor reactor not only for the suspended cell cultures but also in the case of the microcarrier systems.

The mean Kolmogorov scale, $\langle\eta\rangle = (\nu^3/\langle\epsilon\rangle)^{1/4}$ was found to be around 47.7 μm at 200 rpm for both the analytical and numerical estimations (Table 11). As the magnitude of the VEDR decreases with the decrease in the rotational speed, the Kolmogorov scale increases being inversely proportional to the VEDR. Therefore, at 150, 100 and 50 rpm the mean Kolmogorov scale would be 58, 74 and 115, respectively, based on the analytical estimations as shown in Table 12. In terms of comparison with the spinner flask bioreactor of Kaiser et al. (2013), it can be seen that for similar Re/Re_T ratio of ≈ 0.14 the minimum Kolmogorov scale value is 2.5 times bigger, while the mean Kolmogorov scale is also comparatively on the higher side. In comparison with the study of Hewitt et al. (2011) who also used the spinner vessel, the mean Kolmogorov scale was found to be much higher in the present study of Taylor reactor even though the Re/Re_T ratio was comparatively higher.

The Kolmogorov scale has significant importance for the culturing of animal cells in bioreactors in suspension and on microcarriers. Kunas e Papoutsakis (1990) observed increase in the cell damage due to the fluid hydrodynamic forces for cell culture in suspension when the Kolmogorov eddy size approaches the cell size. They conducted these experiments in the absence of the bubbles to clarify that the damage is directly related to fluid hydrodynamic forces only. At the same time, there is no proof if there is any interaction between the cells and eddies or how the cells are damaged. Although, there may not be a direct relation with the Kolmogorov scale and a certain amount of turbulence might be necessary to ensure adequate mixing and mass transfer within the bioreactor, a significant amount of turbulence is known to damage the animal cells. Smith e Greenfield (1992) managed to culture the animal cells at a Reynolds No. of 25,000 in a tank stirred with Rushton turbine at a rotational speed of 600 rpm with estimated maximum and mean VEDR of 21.8 and 0.697 m^2s^{-3} (SINGH, 2011), respectively, corresponding to the minimum and mean Kolmogorov scale of 15 and 35 μm.

For the animal cell cultures requiring microcarriers even milder hydrodynamics forces are required in the bioreactor (IBRAHIM; NIENOW, 2004). Croughan, Hamel e Wang (1986) and Hewitt et al. (2011) observed damage to cells when the Kolmogorov eddy size was below the $2/3^{rd}$ of the size of the microcarriers, and at half of the size of the microcarriers the damage to cells was detrimental. They worked with the microcarriers of the size of 183 and 175 μm, respectively, and found no damage to cells when the eddy sizes were above 120 μm. On the other hand, Kaiser et al. (2013) did not detect any cell damage for microcarriers of the size of 180 μm for a value of minimum Kolmogorov scale of 44 μm. It should be remembered that the Kolmogorov theory should be looked at critically when the Reynolds number is less than 104 because of the necessity of highly turbulent flow in the vessel for it to be applicable (HEWITT et al., 2011; KAISER et al., 2013).

Although, the suspended cell culture systems have been cultured at high Reynolds number, the microcarrier systems have always been cultured around the just suspension speed which is normally much lower than then Re_T, in order to avoid cell damage. Croughan, Hamel e Wang (1986) and Hewitt et al. (2011) have suggested of increasing the kinematic viscosity around when working with microcarrier culture systems. Increasing the kinematic viscosity will result an increase in the Kolmogorov scale being directly proportional to it, but will also reduce the Reynolds number and making the Kolmogorov theory more questionable (HEWITT et al., 2011). Considering that the microcarrier culture systems will always be cultivated in the transition region and the questionable application of Kolmogorov theory in this region, it is more prudent to use the maximum and/or local values of VEDR in conjunction with the microcarrier size as the criteria to relate to cell death or damage for the microcarrier culture systems.

5.5 Conclusions

The aim of this study was to understand the impact of the changes in the geometrical configuration, namely, off-bottom clearance area and different bottom shapes of the outer cylinder, of a Taylor bioreactor on its flow structure and its practical impact on being used as a bioreactor. Considering the time, computational cost and the effectiveness of the different unsteady RANS based turbulence models (SINGH; FLETCHER; J., 2011), the SST turbulence model was used to observe the flow profiles in these different geometry types. A grid and time-step independence analysis was also conducted, along with the implementation of best numerical practices, and the comparison of the sliding mesh and MRF technique.

Grid independence study showed that the grid size equivalent to that of Kolmogorov scale is necessary for complete grid independence, which in turn will require a significant computational effort. Sliding mesh technique, which is necessary in the case of stirred tank simulations, did not improve on the simulations conducted using the MRF technique in the Taylor reactor. Sliding mesh is not only computationally more expensive but its implementation also requires a comparatively more complex geometry. It is understood that the effectiveness of the MRF technique is due to the simpler Taylor reactor geometry which only requires the rotation of inner cylindrical wall. Therefore, it is practical to use MRF technique in simpler geometrical cases such as that of Taylor reactor.

The radial velocity flow profile showed that within 80 % of the gap-width between R_b= 0.1 to 0.9, the magnitude of the velocity is constant at around 50 % of the tip velocity. The maximum value of the VEDR was found to be 3.88 W/kg at a rotational speed of 200 rpm. This value is much smaller than the sub-lethal value of 60 W/kg for the CHO cell lineage, but other cell lines may be much more sensitive compared to the more established CHO cell line. Additionally, the maximum value of VEDR is only attained on or very near to the wall in the thick viscous sub-layer where the cells may never reach due to the viscous sub-layer for providing resistance to momentum, mass and energy transfer. Away from the walls in the bulk region comprising of the 80 % of the gap width, the VEDR values are much smaller and of similar magnitude values. This aspect is of great consequence because in the case of animal cell cultures, the cell lines within the Taylor bioreactor will spend most of the time in the vicinity of these values of similar and weak magnitude, and only a fraction of its times will be spent near the high gradients located near the wall.

The observation of accumulation of animal cells on the bottom of the dished surfaced reactor which led to this study is confirmed through the flow profiles where it can be seen that the magnitude of the velocity is below 30 % for 70 % of the reactor. Whereas, the idea that dished inward surface could have aided in reducing the dead zone are in the bottom of the reactor is proved wrong, as the velocity magnitude for this surface is smaller as compared to the dished outward. In comparison to the curved surfaces, the flat surface for the outer cylinder has the least adverse effect on the gap-width area for similar off-bottom clearance areas.

The height of off-bottom clearance area also impacts the flow structures adversely, and if feasible should be avoided or kept to the minimum possible value. Higher the off-bottom clearance area, larger the volume there is in the dead-zone area due to incapability of the inner rotating cylinder to impart any sort of momentum to the fluid lying in the off-bottom clearance area. Unless there is design change to enhance mixing in the off-bottom clearance area, it can be concluded that to avoid dead zones on the bottom of the reactor, and to enhance mixing, dished surfaces on the bottom of the reactor should be avoided along with off-bottom clearance area. Flat bottom surface with zero off-bottom clearance is ideal in the case of using Taylor bioreactor to work with animal cell cultures especially when cultivated on the microcarriers to avoid accumulation of microcarriers, and thus animal cell cultures in the quasi stagnant zone of the off-bottom clearance area. Perhaps, a future experimental and numerical study on the recirculation to generate some axial flow in the off-bottom clearance area could improve this geometrical constraint.

In comparison with the spinner vessel for similar Re/Re_T ratio, the maximum and mean VEDRs were always found to be of lower magnitude values. In similar aspect, the minimum and mean Kolmogorov scales were found to be always on the higher. Additionally, due to much less difference between the maximum and the mean values, the Taylor reactor presents more uniform structures in comparison to the spinner vessel. In this sense, the local and maximum VEDR value is also an important criterion to observe and compare with the cell death or damage in bioreactors. These attributes clearly confirm that the Taylor reactor is adequate for culturing of animal cells not only in suspension but also for the microcarrier culture systems.

6 Conclusions

The main of this thesis was to understand in detail the hydrodynamics of the TVR with regards to its feasibility as a bioreactor for cultivating animal cell lines of biotechnological interest. Two different methods were used to study the TVR: an experimental 2D-PIV and numerical CFD. Considering the importance of the VEDR in the characterization of the cell death, it was sought that the smallest feasible spatial resolution be achieved for both the experimental and numerical methods, in order to achieve a grid structure closest to the Kolmogorov micro-scale of turbulence. Special attention was paid to all the basic aspect of the experimental, PIV and numerical, CFD, methods. In addition, two important geometrical configurations, namely off-bottom clearance area and outer cylinders bottom shape, were studied with the numerical method to understand their impact on the flow structure and the usage of the TVR as a bioreactor.

In order to capture the smallest feasible spatial resolution, limited by technological advancements and/or cost, for the PIV method, all basic parameters, such a size and concentration of particles, time-step between the double frame image, ICS window and overlap ratio, were found to play a significant role and have to be chosen carefully as they are inter-dependent. Smaller the size of ICS window, smaller the spatial resolution will be, but will also require smaller size of particles and time-step while maintaining an optimum concentration. The overlap ratio comes into play when the ICS window is grid-dependent; otherwise, overlap ratio basically only increases the number of data points. Each increase in the overlap ratio, decreases the spatial resolution, but again attention will be required in choosing the size of particles, their concentration and the time-step. Although, the results may improve for an increase in the overlap ratio by reducing the spatial resolution, the overlap ratio does not represent true spatial resolution because its results are obtained by manipulating the basic ICS grid structure at 0 % overlap ratio.

The PIV being a 2D method, only two out of three mean and three out of six fluctuating velocity components, and, hence, five out of 12 gradients of these mean and fluctuating velocity components were available. The mean radial velocity component was found to be only 10 % of the tangential components, and the axial components is also in the same range. The maxima of this radial component was found in the center of the gap-width in the outward and inward region in the shape of upward and downward parabolas, respectively; whereas, the maxima of the tangential component was on the inner wall due to the inner rotating cylinder. A new analytical expression was derived for the mean tangential velocity component in the center of vortex region, and it was found to fit the measurements much better than the classical log law expression. Such strong tangential flow implies that it will have a strong contribution in the kinetic energy and its dissipation, and demonstrated the importance of a very fine radial grid to capture its propagation from the rotating inner wall towards the stationary outer cylindrical wall.

The normal tangential stress had two local maximas, one near each wall, because of the steep decreases in the boundary layer area in the tangential velocity component, and the bulk zone had much smaller and similar magnitude values due to the near constant magnitude of the mean tangential velocity component in the bulk zone. The normal radial stress had its maxima located in the center of gap-width but its magnitude was found to be around 5 times smaller than the tangential normal stress. The radial tangential shear stress was found to be around 15 times smaller than the maxima of the tangential normal stress.

The VEDR of mean flow kinetic energy is mainly composed of the $(\frac{\partial(\overline{U_\theta}/r)}{\partial r})^2$ gradient, and the gradient, $\overline{(\frac{\partial(u'_\theta/r)}{\partial r})^2}$ is the major component of the turbulence VEDR especially in the boundary layer area. Such a huge of single gradient on the VEDR estimations render the application of isotropic and axi-symmetric assumptions to be invalid in this case and leads to over-estimation. The VEDR was found to be stronger in the boundary layer area where the viscous forces are dominant, while the dissipation of turbulent kinetic energy was at-least an order higher than its mean flow counterpart in the bulk zone.

However, the limited number of results that can be achieved due to practical reasons is one of the shortfalls of the experimental method, and is one of the main reason behind the popularity of the numerical methods which gives access to the whole geometry. Another shortcoming is being the 2D method, though there are 3D methods available but the spatial resolution is significantly coarser. Nonetheless, the experimental methods are still important because they provide true picture of flow structures which help in validation of the numerical methods, and demonstrating their limitations.

The validation of the DNS model showed the necessity of improvement in the grid structure of the numerical mesh, not only in the axial and tangential directions where the nodes were coarser but also in the radial direction, especially the bulk zone where significant underestimation of the VEDR of TKE was observed in spite of a radial mesh size of 184 μm in the center of gap-width. The improved mesh size would result in something of the order of 100 of millions of nodes, and was not practical in the present case scenario. However, this will help in generating a better grid structure in the laboratory scale TVR of much smaller size. Overall, despite the ideal criteria of 100 % concordance was not achieved between the numerical and experimental methods, the qualitative comparison was very good with the shape and structure of the flow being well predicted for all the presented parameters. Quantitatively, the mean velocity components and its gradients were in good agreement with PIV data, but the fluctuating velocity components and their gradients were underestimated due to the comparatively poor grid structure. Considering the clear evidence of good amount of concordance, especially the good qualitative comparison, between these two methods which indicates that results are not hypothetical, these numerical results can be considered validated.

The 3D numerical simulations gave access to certain parameters which were not accessible with a 2D PIV method, such as vortex identification, anisotropy, and all 12 gradients of the VEDR. Vortex identification using the λ_2-definition method showed the excessive damping of turbulence by the RANS based model which was found to improve significantly with the SAS-SST model, also a RANS model but with an improvement in turbulence length scale which adjusts it to the directly resolved turbulence structures. Among the different turbulence models, the RSM and LES-Smagorinsky presented the worst comparison with the DNS model even for the mean velocity components. The two equation turbulence models, namely, k-ϵ, SST and SAS-SST, captured well the mean velocity components but were also poor in the prediction of the Reynolds normal and shear stress. Although, the modeled TKE and its dissipation for the RANS based model improved significantly, these models could not capture well the structure of these parameters in comparison with the DNS model. Only the LES-WALE model's estimations were in sync with the DNS model for all of the parameters presented here.

The anisotropy study revealed that near the walls bi-dimensionality is the prevalent state; while, in the bulk zone the isotropic state is found in the center of vortex region, and oscillates towards the axisymmetry state towards the outward and inward regions. The composition of the 12 gradients of the VEDR further confirmed that the $(\frac{\partial(\overline{U_\theta}/r)}{\partial r})^2$ and $\overline{(\frac{\partial(u'_\theta/r)}{\partial r})^2}$ gradients are the major components of the VEDR of the mean flow and turbulent kinetiec energy, respectively. Additionally, the three second-order radial gradients alone accounted for at-least 90 % of the VEDR of mean flow and turbulent kinetic energy through-out the reactor. A significant advantage is that these numerical results are available through-out the geometry in complete contrast with the experimental results which are available only at a particular location for each experiment. The downside is the time of around 1-4 months to achieve statistically converged solutions, based on present computational resources and depending upon the chosen turbulence model.

The geometrical features of curved surface of outer bottom and off-bottom clearance area which are of practical importance in stirred vessels, impact adversely the flow structures in the Taylor bioreactor due to poor axial velocity component. The magnitude of the velocity remained below 30 % for 70 % of the reactor for the curved surfaces, while the flat surfaces offered the least adverse effect on the gap-width area of the TVR. Flat bottom surface with zero off-bottom clearance were found to be the ideal case scenario because increase in the off-bottom clearance area presented larger volume of the dead-zone area due to incapability of the inner rotating cylinder to impart any sort of momentum to the fluid lying in the off-bottom clearance area. Perhaps, as part of the future work different feasibility studies can be conducted in order to enhance flow in the off-bottom clearance area. One possible option is create an influx of axial flow through recirculation to generate some movement in the off-bottom clearance area.

The most significant advantage of the TVR to be used as a bioreactor is that in the bulk zone comprising of the 80 % of the gap-width area, where the cell cultures will spend most of the time, the velocity magnitude is of around 50 % of the maximum and VEDR values are around 10 times smaller in comparison to the boundary layer area. This clearly confirms that the cell cultures will have similar and milder hydrodynamics forces, and should be considered as encouraging factor to culture animal cells. In comparison with the spinner vessel for similar Re/ReT ratio, the maximum and mean VEDRs were always found to be of lower magnitude values, and due to much less difference between the maximum and the mean values, the Taylor bioreactor presents more uniform structures in comparison to the spinner vessel. These attributes further confirm that the Taylor bioreactor is adequate for culturing of animal cells not only in suspension but also for the microcarrier culture systems.

As these studies were conducted as a single phase study, the next step will be to conduct a multiphase study with the microcarriers both as a discrete phase and continuous phase. The multiphase study will not only help in observing the behavior of these particles in a Taylor-Vortex but also directly and/or indirectly estimating the stresses that these microcarrier particles might encounter. This multiphase study should also shed some light on the estimation and verification of just suspension speed, sedimentation and aggregate formation. On the other hand, the cells will be cultured in the TVR at three different scales to observe the feasibility of using it an industrial scale. Finally, the VEDR obtained from the numerical study will be correlated with the animal cell culture experiments to formulate a general model on the impact of hydrodynamics on animal cell cultures with and without microcarriers.

Referências

ABIDE, S.; VIAZZO, S. A 2d compact fourth-order projection decomposition method. *Journal of Computational Physics*, v. 206, n. 1, p. 252–276, 2005. Citado na página 40.

ABU-REESH, I.; KARGI, F. Biological responses of hybridoma cells to defined hydrodynamic shear stress. *Journal of Biotechnology*, v. 9, p. 913–919, 1989. Citado na página 34.

AGARWAL, A. Advent and maturation of regenerative medicine. *Tissue Engineering and Regenerative Medicine*, v. 10, n. 4, p. 155–159, 2013. Citado na página 157.

AKONUR, A.; LUEPTOW, R. M. Three-dimensional velocity field for wavy taylor-couette flow. *Physics of Fluids*, v. 15, n. 4, p. 947–960, 2003. Citado na página 37.

ALOI, L. E.; CHERRY, R. S. Cellular response to agitation characterized by energy dissipation at the impeller tip. *Chemical Engineering Science*, v. 51, n. 9, p. 1523–1529, 1995. Citado na página 35.

ALOI, L. E.; CHERRY, R. S. Cellular response to agitation characterized by energy dissipation at the impeller tip. *Chemical Engineering Science*, v. 51, n. 9, p. 1523–1529, 1996. Citado na página 34.

ANSYS-FLUENT. [S.l.]: http://www.ansys.com/, 2010. Citado 2 vezes nas páginas 97 e 161.

AUBIN, J.; FLETCHER, D. F.; XUEREB, C. Modeling turbulent flow in stirred tanks with cfd: the influence of the modeling approach, turbulence model and numerical scheme. *Experimental Thermal and Fluid Science*, v. 28, n. 5, p. 431–445, 2004. Citado na página 101.

BAKKER, A.; OSHINOWO, L. M. Modelling of turbulence in stirred vessels using large eddy simulation. *Chemical Engineering Research and Design*, v. 82, n. 9, p. 1169–1178, 2004. Citado na página 98.

BALDI, S.; YIANNESKIS, M. On the quantification of energy dissipation in the impeller stream of a stirred vessel from fluctuating velocity gradient measurements. *Chemical Engineering Science*, v. 59, n. 13, p. 2659–2671, 2004. Citado na página 37.

BARTELS, C. et al. Computational fluid dynamics applications on parallel-vector computers: computations of stirred vessel flows. *Computers and Fluids*, v. 31, n. 1, p. 69–97, 2002. Citado na página 98.

BILSON, M.; BREMHORST, K. Direct numerical simulation of turbulent taylor-couette flow. *Journal of Fluid Mechanics*, v. 579, p. 227–270, 2007. Citado 12 vezes nas páginas 39, 71, 106, 111, 117, 123, 125, 127, 129, 135, 136 e 137.

BRAUCKMANN, H. J.; ECKHARDT, B. Direct numerical simulations of local and global torque in taylor–couette flow up to re = 30 000. *Journal of Fluid Mechanics*, v. 718, p. 398–427, 2013. Citado na página 39.

BRIONES, M. A. G.; CHALMERS, J. J. Flow parameters associated with hydrodynamic cell injury. *Biotechnology and Bioengineering*, v. 44, p. 1089–1098, 1994. Citado na página 33.

BRUCATO, A. et al. Numerical prediction of flow fields in baffled stirred vessels: A comparison of alternative modelling approaches. *Chemical Engineering Science*, v. 53, n. 21, p. 3653–3684, 1998. Citado na página 162.

CHAUDACEK, M. W. Solids suspension behaviour in profiled bottom and flat bottom mixing tank. *Chemical Engineering Science*, v. 40, n. 3, p. 385–392, 1985. Citado na página 157.

Chapter three - taylor-vortex bioreactors for enhanced mass transport. In: CHAUDHURI, J.; AL-RUBEAI, M. (Ed.). *Bioreactors for Tissue Engineering-Principles,Design and Operation*. P.O. Box 17, 3300 AA Dordrecht, The Netherlands: Springer, 2005. p. 47–86. Citado na página 33.

CHISTI, Y. Hydrodynamic damage to animal cells. *Critical Reviews in Biotechnology*, v. 21, p. 67–110, 2001. Citado na página 34.

CHU, L.; ROBINSON, D. K. Industrial choices for protein production by large-scale cell culture. *Current Opinion in Biotechnology*, v. 12, p. 180–187, 2001. Citado na página 32.

CHUNG, S. Y.; SUNG, H. J. Large-eddy simulation of turbulent flow in a concentric annulus with rotation of an inner cylinder. *International Journal of Heat and Fluid Flow*, v. 26, n. 2, p. 191–203, 2005. Citado 10 vezes nas páginas 39, 40, 106, 111, 129, 135, 136, 137, 142 e 146.

COSTA, A. R. et al. Guidelines to cell engineering for monoclonal antibody production. *European Journal of Pharmaceutics and Biopharmaceutics*, v. 74, p. 127–138, 2010. Citado na página 32.

COUFORT, C. *Analyse experimentale de la floculation en reacteur de Taylor-Couette: Influence de l'hydrodynamique sur les phenomenes d'agglomeration et de rupture*. Tese (Doutorado) — Institut National des Sciences Appliquées (INSA) de Toulouse, 2004. Citado 3 vezes nas páginas 159, 165 e 166.

COUFORT, C.; BOUYER, D.; LINE, A. Flocculation related to local hydrodynamics in a taylor–couette reactor and in a jar. *Chemical Engineering Science*, v. 60, n. 8-9, p. 2179–2192, 2005. Citado 7 vezes nas páginas 15, 37, 39, 159, 163, 166 e 174.

CROUGHAN, M. S.; HAMEL, J. F.; WANG, D. I. C. Hydrodynamic effects on animal cells grown in microcarrier cultures. *Biotechnology and Bioengineering*, v. 95, n. 2, p. 295–305, 1986. Citado 4 vezes nas páginas 172, 173, 175 e 176.

CURRAN, S. J.; BLACK, R. A. Quantitative experimental study of shear stresses and mixing in progressive flow regimes within annular-flow bioreactors. *Chemical Engineering Science*, v. 59, n. 24, p. 5859–5868, 2004. Citado 2 vezes nas páginas 33 e 158.

CURRAN, S. J.; BLACK, R. A. Oxygen transport and cell viability in an annular flow bioreactor: Comparison of laminar couette and taylor-vortex flow regimes. *Biotechnology and Bioengineering*, v. 89, n. 7, p. 766–774, 2005. Citado 2 vezes nas páginas 33 e 158.

DELAFOSSE, A. et al. Estimation of the turbulent kinetic energy dissipation rate from 2d-piv measurements in a vessel stirred by an axial mixel ttp impeller. *Chemical Engineering Science*, v. 66, n. 8, p. 1728–1737, 2011. Citado 9 vezes nas páginas 37, 59, 60, 61, 83, 84, 85, 86 e 112.

DELAFOSSE, A. et al. Les and urans simulations of hydrodynamics in mixing tank: comparison to piv experiments. *Chemical Engineering Research and Design*, v. 86, n. 12, p. 1322–1330, 2008. Citado na página 40.

DENG, R. et al. Taylor vortex flow in presence of internal baffles. *Chemical Engineering Science*, v. 65, n. 16, p. 4598–4605, 2010. Citado na página 37.

DERKSEN, J.; AKKER, H. E. Van den. Large eddy simulations on the flow driven by a rushton turbine. *American Institute of Chemical Engineers. AIChE Journal*, v. 45, p. 209–221, 1999. Citado na página 40.

DONG, S. Direct numerical simulation of turbulent taylor-couette flow. *Journal of Fluid Mechanics*, v. 587, p. 373–393, 2007. Citado na página 39.

DOUAIRE, M. *Etude experimentale et numerique de la response de Lactococcus Lactis NCDO2118 aux conditions hydrodynamiques locales en reacteur Couette.* Tese (Doutorado) — Institut National des Sciences Appliquées (INSA) de Toulouse, 2010. Citado na página 39.

DOUAIRE, M. et al. A unique phenotypic modification of lactococcus lactis cultivated in a couette bioreactor. *Biotechnology and Bioengineering*, v. 108, n. 3, p. 559–571, 2010. Citado na página 165.

DUCCI, A.; YIANNESKIS, M. Direct determination of energy dissipation in stirred vessels with two-point lda. *American Institute of Chemical Engineers. AIChE Journal*, v. 51, n. 8, p. 2133–2149, 2005. Citado 2 vezes nas páginas 84 e 85.

DUSTING, J.; BALABANI, S. Mixing in a taylor–couette reactor in the non-wavy flow regime. *Chemical Engineering Science*, v. 64, n. 13, p. 3103–3111, 2009. Citado na página 37.

ECKER, D. M.; JONES, S. D.; LEVINE, H. L. The therapeutic monoclonal antibody market. *mAbs*, v. 7, n. 1, p. 9–14, 2015. Citado 2 vezes nas páginas 11 e 31.

ESCUDIE, R. *Structure locale de l'hydrodynamique générée par une turbine de Rushton.* Tese (Doutorado) — Institut National des Sciences Appliquées (INSA) de Toulouse, 2001. Citado 2 vezes nas páginas 115 e 146.

FRIESS, C.; PONCET, S.; VIAZZO, S. Taylor-couette-poiseuille flows: from rans to les. In: *International Symposium on Turbulence and Shear Flow Phenomena (TSFP-8)*. Poitiers, France: [s.n.], 2013. Citado 8 vezes nas páginas 39, 40, 106, 129, 135, 136, 137 e 142.

GODOY-SILVA, R. et al. Physiological responses of cho cells to repetitive hydrodynamic stress. *Biotechnology and Bioengineering*, v. 103, n. 6, p. 1103–1117, 2009. Citado 4 vezes nas páginas 16, 34, 35 e 172.

GODOY-SILVA, R.; MOLLET, M.; CHALMERS, J. J. Evaluation of the effect of chronic hydrodynamical stresses on cultures of suspensed cho-6e6 cells. *Biotechnology and Bioengineering*, v. 102, n. 4, p. 1119–1130, 2009. Citado 3 vezes nas páginas 34, 35 e 92.

GONG, Y.-W. et al. Age-related responses of suspension cultured taxus cuspidata to hydrodynamic shear stress. *Biochemical Engineering Journal*, v. 32, p. 113–118, 2006. Citado 2 vezes nas páginas 33 e 158.

GREGORIADES, N. et al. Cell damage of microcarrier cultures as a function of local energy dissipation created by a rapid extensional flow. *Biotechnology and Bioengineering*, v. 69, n. 2, p. 171–182, 2000. Citado na página 34.

HARTMANN, H.; DERKSEN, J. J.; AKKER, H. E. A. V. D. Macroinstability uncovered in a rushton turbine stirred tank by means of les. *AICHE JOURNAL*, v. 50, n. Compendex, p. 2383–2393, 2004. Citado na página 161.

HARTMANN, H. et al. Assessment of large eddy and rans stirred tank simulations by means of lda. *Chemical Engineering Science*, v. 59, n. 12, p. 2419–2432, 2004. Citado na página 40.

HAUT, B. et al. Hydrodynamics and mass transfer in a couette–taylor bioreactor for the culture of animal cells. *Chemical Engineering Science*, v. 58, n. 3-6, p. 777–784, 2003. Citado 2 vezes nas páginas 33 e 158.

HEATHMAN, T. R. J. et al. The translation of cell-based therapies: clinical landscape and manufacturing challenges. *Regenerative Medicine*, v. 10, n. 1, p. 49–64, 2015. Citado na página 157.

HEWITT, C. J. et al. Expansion of human mesenchymal stem cells on microcarriers. *Biotechnology Letters*, v. 33, p. 2325–2335, 2011. Citado 5 vezes nas páginas 172, 173, 174, 175 e 176.

HOUT, R. V.; KATZ, J. Measurements of mean flow and turbulence characteristics in high-reynolds number counter-rotating taylor-couette flow. *Physics of Fluids*, v. 23, n. 10, p. 105102–11, 2011. Citado 7 vezes nas páginas 37, 79, 87, 129, 137, 150 e 174.

HUISMAN, S. G. et al. Logarithmic boundary layers in strong taylor-couette turbulence. *Physical Review Letters*, v. 110, n. 26, p. 264501–5, 2013. Citado 4 vezes nas páginas 71, 72, 109 e 127.

HWANG, J.-Y.; YANG, K.-S. Numerical study of taylor-couette flow with an axial flow. *Computers and Fluids*, v. 33, p. 97–118, 2004. Citado 2 vezes nas páginas 163 e 165.

IBRAHIM, S.; NIENOW, A. W. Suspension of microcarriers for cell culture with axial flow impellers. *Chemical Engineering Research and Design*, v. 82, n. A9, p. 1082–1088, 2004. Citado 3 vezes nas páginas 157, 172 e 175.

JAIN, E.; KUMAR, A. Upstream processes in antibody production: Evaluation of critical parameters. *Biotechnology Advances*, v. 26, p. 46–72, 2008. Citado 2 vezes nas páginas 32 e 158.

JEONG, J.; HUSSAIN, F. On the identification of a vortex. *Journal of Fluid Mechanics*, v. 285, p. 69–94, 1995. Citado 2 vezes nas páginas 40 e 115.

JOSHI, J. B.; ELIAS, C. B.; PATOLE, M. S. Role of hydrodynamic shear in the cultivation of animal, plant and microbial cells. *The Chemical Engineering Journal*, v. 62, p. 121–141, 1996. Citado 2 vezes nas páginas 33 e 35.

KAISER, S. C. et al. Fluid flow and cell proliferation of mesenchymal adipose-derived stem cells in small-scale, stirred, single-use bioreactors. *Chemie Ingenieur Technik*, v. 85, n. 1-2, p. 95–102, 2013. Citado 4 vezes nas páginas 172, 173, 174 e 175.

KOBAYASHI, M. et al. An experimental study on turbulent taylor vortex flow between concentric cylinders. *JSME International Journal II*, v. 33, n. 3, p. 436–445, 1990. Citado 19 vezes nas páginas 37, 63, 69, 72, 73, 79, 83, 103, 106, 117, 122, 123, 125, 129, 135, 136, 137, 168 e 169.

KRETZMER, G. Industrial processes with animal cells. *Applied Microbiology Biotechnology*, v. 59, p. 135–142, 2002. Citado 2 vezes nas páginas 31 e 32.

KUNAS, K. T.; PAPOUTSAKIS, E. T. Damage mechanisms of suspended animal cells in agitated bioreactors with and without bubble entrainment. *Biotechnology and Bioengineering*, v. 36, n. 5, p. 476–483, 1990. Citado 5 vezes nas páginas 33, 34, 35, 92 e 175.

LATHROP, D. P.; FINEBERG, J.; SWINNEY, H. L. Transition to shear driven turbulence in couette-taylor flow. *Physical Review A*, v. 46, n. 10, p. 6390–6408, 1992. Citado 5 vezes nas páginas 43, 87, 153, 159 e 174.

LAUNDER, B. E.; REECE, G. J.; RODI, W. Progress in the developments of a reynolds-stress turbulence closure. *Journal of Fluid Mechanics*, v. 68, p. 537–566, 1975. Citado na página 101.

Microcarrier culture systems. In: LUBINIECKI, A. S. (Ed.). *Large scale mammalian cell culture technology*. New York: Marcel Dekker, 1990. Citado na página 157.

LUMLEY, J. L.; NEWMAN, G. R. The return to isotropy of homogenous turbulence. *Journal of Fluid Mechanics*, v. 85, p. 161–178, 1977. Citado na página 146.

LUO, J. Y. et al. Full flow computation of mixing in baffled stirred vessels. *Chemical Engineering Research and Design*, v. 71, n. A3, p. 342–344, 1993. Citado na página 162.

Fermentor design. In: LYDERSEN, B. K.; D'ELIA, N. A.; NELSON, K. L. (Ed.). *Bioprocess engineering: systems, equipment and facilities*. New York: Wiley, 1994. Citado na página 157.

Large scale animal cell culture. In: LYDERSEN, B. K.; D'ELIA, N. A.; NELSON, K. L. (Ed.). *Bioprocess engineering: systems, equipment and facilities*. New York: Wiley, 1994. Citado na página 157.

MA, N.; KOELLING, K. W.; CHALMERS, J. J. Fabrication and use of a transient contractional flow device to quantify the sensitivity of mammalian and insect cells to hydrodynamic forces. *Biotechnology and Bioengineering*, v. 80, n. 4, p. 428–437, 2002. Citado 2 vezes nas páginas 34 e 35.

MASON, C. et al. The global cell therapy industry continues to rise during the second and third quarters of 2012. *Cell Stem Cell*, v. 11, p. 735–739, 2012. Citado na página 157.

MAVROS, P. Flow visualization in stirred vessels: A review of experimental techniques. *Chemical Engineering Research and Design*, v. 79, n. 2, p. 113–127, 2001. Citado na página 37.

MCELIGOT, D. et al. Effects of pressure gradients on entropy generation in the viscous layers of turbulent wall flows. *International Journal of Heat and Mass Transfer*, v. 51, p. 1104–1114, 2008. Citado 5 vezes nas páginas 87, 88, 91, 150 e 151.

MENTER, F. R. Two-equation eddy-viscosity turbulence models for engineering applications. *AIAA Journal*, v. 32, p. 1598–605, 1994. Citado 2 vezes nas páginas 100 e 161.

MENTER, F. R. Review of the shear-stress transport turbulence model experience from an industrial perspective. *International Journal of Computational Fluid Dynamics*, v. 23, n. 4, p. 305 – 316, 2009. Citado 2 vezes nas páginas 101 e 117.

MENTER, F. R.; EGOROV, Y. A scale-adaptive simulation model using two-equation models. In: *43rd AIAA Aerospace Sciences Meeting and Exhibit, January 10, 2005 - January 13, 2005*. [S.l.]: American Institute of Aeronautics and Astronautics Inc., 2005. (43rd AIAA Aerospace Sciences Meeting and Exhibit - Meeting Papers), p. 271–283. Citado na página 117.

MENTER, F. R.; EGOROV, Y. The scale-adaptive simulation method for unsteady turbulent flow predictions. part 1: Theory and model description. *Flow, Turbulence and Combustion*, v. 85, n. 1, p. 113 – 138, 2010. Citado na página 101.

MENTER, F. R. et al. The scale-adaptive simulation method for unsteady turbulent flow predictions. part 2-application to complex flows. *Flow, Turbulence and Combustion*, v. 85, n. 1, p. 139 – 165, 2010. Citado na página 101.

MOLLET, M. et al. Acute hydrodynamic forces and apoptosis: A complex question. *Biotechnology and Bioengineering*, v. 98, n. 4, p. 772–788, 2007. Citado na página 34.

MOLLET, M. et al. Computer simulations of the energy dissipation rate in a fluorescence-activated cell sorter: Implications to cells. *Biotechnology and Bioengineering*, v. 100, n. 2, p. 260–272, 2008. Citado na página 34.

MOLLET, M. et al. Bioprocess equipment: Characterization of energy dissipation rate and its potential to damage cells. *Biotechnology Progress*, v. 20, n. 5, p. 1437–1448, 2004. Citado 2 vezes nas páginas 34 e 172.

NASER, J. A. Prediction of newtonian and non-newtonian flow through concentric annulus with centerbody rotation. In: _____. [S.l.: s.n.], 1997. (International Conference on CFS in Mineral and Metal Processing and Power Generation), p. 273–278. Citado na página 39.

NIENOW, A. W. Reactor engineering in large scale animal cell culture. *Cytotechnology*, v. 50, p. 9–33, 2006. Citado na página 32.

O'CONNOR, K. C. et al. Prolonged shearing of insect cells in a couette bioreactor. *Enzyme and Microbial Technology*, v. 31, n. 5, p. 600–608, 2002. Citado 2 vezes nas páginas 33 e 158.

OGUIC, R.; VIAZZO, S.; PONCET, S. Numerical simulations of a middle gap turbulent taylor-couette-poiseuille flow. *In:Direct and Large Eddy Simmulation IX*, Dresden, 2013. Citado 6 vezes nas páginas 39, 40, 106, 111, 129 e 146.

OZTURK, S. S. Engineering challenges in high density cell culture systems. *Cytotechnology*, v. 22, n. 1-3, p. 3–16, 1996. Citado na página 32.

PAWAR, S. B.; THORAT, B. N. Cfd simulation of taylor–couette flow in scraped surface heat exchanger. *Chemical Engineering Research and Design*, v. 90, n. 3, p. 313–322, 2012. Citado 2 vezes nas páginas 39 e 163.

PIRRO, D.; QUADRIO, M. Direct numerical simulation of turbulent taylor–couette flow. *European Journal of Mechanics - B/Fluids*, v. 27, n. 5, p. 552–566, 2008. Citado 2 vezes nas páginas 39 e 106.

PONCET, S.; HADDADI, S.; VIAZZO, S. Numerical modeling of fluid flow and heat transfer in a narrow taylor–couette–poiseuille system. *International Journal of Heat and Fluid Flow*, v. 32, n. 1, p. 128–144, 2011. Citado 10 vezes nas páginas 39, 106, 111, 129, 135, 137, 142, 146, 161 e 163.

PONCET, S.; VIAZZO, S.; OGUIC, R. Large eddy simulations of taylor-couette-poiseuille flows in a narrow-gap system. *Physics of Fluid*, v. 26, p. 105108–1:27, 2014. Citado 3 vezes nas páginas 71, 72 e 146.

QUADRIO, M.; LICHINI, P. Direct numerical simulation of the turbulent flow in a pipe with annular cross-section. *European Journal of Mechanics B/Fluids*, v. 21, p. 413–427, 2002. Citado na página 39.

SAARENRINNE, P.; PIIRTO, M. Turbulent kinetic energy dissipation rate estimation from piv velocity vector fields. *Experiments in Fluids*, v. 29, n. 1 Supplement, p. 300–307, 2000. Citado na página 61.

SANTIAGO, P. A.; GIORDANO, R. d. C.; SUAZO, C. A. T. Performance of a vortex flow bioreactor for cultivation of cho-k1 cells on microcarriers. *Process Biochemistry*, v. 46, n. 1, p. 35–45, 2011. Citado 5 vezes nas páginas 33, 35, 158, 159 e 172.

SCHNEIDER, M. et al. Bubble free oxygenation by means of hydrophobic porous membranes. *Enzyme and Microbial Technology*, v. 17, n. 9, p. 839–847, 1995. Citado na página 35.

SHARP, K. V.; ADRIAN, R. J. Piv study of small-scale flow structure around a rushton turbine. *American Institute of Chemical Engineers - AIChE*, v. 47, n. 4, p. 766–778, 2001. Citado 4 vezes nas páginas 38, 83, 85 e 148.

SHENG, J.; MENG, H.; FOX, R. O. A large eddy piv method for turbulence dissipation rate estimation. *Chemical Engineering Science*, v. 55, n. 20, p. 4423–434, 2000. Citado na página 37.

SINGH, H. *Modelling of shear sensitive cells in stirred tank reactor using computational fluid dynamics*. Tese (Doutorado) — University of Canterbury, Christchurch, New Zealand, 2011. Citado 3 vezes nas páginas 36, 92 e 175.

SINGH, H.; FLETCHER, D. F.; J., N. J. An assessment of different turbulence models for predicting flow in a baffled tank stirred with a rushton turbine. *Chemical Engineering Science*, v. 66, n. 23, p. 5976–5988, 2011. Citado 5 vezes nas páginas 40, 102, 159, 161 e 176.

SINGH, V. Disposable bioreactor for cell culture using wave-induced agitation. *Cytotechnology*, v. 30, n. 1-3, p. 149–158, 1999. Citado na página 32.

SMIRNOV, P. E.; MENTER, F. R. Sensitization of the sst turbulence model to rotation and curvature by applying the spalart-shur correction term. *Journal of Turbomachinery*, v. 131, n. 4, p. 1–8, 2009. Citado 2 vezes nas páginas 102 e 161.

SMITH, C. G.; GREENFIELD, P. F. Mechanical agitation of hybridoma suspension cultures: Metabolic effects of serum, pluronic f68, and albumin supplements. *Biotechnology and Bioengineering*, v. 40, n. 9, p. 1045–1055, 1992. Citado 3 vezes nas páginas 36, 92 e 175.

SMITH, G. P.; TOWNSEND, A. A. Turbulent couette flow between concentric cylinders at large taylor numbers. *Journal of Fluid Mechanics*, v. 123, p. 187–217, 1982. Citado 2 vezes nas páginas 37 e 106.

SOBOLICK, V. et al. Wall shear rates in taylor vortex flow. *Journal of Applied Fluid Mechanics*, v. 4, n. 2, p. 25–31, 2011. Citado na página 163.

SPALART, P. R.; SHUR, M. On the sensitization of turbulence models to rotation and curvature. *Aerospace Science and Technology*, v. 1, n. 5, p. 297–302, 1997. Citado na página 102.

In: STANBURY, P. F.; WHITAKER, A.; HALL, S. J. (Ed.). *Principles of fermentation technology. 2nd ed.* Oxford: Elsevier, 1995. Citado na página 157.

STANISLAS, M. et al. Main results of the third international piv challenge. *Experiments in Fluids*, v. 45, p. 27–71, 2008. Citado na página 38.

SUBRAMANIAN, R. S. *Viscous Dissipation Term*. 2015. Disponível em: <http://web2.clarkson.edu/projects/subramanian/ch560/notes/ViscousDissipation.pdf>. Citado na página 47.

TANZEGLOCK, T. *A Novel Lobed Taylor-Couette Bioreactor for the Cultivation of Shear Sensitive Cells and Tissues*. Tese (Doutorado) — Technical University Braunschweig, Germany, 2008. Citado 2 vezes nas páginas 33 e 158.

THOMAS, C. R.; AL-RUBEAI, M.; ZHANG, Z. Prediction of mechanical damage to animal cells in turbulence. *Cytotechnology*, v. 15, n. 1-3, p. 329–335, 1994. Citado na página 34.

TOKGOZ, S. et al. Spatial resolution and dissipation rate estimation in taylor–couette flow for tomographic piv. *Experiments in Fluids*, v. 53, n. 3, p. 561–583, 2012. Citado 10 vezes nas páginas 11, 37, 38, 58, 62, 84, 87, 129, 150 e 174.

TRAMPER, J. et al. Shear sensitivity of insect cells in suspension. *Enzyme and Microbial Technology*, v. 8, n. 1, p. 33–36, 1986. Citado 2 vezes nas páginas 34 e 35.

VIAZZO, S. et al. High-order large eddy simulations of confined rotor-stator flows. *Flow, Turbulence and Combustion*, v. 88, n. 1-2, p. 63–75, 2012. Citado na página 129.

WANG, L.; OLSEN, M. G.; VIGIL, R. D. Reappearance of azimuthal waves in turbulent taylor–couette flow at large aspect ratio. *Chemical Engineering Science*, v. 60, n. 20, p. 5555–5568, 2005. Citado na página 37.

WANG, L.; VIGIL, R. D.; FOX, R. O. Cfd simulation of shear-induced aggregation and breakage in turbulent taylor–couette flow. *Journal of Colloid and Interface Science*, v. 285, n. 1, p. 167–178, 2005. Citado na página 163.

WEICKERT, M. et al. Investigation of the les wale turbulence model within the lattice boltzmann framework. *Computers and Mathematics with Applications*, v. 59, n. 7, p. 2200–2214, 2010. Citado na página 40.

WENDT, F. Turbulente strömungen zwischen zwei rotierenden konaxialen zylindern. *Ing Arch*, v. 4, p. 577–595, 1933. Citado 7 vezes nas páginas 43, 46, 87, 127, 153, 165 e 173.

WERELEY, S. T.; LUEPTOW, R. M. Spatio-temporal character of non-wavy and wavy taylor–couette flow. *Journal of Fluid Mechanics*, v. 364, p. 59–80, 1998. Citado na página 37.

WERELEY, S. T.; LUEPTOW, R. M. Velocity field for taylor-couette flow with an axial flow. *Physics of Fluids*, v. 11, n. 12, p. 3637–3649, 1999. Citado na página 165.

WU, J.; GOOSEN, M. F. A. Evaluation of the killing volume of gas bubbles in a sparged animal cell culture bioreactors. *Enzyme and Microbial Technology*, v. 17, p. 1063–1042, 1995. Citado na página 35.

WURM, F. M. Production of recombinant protein therapeutics in cultivated mammalian cells. *Nature Biotechnology*, v. 22, n. 11, p. 1393–1398, 2004. Citado na página 32.

YEOH, S. L. et al. Large eddy simulation of turbulent flow in a rushton impeller stirred reactor with sliding-deforming mesh methodology. *Chemical Engineering and Technology*, v. 27, n. 3, p. 257–263, 2004. Citado na página 162.

YEOH, S. L.; PAPADAKIS, G.; YIANNESKIS, M. Numerical simulation of turbulent flow characteristics in a stirred vessel using the les and rans approaches with the sliding/deforming mesh methodolgy. *Institution of Chemical Engineering*, v. 82, n. A7, p. 834–848, 2004. Citado na página 162.

ZHU, X. H. et al. Study of cell seeding on porous poly(d,l-lactic-co-glycolic acid) sponge and growth in a couette–taylor bioreactor. *Chemical Engineering Science*, v. 65, n. 6, p. 2108–2117, 2010. Citado 2 vezes nas páginas 33 e 158.

APÊNDICE A – Matlab File

This matlab file was used to create the matrix structure of the velocity vectors from the *.txt files obtained from the PIV image files. These velocity vectors were then used to estimate the mean and fluctuating velocity components, and their gradients to estimate the VEDR. These files are for 2D PIV method, the numerical method is 3D and is very similar to this 2D PIV methodology. Therefore, only the 2D PIV matlab file is presented here.

```
%% In This section we read the data
clear all;
close all;
clf
%%%%%%%%%%%%%%%%%%%%%%%%%%%%%%%%%%%%%%%%%%%%%%%%%%%%%%%%%%%%%%%%%
% Program for the treatment of the PIV data                   %%%
% First written by Gabelle JC et Line Alain on Novembre 2011  %%%
% Modified by Harminder Singh on July 2013                    %%%
%%%%%%%%%%%%%%%%%%%%%%%%%%%%%%%%%%%%%%%%%%%%%%%%%%%%%%%%%%%%%%%%%
tic % In order to estimate the time that will take to Finish
% has to follow by a "toc" in the end
%%%%%%%%%%%%%%%%%%%%%%%%%%%%%%%%%%%%%%%%%%%
%%%%%%%%%%%%%%%%%%%%%%%%%%%%%%%%%%%%%%%%%%%
Tot = 2499;
%%%%%%%%%%%%%%%%%%%%%%%%%%%%%%%%%%%%%%%%%%%

%%%%%%%%%%%%%%%%%%%%%%%%%%%%%%%%%%%%%%%%%%%%%%%%%%%%%%%%%%%%%%%%%%%%%%%%%
% Start of the programm %%%%%%%%%%%%%%%%%%%%%%%%%%%%%%%%%%%%%%%%%%%%%%%%%
% Initialising the no of figures
n_figure = 0 ;

%Name of the files to be read
file = (114rpm.3p0qjdkr.);

% First reading of the file to define the size of the vectors
num=1;
% concatenation for the name of the document
imag=strcat(file,00000,num2str(num),.txt);

fid1 =  fopen(imag,r);

[a b x y u v st] = textread(imag,%f%f%f%f%f%f%f,headerlines,6);
% headerlines,6 tells matlab not to read first six lines because those
```

```
  % are just text and not data.

% First, the matrix of the coordinates is created
% X is no of lines and Y represent columns
%With reference to PIV, Y represent the radial direction, and X represent
%the X-axis

NY=249;
NX=299;
X=zeros(NX,NY);
Y=zeros(NX,NY);

for j=1:NX
    X(j) = x(1+(j-1)*NY);
    for i=1:NY
        X(j,i)=x(1+(j-1)*NY);
    end
end
for l=1:NX
    for k=1:NY
        Y(l,k)=y(k);
    end
end

    status=fclose(fid1);

% Intialising the vectors
U=zeros(NX,NY,Tot);
V=zeros(NX,NY,Tot);
St=zeros(NX,NY,Tot);
% Reading of the velocity vectors
for num=1:Tot

    if num<=9;
        % concatenation for the name of the file
      imag=strcat(file,00000,num2str(num),.txt);
    end

    if num>9;
      imag=strcat(file,0000,num2str(num),.txt);
    end

    if num>99;
      imag=strcat(file,000,num2str(num),.txt);
    end

    if num>999;
```

```
      imag=strcat(file,00,num2str(num),.txt);
    end

    fid1 =  fopen(imag,r);

  [a b x y u v st] = textread(imag, %f%f%f%f%f%f%f,headerlines,6);
  % headerlines,6 tells matlab not to read first six lines because those
  % are just text and not data.

%Matrix of velocity vector is created

   for j=1:NX
       for k=1:NY
           i=(j-1)*NY+k;
           U(j,k,num)=u(i);
           V(j,k,num)=v(i);
           St(j,k,num)=st(i);
       end
   end

    status=fclose(fid1);

end

save Data_champs Tot NX NY Y X U V St -v7.3

% Initialising of vectors
UmeanCM=zeros(NX,NY);
VmeanCM=zeros(NX,NY);
uflucCM=zeros(NX,NY,Tot);
vflucCM=uflucCM;
uflucFM=zeros(NX,NY,Tot);
vflucFM=uflucFM;
u2CM=uflucFM;
v2CM=u2CM;
uvCM=u2CM;
u2meanCM=zeros(NX,NY);
v2meanCM=zeros(NX,NY);
uvmeanCM=zeros(NX,NY);

% Calculating the averaged velocity components by neglecting the modified
% vectors, and thus considering only the vectors that were actually
% present in the PIV grid and neglecting the vectors which were estimated
% as the mean of the neighbours. These vectors are termed as CM in the end

 for j=1:NX
     for k=1:NY
```

```
          Ind(j,k)=0;
          for num=1:Tot
              if St(j,k,num)==0
                  Ind(j,k)=Ind(j,k)+1;
                  UmeanCM(j,k)=UmeanCM(j,k)+U(j,k,num);
                  VmeanCM(j,k)=VmeanCM(j,k)+V(j,k,num);
              end
          end
          UmeanCM(j,k)=UmeanCM(j,k)/Ind(j,k);
          VmeanCM(j,k)=VmeanCM(j,k)/Ind(j,k);
     end

 end

 %Similarly calculating the fluctuating velocity components by neglecting
 %the modified vectors.

  for j=1:NX
     for k=1:NY
           Ind1(j,k)=0;
          for num=1:Tot
              if St(j,k,num)==0
                  Ind1(j,k)=Ind1(j,k)+1;
                  uflucCM(j,k,num)=U(j,k,num)-UmeanCM(j,k);
                  vflucCM(j,k,num)=V(j,k,num)-VmeanCM(j,k);
                  u2CM(j,k,num)= uflucCM(j,k,num)* uflucCM(j,k,num);
                  v2CM(j,k,num)= vflucCM(j,k,num)* vflucCM(j,k,num);
                  uvCM(j,k,num)= uflucCM(j,k,num)* vflucCM(j,k,num);
                  u2meanCM(j,k)=u2meanCM(j,k)+u2CM(j,k,num);
                  v2meanCM(j,k)=v2meanCM(j,k)+v2CM(j,k,num);
                  uvmeanCM(j,k)=uvmeanCM(j,k)+uvCM(j,k,num);
              end
          end
         u2meanCM(j,k)=u2meanCM(j,k)/Ind1(j,k);
         v2meanCM(j,k)=v2meanCM(j,k)/Ind1(j,k);
         uvmeanCM(j,k)=uvmeanCM(j,k)/Ind1(j,k);
     end
  end

save Data_meanCM Tot NX NY X Y UmeanCM VmeanCM u2meanCM v2meanCM uvmeanCM
save Data_flucCM Tot NX NY X Y uflucCM vflucCM u2CM v2CM uvCM -v7.3

%Calculating the mean of all of the vectors over the total number of time
%steps, and termed as FM in the end
UmeanFM=mean(U,3);
VmeanFM=mean(V,3);

```

```

%Calculating the fluctuating velocity components of all of the vectors
%
for i = 1:Tot
    uflucFM(:,:,i)=U(:,:,i)-UmeanFM(:,:);
    vflucFM(:,:,i)=V(:,:,i)-VmeanFM(:,:);
end
%
u2FM=uflucFM.*uflucFM;
v2FM=vflucFM.*vflucFM;
uvFM=uflucFM.*vflucFM;
u2meanFM=mean(u2FM,3);
v2meanFM=mean(v2FM,3);
uvmeanFM=mean(uvFM,3);

save Data_meanFM Tot NX NY X Y UmeanFM VmeanFM u2meanFM v2meanFM uvmeanFM
save Data_flucFM Tot NX NY X Y uflucFM vflucFM u2FM v2FM uvFM -v7.3


% tests if the results are acceptable (makes sense) or not
n_figure=n_figure+1;
figure(n_figure)
toto=reshape(UmeanCM,NX*NY,1);hist(toto,50)

n_figure=n_figure+1;
figure(n_figure)
toto1=reshape(VmeanCM,NX*NY,1);hist(toto1)

n_figure=n_figure+1;
figure(n_figure)
tata=reshape(u2meanCM,NX*NY,1);hist(tata,50)

n_figure=n_figure+1;
figure(n_figure)
tata1=reshape(v2meanCM,NX*NY,1);hist(tata1,50)

n_figure=n_figure+1;
figure(n_figure)
tata2=reshape(uvmeanCM,NX*NY,1);hist(tata2,50)


% From these figures we choose the data that is between the inner and outer
% cylinder walls, neglecting the rest

Ynew=Y((34:133),(16:241));
Xnew=X((34:133),(16:241));
Unew=U((34:133),(16:241),:);
```

```
Vnew=V((34:133),(16:241),:);
Stnew=St((34:133),(16:241),:);
Umoynew=UmeanCM((34:133),(16:241));
Vmoynew=VmeanCM((34:133),(16:241));
uflucnew=uflucCM((34:133),(16:241),:);
vflucnew=vflucCM((34:133),(16:241),:);
u2new=u2CM((34:133),(16:241),:);
v2new=v2CM((34:133),(16:241),:);
uvnew=uvCM((34:133),(16:241),:);
u2meannew=u2meanCM((34:133),(16:241));
v2meannew=v2meanCM((34:133),(16:241));
uvmeannew=uvmeanCM((34:133),(16:241));
UmoyFMnew=UmeanFM((34:133),(16:241));
VmoyFMnew=VmeanFM((34:133),(16:241));
uflucFMnew=uflucFM((34:133),(16:241),:);
vflucFMnew=vflucFM((34:133),(16:241),:);
u2FMnew=u2FM((34:133),(16:241),:);
v2FMnew=v2FM((34:133),(16:241),:);
uvFMnew=uvFM((34:133),(16:241),:);
u2FMmeannew=u2meanFM((34:133),(16:241));
v2FMmeannew=v2meanFM((34:133),(16:241));
uvFMmeannew=uvmeanFM((34:133),(16:241));

Ycut=Ynew;
Xcut=Xnew;
Ucut=Unew;
Vcut=Vnew;
Stcut=Stnew;
UmeancutCM=Umoynew;
VmeancutCM=Vmoynew;
uflucCutCM=uflucnew;
vflucCutCM=vflucnew;
u2cutCM=u2new;
v2cutCM=v2new;
uvcutCM=uvnew;
u2meancutCM=u2meannew;
v2meancutCM=v2meannew;
uvmeancutCM=uvmeannew;
UmeancutFM=UmoyFMnew;
VmeancutFM=VmoyFMnew;
uflucCutFM=uflucFMnew;
vflucCutFM=vflucFMnew;
u2cutFM=u2FMnew;
v2cutFM=v2FMnew;
uvcutFM=uvFMnew;
u2meancutFM=u2FMmeannew;
v2meancutFM=v2FMmeannew;
```

```
uvmeancutFM=uvFMmeannew;


NXcut=133-34+1;
NYcut=241-16+1;

Totcut=Tot;
%%%%%%%%%%%%%%%%%%%%%%%%%%%%%%%%%%%%%%%%%%%%%%%%%%%%%%%%%%%%
% saving all the data in seperate files in order to keep a small size,
% otherwise a single file may become 100s of Gigabytes
save Data_champscut Totcut NXcut NYcut Ycut Xcut Ucut Vcut Stcut
save Data_meanCCM UmeancutCM VmeancutCM u2meancutCM v2meancutCM uvmeancutCM
save Data_fluccutCM uflucCutCM vflucCutCM u2cutCM v2cutCM uvcutCM
save Data_meanCFM UmeancutFM VmeancutFM u2meancutFM v2meancutFM uvmeancutFM
save Data_fluccutFM uflucCutFM vflucCutFM u2cutFM v2cutFM uvcutFM

%% In this section, the VEDR of Mean flow kinetic energy is estimated

%%%%%%%%%%%%%%%%%%%%%%%%%%%%%%%%%%%%%%%%%%%%%%%%%%%%%%%%%%%%%%%%%
% Program for the treatment of the PIV data                   %%%
% Written by Harminder Singh on July 2013                     %%%
%%%%%%%%%%%%%%%%%%%%%%%%%%%%%%%%%%%%%%%%%%%%%%%%%%%%%%%%%%%%%%%%%


% we have velocity as radial and tangential components, so we have
% to generate VEDR in cylindrical co-ordinates as
% VEDR=mu*(2(durdrsq+(1/rduthdth+ur/r)2+duzdzsq)+(rd(uth/r)dr+1/rdurdth)2+
%  (1/rduzdth+duthdz)2+(durdz+duzdr)2
% % r is radial direction with changing gradients in meteres
Y=Ycut(1,:);
X=Xcut(:,1);
L=length(Y);
C=length(X);

th=atan((Xcut./1000)./(Ycut./1000));
r=Ycut;

dth=zeros(C,L);
%
for i=2:C
    for j=1:L
        dth(i,j)=(-th(i,j)+th(i-1,j));
    end
end

dr=(r(1,3)-r(1,1))/1000; % Radial gradient and equivalent of 2*dr

```

```
Ra=r;

durdthmf=zeros(C,L);
duthdthmf=durdthmf;
durdrmf=durdthmf;
duthdrmf=durdthmf;

for j=2:C
    for i=2:L-1

durdthmf(j,i)=(VmeancutFM(j,i+1)-VmeancutFM(j,i-1))./(2.*dth(j,i));
duthdthmf(j,i)=((UmeancutFM(j,i+1)-UmeancutFM(j,i-1))./(2.*dth(j,i)))
./Ra(j,i)+VmeancutFM(j,i)./Ra(j,i);
durdrmf(j,i)=(VmeancutFM(j,i+1)-VmeancutFM(j,i-1))./dr;
duthdrmf(j,i)=(((UmeancutFM(j,i+1)./Ra(j,i+1))-(UmeancutFM(j,i-1)
./Ra(j,i-1)))./dr).*Ra(j,i);
    end
end

save Data_MeanGrad durdthmf duthdthmf durdrmf duthdrmf -v7.3

durdthduthdrmf=durdthmf.*duthdrmf;
durdthsqmf=durdthmf.^2;
durdrsqmf=durdrmf.^2;
duthdthsqmf=duthdthmf.^2;
duthdrsqmf=duthdrmf.^2;

save Data_MeanGradSq durdthduthdrmf durdthsqmf durdrsqmf duthdthsqmf
duthdrsqmf -v7.3

nu=1e-06;
VEDRmf=nu*(2*(duthdthsqmf+durdrsqmf)+meandurdthsqmf+duthdrsqmf+2*durdthduthdrmf);

save Data_VEDRMF VEDRmf
%% Now, the turbulence VEDR is estimated

%%%%%%%%%%%%%%%%%%%%%%%%%%%%%%%%%%%%%%%%%%%%%%%%%%%%%%%%%%%%%%%%%
% Program for the treatment of the PIV data                   %%%
% Written by Harminder Singh on July 2013                     %%%
%%%%%%%%%%%%%%%%%%%%%%%%%%%%%%%%%%%%%%%%%%%%%%%%%%%%%%%%%%%%%%%%%

durdthT=zeros(C,L,Totcut);
duthdthT=durdthT;
durdrT=durdthT;
duthdrT=durdthT;

for j=2:C
```

```
    for i=2:L-1

durdthT(j,i,:)=(vflucCutFM(j,i+1,:)-vflucCutFM(j,i-1,:))./(2.*dth(j,i));
duthdthT(j,i,:)=((uflucCutFM(j,i+1,:)-ufluc_CutFM(j,i-1,:))./(2.*dth(j,i)))
./Ra(j,i)+vflucCutFM(j,i,:)./Ra(j,i);
durdrT(j,i,:)=(vflucCutFM(j,i+1,:)-vflucCutFM(j,i-1,:))./(dr);
duthdrT(j,i,:)=(((uflucCutFM(j,i+1,:)./Ra(j,i+1))-(uflucCutFM(j,i-1,:)
./Ra(j,i-1)))./(dr)).*Ra(j,i);
    end
end


save Data_FlucGrad durdthT duthdthT durdrT duthdrT -v7.3

durdthduthdrT=durdthT.*duthdrT;
durdthsqT=durdthT.^2;
durdrsqT=durdrT.^2;
duthdthsqT=duthdthT.^2;
duthdrsqT=duthdrT.^2;

save Data_FlucGrad durdthduthdrT durdthsqT durdrsqT duthdthsqT duthdrsqT -v7.3


mdurdthsqT=mean(durdthsqT,3);
mduthdthsqT=mean(duthdthsqT,3);
mdurdrsqT=mean(durdrsqT,3);
mduthdrsqT=mean(duthdrsqT,3);
mdurdthduthdrT=mean(durdthduthdrT,3);

save Data_FlucGradM mdurdthsqT mduthdthsqT mdurdrsqT mduthdrsqT mdurdthduthdrT


nu=1e-06;
TEDR=nu*(2*(mduthdthsqT+mdurdrsqT)+mdurdthsqT+mduthdrsqT+2*(mdurdthduthdrT));

save Data_TEDR TEDR

%%
```

Índice

Chine hamster ovary, 33
Computational fluid dynamics, 37

Direct numerical simulation, 39

Interrogation cell size, 37

Large eddy simulation, 39
Laser Doppler anemometry, 37

Mean flow kinetic energy, 47
Multiple reference frame, 102

Off-bottom clearance, 44

Particle image velocimetry, 37

Reynolds averaged Navie-Stokes, 39
Reynolds stress model, 39
Root mean square, 105

Scale adaptive simulation, 40
Shear stress transport, 40
Sub grid scale, 98

Taylor vortex bioreactor, 33
Turbulent kinetic energy, 39

Visocus energy dissipation rate, 34

Wall adapting local eddy, 40